NANOSCALE CHARACTERIZATION OF ELECTROLYTE DIFFUSION, INTERFACE MORPHOLOGY DISRUPTION AND SURFACE DYNAMICS OF POLYMER MELT FILMS ADSORBED ON GRAPHENE

A Dissertation
Presented to
The Graduate Faculty of The University of Akron

In Partial Fulfillment
of the Requirements for the Degree
Doctor of Philosophy

Feipeng Yang
December, 2018

NANOSCALE CHARACTERIZATION OF ELECTROLYTE DIFFUSION, INTERFACE MORPHOLOGY DISRUPTION AND SURFACE DYNAMICS OF POLYMER MELT FILMS ADSORBED ON GRAPHENE

Feipeng Yang

Dissertation

Approved:	Accepted:
Advisor Dr. Mark D. Foster	Department Chair Dr. Tianbo Liu
Co-advisor Dr. Mark D. Soucek	Dean of the College Dr. Ali Dhinojwala
Committee Chair Dr. Mesfin Tsige	Dean of the Graduate School Dr. Chand Midha
Committee Member Dr. Ali Dhinojwala	Date
Committee Member Dr. Qixin Zhou	

ABSTRACT

Significant efforts have been made to understand corrosion since it is important both scientifically and technologically, as the direct cost resulting from corrosion and its prevention has become a non-negligible portion of the gross domestic product. While considerable effort has been made to understand the macroscopic corrosion behavior and empirical knowledge of effective corrosion mitigation strategies is available, a nanoscale description of corrosion processes is still lacking. This dissertation describes efforts to establish a fundamental understanding of the corrosion process at the coating/metal interface on the nanoscale.

The dissertation is divided into three parts. In the first part, a nanoscale depiction of the influence of ions on the diffusion of water is garnered from the analysis of X-ray and neutron reflectivity (XR/NR) and electrochemical impedance spectroscopy (EIS) data since metal, water and oxygen are three key ingredients in corrosion and ions play an important part in accelerating corrosion. The diffusion of water or electrolyte in thin polymeric films in different directions, parallel to the film or perpendicular to it, was distinguished. XR/NR measurements were used to probe the diffusion parallel to the film using a customized diffusion cell and that rate was found to be orders of magnitude larger than the diffusion rate in bulk epoxy. In contrast, when EIS data were analyzed using equivalent electrical circuit (EEC) model fitting, the penetration (diffusion perpendicular to the film) rate was found to be orders of magnitude smaller than the diffusion rate in bulk epoxy. Consistent results from XR, NR and EIS showed that the diffusion rates of electrolyte in both the lateral and perpendicular directions are lower than those of water (H_2O/D_2O), and that the higher the ion concentration, the lower the rate of diffusion. Reflectivity measurements probing at small (nm) length scales and also comparatively short times (hours) complement the widespread use of EIS and provide a means of quantitatively investigating phenomena that occur rapidly as a first step in the metallic substrate corrosion.

The second part of this dissertation provides a detailed description of the changes in an epoxy/aluminum interface morphology that occur upon exposure of the interface to water or electrolytes, with information derived from X-ray off-specular scattering and atomic force microscopy (AFM). The interface is quantitatively described using a self-affine model of a randomly rough interface based on height difference correlation function with parameters of roughness, jaggedness, and correlation length. “Rocking curve” measurements show the interface becomes more rough, the texture becomes more jagged and the correlation length becomes smaller. Different electrolytes (NaCl and NaI aqueous solutions) have similar effects on the disruption of the interface morphology, and H_2O is less disruptive to the interface as compared to the two electrolytes.

In the last part of this dissertation, the surface fluctuations of polystyrene (PS) melt films adsorbed on graphene are compared to the surface fluctuations on films adsorbed on single crystal silicon wafers. The surface fluctuations on polymer thin films have received

intense interest since surface fluctuations influence important interfacial properties such as wetting, adhesion, and tribology. Additionally, for sufficiently thin films the surface fluctuations also reflect realities of the chain adsorption and organization at the interface with the substrate and those features of films should be important for dictating the resistance to water or electrolyte incursion at a substrate/film or matrix/filler interface. For $8R_g$ thick entangled linear polystyrene (PS) films on silicon ($8R_g$ PS/Si) the surface fluctuations can be described using a hydrodynamic continuum theory (HCT), which assumes the thin film viscosity is equivalent to the bulk viscosity throughout its entire depth. For 131000 g/mol linear PS, when the thickness of the film is less than $4R_g$, the surface fluctuations show confinement effects and the fluctuations are slowed. The surface fluctuations for an $8R_g$ thick PS film on graphene ($8R_g$ PS/Graphene) are three orders of magnitude slower than those on $8R_g$ PS/Si. The 170°C data from the $3R_g$ PS/Si, $8R_g$ PS/Si and $8R_g$ PS/Graphene samples collapse on a universal curve using a two-layer model with a 75 nm (ca. $7R_g$) thick highly viscous layer on graphene and a 14 nm (ca. $1.5R_g$) thick highly viscous layer on silicon. The layer left after a rinsing and drying procedure reflects a 2.4 times thicker strongly adsorbed layer on graphene compared to that on silicon. Thus the effect of adsorption of melt PS chains on graphene on dynamics of the chains near the graphene is far more profound than the effect of adsorption of PS chains on silicon. This remarkable slowing of material near the polymer/graphene interface could have important implications for the performance of other graphene containing composites and coating systems when the polymer is able to interact as strongly with graphene as does PS.

DEDICATION

To my parents, Caiwang Yang and Yanxia Wang,

my cousin, Mengqi Lu, and my wife, Xiaohui Zhang

ACKNOWLEDGEMENTS

I would like to acknowledge my advisor, Dr. Mark D. Foster in the Department of Polymer Science, and my co-advisor, Dr. Mark D. Soucek in the Department of Polymer Engineering, for their guidance and support in the last five years. I would like to thank Dr. Mesfin Tsige in the Department of Polymer Science, for his help in simulation in my graphene research and for the helpful discussions throughout my doctoral studies. I also would like to express my gratitude to Dr. Ali Dhinojwala in the Department of Polymer Science and Dr. Qixin Zhou in the Department of Chemical and Biomolecular Engineering for their insightful thoughts and practical wisdom from which I benefited significantly.

I am deeply impressed by Dr. Suresh Narayanan at Advanced Photon Source (APS), Argonne National Laboratory because of his rigorous scholarship and profound knowledge. I am sincerely grateful not only for his professional guidance during our beam time at 8-ID-I, but also for the concern he showed for the next generation of scientists and engineers. I would like to thank Dr. Zhang Jiang for his professional help with the analysis of some scattering data. I also thank Ms. Jenia (Evguenia) Karapetrova for her help during my beam time at 33-BM-C.

I would like to thank Dr. Guangcui Yuan, Dr. Brian Kirby, and Dr. Brian Maranville for their help during my beam times at NIST Center for Neutron Research beam lines

Neutron Reflectometer Horizontal Sample (NG7), Polarized Beam Reflectometer (PBR), and Off-Specular Reflectometer (MAGIK), respectively.

I appreciate the help from Dr. Yu Zhu in the Department of Polymer Science and his students, Mr. Kewei Liu, Ms. Leyao Zhou. I would also like to extend my gratitude to Dr. Zhenmeng Peng in the Department of Chemical and Biomolecular Engineering, and his student, Mr. Yanbo Pan. The graphene work would never have been possible without their help. I am deeply grateful to Dr. Yu Zhu and Dr. Stephen Z.D. Cheng for their insightful suggestions on the characterization.

I sincerely appreciate Dr. Coleen Pugh in the Department of Polymer Science, Dr. Xinru Jia, Dr. Yun Yan and Dr. Jianbin Huang from Peking University, Dr. Chunying Shu from the Institute of Chemistry Chinese Academy of Sciences (ICCAS), Dr. Lining Gao and Dr. Peijun Xu from Chang'an University. Without the help from any of them, I would not have been able to make this work possible.

I would also like to thank Edward Laughlin, a staff member of the Department of Polymer Science, and Owen Steven Roberts, the instrument technician of the Department of Chemical and Biomolecular Engineering, for their efforts in fixing equipment. I appreciate Dr. Zhorro George Nikolov, the instrumentation scientist at National Polymer Innovation Center (NPIC), for the maintenance of the Surface and Optical Analysis (SOA) Facility. I also appreciate the help from Melissa Bowman, an administrative staff member of the Department of Polymer Science, who replied to plenty of my emails during the process of my application for the Ph.D. program here at The University of Akron.

I appreciate the help from the group members of both my research groups. I acknowledge the support of National Institute of Standards and Technology, U.S. Department of Commerce, in providing the neutron research facilities used in this work. This research used resources of the Advanced Photon Source, a U.S. Department of Energy (DOE) Office of Science User Facility operated for the DOE Office of Science by Argonne National Laboratory under Contract No. DE-AC02-06CH11357.

I would like to wholeheartedly thank my parents in China for their unconditional support. I was lucky to be born in a time, probably the best of times in the last several hundred years in the history of my motherland (The People's Republic of China), right in the process of her rejuvenation. I hope I can make my own contribution to this historic process.

This dissertation is dedicated to my father Caiwang Yang, my mother Yanxia Wang, who devoted to their entire career to the cause of education in China; my cousin, Mengqi Lu, who is pursuing her doctorate in oncology; and also my lovely wife, Xiaohui Zhang.

TABLE OF CONTENTS

Page

CHAPTER

LIST OF TABLES

LIST OF FIGURES

Figure Page

CHAPTER I

INTRODUCTION

"There's plenty of room at the bottom."

—Dr. Richard P. Feynman (Pasadena, December 1959)

Half a century ago, Dr. Feynman delivered his famous lecture at the annual American Physical Society meeting at Pasadena, which is considered as the inception of the nanotechnology, and it develops rapidly since then. However, despite the importance of corrosion from the perspective of both science and technology and the large amount of efforts made to the understanding of macroscopic corrosion behavior, a nanoscale depiction of corrosion process is still not available[1].

Corrosion is the reaction of a metal with its environment with a subsequent deterioration in properties[2]. With the protection from organic coatings, corrosion of the metal initiated by water or electrolyte usually happens at the organic coating/metal substrate interface. The direct economic cost resulting from corrosion and its preventative methods is accountable for a non-negligible portion of the gross domestic product[3]. In addition, subsidiary costs associated with corrosion include environmental catastrophes and casualties usually from sudden failure of load-bearing components. Outdoor exposure and accelerated weathering are the two methods widely used in industry to evaluate the performance of an organic coating, both of them are based on empirical evaluations and are time consuming. A characterization method with the resolution on the order of nanometers, i.e. from the “bottom”, would make such evaluations faster, help understand how water or electrolyte diffuse to the coating/metal interface, and how corrosion happens on a much smaller scale.

In the study of the water or electrolyte diffusion, gravimetric methods[4], Fourier transform infrared spectroscopy (FT-IR)[4–9], scanning Kelvin probe (SKP)[9–13], computed tomography (CT)[14] and fluorescence microscopy[15] have been used in the investigation of water uptake. In the first part of this dissertation, with implementation of X-ray/neutron reflectivity (XR/NR) with resolution on the order of nanometers, and electrochemical impedance spectroscopy (EIS) as a complementary method, we have distinguished the diffusion in both lateral and perpendicular directions with respect to the thin film surface. The lateral diffusion rate was orders of magnitude larger compared with that in bulk epoxy, while the penetration rate was orders of magnitude smaller than that in bulk epoxy. Results from XR, NR and EIS indicated that in both directions the diffusion rate of electrolyte was slower than that of H_2O/D_2O, and with an increasing in ionic concentration, the diffusion rate of electrolyte decreased. Probing on such short length scales also makes it possible to study changes that happen rapidly as a first step in the metallic substrate corrosion process.

The second part gives results from the interrogation of the interface morphology between a metal substrate and an anti-corrosion organic coating using X-ray off-specular scattering with atomic force microscopy (AFM) as a complementary technique. Such efforts were built on pioneering scattering studies on an analytical rough surface model which regards the surface as composed of randomly disposed mirror-like facets by Torrance et al.[16] in the 1960s, and theoretical description of such rough surface scattering by Sinha et al.[17] in the 1980s. Later in the 1990s, Schwarz et al.[18] characterized the off-specular scattering of the water-vapor interface, Sinha et al.[19,20] did a time-resolved, in situ off-specular scattering measurements to study the electrochemical pitting of Cu surfaces in electrolyte, Müller-Buschbaum et al.[21,22] showed with "detector scan" off-specular measurements that supported spun-cast polymer films had surface morphologies conformal with the polymer substrate interface. Singh et al.[23] used off-specular neutron scattering to describe the morphologies from two interfaces associated with a corroded Ni film. Simultaneous analyses of X-ray off-specular scattering measurements and AFM images showed that this buried interface was roughened on the scale of nanometers with water or electrolyte exposure of the coating and that the details of this roughening differ with the type of crosslinker used in the epoxy coating. With exposure the texture also becomes more jagged and the correlation length becomes smaller from the results of "rocking curve" measurements. The effects of different electrolytes and H_2O were also compared, NaCl and NaI solutions disrupt the interface morphology similarly, and H_2O has less capability in disrupting the interface compared with both electrolytes.

The last part of this dissertation, discusses the surface fluctuations of polystyrene (PS) thin melt films adsorbed on graphene were probed with X-ray photon correlation spectroscopy (XPCS)[24–35] and illustrated with hydrodynamic continuum theory (HCT)[25,36,37]. Several attempts to enhance the performance of anti-corrosion coatings by integrating graphene were reported based on the evidence that graphene can strongly affect the management of water in the film[38–43]. The behavior of water at the interfaces with such fillers in corrosion protection coatings most likely depends on details of the polymer-filler interaction including the degree to which such interactions slow down the movement at and near the interface. It has been proposed that in the area of corrosion, high atom density in the protective coating near the metal surface could provide better anticorrosion properties[44,45]. Thus, the high density of carbon atoms in the aromatic hexagonal lattice in graphene suggests the potential use of graphene in the area of anti-corrosion coatings especially for high value asset corrosion prevention.

The phenomenon of surface fluctuations of entangled melt films is an important scientific and technological problem with applications in areas including, but not limited to, wetting, adhesion[46,47], and tribology. Simulations from Rissanou et al.[48] showed the effect of graphene layer numbers on the dynamical properties of a graphene sheet supported PS film. Tsige et al.[49] demonstrated the most significant difference in relaxation time between the PS on graphite and α-quartz came from a region within 3 nm from the substrate. No experimental investigations have been reported in the graphene-thin film interfacial interaction possibly because of it is a “buried” interface, and not easily probed. The involvement of X-ray photon correlation spectroscopy (XPCS)[50] in the characterization of the thin film surface dynamics and the use of Guiselin[51] approach in the analysis of the strongly adsorbed layer will contribute to the investigation of the dynamics of polymer chain segments at the interface between graphene and the polymer thin film adsorbed on it. Surface dynamics of a thin PS melt film adsorbed on a PS substrate are substantially altered when the substrate is changed from silicon to graphene. The surface dynamics of

$8R_g$ PS on graphene was slowed down more than two orders of magnitude compared with that on hydrogen-passivated silicon (H-Si), and the thickness of the strongly adsorbed layer on graphene substrate (8.2 nm) was more than twice as that on H-Si (3.4 nm), which is because of the difference in the substrate surface energy.

Additionally, there has been a debate for a long time about the correlation between glass transition temperature (T_g) and polymer film thickness, including the origin of the changes[52,53]. The correlation reported between T_g and film thickness includes decreasing of T_g with the decrease of film thickness[54–57], remaining the same[58,59], increasing[60–63], or varying in different ways depending on the specific system[53,64,65]. The XPCS technique used here will also help better understand this question by investigating films with various thickness values and molecularly altering the interfacial interaction by substrate modification, including, but not limited to, graphene. The approach of using a surface dynamics technique to probe an extremely thin film, in which case the hydrodynamics of the entire film matters, provides a way to investigate interfacial properties at the thin film/substrate interface since the mobility of the surface is related to the mobility of material next to the interface. The dynamics of chain at a buried interface between a melt and hard surface are hard to study by other means.

The three parts of the work in this dissertation regarding the phenomena at the “bottom” are interconnected, using different X-ray and neutron scattering methods to study thin film properties on the nanometer scale. These efforts at the “bottom”, on the length scale of nanometers, provide information not available with previous empirical evaluations of anti-corrosion organic coatings made at the macroscopic scale, and opens more opportunities, indicating “plenty of room” at this level. The nanoscale investigation using scattering methods makes it possible to observe changes that happen rapidly in the corrosion process. Additionally, these scattering measurements help to understand the mechanism of corrosion on the nanometer scale, to probe the buried interface morphology between a metal substrate and an anti-corrosion organic coating where no other techniques are available, and to interrogate surface dynamics of polymer melt films and show the possibility to characterize the interfacial properties at the film/substrate interface of an extremely thin film difficult to study in other ways.

CHAPTER II

BACKGROUND

2.1 Corrosion and Its Implication

From the perspective of corrosion science and engineering, corrosion designates the reaction of a material with its environment resulting in a subsequent deterioration in properties[66]. The material here can be either a metal or nonmetallic substance, such as glass and concrete. However, the discussion here is restricted to metallic corrosion, or more specifically, the corrosion of aluminum metals. Direct cost resulting from corrosion, and its prevention have been responsible for a significant portion of the gross domestic product (GDP)[3]. Based on a government report in 2002, the direct costs of corrosion in the U.S. were $276 billion, which is more than 3.1% of the GDP. This cost is larger than the total financial cost of all the fires, hurricanes, and earthquakes in the nation, although those disasters received much more attention[67]. Direct costs include repainting of the infrastructure, replacement of corroded parts, and many other maintenance costs. Additionally, corrosion usually results in severe consequences including environmental catastrophes and casualties usually from sudden failure of load bearing components[68,69]. Such indirect costs are usually difficult to quantify, although they may be as much as the direct costs being evaluated. Examples of such costs include the costs of plant shutdowns, contamination of products, and loss of efficiency[67].

2.2 Metallic Corrosion and Protection

2.2.1 Metallic Corrosion

Metallic corrosion is an electrochemical process in which metal returns to its thermodynamically stable state, such as minerals[70]. There are three key components in a corroding system: anode, cathode, and electrolyte. Generally, the anode in corrosion is the metal, which releases electrons; the cathode is the material which is in contact with the anode and which receives electrons from the anodes; and the electrolyte is the conductive medium in which the corrosion takes place. The driving force is the change in Gibbs free energy, ΔG, which is made up of the decrease in the Gibbs function of the metal and its environment combination in the process of corrosion. For a spontaneous corrosion reaction, ΔG is negative, which indicates a lower energy for the corrosion products when compared as the metal and its environment.

As an electrochemical process, corrosion can be divided into cathode and anode half-cell reactions, both of which happen at the organic coating/metal substrate interface. The anode half-cell reaction is where the anode metal corrodes, and dissolves into the electrolyte as metallic ions. In the case of aluminum corrosion, the reaction is

$$\mathrm{Al} \rightarrow \mathrm{Al}^{3+} + 3\mathrm{e}^{-} \qquad (2.1)$$

in which each aluminum atom donates three electrons. The cathode half-cell reaction consumes the electrons donated by the reducible species from the electrolyte in the anode half-cell reaction; the cathode itself does not react. The anode and cathode half-cell reactions are referred to as oxidation and reduction reactions in organic chemistry. The most common cathode half-cell reaction is the consumption of electrons by dissolved oxygen,

$$\mathrm{O_2 + 2H_2O + 4e^- \rightarrow 4OH^-} \ . \tag{2.2}$$

If the environment is acidic, electrons will be consumed by protons, as in

$$\mathrm{2H^+ + 2e^- \rightarrow H_2(g)} \tag{2.3}$$

where (g) refers to the gas state. The hydrogen reduction reaction is not as important as the reaction involved with O_2 in water, since water does not contain enough hydrogen ions. The aluminum corrosion reaction product is alumina, $Al(OH)_3$, which precipitates in water following the reaction:

$$\mathrm{4Al + 3O_2 + 6H_2O \rightarrow 4Al(OH)_3} \ . \tag{2.4}$$

Aluminum has a variety of properties such as low density with high strength, thermal and electrical conductivity, non-toxicity and high corrosion resistance. The aluminum corrosion resistance is also influenced by its native oxide layer, Al_2O_3, which is an amorphous uniform oxide layer with a thickness up to several nanometers[71,72]. The native oxide forms rapidly after being removed from the aluminum by the reaction:

$$\mathrm{4Al + 3O_2 \rightarrow 2Al_2O_3} \ . \tag{2.5}$$

The chemical structure of the aluminum oxide layer also influences the adhesion[73] and corrosion properties at the interface between the metal and polymer coating.

2.2.2 Corrosion Protection

Various approaches available to protect metal against corrosion are categorized into three types: chemical, physical, or electrical[74]. Chemical modification usually involves with the adjustment of the pH of the electrolyte or the use of an inhibitor. Electrical modification uses an impressed current to adjust the potential values in order to make it not favorable for corrosion. Using physical barrier or organic coating is the most common technique among numerous methods to protect metal from corrosion. The coating could block electrolyte or reduce the amount of electrolyte coming through the coating. As illustrated in section 2.2.1, electrolyte is one of the three key components in corrosion. The barrier effect of organic coatings can prevent the corrosion electrochemical reactions.

Epoxy, developed immediately after World War II, is one of the most widely used primers in the industrial applications. It provides exceptional adhesion to metallic substrate and good resistance to electrolytes, and is used in coatings, adhesives, electronics and aerospace systems[73]. Epoxies are made from two components, typically, one being an epoxide and the other a crosslinking agent. The oxirane group in an epoxide can react with the amino groups in the crosslinking agent to form crosslinked epoxy as a primer.

Organic coatings based on polymers are generally not reliable for long-term corrosion protection applications because the disordered noncrystalline polymer chains provide pathways for water or electrolytes to the metallic substrate. Hybrid coatings with both organic and inorganic components have been explored in the last several decades[75–77]. The inorganic component in the hybrid coating segregates preferentially to the metallic substrate, improves adhesion[78], reduces the degree of disorder in the film and reduces water or electrolyte diffusion to the coating/metal interface.

Tetraethylorthosilicate (TEOS) as an alkoxide of silicon is generally used as a precursor in the hybrid coatings to provide improved covalent interaction between the metal and the organic component in the coating. Hydrolysis and polycondensation are involved in the polymerization of TEOS. The latter can be divided into two pathways: water-forming condensation and alcohol-forming condensation[78]:

$$\begin{aligned}
&\equiv \mathrm{Si}-\mathrm{OR}+\mathrm{H_2O} \rightleftharpoons\ \equiv \mathrm{Si}-\mathrm{OH}+\ \mathrm{ROH}\ , \\
&\equiv \mathrm{Si}-\mathrm{OR}+\mathrm{HO}-\mathrm{Si}\equiv\ \rightleftharpoons\ \equiv \mathrm{Si}-\mathrm{O}-\mathrm{Si}\equiv+\mathrm{ROH}\ , \\
&\equiv \mathrm{Si}-\mathrm{OH}+\mathrm{HO}-\mathrm{Si}\equiv\ \rightleftharpoons\ \equiv \mathrm{Si}-\mathrm{O}-\mathrm{Si}\equiv+\mathrm{H_2O}\ . \qquad (2.6)
\end{aligned}$$

Thus in this dissertation, hybrid inorganic-organic epoxy coatings are selected for study with multiple techniques, such as X-ray and neutron reflectivity (XR/NR), X-ray off-specular scattering, X-ray photon correlation spectroscopy (XPCS).

2.3 Characterization of Corrosion

In industry, the performance of corrosion protection coatings are evaluated with two kinds of methods: outdoor exposure and accelerated weathering tests[79]. For the former, materials being evaluated are placed under outdoor conditions, with sunlight and temperature variations. Such as test provides a good evaluation of how the material will perform in the environment it is supposed to be used in, although such tests take a long time. For the accelerated weathering tests, conditions such as radiation, humidity, and specific chemical environment can be controlled, attempting to rapidly simulate corrosion in materials during outdoor exposure tests. It usually takes less time for corrosion to happen in accelerated weathering tests, but the results cannot be directly used to predict the lifetime of the coating under normal use conditions. This difficulty arises because the mechanisms by which the sample corrodes are usually different for the two testing methods. Accelerated weathering tests are still used to eliminate candidate coatings with weaknesses. There are long time endeavors to establish a correlation between the two methods (Figure 2.1), but results are not satisfactory.

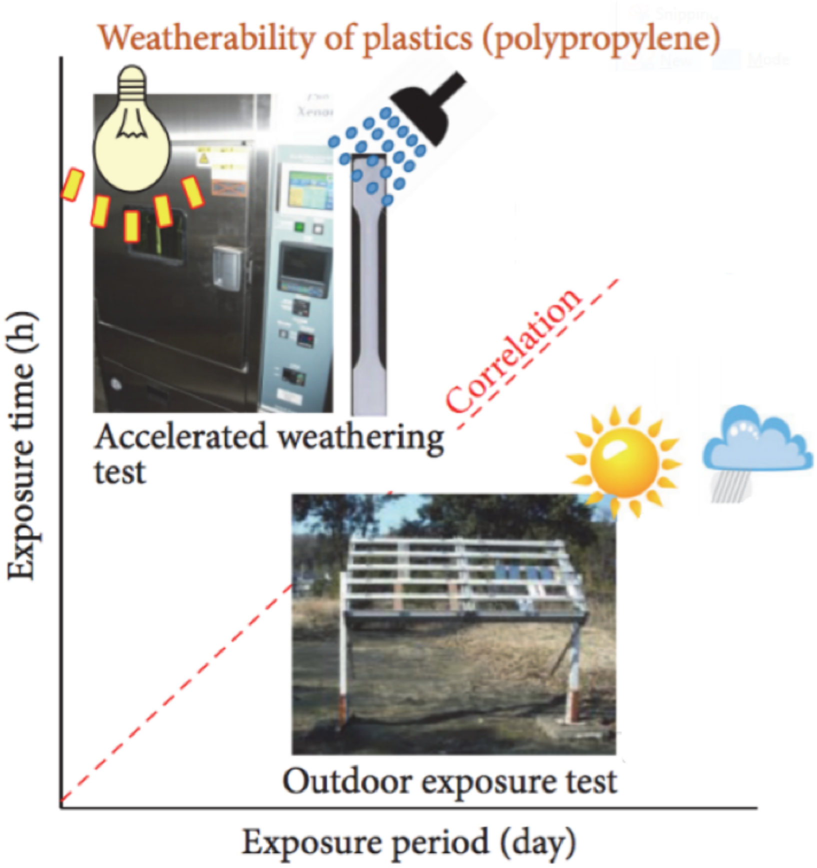

Figure 2.1 Illustration of the type of ideal correlation between the outdoor exposure test and the accelerated weathering test that researchers have hoped for. However, no correlation has been developed. Adapted with permission from *J. Polym.* **2016**, 1-14. Copyright (2016) Hindawi.

In order to make faster evaluations, a nanoscale understanding of the water/electrolyte diffusion into the interface, and the corrosion process is necessary. Scanning Kelvin probe and in situ infrared spectroscopic measurements of water/electrolyte diffusion performed by Wapner et al.[9] indicate the diffusion rate of D_2O along the interface between an epoxy coating and iron is two orders of magnitude larger than the penetration. The hydrated ion diffusion rate is also larger along the interface than that through the coating. A lateral diffusion cell (Figure 2.2) and a penetration cell (Figure 2.3) were used in their study. A silicon crystal at the bottom allows the total reflection of the infrared beam. D_2O was used instead of H_2O since the D_2O infrared bands and those from the epoxy coatings used in the study do not overlap.

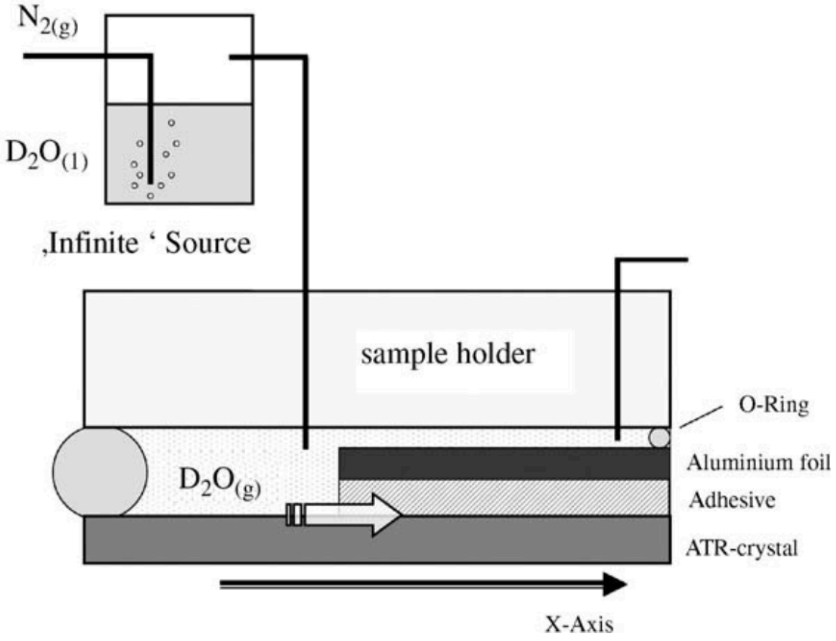

Figure 2.2 Experimental setup for lateral diffusion coefficient measurement with scanning attenuated total reflection infrared spectroscopy (ATR-IR). Adapted with permission from *Electrochimica Acta* **2006**, 51 (16), 3303-3315. Copyright (2006) Elsevier.

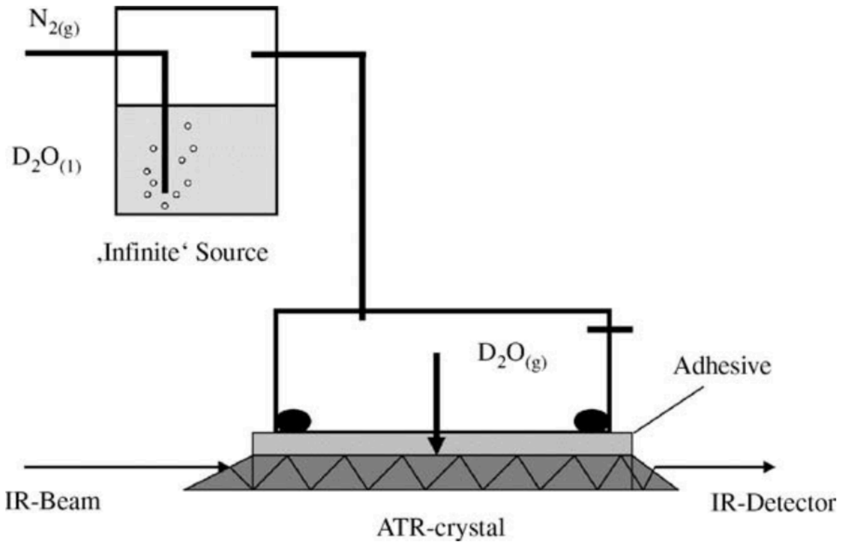

Figure 2.3 Experimental setup for penetration diffusion coefficient measurement with FTIR microscopy. Adapted with permission from *Electrochimica Acta* **2006**, 51 (16), 3303-3315. Copyright (2006) Elsevier.

X-ray and neutron reflectivity (XR/NR) have also been employed in the probing of water diffusion independently by several research groups. Vogt et al.[80] explored the absorption of moisture in supported poly(4-tert-butoxycarbonyloxystyrene) (PBOCSt) films on Al_2O_3 sputter coated silicon wafers. The interfacial concentration of water was decreased with an increase in the hydrophobicity of the interface, as shown in Figure 2.4.

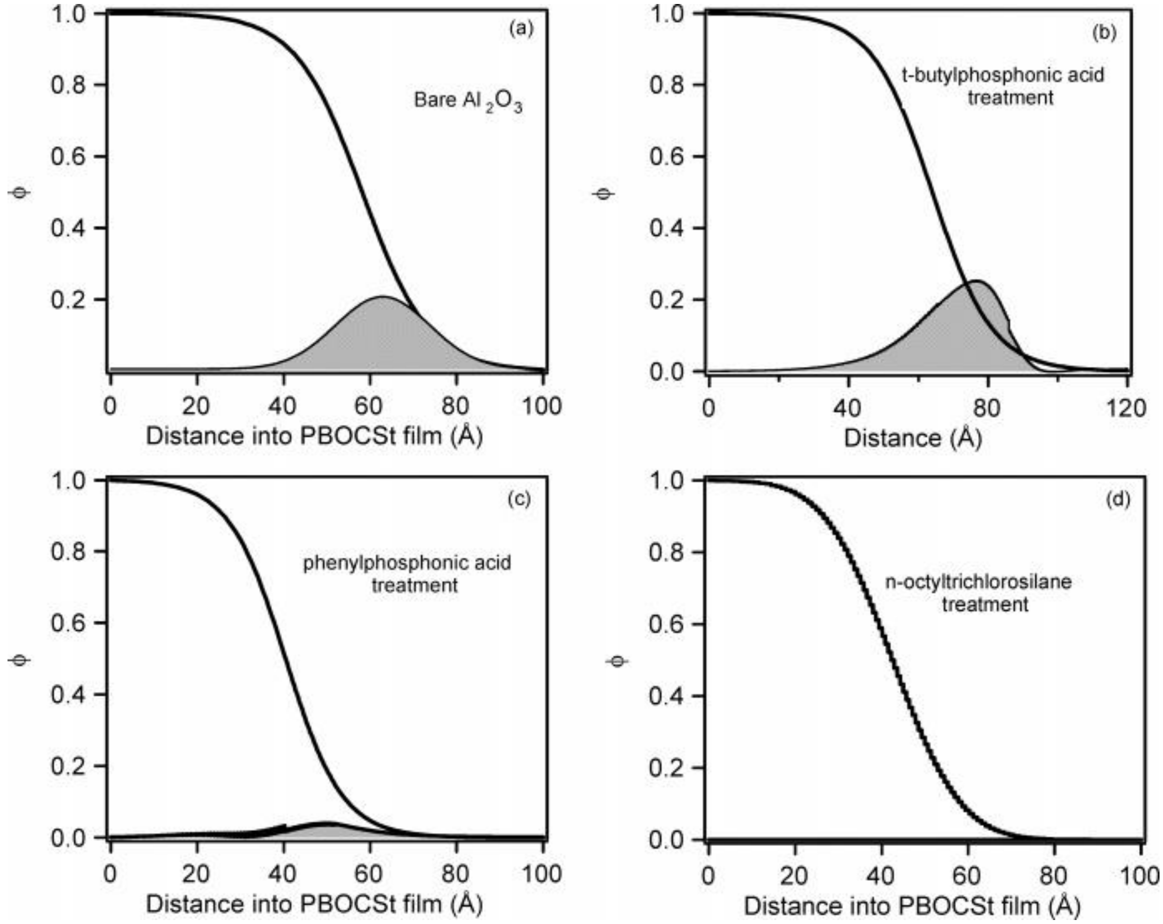

Figure 2.4 Concentration profiles derived from NR data for PBOCSt films supported on Al_2O_3. The total concentration of D_2O (filled) is shown as a function of the distance from solid Al_2O_3. The difference between these two curves is because of the diffuse Al_2O_3/polymer interface. Surfaces were (a) neat Al_2O_3, or treated with (b) tert-butylphosphonic acid, (c) phenylphosphonic acid, and (d) n-octyltrichlorosilane (OTS). Adapted from *Langmuir* **2005**, 21, 2460-2464. Copyright Not subject to U.S. Copyright. Published (2005) American Chemical Society.

Silane molecules have been used for some time for the modification of adhesion of organic coatings with metals. Schaefer et al.[81] studied the interface morphology formed with the application of silane or siloxane coupling agents to improve adhesion between metal surfaces and epoxy-based coatings to understand the mechanism of adhesion. The study indicated that the silane coupling agents are enriched the interface between the metal surface and the coating (Figure 2.5), improved the epoxy coating protection properties and reduced the water volume fraction in the coating to half of the value found without the coupling agent. The reflectivity curves and best fit scattering length density (SLD) profiles are in Figure 2.6. From the detailed shape of the variation of reflectivity with scattering vector, the depth profiles of scattering length density can be inferred; these were related to the morphology. How this is done will be explained in section 3.1.1.

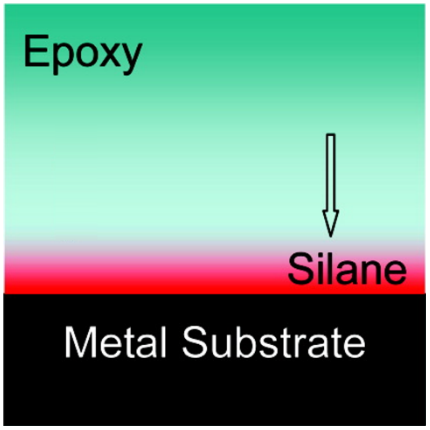

Figure 2.5 Silane enriched hydrophobic dense substrate/coating interfacial layer. Adapted with permission from *Langmuir* **2008**, 24, 13496-13501. Copyright (2008) American Chemical Society.

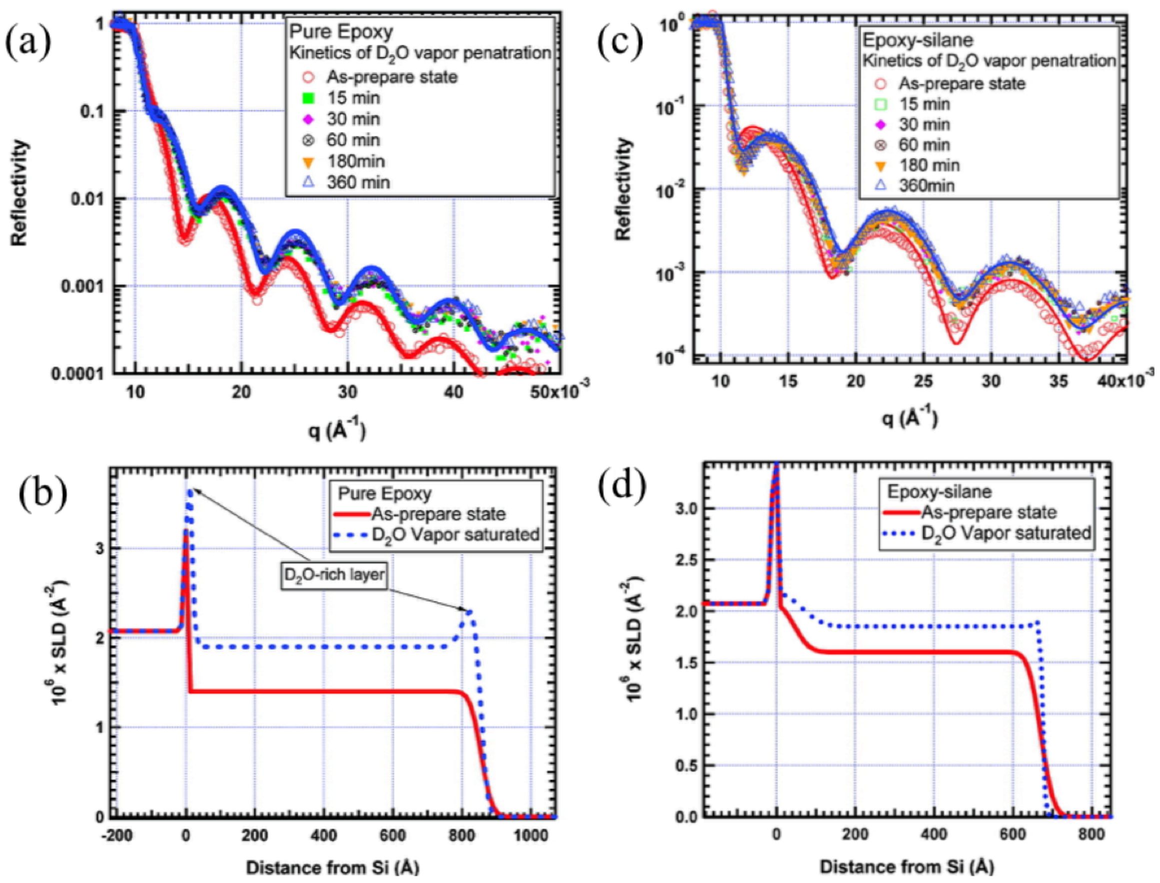

Figure 2.6 NR data from (a) epoxy-coated sample, (c) epoxy-silane mixture coated sample at different time intervals when exposed to D_2O vapor, and best fits using model SLD profiles for (b) epoxy coated sample and (d) epoxy-silane mixture coated sample. Adapted with permission from *Langmuir* **2008**, 24, 13496-13501. Copyright (2008) American Chemical Society.

Hydrophobicity of the substrate surface may not be the only physical property that appears to influence the movement of water into the coating. Karul et al.[82] illustrated that for a series of poly(*n*-alkyl methacrylates), when the alkyl chain length increases, the moisture uptake decreases, since the polymer becomes less hydrophilic. A series of poly(*n*-alkyl methacrylates) were used in their work: poly(methyl methacrylate) (PMMA), poly(*n*-butyl methacrylate) (PnBMA), and poly(*n*-octyl methacrylate) (PnOMA). The equilibrium moisture uptake for these poly(*n*-alkyl methacrylates) are in Figure 2.7.

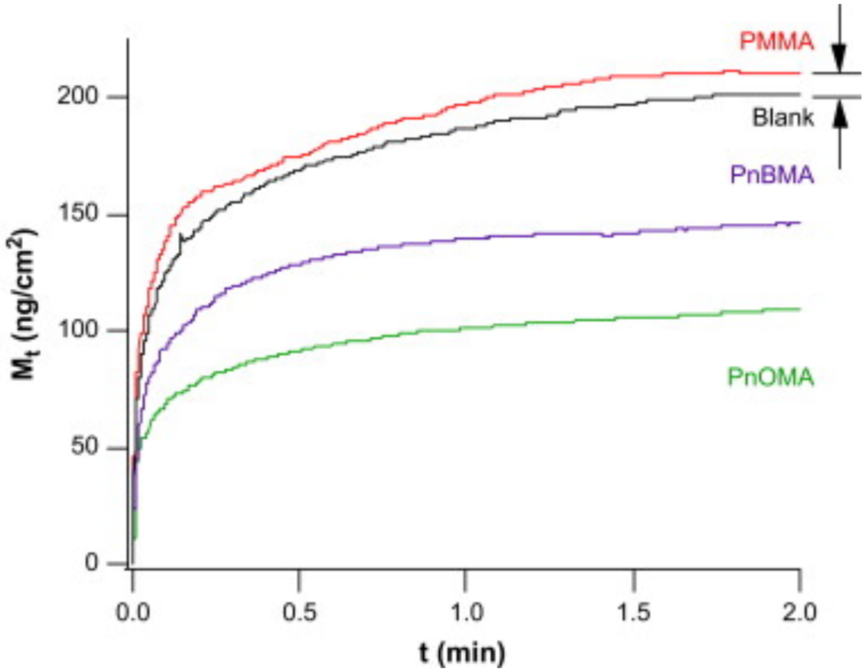

Figure 2.7 Equilibrium moisture uptake into supported thin films of PMMA(11 nm), PnBMA (12 nm) and PnOMA (11 nm). Adapted with permission from *Polymer* **2009**, 50 (14), 3234-3239. Copyright (2009) Elsevier.

Very recently, XR and NR were used in the investigation of iron corrosion in a marine environment by Wood, et al.[83] The corrosion of thin iron films on silicon wafers with electron-beam deposition were characterized with both XR and NR (Figure 2.8). The dissolution and formation of voids underneath the surface were observed in artificial seawater, with relevant XR and SLD profiles in Figure 2.9. Two treatments, ultrapure water soaking or UV/ozone exposure were able to enhance the iron surface protection for an extensive period of time, most of the iron film remained even after 42 days. Different potential corrosion inhibitors with chemical structures shown in Figure 2.10 were explored: DTAB did not improve the corrosion protection of the iron surface, SDS accelerated corrosion, and bis(2-ethylhexyl)phosphate demonstrated an enhancement of protection. Differences were elucidated in terms of preferential adsorption of these inhibitors at anodic and cathodic surfaces[83].

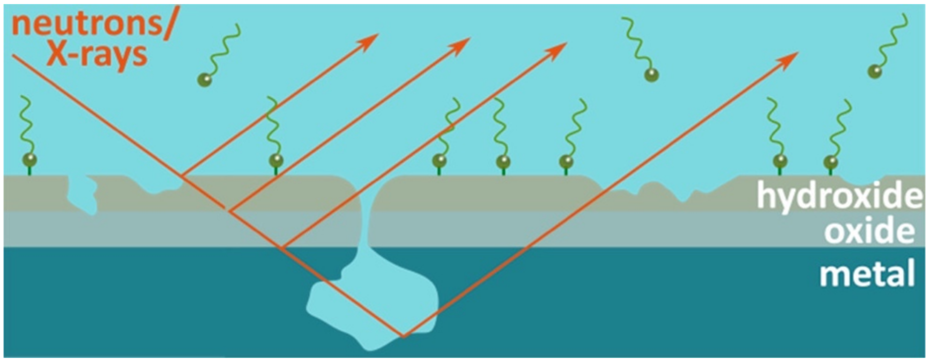

Figure 2.8 Cartoon for the characterization of iron thin film with X-ray and neutron reflectivity (XR/NR). Adapted with permission from *Langmuir* **2018**, 34 (21), 5990-6002. Copyright (2018) American Chemical Society.

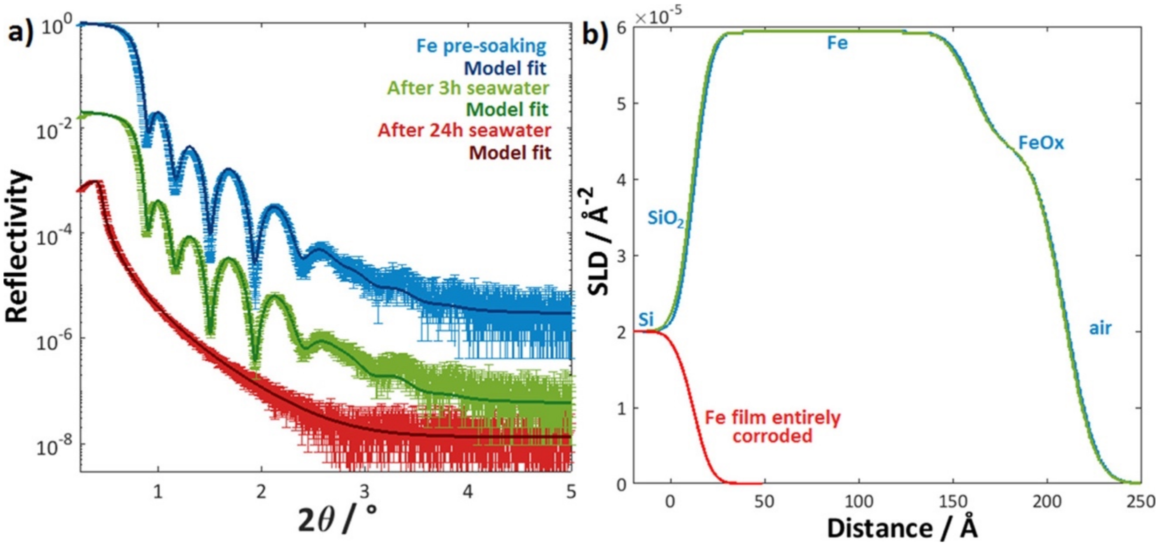

Figure 2.9 (a) XR data (points) and model fits (solid lines) for iron film before and after exposure to artificial seawater for 3 h and 24 h. Data offset vertically for clarity. (b) Best fits using SLD profiles of the model. Adapted with permission from *Langmuir* **2018**, 34 (21), 5990-6002. Copyright (2018) American Chemical Society.

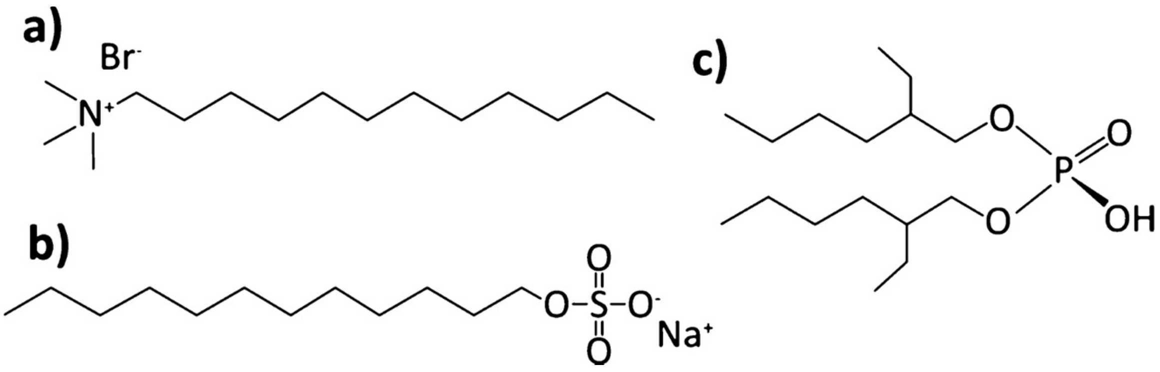

Figure 2.10 Chemical structures for (a) dodecyltrimethylammonium bromide (DTAB), (b) sodium dodecyl sulfate (SDS), and (c) bis(2-ethylhexyl)phosphate. Adapted with permission from *Langmuir* **2018**, 34 (21), 5990-6002. Copyright (2018) American Chemical Society.

2.4 Graphene as a Corrosion Protection Barrier

Graphene has various exceptional properties such as impermeability, transparency, thermodynamic stability and flexibility[41,84,85]. Intensive efforts have been made in the fabrication of graphene with high quality and on a large scale[86], both for academic and industrial purposes. As a perfect two-dimensional crystal material, graphene has been used in membranes, energy, coatings, sensors and electronics, composites, and biomedical drug delivery[87]. Since 2012, graphene has been used in the inhibiting coatings[38,39] to provide a solution to corrosion, one of the greatest challenges faced by the steel industry[43]. Its impermeability to all molecules, including gases and electrolytes, makes graphene an exceptional candidate as an anticorrosion coatings[43]. Although there are some different arguments and concerns about the utilization of graphene in the corrosion protection area[42] based on its inertness at the joint between different metals in the galvanic reactions, and the fact that more reactive metal will corrode preferentially (Figure 2.11), multiple independent research groups reported substantial improvements of the anti-corrosion properties of coatings with graphene or functionalized graphene[38,39,41,88–91], due to the impermeability of graphene as displayed schematically in Figure 2.12.

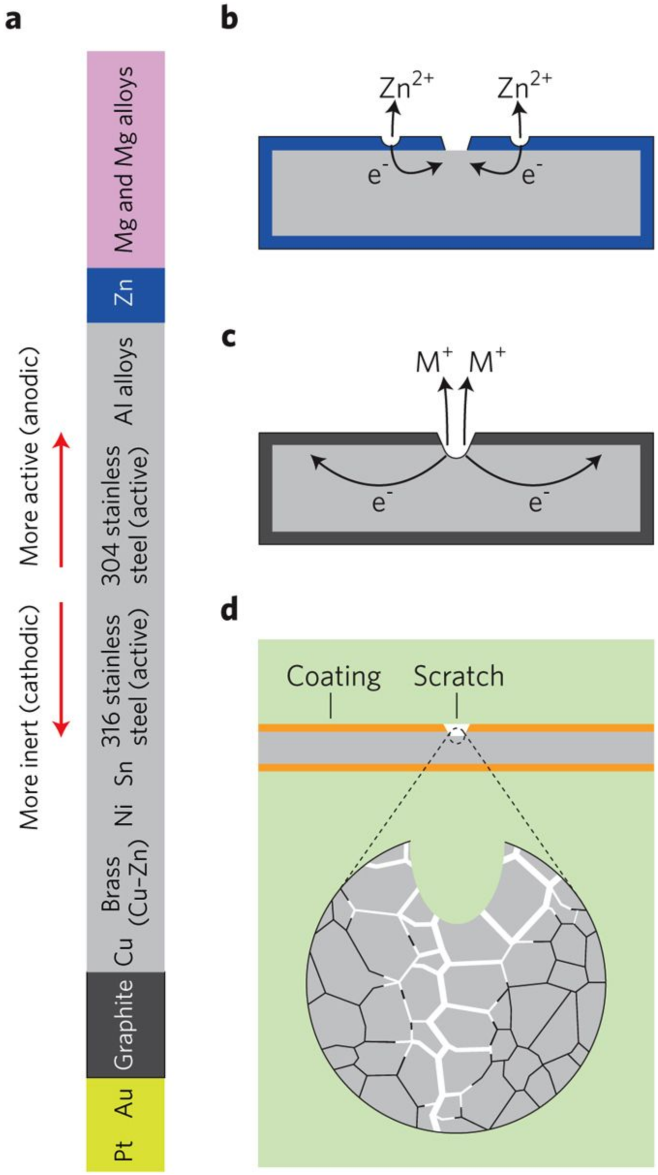

Figure 2.11 (a) The galvanic sequence with various metals and graphite in order of tendency to corrode, (b) An anodic coating (e.g. Zn) as a protection layer for steel in case of scratching, (c) In contrast, with a cathodic coating, local corrosion at scratches accelerates, (d) localized corrosion seriously weaken the metal by etching through grain boundaries. Adapted with permission from *Nature Nanotechnology* **2017**, 12, 834-835. Copyright (2017) Springer Nature.

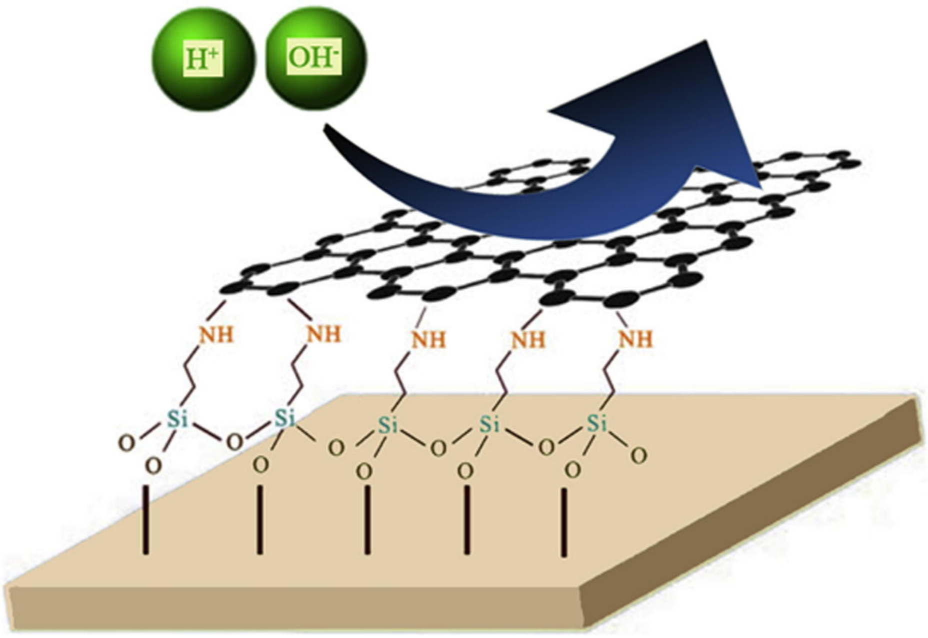

Figure 2.12 A schematic diagram for functionalized graphene coating. Adapted from *FlatChem* **2017**, 1, 11-19. Permission Not Required for Non-commercial Use. Copyright (2017) Elsevier.

It is also possible that the polymer chain mobility next to the surface with the substrate is related to the mechanism of corrosion. Certainly, the movement of water to the interface and along the interface could readily be imagined to be influenced by the mobility of the chains. However, the study of chain dynamics near a buried interface is very challenging. Inevitably, to see the motion of chains one must introduce a contrast mechanism for the experimental probe being used. However, recent work by several groups[82] has shown that the mobility of the chains immediately at the substrate impact behavior through a depth up to several R_g away from the substrate for the case of non-crosslinked melts. If the polymer film is made thin enough, changes in collective movement of the chains, as manifested in hydrodynamic motion characterized by viscosity impact the collective dynamics of surface fluctuations at the surface of the film. In this work, XPCS will be used to probe such fluctuations in the case that the substrate surface is modified with graphene in the hope that this may suggest additional insights into how graphene could impact corrosion protection. Additionally, the surface dynamics of entangled melt films is an important problem from the perspective of both science and technology. Surface dynamics can be adjusted through the modification of substrate chemistry[92], through which the properties such as wetting, adhesion[46,47], and tribology can be modified. Graphene, as a monolayer of sp^2 carbon atoms in an aromatic hexagonal lattice, alters the surface dynamics of substrate adsorbed melt polystyrene (PS) thin film substantially compared with that on silicon. The investigation of surface dynamics with XPCS will benefit applications in areas such as wetting and adhesion, which will also help better understand the role of graphene in the corrosion protection.

2.5 Statement of the Problem

In this research, three central questions were tackled. In the first part, the influence of ions on the water diffusion rate was investigated with XR/NR/EIS and in particular such diffusion in the polymeric films was studied in two different directions: vertical movement through the film, denoted as “penetration” and movement along the interface between film and substrate, denoted as “lateral diffusion”. The probing of the changes over a short length scale (nm) and short times (hours) is key for advancing the understanding of water and electrolyte movement in organic coatings, which is considered as a first step in understanding metallic substrate corrosion.

The second question tackled was “How does the epoxy/metal interface morphology change upon exposure of the interface to water or electrolyte?”. The novel approach taken is to use X-ray off-specular scattering and atomic force microscopy (AFM) to probe on the nanometer length scale an interface otherwise very difficult to quantify.

The third question is how the modification of a substrate surface through the deposition of graphene changes the chain motion at that interface. That interfacial motion is probed indirectly by measuring the surface fluctuations of a thin melt film of polymer chains which are affected by changes at the buried interface. This thin melt film serves as a model system readily connected with other studies on surface fluctuations in the literature and further study are needed to connect the insights for the annealed, uncrosslinked melt film with the case of a polymer coating that is annealed, but which crosslinks when at elevated temperatures.

CHAPTER III

EXPERIMENT

3.1 Scattering Characterization Methods

The use of a suite of scattering characterization methods including X-ray/neutron reflectivity (XR/NR) and X-ray off-specular scattering provided answers to the central fundamental research questions just summarized. These scattering methods can nondestructively and sensitively probe surfaces and interfaces in situ with depth resolution of 1-2 nm. The probing of changes on this short length scale, and also over a short time period is a key for advancing the understanding of the diffusion of water or electrolyte, disruption of interface morphology and changes in the mobility of chains adjacent to a substrate when the substrate surface is modified to engineer interactions at that interface. The principles of these scattering methods are discussed in this chapter.

3.1.1 X-ray and Neutron Reflectivity (XR/NR)

X-ray reflectivity (XR) and neutron reflectivity (NR) are nondestructive techniques to study thin film properties on the nanoscale, and are widely used in situ, especially in studies of kinetics. XR and NR are carried out with the reflection angle equivalent to that of incidence, i.e. they collect the specular scattering, as shown in Figure 3.1. The difference between XR and NR originates from the differences in the scattering lengths, b, to which they are sensitive. For XR, b is a function of electron density. For NR, b depends on the character of the atomic nuclei in a material, which varies even with isotopic identity. Film properties derived from XR and NR include the film thickness, roughness, and the depth profile of scattering length density (SLD), which depends on the elemental composition and film mass density. Generically, SLD can be calculated using $SLD = \frac{N_A \cdot \rho}{M} \cdot (\sum b_i)$, in where ρ is the mass density; N_A is the Avogadro's number; b_i is the scattering length of element i; and M is the reference chemical structure molecular weight for which the sum over i is calculated.

Generally, an incident beam with a wave vector $\boldsymbol{k}_i$ ($|k_i| = 2\pi / \lambda$) coming at a certain angle with respect to the surface interacts with the film through absorption and scattering. The radiation reflected at the angle of 2θ with respect to the incident direction is described with a wave vector $\boldsymbol{k}_s$. The momentum change with this scattering is defined by the scattering vector $\boldsymbol{q} \equiv \boldsymbol{k}_s - \boldsymbol{k}_i$. For reflectivity, the scattering vector magnitude is $q = 4\pi \cdot \sin\theta/\lambda$, which involves the incident beam wavelength and the incident angle. For specular reflectivity, the scattering wave vector $\boldsymbol{q} = \boldsymbol{q}_z$, is perpendicular to the film surface. Thin film properties can be derived from the analysis of reflectivity, when and only when there is enough contrast among different layers of the film. Contrast comes from the difference in SLD values for different parts of the sample.

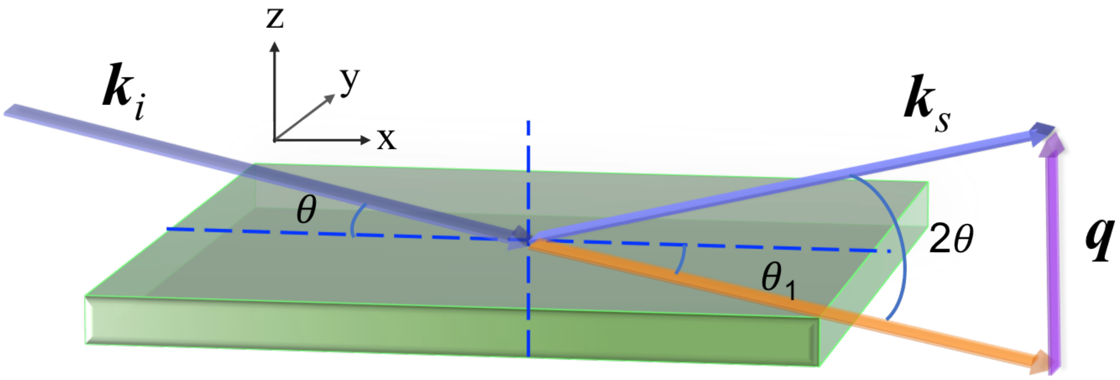

Figure 3.1 Schematic of specular scattering. For reflectivity (specular scattering), the scattering wave vector is perpendicular to the sample surface, in which case $\boldsymbol{q} = \boldsymbol{q}_z$.

The quantity of reflectivity, which is the ratio of the reflected radiation intensity to the incident beam intensity at an interface, is determined by the refractive indices, n_i, of the two materials adjacent to that interface. For X-rays and neutrons and condensed matter, the value of the refractive index is a little less than one,

$$n = 1 - \delta + i\beta \ , \qquad (3.2)$$

where δ is the real part describing the real portion of the atomic scattering and β is the imaginary part describing the absorption part of the atomic scattering. The real portion of the refractive index can be illustrated in terms of electron density, ρ_e,

$$\delta = \frac{\lambda^2}{2\pi}\rho_e r_o \ , \qquad (3.3)$$

where λ is the wavelength of radiation and r_o is the classical electron radius (2.82×10^{-6} nm). The absorption part of the atomic scattering factor is determined by the mass absorption coefficient, μ,

$$\beta = \frac{\mu\lambda}{4\pi} \,. \tag{3.4}$$

For neutrons the imaginary part is generally small compared with the real part, and the real part can be described by

$$\delta = \frac{\lambda^2}{2\pi}\left(\frac{b}{V}\right) , \tag{3.5}$$

where b/V is the scattering length density (SLD) For most materials, the value of δ for both XR and NR is on the order of 10^{-6} Å^{-2}.

Reflectivity curve detailed features influenced by correlations in electron density or refractive index in areas probed in the experiment are depicted with differential scattering cross-section, $\mathrm{d}\sigma/\mathrm{d}\Omega(q)$, which can be divided into three terms,

$$\frac{d\sigma}{d\Omega}(q) = r_0^2(\Delta\rho_e)^2 S_T S(q) \,. \tag{3.6}$$

The first term, $r_0^2(\Delta\rho_e)^2$, is the contrast factor, reflecting mean square SLD fluctuation in the probed system. The second one S_T is the total interface area in the probed volume, varying with the illuminated volume and phase volume fractions. The last one is the structure factor $S(q)$, dictated by the interfacial structure, regardless of the chemistry of the sample.

According to the law of reflection, the angle of reflectance is equal to the incident angle, θ, and following Snell's law, the refracted angle, θ_1, can be derived by

$$\mathrm{n} \cdot cos\theta = n_1 \cdot cos\theta_1 \,. \tag{3.7}$$

As θ is declining to zero, a critical value, θ_c, will be reached under which circumstance the refracted angle is zero. θ_c for incidence from vacuum can be related to the refractive index by

$$\theta_c = \sqrt{2\delta} = \lambda\sqrt{\frac{\rho}{\pi}}\,. \tag{3.8}$$

When the angle of incidence is above the critical angle, a portion of the radiation will be refracted. The reflectivity, *R*, is the ratio of the reflected intensities to the incident field amplitudes. For an ideal interface, the reflectivity R is derived by Fresnel et al[93],

$$\mathrm{R} = \left|\frac{k_{z,0} - k_{z,1}}{k_{z,0} + k_{z,1}}\right|^2 , \tag{3.9}$$

which applies to both X-ray and neutron radiations. From Porod's law[93], for $\theta \gg \theta_c$, reflectivity decreases rapidly as a function of q^{-4}, where q is equal to $2k_{z,0}$.

An XR curve example is in Figure 3.2. It comes from an epoxy film on top of a 40 nm aluminum layer on a silicon wafer, Epoxy/Al/Si. Large amounts of information can be derived from the analysis of an XR curve. (1) The envelope of the reflectivity decreases rapidly, as a function of q^{-4} for smooth interfaces; for rough interfaces, the reflectivity decays faster than q^{-4}. (2) The decrease in intensities starts immediately after $q_z = q_c$, which is the critical edge determined by the larger of two SLDs, either of the substrate or of the film. (3) Kiessig fringes emerge after the critical edge, due to the interference from reflections from several interfaces within the sample. Two distinctive spacings of fringes correspond to different layer thicknesses in the sample. The spacing between adjacent fringes can be used to estimate the layer thickness of the film,

$$d \cong \frac{2\pi}{\Delta q_z}, \tag{3.10}$$

where d is the layer thickness, and Δq_z is the difference in q_z between adjacent maximum or minimum of the fringes under the circumstance of $q \gg q_c$. Otherwise, Δq_z should be calculated as $\Delta q = \sqrt{q_{j,1}^2 - q_c^2} - \sqrt{q_j^2 - q_c^2}$, where $q_{j,1}$ is the value of q at the position of the (j+1)th maximum or minimum in vacuum or air, q_j is the value of q at the position of the jth maximum or minimum in vacuum or air, and q_c is measured in vacuum or air.

A detailed analysis of the reflectivity data based on a multilayer structural model nonlinear least squares regression using software MotoFit developed by Andrew Nelson from the Australian Nuclear Science and Technology Organisation gives more parameters such as layer thickness, roughness, and SLD depth profile (Figure 3.3), which is dictated by the film elemental composition and mass density. The quality of the fitting is characterized by

$$\chi^2 = \frac{1}{n+1} \sum_i \frac{(R - R_i)^2}{\sigma_i^2}, \tag{3.11}$$

in which χ^2 is a depiction of the difference between the experimental data and the fitting from the multilayer structural model.

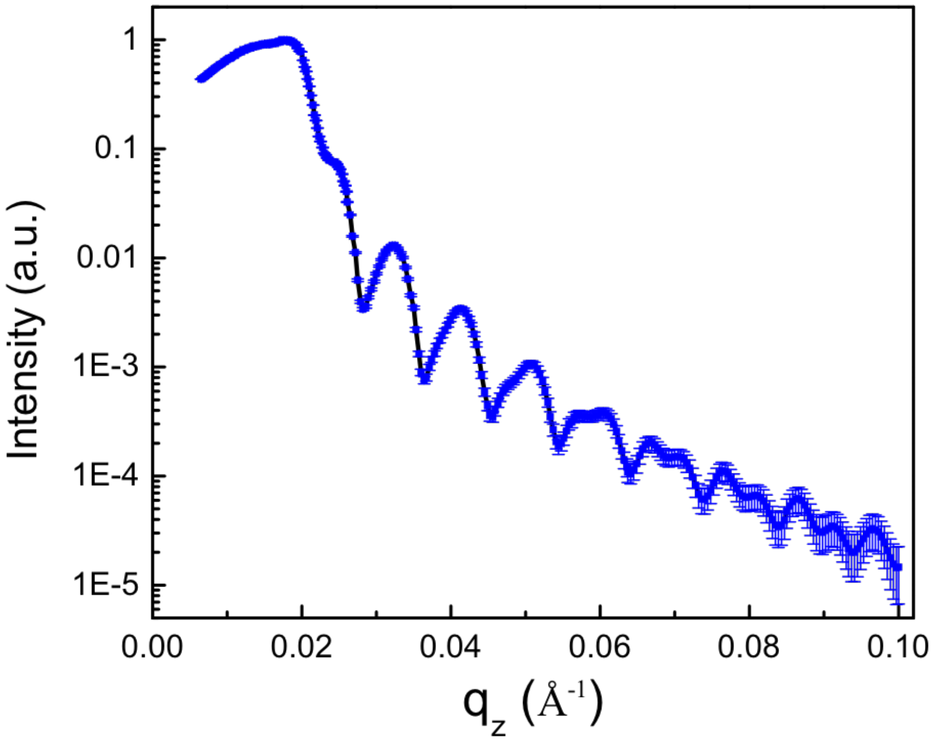

Figure 3.2 X-ray reflectivity (XR) with the nonlinear least square regression using a multilayer structural model for the sample Epoxy/Al/Si.

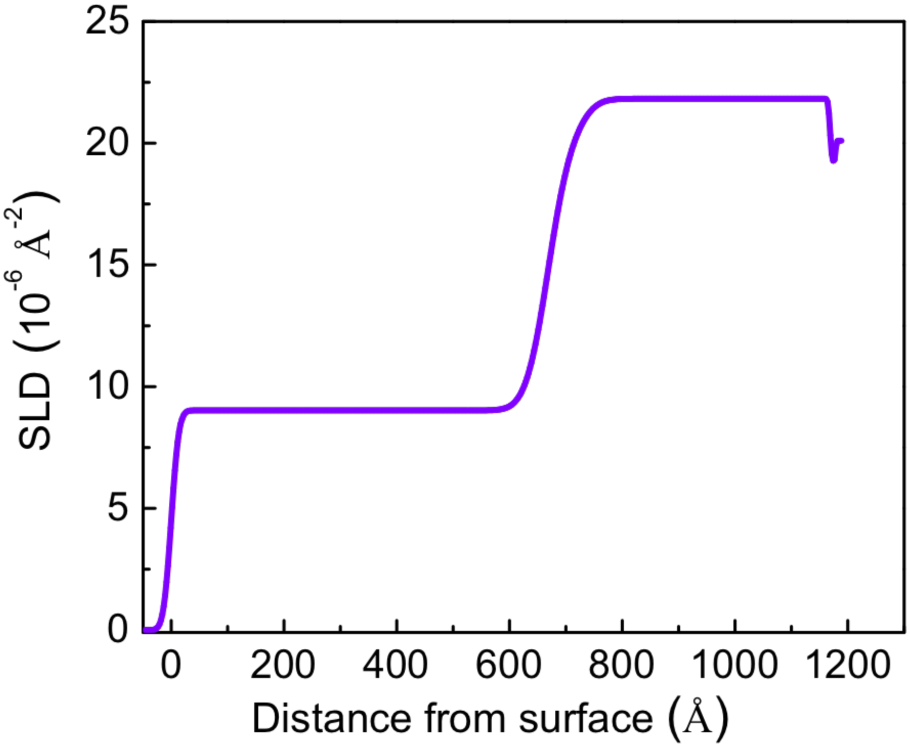

Figure 3.3 SLD profile corresponding to the best fit of the XR curve using a multilayer structural model.

3.1.2 X-ray Off-specular Scattering

In off-specular scattering, the angle of reflection is different from the angle of incidence, usually within a few degrees from the specular condition; it is a type of small angle scattering. The intensity is also collected as a function of the scattering wave vector, $\boldsymbol{q}$, which is the wavevector transfer in the scattering, $\boldsymbol{q} \equiv \boldsymbol{k}_s - \boldsymbol{k}_i$. In scattering experiments, the reflectivity measured at the specular condition is generally lower than that of the theoretical value, attributing to these off-specular scattered radiations. The scattering wave vector, $\boldsymbol{q}$, in specular reflectivity is perpendicular to the sample surface, from which root mean square roughness (rms) can be derived. The reflected specular radiation corresponds to the coherent component of the reflected beam. In off-specular scattering, $\boldsymbol{q}$, from which lateral correlations and interfacial jaggedness can be obtained, has components both vertical and parallel with respect to the sample. Such off-specular scattered beam originates from the incoherent portion of the reflected radiation[94].

The grazing incidence off-specular scattering using X-rays was first observed by Yoneda[95] in the 1960s. The explanation of the intensity variation resulting from off-specular scattering[96] started in the 1970s. Efforts to understand the off-specular X-ray scattering from rough surfaces involve the description of the scattering from an "interphase" of finite thickness into the interfacial problem. The interface structure described using correlations at the interface and composition variation across the "interphase" is considered an indirect description. Such methods include Born approximation[17,97] and Distorted Wave Born Approximation[17,98] (DWBA). In Born approximation, the reflection is considered as a scattering from independent electrons being irradiated. The DWBA assumes that the undisturbed states correspond to two different wave fields in an ideal system[94].

3.1.2.1 Born Approximation

Born approximation is based on the scattering from a single rough surface as the simplest approach in which the atomic structure will be ignored[17]. This assumption is valid in small angle scattering measurements where $qa \ll 1$, in which q is the scattering wave vector, and a is a typical length scale for the inhomogeneity within the surface. The differential cross section is composed of the specular and off-specular components,

$$\frac{d\sigma}{d\Omega} = \frac{r_0^2(\Delta\rho_e)^2}{q_z^2} \iint_{S_0} dxdy \iint_{S_0} dx'dy' \cdot e^{-iq_z[z(x,y)-z(x',y')]} e^{-i[q_x(x-x')-q_y(y-y')]} \qquad (3.12)$$

in which S_0 is the (x, y) plane surface, $z(x, y)$ is the surface height above the plane surface at (x, y), and $\Delta\rho_e$ is equivalent to ρ_e of the condensed medium[99]. It is assumed that $[z(x,y) - z(x',y')]$ is a Gaussian random variable with its distribution as a function of the relative plane surface coordinates $(X, Y) = (x' - x,\ y' - y)$,

$$g(X,Y) = 2\langle[z(x',y') - z(x,y)]^2\rangle\ , \qquad (3.13)$$

and

$$C(X,Y) \equiv \langle z(X,Y)z(0,0)\rangle = \sigma^2 - \frac{1}{2}g(X,Y) \qquad (3.14)$$

where $C(X,Y)$ is the height-height correlation function. Assume $g(R)$ approaches zero with some finite R, the scattering function $S_{\mathrm{diff}}(\boldsymbol{q})$ is

$$S_{diff}(q) = \frac{e^{-q_z^2\sigma^2}}{q_z^2} \iint_{S_0} dXdY\left(e^{q_z^2 C(X,Y)} - 1\right)e^{-i(q_xX+q_yY)} \qquad (3.15)$$

Numerical methods were used to solve equation (3.15) by Sinha et al.[3] using a self-affine model. When the surfaces are isotropic,

$$g(X,Y) = g(R) = AR^{2h} \quad (0 < h < 1) \,, \tag{3.16}$$

in which $R \equiv (X^2 + Y^2)^{1/2}$, A is an arbitrary unit vector, and h is a description of the jaggedness, with h = 0 describing an extreme jagged surface, and h = 1 depicting a smooth surface. For self-affine rough surfaces, at large distances the surface appears flat, since $|z(R) - z(0)|/R$ approaches 0 as R approaches ∞, but when $R \ll R_0$, where

$$R \equiv A^{\frac{1}{2(1-h)}} \,. \tag{3.17}$$

The surface appears to be fractal, with the fractal dimension of

$$D_s = 3 - h \,. \tag{3.18}$$

Equation (3.16) is an ideal case, while the root mean square roughness may saturate at a value of σ^2. Under this circumstance,

$$g(R) = 2\sigma^2[1 - e^{-(R/\xi)^{2h}}] \,, \tag{3.19}$$

in which ξ is a cutoff length for the roughness.

The born approximation is considered to be valid when the q_z value is large enough, $q_z\sigma \gg 1$. Below the critical angle for total reflection, born approximation cannot be used in describing the reflectivity below unity because of the losses due to off-specular scattering. Additionally, when the electron density contrast $\Delta\rho_e$ becomes small, the diffuse scattering is less pronounced, which makes it difficult to investigate a polymer/polymer interface with X-ray off-specular scattering.

3.1.2.2 Distorted Wave Born Approximation (DWBA)

A more rigorous formalism established to describe the off-specular scattering is the distorted wave born approximation (DWBA). The DWBA is a time-dependent first-order perturbation theory[100], in which a perturbation theory is involved[3]. The crucial approximation of the DWBA is the use of a perturbation on the exact solution; it takes the refraction at a smooth interface into consideration. The X-rays obey the stationary wave equation,

$$C(x,y) = V_1(x,y) + V_2(x,y) \ , \tag{3.20}$$

in which V is the interaction potential, with V_1 corresponding to the average smooth interface. The incident beam wave vector, reflected beam wave vector, and transmitted beam wave vector for the smooth interface are $\boldsymbol{k}_1$, $\boldsymbol{k}_1'$, and $\boldsymbol{k}_1^t$, respectively. V_2 is the perturbation on V_1 resulting from roughness, in which a time reversed scattering is considered, in which $-\boldsymbol{k}_2$, $-\boldsymbol{k}_2'$, and $-\boldsymbol{k}_2^t$ are the incident beam wave vector, specular reflected beam wave vector and transmitted beam wave vector, respectively.

The scattering intensity in DWBA is calculated by Sinha et al.[3],

$$\left[\frac{d\sigma}{d\Omega}\right]_{diff} = L_x L_y \frac{\left|k_0^2(1-n^2)\right|^2}{16\pi^2} \cdot |T_i(\boldsymbol{k}_1)|^2 |T_i(\boldsymbol{k}_2)|^2 S(\boldsymbol{q}^t) \ , \tag{3.21}$$

in which $\boldsymbol{k}_1$ and $\boldsymbol{k}_2$ are the incident and scattering wave vectors, respectively, while k_0 is the magnitude of the wave vector. $S(\boldsymbol{q}^t)$ is the Born approximation with $\boldsymbol{q}$ replaced by the value of the medium under the interface.

$$S(\boldsymbol{q}^t) = \frac{1}{\left|q_z^t\right|^2} e^{-\left[\left(q_z^t\right)^2 + \left(q_z^{t*}\right)^2\right]\sigma^2/2} \iint_{S_0} dXdY \, e^{i(q_x X + q_y Y)} \left(e^{\left|q_z^t\right|^2 C(X,Y)} - 1\right) \tag{3.22}$$

The DWBA expression is similar to that of Born approximation in the diffuse scattering cross section. The major difference is that the transmission functions for the incident and scattered radiations are considered in the DWBA, and the wavevector transfer in the medium (q_z^t) is used instead of that in the vacuum (q_z). The inclusion of the transmission coefficient in equation (3.21) predicts an important feature of the off-specular scattering, i.e. the occurrence of a maximum in the off-specular scattering when either the angle between the surface and $\boldsymbol{k}_1$ or $\boldsymbol{k}_2$ is equivalent to the critical angle, θ_c. These peaks are referred to as Yoneda peak[95], named after Yoneda who first observed such an angle in a rocking curve scattering experiment.

For $q_z\sigma \leq 1$, the DWBA works well, while the Born approximation diverges rather than saturates at total reflection. Conversely, when $q_z\sigma \gg 1$, Born approximation is considered to be a more accurate description, while the DWBA yields an estimate too large for reflectivity, as a result of the Fresnel eigenstates which form the basis for the perturbation theory. Furthermore, on a rough surface, $|R|^2 < 1$, and q_z is smaller than q_c ($q_c^2 \equiv 4k_0^2(1 - n^2)$), which is the value of q_z at the critical angle in specular reflection because of off-specular scattering losses, though DWBA does not correctly show this.

3.1.3 X-ray Photon Correlation Spectroscopy (XPCS)

Advanced third-generation synchrotron radiation sources made it possible to deliver coherent X-ray beams with intensities orders of magnitude higher than previously achievable, which provided possibilities for advanced techniques such as X-ray photon correlation spectroscopy (XPCS)[101–103]. XPCS investigates the dynamics of matter through the analysis of the time correlations of scattered photons. It usually measures comparatively low frequency dynamics (10^6 Hz to 10^{-3} Hz) in a scattering vector, q, range of 1×10^{-3} Å^{-1} up to several Å^{-1}. Figure 3.4 illustrates the frequency-wavevector range covered by XPCS and complementary techniques used in probing the dynamics of disordered systems, including surface fluctuations. By "surface fluctuations" we mean thermally stimulated lateral variations in height that vary as a function of time, and happen over a range of length scales. The capability of XPCS to probe scattering over a certain range of q makes it suitable for the characterization of such surface dynamics.

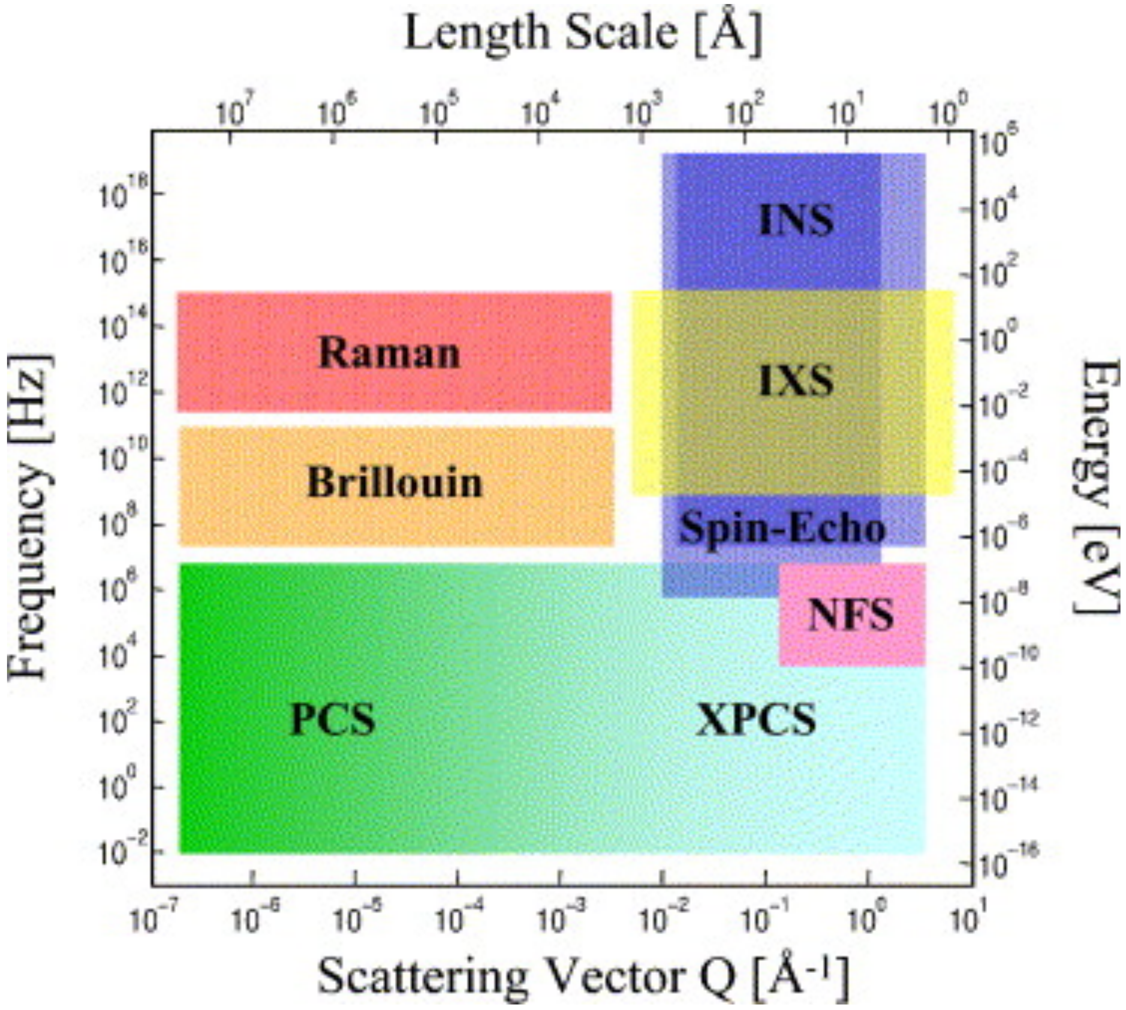

Figure 3.4 Frequency-scattering vector space covered by X-ray photon correlation spectroscopy (XPCS) and other techniques: photon correlation spectroscopy with visible coherent light (PCS), Raman and Brillouin scattering, inelastic neutron (INS) and X-ray scattering (IXS), neutron spin-echo and nuclear forward scattering (NFS). Adapted with permission from *J. Alloys Compd*. **2004**, 362 (1-2), 3-11. Copyright (2012) Elsevier.

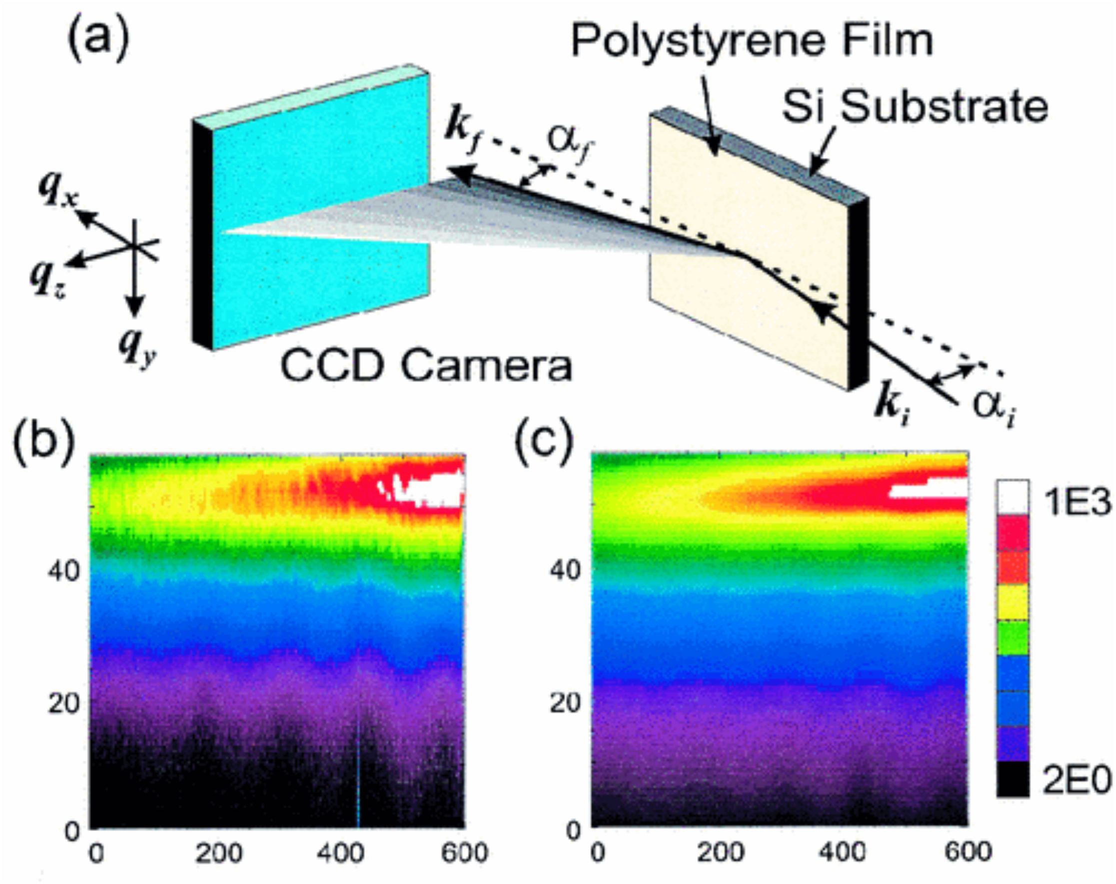

Figure 3.5 (a) Scheme of the experimental setup for XPCS in reflection geometry. (b) CCD image of the time-averaged diffuse scattering. (c) Simulated time-averaged diffuse scattering from a capillary wave model for a film sample with thickness 84 nm at 160°C that provides the best fit with the data in (b). Axes are labeled with pixel numbers. Adapted with permission from *Phys. Rev. Lett.* **2003**, 90 (6), 068302. Copyright (2003) American Physical Society.

If a coherent beam is scattered from a disordered system, it will produce an off-specular scattering pattern, which is usually referred to as a “speckle pattern”. Figure 3.5 is the time averaged off-specular pattern for an XPCS measurement from the surface of a film. In the time-averaged pattern the speckles are no longer visible. The speckle pattern at any moment is connected to the specific spatial arrangement of the atoms at that moment in the volume near the surface that is probed by the X-rays. Coherent X-ray beams make such observations[104]. If the atom spatial arrangement varies in time, the speckle pattern will change in time accordingly. Its intensity is recorded using a two-dimensional charge coupled device (CCD) camera downstream of the sample. Both transmission[105] and reflection[106] sample geometry have been used in earlier work.

The XPCS experiments in Figure 3.5 were conducted at 8-ID-I at the Advanced Photon Source (APS), Argonne National Laboratory, using a geometry and analysis procedure described in Figure 3.6. The $q_{||}$ range used at 8-ID-I for the XPCS measurements is typically from 10^{-4} Å^{-1} to 10^{-3} Å^{-1}. The range of accessible relaxation times derived is from 10^{-1} to 10^{3} seconds with the detector typically used, though very recently fast detectors have made it possible to push the accessible relaxation times down into the microsecond range. In principle, XPCS works in the similar way as dynamic light scattering (DLS). Both techniques require coherence, although the coherence in DLS (done with visible light) is much better than that in XPCS. That is the reason why XPCS requires a high intensity third generation synchrotron source.

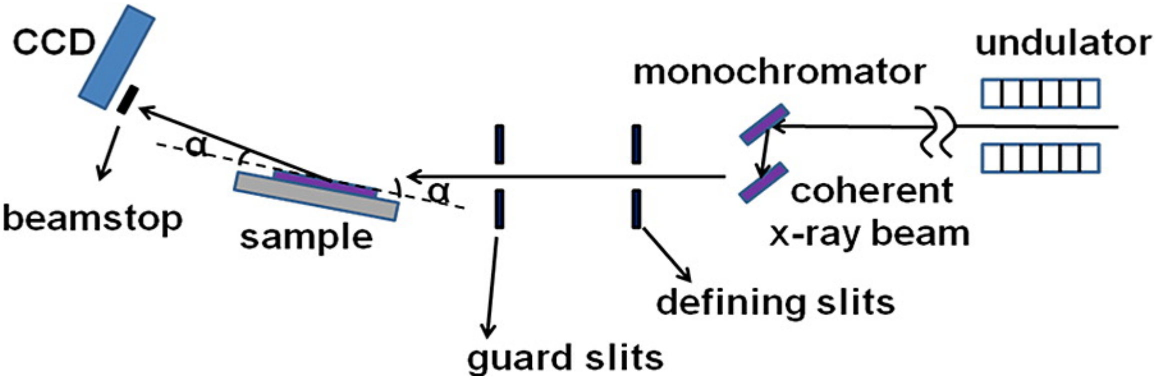

Figure 3.6 Schematic of the beamline 8-ID-I for surface XPCS measurements at the Advanced Photon Source (APS) when run in reflection geometry. Adapted with permission from *Macromolecules* **2012**, 45 (15), 6210-6219. Copyright (2012) American Chemical Society.

A partially coherent monochromatic beam of X-ray with its wavelength on the order of Ångströms makes it possible to detect length scales much smaller than those in DLS. The incident angle, θ, is below the PS critical angle at this wavelength (0.16°), thus the penetration of X-ray in the film is limited to 9 nm in depth. Thus the scattering from the polymer/substrate interface can be neglected. There is scattering from density fluctuations within that top 9 nm of polymer, but the intensity of that scattering is also negligible compared to the scattering from the polymer/air surface, where the contrast is much stronger. The intensity is recorded with a two-dimensional CCD camera downstream of the sample[107]. The fluctuations in the coherent speckle pattern were collected from random polymer thin film surface fluctuations at temperatures higher than the bulk glass transition temperature ($T_{g,bulk}$). Every time when the speckle pattern is captured, it is referred to as a "frame". The intervals between the frame is the "delay time". This surface fluctuation is represented by the normalized intensity-intensity autocorrelation function (g_2),

$$g_2(q_{\|}, t') = \frac{\langle I(q_{\|}, t') I(q_{\|}, t'+t) \rangle}{\langle I(q_{\|}, t') \rangle^2}, \tag{3.23}$$

where $I(q_{\|}, t')$ is the scattering intensity at wave vector transfer $q_{||}$ at time t', and the angular brackets denote ensemble average for the delay time, t. A single-exponential decay function, $g_2 = 1 + \beta \exp(-2t / \tau)$, was used in the fitting of the g_2 data for overdamped capillary waves[108], where β is the coherent contrast and τ is the relaxation time for equilibrium surface height fluctuations.

Hydrodynamic continuum theory (HCT)[25,36,37] represents the universal dependence of the normalized relaxation time, τ/h, as a function of the dimensionless in-plane scattering vector, $q_{||}h$, for films with different thicknesses, h, when the temperatures are sufficiently greater than the $T_{g,\text{bulk}}$. The surface of such melt exhibit overdamped capillary waves with a relaxation time τ depending on film viscosity (η), film thickness (h), surface tension (γ), and scattering wave vector ($q_{||}$)[108]. For a sufficiently thick supported melt film and a nonslip boundary at the film/substrate, the HCT gives the normalized relaxation time τ/h as a function of $q_{||}h$ as

$$\frac{\tau}{h} = \frac{2\eta\left[cosh^2(q_{\|}h) + (q_{\|}h)^2\right]}{\gamma q_{\|}h\left[cosh(q_{\|}h)sinh(q_{\|}h) - q_{\|}h\right]}, \tag{3.24}$$

in which the normalized relaxation time, τ/h, changes in a universal way as a function of the dimensionless in-plane scattering vector, $q_{||}h$. According to HCT theory, for a given temperature and a given polymer but different thickness, τ/h and $q_{||}h$ should collapse onto a single universal curve. A deviation from this universal curve will be evidence of the existence of confinement effects.

Full frame mode is used to capture the off-specular scattering, in which the whole area of the CCD camera was used. Full frame mode is good for slow surface fluctuation (100 seconds < τ < 2000 seconds) characterization. Speckle pattern sequences are collected as a function of time. The time intervals between two contiguous frames, “sleep time”, will be increased when the relaxation time is large, in order to avoid radiation damage. During the sleep time, a fast shutter is used to block the X-ray to reduce X-ray exposure on the spot being studied. Using the dynamics measured at multiple spots will further reduce beam damage and also get better statistics from their averaged autocorrelation function. X-ray reflectivity (XR) measurements are conducted before and after each measurement of XPCS to compare the film thickness to leave out results from severe beam damage; comparisons between correlation functions derived from the first and second half of the frames are made to exclude other suspicious results from beam damage.

3.2 Complementary Characterization Methods

In addition to the scattering methods introduced, several complementary characterization techniques are used to provide additional information in the analysis of thin film properties in order to better understand the water/electrolyte diffusion, interface morphology disruption and surface dynamics of polymer films adsorbed on graphene.

3.2.1 Atomic Force Microscopy (AFM)

Atomic force microscopy (AFM) is an established type of scanning probe microscope (SPM) that collects images of surfaces with a physical probe that scans the sample. It is one of the most broadly used methods in the characterization of surfaces, in areas including functional nanocrystals[109], biomaterials[110,111], two-dimensional crystals[112], and sensor applications[113,114]. The principle is based on the mechanical probe-surface interactions between a surface and an AFM tip as a function of position[115].

The AFM tip is used in a raster pattern to obtain topographic images with nanometer scale resolution. A series of thin film properties including but not limited to relative height, surface morphology, roughness, in-plane molecular ordering, and surface defect can be measured. AFM is sensitive to a various forces, including electrostatic force, van der Waals force, friction force, and adhesion force. Different modes such as tapping[116,117], noncontact[118], contact[119], chemical force[120,121] and friction modes[122] have been developed and applied in different polymer surface studies.

The piezoelectric scanner moves the tip with regard to the sample. This movement is measured by the deflection of the low spring constant cantilever, on the end of which an AFM tip is located. Cantilevers available commercially have micrometer-size dimensions, and spring constants in the range of 0.01 to 100 N/m. The tip has a typical radius of a few nanometers and a height usually of a couple of micrometers. A feedback loop watches the tip-sample force[123–126] and corrects the sample vertical direction position to keep the force constant in constant-force mode or adjust the force on the sample to hold the vertical direction position constant in constant-height mode. Tapping mode has high image resolution of surface morphology with little damage to the sample by eliminating the lateral forces inherent to contact mode AFM; thus it is very suitable to study polymer film properties.

Surface morphology characterized by AFM is complementary to the reflectivity measurement since the two techniques are based on different principles. Reflectivity provides statistically averaged information on the sample surface within the entire footprint, where the sample surface is illuminated with the incident beam. AFM presents an image of a surface with local morphological details. The footprint in a reflectivity is of several square centimeters (i.e. 1 cm × 2 cm), where AFM can be done for the maximum surface area of less than 0.01 cm^2 (87 μm × 87 μm in Dimension Icon). The reflectivity is able to provide a measurement of the roughness of buried interfaces, while AFM measurements are limited to the surface of the specimen. All images are obtained at room temperature in the atmosphere and the rms roughness can be obtained by analyzing of AFM images using software NanoScope Analysis from Bruker Inc.

To compare surface structure information from AFM images and that from off-specular scattering, $\exp[iq_z h_{\mathrm{AFM}}(x, y)]$ and the squared two-dimensional Fourier transformation were derived from the surface height profile $h_{\mathrm{AFM}}(x, y)$[116]. Since the X-ray measurement integrates over q_y, the $S_{\mathrm{AFM}}(q_x, q_z)$ as a function of the X-ray scattering function $S(q_x, q_z)$ is

$$S_{AFM}(q_x, q_z) = \frac{1}{q_z^2} \cdot \int dq_y \cdot \left| \iint d_x d_y e^{iq_z h_{AFM}(x,y)} e^{i(q_x x + q_y y)} \right|^2 . \qquad (3.25)$$

Each AFM image offers a segment of $S_{\mathrm{AFM}}(q_x, q_z)$ over a certain range of q. Such Fourier transform of the displacement-displacement correlation function from AFM images yields the wave number distribution in Fourier spectrum of the rough surface and describes the power spectral density (PSD)[127]. The agreement between the PSD from AFM images and X-ray off-specular scattering from a 31 nm PS brush is excellent, as shown in Figure 3.7.

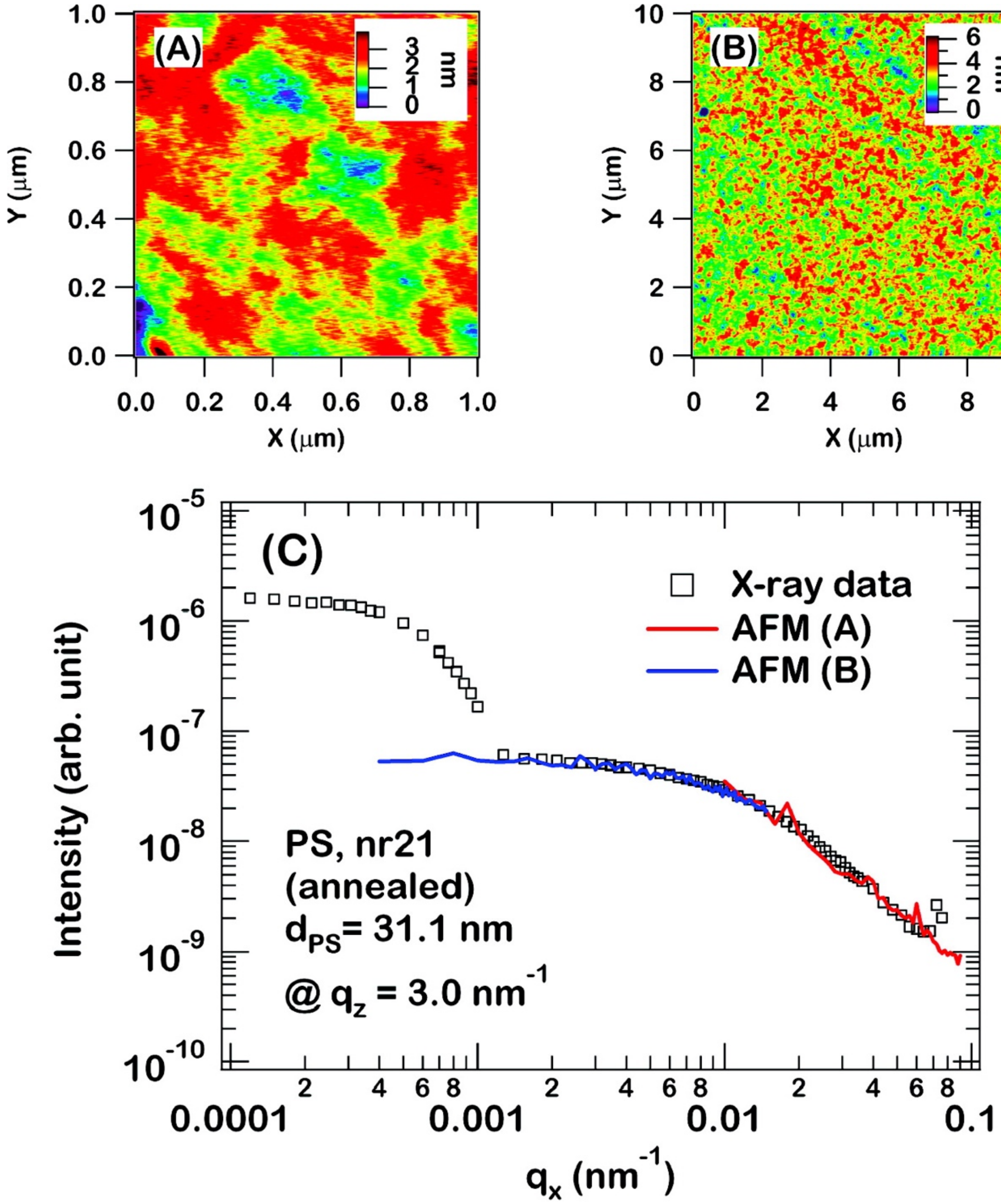

Figure 3.7 AFM images of (a) 1 μm × 1 μm and (b) 10 μm × 10 μm areas and (c) comparison of $S_{AFM}(q_x, q_z)$ calculated using equation 3.3 from these two images with the X-ray off-specular scattering intensities for a 31 nm thick PS brush. Adapted with permission from *Macromolecules* **2007**, 40, 6361-6369. Copyright (2007) American Chemical Society.

3.2.2 Electrochemical Impedance Spectroscopy (EIS)

Electrochemical impedance spectroscopy, EIS, measures the impedance variation as a function of frequency. EIS is done by either applying a series of AC currents and probing the response of potential or applying a series of AC potentials and measuring the response of current. Data measured in EIS are usually presented in the form of Bode plot, which presents phase and log (amplitude) as a function of log (frequency), or in the form of Nyquist plot, which has the imaginary part vs. the real part of the impedance, but does not involve the frequency measured at each point. A Nyquist plot example is in Figure 3.8. Each point on the plot denotes a vector from the origin, corresponding to the magnitude (modulus) and phase angle of the impedance at that certain frequency. When the frequency decreases, the impedance increases and shifts along the semicircle in the direction away from the origin.

Three criteria must be met to get a valid result[128]: (1) Linearity: the system response should be proportional to the perturbation; this was approached by small amplitude perturbations; (2) Causality: the system response should be a direct consequence of the perturbation; (3) Stability: The system should exhibit a single value for a given perturbation.

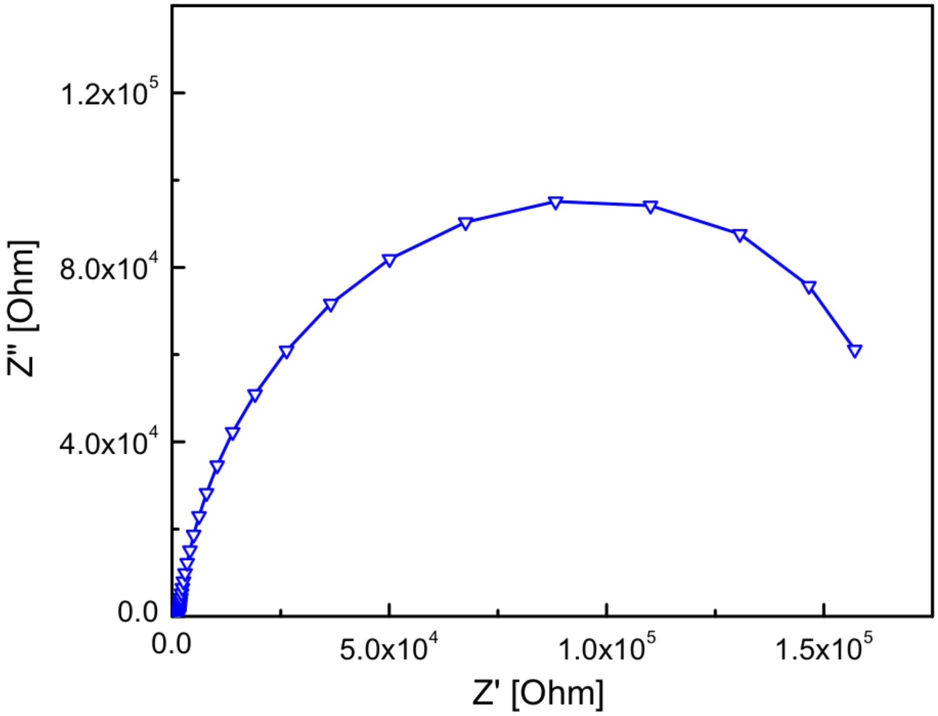

Figure 3.8 A Nyquist plot of impedance in which x-axis and y-axis are real and imaginary parts of the impedance, respectively.

The three-electrode EIS setup is generally used in the measurement of water or electrolyte diffusion or coating degradation. A schematic for this set up is in Figure 3.9. A perspex cylinder is attached to the coating with an O-ring and a glass tube clamp. The coating surface within the O-ring is the testing area. The cylinder is filled by working fluids, either water or electrolyte such as 3.5 wt % NaCl aqueous solution. A three-electrode system used in this setup includes a saturated calomel reference electrode, a platinum counter electrode, and a working electrode which is the metal substrate[129]. Usually, EIS measurements are done at room temperature, 25°C.

Appropriate equivalent electrical circuit (EEC) is necessary in the evaluation of the EIS data. A schematic diagram for a simple model for organic coatings on metal substrate in Figure 3.10 is proposed by Mansfeld et al.[130] In this model, R_s denotes the electrolyte resistance, R_c refers to the coating resistance, and C_c is the coating capacitance. For a coating in dry condition, the Z_f and R_c are large enough that the total impedance is R_sC_c. As a consequence of the water/electrolyte diffusion into the coating, the EEC turns into $R_s(C_cR_c)$. These EEC elements have similar characteristics to the actual processes being considered, and the parameters used in the fitting between these EEC elements and real data are adjusted to achieve the optimal fit.

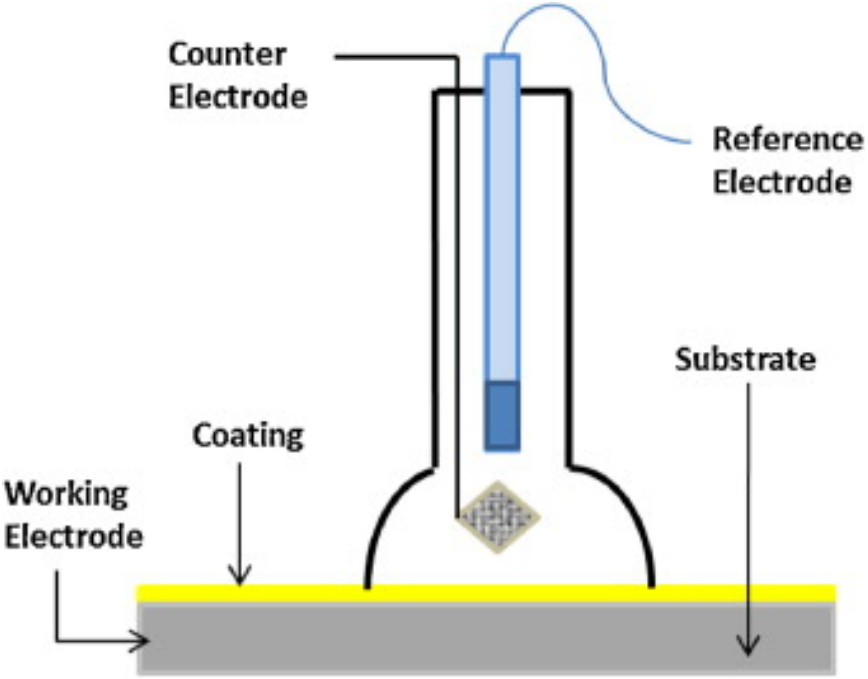

Figure 3.9 A schematic of the three-electrode EIS setup. Adapted with permission from *Prog. Org. Coatings* **2013**, 76 (11), 1674-1682. Copyright (2013) Elsevier.

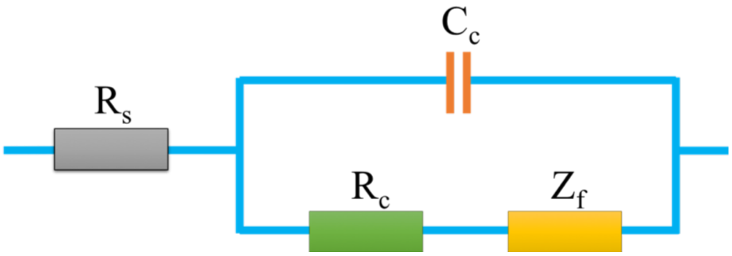

Figure 3.10 Equivalent electrical circuit (EEC) used in the fitting of EIS data for organic coatings on metal substrates.

3.2.3 Spectroscopic Ellipsometry

Ellipsometry was developed in the early 1970s as an optical technique utilizing the reflection of light from samples. It is widely used in the measurement of thin film thickness and properties[131–134]. Ellipsometry is used both in academic research areas such as surface and interface science, and in industries such as optical coatings, dielectrics, and composites of materials.

Ellipsometry measures the variation of a polarized light upon its reflection on the surface of a sample. Light can be depicted as an electromagnetic wave; the polarization of light refers to electromagnetic wave behavior as a function of time in space. The propagation direction of a wave is orthogonal to its electric field; consequently, a wave travelling by the z-direction could be represented with its x- and y- components. The electric field of the light used in ellipsometry follows a specific path, which is recognized as polarized light. When the two orthogonal electric waves are in-phase, the radiation after its reflection on the surface will be linearly polarized, and the orientation is dictated by the relative amplitudes of the two light waves. An elliptical polarization is a combination of two orthogonal waves with arbitrary phase and amplitude, as revealed in Figure 3.11.

The polarization variation is described using two parameters, phase angle, Δ, and amplitude ratio, Ψ. These two parameters depend on the thickness of films and optical properties such as refractive index. A complex ellipsometric parameter, ρ, is associated with the amplitude ratio, phase angle, and complex Fresnel reflection coefficients,

$$\rho = \frac{R_p}{R_s} = tan\Psi e^{i\Delta} , \qquad (3.26)$$

in which R_s and R_p are the complex Fresnel reflection coefficient for s- and p-polarized light, respectively[134]. A schematic of an ellipsometry experiment is in Figure 3.12, in which the incident light is linear with p- and s- components. Ellipsometry measures the phase angle and amplitude of the reflected light for both the p- and s- polarized light. From ellipsometry measurement, the optical constants and film thickness can be garnered. The optical constants extinction coefficient k, and refractive index n, can be correlated to the real ε_1, and imaginary ε_2, components of the dielectric function, ε.

$$\varepsilon_1 = n^2 - k^2$$

$$\varepsilon_2 = 2nk \qquad (3.27)$$

The raw data from the ellipsometry measurements are usually presented in the pseudo-dielectric function,

$$\langle\varepsilon\rangle = \langle\varepsilon_1\rangle + i\langle\varepsilon_2\rangle = sin^2(\theta)\left[1 + \left(\frac{1-\rho}{1+\rho}\right)^2 tan^2(\theta)\right] \qquad (3.28)$$

in which θ is the incident angle, ρ is defined by the equation 3.26.

The analysis of the ellipsometry data is based on the construction of a proper model, calculating its predicted response with Fresnel's equations, and comparing the calculated values to experimental data. The unknown material properties such as optical constants and film thickness are varied to improve the fitting between the model and experimental data until the smallest mean squared error is reached, following the general regression routine.

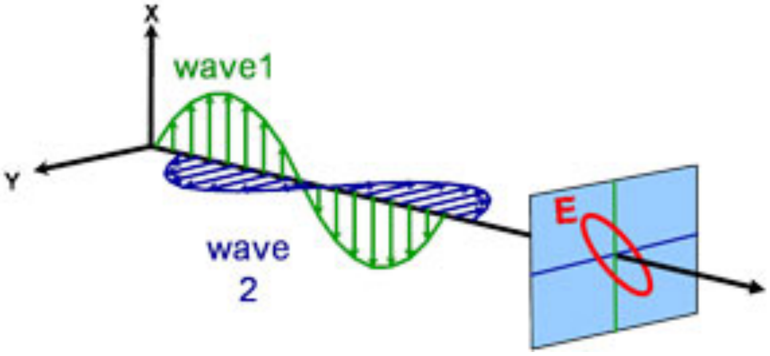

Figure 3.11 A schematic of two orthogonal electric waves and the resulting polarized light. Adapted from J.A. Woollam Co. http://www.jawoollam.com (accessed Sept 10, 2018)

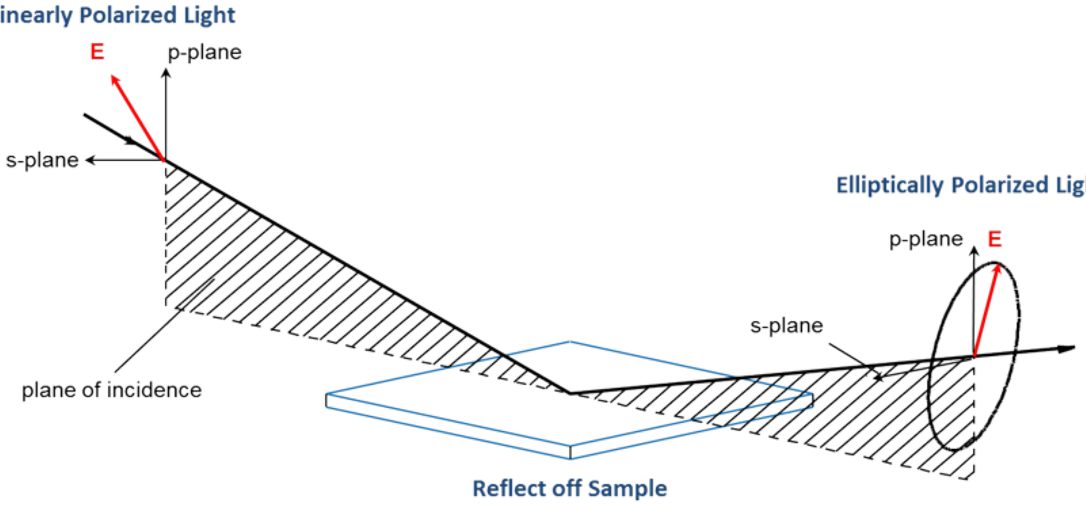

Figure 3.12 A schematic of a spectroscopic ellipsometry measurement. Adapted from J.A. Woollam Co. http://www.jawoollam.com (accessed Sept 10, 2018)

3.2.4 Raman Spectroscopy

Raman spectroscopy is broadly utilized in the characterization of both the quality and the number of layers of the graphene[135,136]. It gives data averaged over a large area and provides a chemical fingerprint of the graphene. There are three graphene signature peaks in its Raman spectrum: *G* mode at ca. 1580 cm^{-1}, *D* mode at ca. 1350 cm^{-1}, and *2D* mode at ca. 2670 cm^{-1}, which is a second order *D* mode requiring no defects for activation[137–139]. The *G* mode, *D* mode and *2D* mode are a doubly degenerate zone center E_{2g} mode, a ring-breathing mode that is activated near defects, and a second order *D* mode requiring no defects for activation, respectively[140]. Information regarding the graphene quality and the number of layers can be derived from the analysis of the line shapes, positions, and relative intensities of the modes[141–143]. It has been well accepted that the *2D* peak to *G* peak (I_{2D}/I_G) intensity ratio and the *2D* peak average full width half maximum (FWHM) are key parameters reflecting the charge impurities on the graphene surface[144–146], from which the number of graphene layers and the grain size can be estimated[147]. The grain size can be derived from I_D/I_G using the equation[148] $I_D/I_G = C(\lambda) / L_a$, in which λ (nm) is the wavelength of incident light, L_a (nm) is the grain size, and $C(\lambda)$ is a constant as $2.4 \times 10^{-10} \cdot \lambda^4$. As the graphene layer number increases, FWHM increases and the I_{2D}/I_G decreases[149,150]. When the I_{2D}/I_G from the Raman spectra is larger than one, it is considered to be a monolayer of graphene.

3.2.5 Nanoindentation

Nanoindentation can be employed in the measurement of the hardness and elastic modulus of a material through the analysis of the load-displacement curve during the loading and unloading processes[151–153]. Nanoindentation was used in the investigation of poly(ethylene terephthalate) by Ion et al.[154] in 1990 and subsequently in the characterization of poly(methyl methacrylate) by Briscoe et al.[155] in 1996. The force-displacement curve represents the load variation as a function of displacement during the process of pressing the indenter continuously into the film being measured and also the unloading process[152]. The unloading curve analysis is shown in Figure 3.13. $h_{\max}$ refers to the maximum indenter displacement when the maximum load, $P_{\max}$, is applied. h_r denotes the residual displacement, and h_c describes the elastic deformation, which comes from the intercept of the tangent line from the unloading curve and the displacement axis. Stiffness, S, is the tangent line slope at the maximum displacement.

$$S \equiv \left(\frac{\partial P}{\partial h}\right)_{h_{max}}. \tag{3.29}$$

Geometrically, it follows that,

$$h_c = h_{max} - \left(\frac{P}{\frac{\partial P}{\partial h}}\right)_{h_{max}} = h_{max} - \left(\frac{P}{S}\right)_{h_{max}}. \tag{3.30}$$

Analytical approaches are used in the evaluation of the stiffness, S, at the maximum penetration depth, by fitting the data for the unloading process to the functional form,

$$P = \alpha(h - h_r)^m \tag{3.31}$$

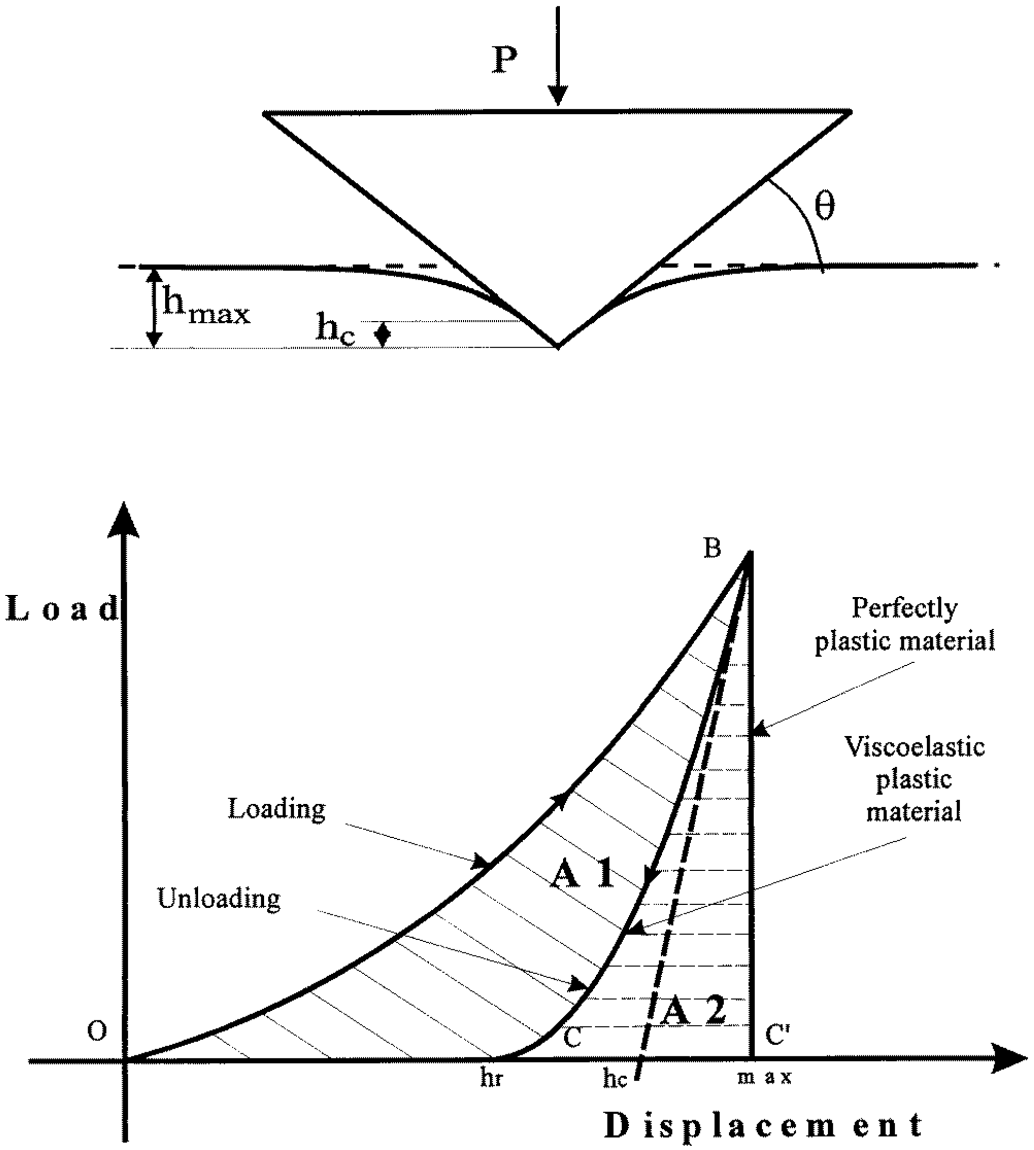

Figure 3.13 A schematic of a tip used in nanoindentation measurements, and a load-displacement curve including both the loading and unloading processes. Adapted with permission from *J. Phys. D. Appl. Phys*. **1998**, 31, 2395-2405. Copyright (1998) IOP Publishing.

in which α and m are the fitting parameters. The parameter m is a power law exponent depending on the indenter geometry. α is determined from the sample Poisson's ratio, the sample elastic modulus, the geometric constants, the indenter Poisson's ratio, and the indenter elastic modulus.

After obtaining a best fit, a derivative, the contact stiffness, *S*, applied at the point with the maximum loading is derived analytically[151] using the expression,

$$S = 2aE_r = \frac{2}{\sqrt{\pi}} E_r \sqrt{A} \, , \tag{3.32}$$

in which a is the contact radius, A is the projected contact area, and E_r is the reduced modulus. E_r describes the deformation from both the indenter and the sample[153],

$$\frac{1}{E_r} = \frac{1-v^2}{E} + \frac{1-v_i^2}{E_i}, \tag{3.33}$$

where E, E_i, v, and v_i are the sample elastic modulus, indenter elastic modulus, Poisson's ratio of the sample, and Poisson's ratio of the indenter, respectively. The normal hardness is evaluated using the general formula[152],

$$H(h_c) = \frac{P_{max}}{A_{max}} = \frac{P_{max}}{c h_c^2} \, , \tag{3.34}$$

in which c is a constant characteristic of the indenter geometry. Paraboloid of revolution, flat-ended cylindrical punch, cone, and Berkovich are four tip geometries commercially available. When thin films on substrates of much larger modulus are studied with nanoindentation, in order to obtain quantitative analysis one must account for the properties of the film and also the substrate. Qualitatively it may still be possible to see differences between thin films on such a hard substrate, but the modulus (hardness) of the substrate plays a significant part in affecting the shapes of the curves.

3.3 Sample Preparation

3.3.1 Silicon Wafer

N-type [1 0 0] prime silicon wafers (El-Cat Inc.) were used for X-ray and neutron scattering experiments. The thicknesses of the silicon wafers used in the X-ray and neutron scattering experiments were 0.7 mm and 5 mm, respectively. Organic impurities on the surface of each silicon wafer were removed by placing in piranha solution (H_2O_2:H_2SO_4 = 3:7 by volume) at 100 °C for 30 min (*Warning: Piranha solution presents an explosion danger and should be handled with extreme care; it is a strong oxidant and reacts violently with organic materials. All work should be performed in a fume hood. Wear proper protective equipment.*) The native oxide layer was etched by submerging the clean wafer into a 1% aqueous solution of hydrofluoric acid for 1 minute, rinsing with ultra-purified water and drying with high-purity nitrogen (N_2) gas.

3.3.2 Aluminum Substrate

Aluminum was selected as the metal of choice in this study because of its wide application in areas such as automobiles[156], aircraft[157], and aerospace[158,159]. In the scattering study of thin films, including X-ray/neutron reflectivity (XR/NR) and X-ray off-specular scattering, samples must meet rigorous requirements, such as planarity, smoothness, thickness uniformity and also sufficient electron density differences between the different components to be distinguished[99]. A crucial part of the sample preparation is depositing aluminum thin films on the silicon wafer substrates controllably and reproducibly. There are various techniques to make such films, including direct current (DC) magnetron sputtering and thermal evaporation. Both techniques are physical vapor deposition (PVD) processes in which the material starts from a condensed phase, moves to a vapor phase and eventually back to a condensed phase in the form of a thin films. PVD is widely used in the preparation of thin films and differs from chemical vapor deposition (CVD) by the absence of chemical reaction at the surface of the coated substrate. Both direct current (DC) magnetron sputtering and thermal evaporation were employed in the preparation of the aluminum substrates used in this work.

3.3.2.1 Direct Current (DC) Magnetron Sputtering

Direct current (DC) magnetron sputtering is based on the principle of PVD that a portion of the target is vaporized and deposited on the substrate as a film through adsorption and diffusion of atoms. The deposition of aluminum[160,161] and co-deposition of aluminum together with other kinds of metals[162] have been the subjects of intense research over three decades[163–166]. DC sputtering functions with a constant voltage and offers controllability and uniformity over a relatively large area on the substrate[162]. A schematic of the Denton Vacuum Discovery 550 Sputtering System used in the Center for Nanoscale Science and Technology (CNST) NanoFab Class 100 Clean Room located in the National Institute of Standards and Technology (NIST) is shown in Figure 3.14. Aluminum with the purity of 99.999% was used as the target. Each time before the start of the deposition, the chamber was pumped down to 2.6×10^{-5} Pa (2×10^{-7} Torr) with a turbo pump to limit possible contamination in the chamber. The actual deposition pressure was much higher than the chamber base pressure, normally on the order of mTorr. This pressure was reached by backfilling with an inert gas, such as argon. Plasma was sparked in the deposition chamber near the target, which acted as a cathode. Energy and momentum transfer to the target caused the aluminum atoms to be removed from the target and to travel to the substrate.

A 40 nm thick aluminum layer on a silicon wafer was obtained in order to meet the requirement of XR/NR for sample thicknesses of tens of nanometers if we wish to be able to resolve the layer thickness. Wafers were cleaned with piranha solution right before being loaded into the sputtering chamber. Manual mode was used for the sputtering process in order to obtain experimental conditions for deposition of aluminum films with optimal surface roughness. This is the procedure that was used. (1) Set argon gas flow to 30 sccm (standard cubic centimeters per minute), set power to 100 W. (2) While keeping the shutter closed, switch "on" gas switch to allow the inflow of argon and switch "on" the substrate stage rotation, which will result in films with better uniformity. (3) Turn power switch to "on". (4) Adjust argon flow rate and power to 20 sccm, 75 W to spark the plasma, and then to 10 sccm, 50 W, respectively. (5) Open the shutter to start deposition and keep open for 500 seconds. (6) Close the shutter, turn off power, stop substrate rotation, and stop argon inflow.

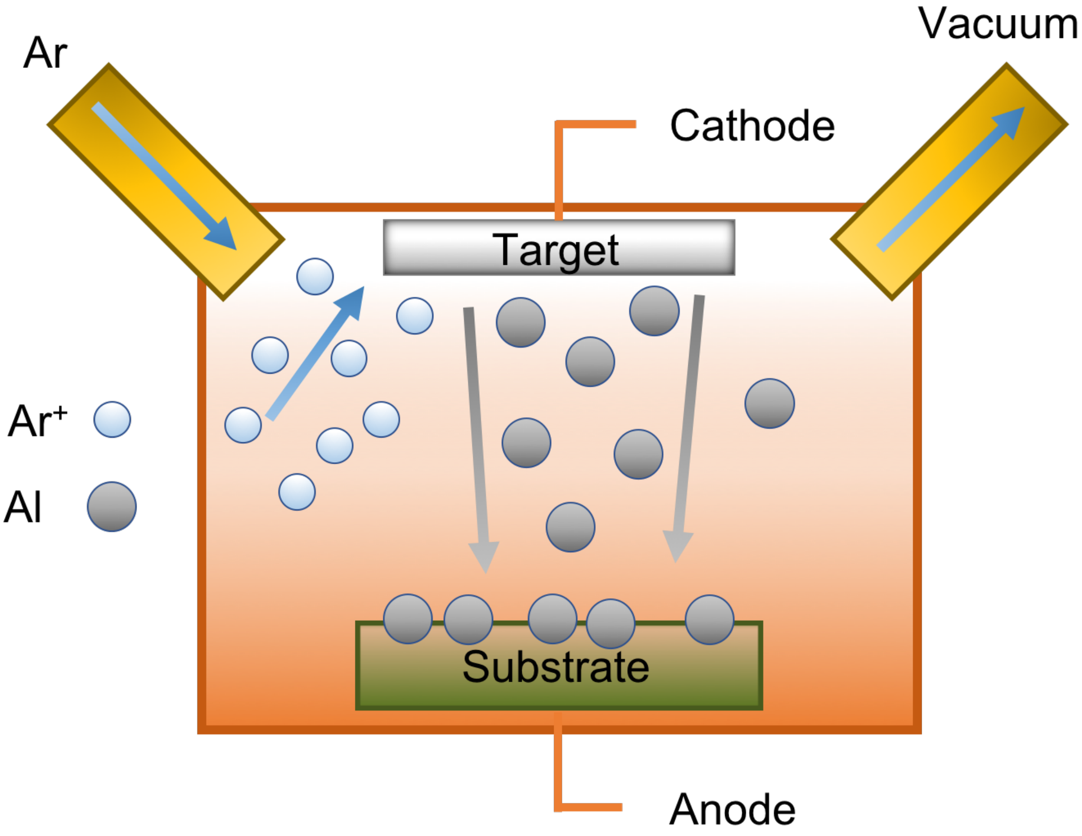

Figure 3.14 A schematic for direct current (DC) magnetron sputtering system.

3.3.2.2 Thermal Evaporation

Thermal evaporation involves evaporating a metal in the evaporation source, allowing it to diffuse in high vacuum on the order of 10^{-6} Torr, and then being deposited on the substrate. A schematic of the chamber used here is shown in Figure 3.15. Electrical current was applied to the evaporation source to heat it. The evaporation source used here was an alumina coated tungsten basket. A turbo-pumped vacuum chamber was used to increase the evaporated material mean free path by reducing the probability for the atoms from the target to collide with background gas molecules. Performing the deposition with a poor vacuum will result in discontinuous, rough films.

Several factors in the deposition have influences on the film quality: evaporation rate, substrate geometry and sample-to-source distance. For a given system, the sample to source distance is the same, but it can vary from one system to another. Samples closer to the evaporation source experience a higher deposition rate[167]. Substrate geometry is significant only in depositions for a three-dimensional substrate, but not important in the deposition for a smooth, two-dimensional substrate. A rotating stage is used to further improve the film uniformity. The evaporation rate is controlled by the input power used to heat the evaporation source. The films form as the evaporated atoms adsorb to the substrate surface, resulting in adsorbed atoms that diffuse on the substrate surface. The magnitude of the thermal energy of the adsorbed atoms as compared to the activation energy required to get to an adjoining site determines the diffusion of the adsorbed atoms on the substrate[168,169]. An increase in the evaporation rate reduces the time for the diffusion of adsorbed atoms at the lowest points on the substrate surface, resulting in increased roughness and defects in the film.

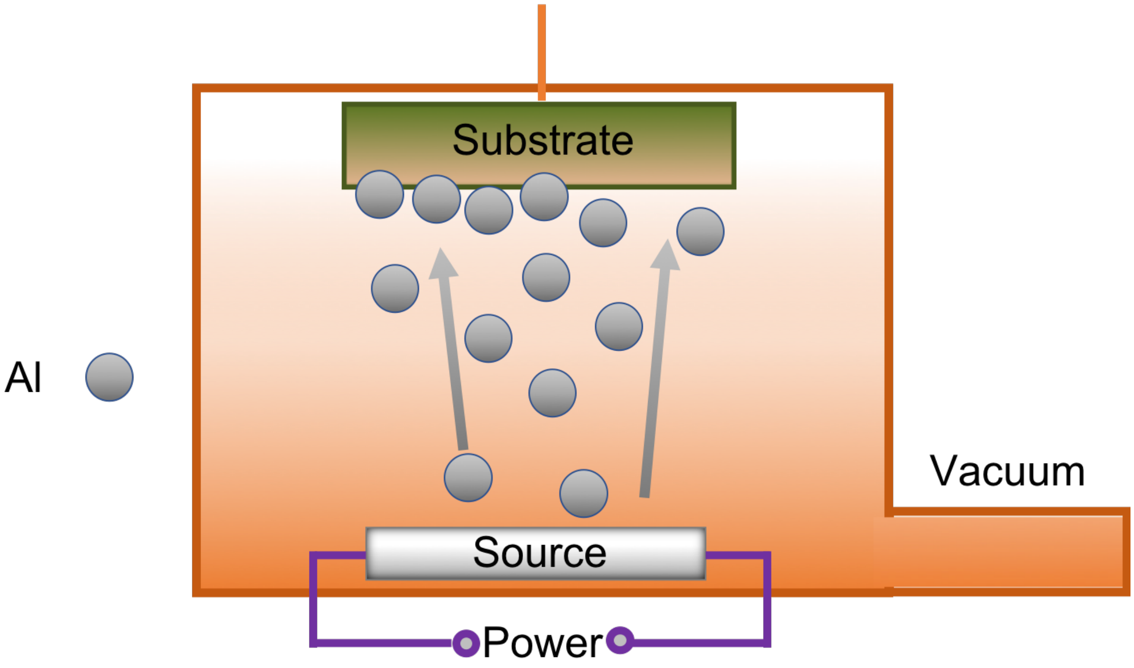

Figure 3.15 A schematic for thermal evaporation system.

The rate of evaporation can be controlled by the power input for a given material, but the quality of the film, characterized as surface roughness or defect density, is a function of the vacuum chamber pressure. The evaporation rate of a given material, whether in solid or liquid phases, is proportional to $P_e(\mathrm{T}) - P_h$, where $P_e(\mathrm{T})$ is the equilibrium pressure at temperature T, and P_h is the hydrostatic pressure. In theory, the equilibrium pressure could be derived from the Clausius-Clapeyron equation[170],

$$\frac{dP_e}{dT} = \frac{\Delta H(T)}{T\Delta V} \tag{3.35}$$

where the $\Delta H(T)$ is the enthalpy variation upon evaporation, and ΔV is the variation in volume between the condensed phases (liquid/solid) and vapor phases. Actually, experimental data and empirical formulas are more valuable to acquire the vapor pressure of a given material. The equilibrium pressure of liquid Al is

$$\log P\,(\text{torr}) = -\,15993/T + 12.409 - 0.999\log T - 3.52 \times 10^{-6}T \tag{3.36}$$

where $-\,15993/T + 12.409$ is considered to be the main term, and the other terms represent small corrections. The equation for evaporation is

$$\emptyset_e = \frac{\alpha_e N_A (P_e - P_h)}{\sqrt{2\pi MRT}} \tag{3.37}$$

where $\emptyset_e$ is the evaporation flux, α_e is the evaporation coefficient ($0 < \alpha_e < 1$), P_e is the equilibrium pressure and P_h is the hydrostatic pressure, M is molar mass, T is absolute temperature, and R is the gas constant ($8.314\ \text{J}\cdot\text{K}^{-1}\cdot\text{mol}^{-1}$). To achieve the maximum deposition rate, it is necessary to reduce P_h to zero and maximize the coefficient of evaporation, $\alpha_e = 1$, which gives

$$\emptyset_e = 3.513 \times 10^{22} \frac{P_e}{\sqrt{MT}} \cdot \frac{molecules}{cm^2} \tag{3.38}$$

or to multiply the deposition rate above with the atomic mass to get a rate with mass units

$$\Gamma_e = 5.84 \times 10^{-2} \cdot \sqrt{\frac{M}{T}} \cdot P_e \cdot \frac{g}{cm^2 \cdot s} \tag{3.39}$$

where M and T are molar mass and temperature, respectively. For aluminum deposition, M is 27 g/mol. From the diagram of vapor pressure, in order to obtain $P_e = 10^{-4}$ Torr, T needs to be 980°C. The rate of mass evaporation is then $\Gamma_e = 5.84 \times 10^{-7}\ \text{g}\cdot\text{cm}^{-2}\cdot\text{s}^{-1}$. Multiple deposition rates were tried, and the rate of 1 Å/s gave the optimal surface roughness of 1.63 ± 0.15 nm.

3.3.2.3 Characterization of Aluminum Substrate

The quality of the aluminum films deposited using DC sputtering or thermal evaporation was characterized with X-ray reflectivity (XR) and atomic force microscopy (AFM). XR measurements were done using a homebuilt rotating anode source (18 kW, RA-HF18, Rigaku) reflectometer with CuK$_\alpha$ radiation ($\lambda = 1.54$ Å). XR was measured with the reflection angle equals to the incidence angle with regard to the surface. The XR and scattering length density (SLD) plots for aluminum surface prepared with the lowest surface roughness are shown in section 4.2.3, the roughness from the best fitting result is 1.90 nm.

AFM was also used in the investigation of the aluminum surface roughness. The averaged rms roughness derived from tapping mode AFM images on several spots of the same sample surface is 1.63 ± 0.15 nm. The value of the roughness from the fitting of XR plots is a little bit larger than that from the AFM images, because XR provides statistically averaged information on the sample surface within the entire footprint where the sample surface is illuminated with the incident beam, while AFM presents an image of a surface with local morphological details. The footprint in a reflectivity measurement is of several square centimeters (i.e. 1 cm × 2 cm), while AFM can be done for the maximum surface area of less than 0.01 cm^2 (87 µm × 87 µm in Dimension Icon).

3.3.3 Epoxy Coating Preparation

Epoxy coatings on silicon wafers and aluminum substrate will be prepared and will be used in experiments investigating the diffusion of water/electrolyte along the interface between protective coating and non-metallic or metallic substrates, or in experiments probing the interfacial morphological alteration with exposure to water/electrolyte. Epoxy was selected because it is one of the most widely used primers[1,171–178], has excellent adhesion to the metallic substrate, and provides good resistance to water or electrolytes.

3.3.3.1 Hybrid Coating Solution

A variety of hybrid coatings have been developed and used as anticorrosion coatings on metallic substrates[75–77]. The inorganic component in the hybrid coating improves adhesion[78], reduces the degree of disorder in an organic coating, and reduces water or electrolyte diffusion to the interface. The formulation used for spin-coating was from two solutions: a 4 wt % solution of tetraethoxysilane (TEOS) in methanol and a methyl isobutyl ketone (MIBK) solution of EPON SU-8 epoxy with epoxide equivalent weight (EEW) of 195-230 (g/eq) and curing agent EPIKURE 6870-W-53, or isophorone diamine (IPDA) at stoichiometric ratios, *r*, of [NH]/[Epoxide] = 0.5. The epoxy resin solution and the TEOS solution were mixed at a weight ratio of epoxy : TEOS = 98:2.

3.3.3.2 Spin-coating

Spin-coating is one of the most common techniques in electronics and the nanotechnology industry. The advantage is that it can form very uniform films with good repeatability. For example, spin-coated polystyrene (PS) films usually have roughness values ranging from 4-6 Å. A typical process consists of several stages. 1) Dispense: a low concentration polymer solution is dispensed onto the substrate; 2) Spinning: a high-speed spin step is used to thin the fluid; during the preliminary stage the majority of the solution is centrifuged off, leaving on the substrate a thin film. 3) Evaporation: a drying step which eliminates the excess solvent; viscosity increases during this process, and the shear thinning process is slowed down. Films formed via spin-coating method usually leave the surface structure in a nonequilibrium stage[22]. Annealing of the sample is necessary to allow the adsorbed layer to reach a steady state, and was performed before XPCS measurements.

Final thickness depends on many factors such as rotational speed, acceleration, solvent used and concentration of polymer solution. For all the samples prepared in this work, the silicon wafers were precleaned with a piranha solution (*Warning: Piranha solution presents an explosion danger and should be handled with extreme care; it is a strong oxidant and reacts violently with organic materials. All work should be performed in a fume hood. Wear proper protective equipment.*), etched with hydrofluoric acid (HF), rinsed with ultra-purified water, dried with high-purity nitrogen, and rinsed with spectroscopy grade solvent. The concentrations of the solutions used vary depending on the target thicknesses of the films. All solutions and solvents had been filtered seven times with a 0.45 μm filter (Whatman, PTFE).

3.3.3.3 Thermal Curing and Annealing

Hybrid epoxy thin film was used for the XR, NR and X-ray off-specular scattering experiment. Spun cast films from the hybrid coating precursor solution were dried and cured at 150 °C in vacuum (at 30 mm Hg, dry ice trap) for two hours.

Polystyrene (PS) samples on hydrogen-passivated silicon wafer or graphene substrate for the XPCS measurements were annealed at 150°C in high vacuum (ca. 1×10^{-7} Pa) for 12 hours in order to remove the residual solvent in such films and ensure the PS chains were in a state close to equilibrium before XPCS measurements.

3.3.3.4 Characterization of Epoxy Coating

Similarly, the epoxy coating surface quality was characterized with XR and AFM, with XR providing statistically averaged information and AFM presenting local details. The XR and SLD curves for the best fitting results are shown in Figure 3.16(a). The epoxy surface roughness was 0.61 nm from the best fitting of reflectivity curve. The AFM results are in Figure 3.16(b). The averaged rms roughness derived from tapping mode AFM images on several spots of the same sample surface was 0.58 ± 0.04 nm.

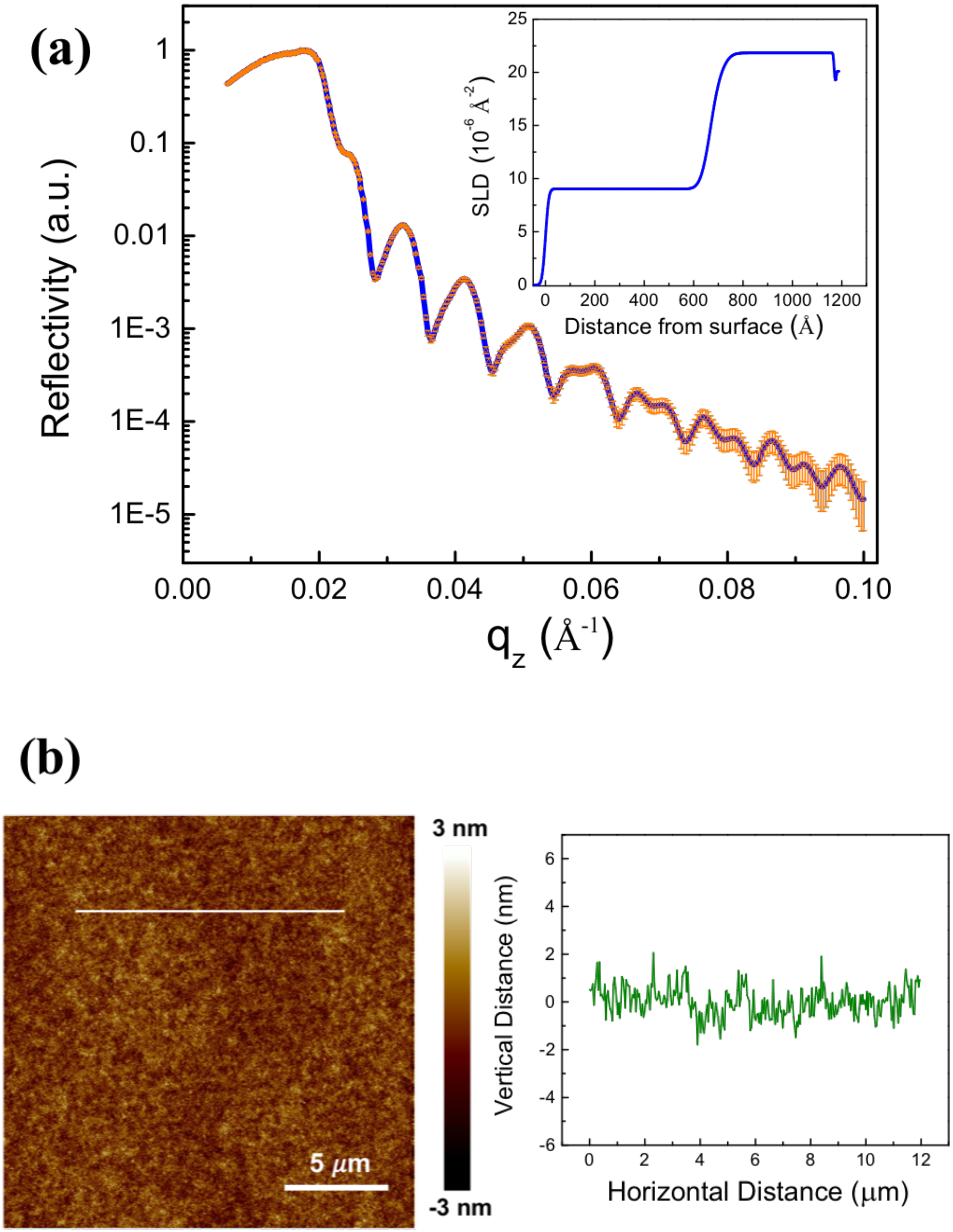

Figure 3.16 (a) XR and the best fitting of the data (χ^2= 0.0106) for epoxy film. (b) The corresponding AFM image of the same epoxy film with a line cut on the AFM image.

3.3.4 Graphene Growth and Transfer

Graphene is a perfect two-dimensional crystal material with a monolayer of sp^2 carbon atoms in an aromatic hexagonal lattice. It has received massive interest since its discovery[84,85] because of its exceptional properties such as impermeability, transparency, flexibility, and thermodynamic stability. Intensive efforts have been made in the fabrication of large scale graphene with high quality[86] and also the transfer process to nonmetallic substrates[179–182]. The methods for graphene preparation include chemical reduction of graphene oxide[183,184], epitaxial growth on SiC substrate[185,186], and chemical vapor deposition[187–190].

3.3.4.1 Graphene Growth by Chemical Vapor Deposition

Chemical vapor deposition, CVD, is considered the most promising way for graphene preparation and scale-up production. Nickel (Ni) and copper (Cu) are the most widely used catalysts in the CVD growth of graphene[191]. Graphene of multiple layers can be prepared by CVD with Ni as the catalyst, while a monolayer can be grown on the surface of a Cu catalyst. To grow large area graphene without defects, it is necessary to reduce the number of nucleation centers by using lower carbon source concentration. A higher reaction temperature will help to overcome the large energy barrier for graphene nucleation and also contribute to the diffusion of carbon atoms to the hexagonal lattice, resulting in fewer defects. Other methods reported include the use of pre-pattern growth seeds[192] and the growth of graphene on liquid metals[189] to further reduce the defects in graphene and increase its crystal size.

3.3.4.2 Graphene Transfer

Various methods were reported to transfer the graphene layer from the Cu surface to another substrate, usually nonmetallic materials[179–182]. Poly(methyl methacrylate), PMMA, was widely used in laboratories to transfer graphene layer. The PMMA transfer process[188] involves (1) spin cast the PMMA on the original Cu supported graphene surface, and thermal curing; (2) etch the Cu with inorganic solution, such as $FeCl_3$ or $(NH_4)_2S_2O_8$ aqueous solution; (3) scoop out the PMMA/graphene and rinse with deionized water and transfer to silicon wafer; (4) dry the PMMA/graphene/Si at 100°C and remove PMMA by acetone; (5) anneal the graphene/Si at 300°C in Argon/H_2 atmosphere. However, because of the strong adsorption between PMMA and graphene[180], PMMA residuals on the graphene surface cannot be avoided. Novel methods using rosin[180], a face-to-face transfer technique[182] and thermal release (TR) tape[193] is reported, which provide new means of damage-free and clean graphene transfer. In this work, multiple graphene transfer methods have been explored, and the TR tape gives the optimal graphene quality on silicon wafer. The detailed process of transfer will be discussed in Chapter VI.

CHAPTER IV

IN SITU STUDY OF THE EFFECT OF IONS ON WATER DIFFUSION IN POLYMER FILMS

Coverage with organic coatings is the most broadly used method for metallic material corrosion protection. Robust coatings have notably extended the life of structural components and greatly reduced the substantial financial cost associated with corrosion by excluding electrolyte or water, one of the three key components of corrosion, from the coating/metal interface. However, the unpredictable failure of load bearing components due to corrosion continues to be a challenge scientifically and technologically, because the results of such failure are usually catastrophic. Empirically, corrosion accelerates in the marine environment with high salt concentrations. However, the diffusion of electrolyte or water and the subsequent corrosion are two separate processes that happen in sequence. Consistent results from X-ray/neutron reflectivity (XR/NR), together with electrochemical impedance spectroscopy (EIS) indicate that the diffusion rate of electrolyte is lower than that of water, and the higher the salt concentration, the lower the rate of diffusion.

4.1 Introduction

The degradation rate of an organic coating/metal substrate interface determines the performance of a coating in a corrosion protection application. Generally, there are two kinds of methods used in industry to evaluate the performance of an organic coating[194], outdoor exposure and accelerated weathering. In the case of outdoor exposure, the testing samples are placed in the actual environment in which they are supposed to be used, usually for months or years, then the degradation of the samples is evaluated. In accelerated weathering, conditions such as radiation, humidity, and specific chemical environment can be controlled. It usually takes less time for corrosion to take place in accelerated weathering, but the results cannot be used to predict the lifetime of testing samples directly because the mechanisms are usually different in outdoor exposure and the accelerated weathering test. Nonetheless, accelerated weathering is still used to provide means to eliminate candidate coatings with certain weaknesses. There have been long time efforts to correlate the two methods, but no significant progress has been made. In order to make faster evaluations, we have to understand how water or electrolyte diffuse to the coating/metal interface, and how corrosion happens on a much smaller scale.

In previous investigations, gravimetric methods[4], Fourier transform infrared spectroscopy (FT-IR)[4–9], and scanning Kelvin probe (SKP)[9–13] have been used intensively. The diffusion directions, either parallel or vertical with respect to the film surface, was distinguished. For example, De Neve et al.[4] found, using gravimetric methods, that water diffusion along the interface is relatively rapid because diffusion is increased by favorable interaction between water and a high energy surface. Wapner et al.[9] proved that the lateral diffusion of water along an interface between epoxy and metal oxide was two orders of magnitude faster than the penetration through the film. In another study of the water absorption and diffusion properties of epoxy coatings, the water uptake derived from dielectric constant values was compatible with that directly measured by gravimetry, using supported films[195]. The effect of silane in epoxy coatings as a barrier that impedes the aggressive specie transportation into the coating/metal interface was compared with that without silane[173,196]. This comparison proved that silane significantly enhanced adhesion and corrosion protection by elimination of salt at the interface, which excluded the key mechanism in pitting corrosion. Additionally, enhanced crosslinking in the *bis*-amino silane films also results in better barrier properties[197]. A separate study compared the *bis*-sulfur silane and *bis*-amino silane film at equilibrium; the *bis*-amino silane absorbed significantly more D_2O than did the *bis*-sulfur silane, and most water is located in the free space rather than swelling the film[198]. Computed tomography (CT) was also applied since it is an imaging technique which allows one to non-destructively obtain multiscale information down to the length scale of tens of nanometers[14]. Characterization with fluorescence microscopy of the local water interaction with epoxy films showed that the epoxy coating water uptake initially happens at sites scattered on the coating surface; the scattered site number density varies among regions of the surface and increases with an ionic concentration decrease or a water activity increase[15].

In this work, we have quantified the diffusion in directions parallel and perpendicular with respect to the thin film surface. Using X-ray/neutron reflectivity (XR/NR), and electrochemical impedance spectroscopy (EIS) as a complementary method, we have found that in both directions, the diffusion rate of the electrolyte is lower than that of H_2O. Additionally, we find that with the increasing ionic concentration, the diffusion rate of electrolyte decreases.

4.2 Experimental Section

4.2.1 Epoxy coating preparation

Silicon wafers of three inch diameter, n-type, (100)-orientation, 1 mm and 5 mm thick, are purchased from El-Cat Inc. The planarity of each candidate wafer had been examined critically; only qualified wafers were used for reflectivity measurements. Wafers were cleaned using piranha solution (H_2O_2:H_2SO_4 = 3:7 by volume) at 100 °C for 30 minutes. (*Warning: Piranha solution presents an explosion danger and should be handled with extreme care; it is a strong oxidant and reacts violently with organic materials. All work should be performed in a fume hood. Wear proper protective equipment.*) Then a 40 nm thick layer of aluminum (Al) was deposited using thermal evaporation at the rate of 1 Å/s. Thermal evaporation provides controllability and uniformity over a relatively large area on the substrate. The quality and roughness of the aluminum was characterized by X-ray reflectivity (XR) and atomic force microscopy (AFM). Spin casting was used in the preparation of the thin epoxy film, on Al or silicon (Si) substrates, in order to make uniform films with good repeatability. Outstanding uniformity and root mean square roughness within range of 3 to 8 Å are readily achievable. A mixture for spin-coating was created from two solutions: a 4 wt % solution of tetraethoxysilane (TEOS, Sigma-Aldrich Inc.) in methanol and a methyl isobutyl ketone (MIBK, Sigma-Aldrich Inc.) solution of EPON SU-

8 epoxy (Momentive Performance Materials Inc.) with epoxide equivalent weight (EEW) of 195-230 (g/eq) and curing agent EPIKURE 6870-W-53 (Hexion Inc.) (used in epoxy coatings for NR measurements), or isophorone diamine (IPDA, Sigma-Aldrich Inc.) (used in epoxy coatings for XR measurements) at stoichiometric ratios, *r*, of [NH]/[Epoxide] = 0.5. The TEOS solution was mixed with the epoxy resin solution at a weight ratio of TEOS : epoxy = 2:98. The substrates, Al or Si, were rinsed with 5 mL MIBK solvent, then approximately 0.5 mL of the prepared solution was dispensed onto the substrate, and spun-cast at the rotation speed of 2000 rpm (revolutions per minute) for 2 minutes. Films spun cast on Al layers from the hybrid coating precursor solution were dried and cured at 150 °C in vacuum (at 30 mm Hg, dry ice trap) for two hours. All solutions and solvents had been filtered five times with a 0.45 µm filter (Whatman, PTFE).

4.2.2 Lateral diffusion cell

For XR/NR characterization of the lateral diffusion of H_2O/electrolyte, a lateral diffusion cell was used. A schematic of the cell is in Figure 4.1. The scratch in the epoxy coating was made intentionally using a diamond pen. A small reservoir was placed above the scratch. The H_2O or D_2O or electrolyte from the chamber has access to the entire depth of the epoxy film as well as to the interface between the epoxy and the substrate. XR or NR was performed on three areas of a sample, at various distances from the scratch, as shown in Figure 4.1. The width of the beam was reduced to 16 mm to get a coarse, but unprecedented lateral resolution of the H_2O/D_2O/electrolyte diffusion. The reduced beam width reduced the beam intensity and increased the time needed to measured up to a given value of q_z with a given statistical precision. The centers of Area 1, Area 2, and Area 3, were at 10, 28, and 46 mm from the scratch, respectively. The timer was started when the H_2O/D_2O/electrolyte was injected into the reservoir.

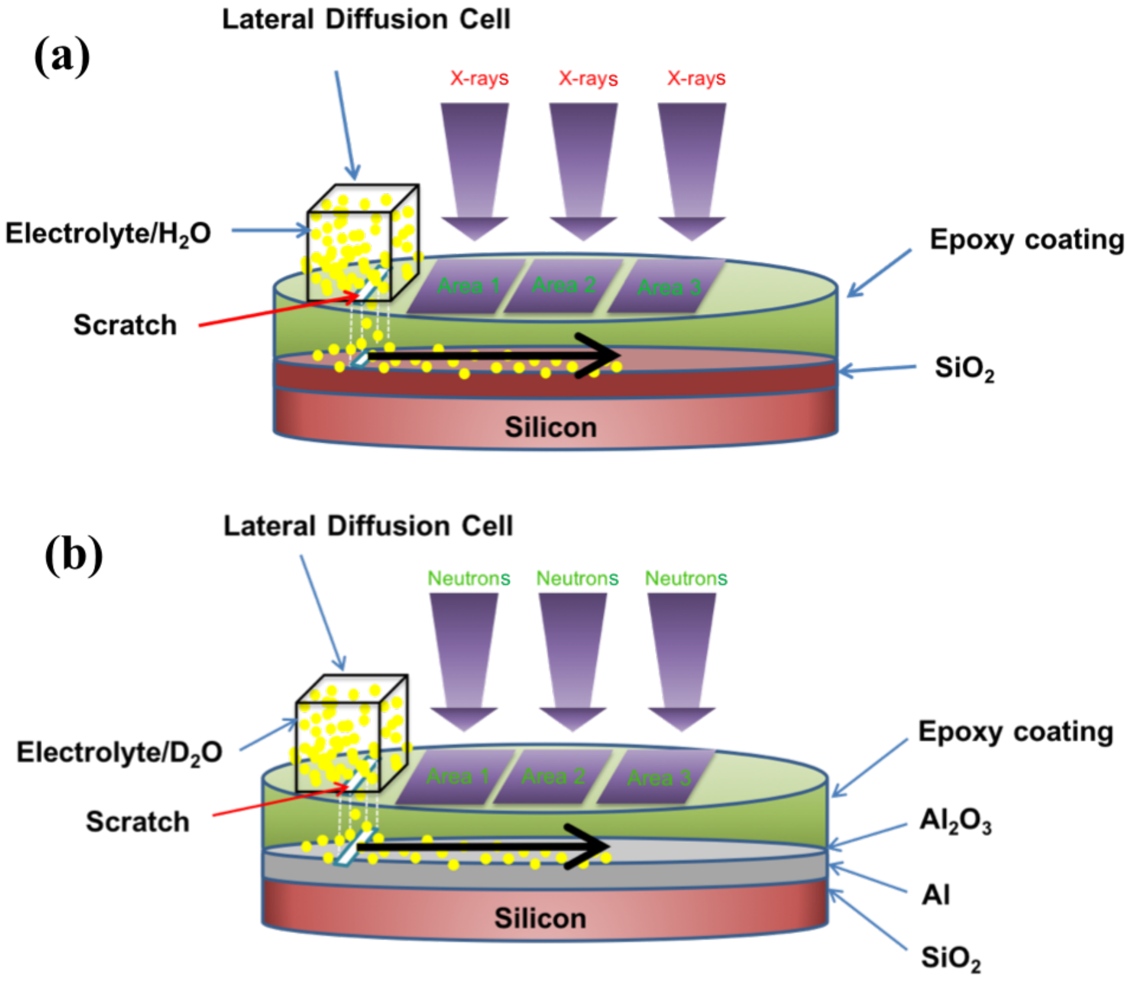

Figure 4.1 Cartoon for lateral diffusion cell used in (a) X-ray Reflectivity (XR) and (b) Neutron Reflectivity (NR) measurements. There is a scratch extending down to the (a) SiO_2/Si substrate for XR measurements and (b) Al_2O_3/Al substrate for NR measurements.

4.2.3 X-ray and neutron reflectivity (XR/NR)

X-ray reflectivity (XR) measurements were done using a homebuilt rotating anode source (18 kW, RA-HF18, Rigaku) reflectometer with CuK$_\alpha$ radiation (λ = 1.54 Å). The aluminum substrate surface morphology was characterized with XR and atomic force microscopy (AFM) before any epoxy coating was applied. Representative XR and AFM data from such a sample are shown in Figure 4.2. The aluminum surface root mean square (rms) roughness derived from the best fitting of the XR profile in Figure 4.2 was 1.90 nm rms, and from tapping mode AFM images on several spots of the same sample was 1.63 ± 0.15 nm. XR and AFM provide complementary information to be used in the fitting of the NR data from a more complicated sample that has an epoxy coating on the aluminum.

An NR experiment was conducted at NG7 Horizontal Neutron Reflectometer in the NIST Center for Neutron Research (NCNR), the National Institute of Standards and Technology (NIST). Specular reflectivity[93,99] was measured as a function of scattering wave vector perpendicular to the sample surface, $q_z = (4\pi/\lambda)\sin\theta$, where θ was the incident angle with respect to the surface and λ was the wavelength of incident beam. Both XR and NR data are plotted as log R vs. q_z, where R (reflectivity) is the intensity ratio of the reflected beam to the incident beam. All measurements were carried out with the angle of reflection equivalent to the incident angle, which corresponds to specular scattering, i.e. reflectivity. Film properties derived from the XR and NR data include the film thickness, roughnesses, and scattering length densities (SLD), which depends on the film mass density and elemental composition. In general, SLD can be calculated using

$$SLD = \frac{N_A \cdot \rho}{M} \cdot \left(\sum b_i\right) \qquad (4.1)$$

where ρ is the mass density; N_A is Avogadro's number; b_i is the scattering length of element i; and M is the molecular weight of the reference chemical structure for which the sum over i is calculated. The scattering length b_i is a function of electron density for X-rays and is simply the neutron scattering length for neutrons. The water uptake was derived by comparing the SLD profiles from both XR and NR. The difference in SLD values among different layers determines the contrast in both XR and NR measurements. XR and NR data analysis were performed using nonlinear least squares regression with a multilayer structural model and the fitting software Motofit by Andrew Nelson from the Australian Nuclear Science and Technology Organisation.

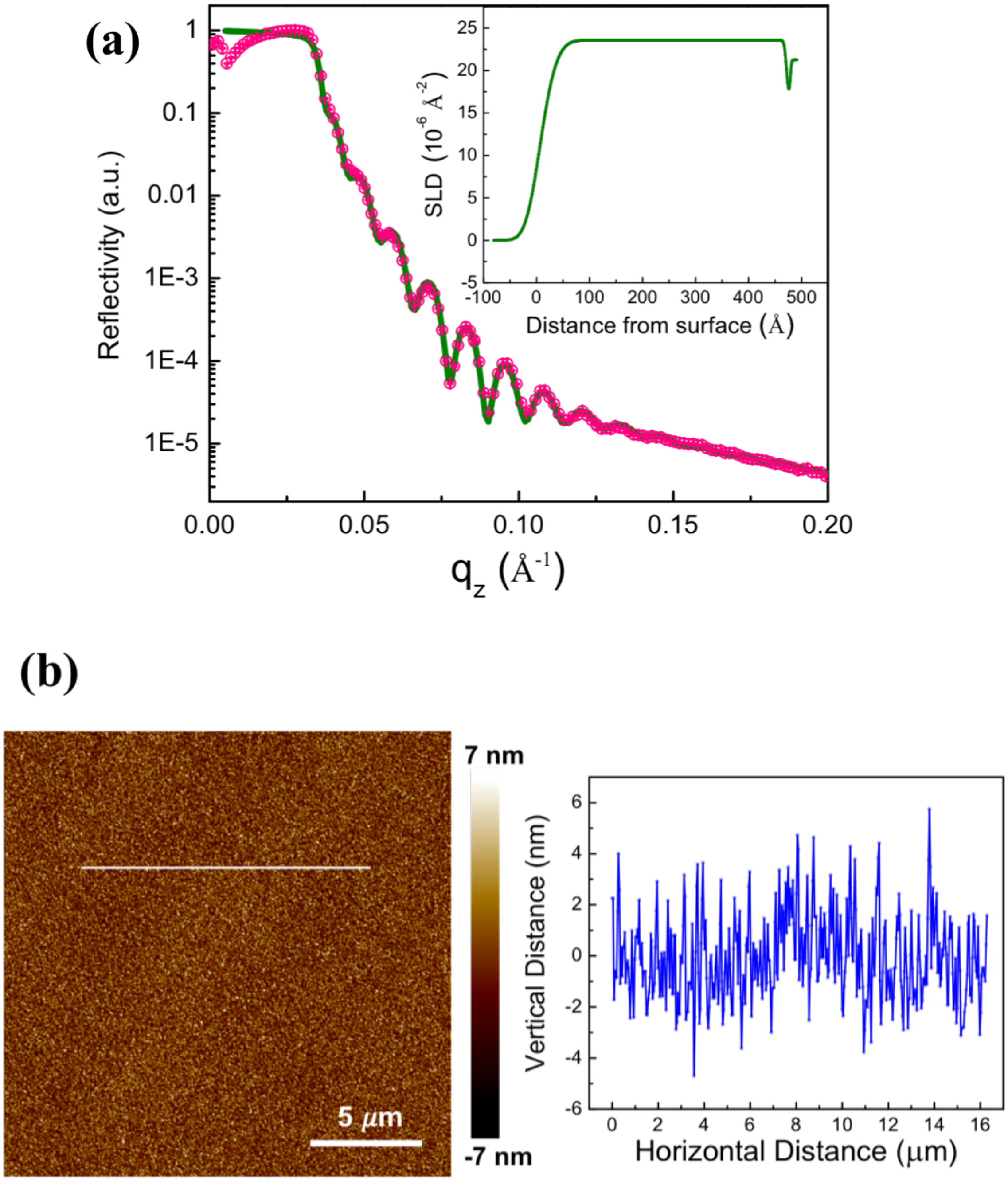

Figure 4.2 (a) XR data and best fit ($\chi^2 = 0.0106$) for an aluminum film on a silicon substrate. (b) The corresponding AFM image of that aluminum film with a line cut from the image.

4.2.4 Electrochemical Impedance spectroscopy (EIS)

Electrochemical impedance spectroscopy (EIS) is one of the most widely used methods in the evaluation of a new coating, both in the laboratory and in industry[195]. The degradation of coatings in water and NaCl solution was compared by Zhou et al.[199]. They found the diffusion of H_2O into the coating from above the coating ("penetration") was faster than the diffusion of 3.5 wt % NaCl (aq). The water and electrolyte uptake were compared using a combination of EIS and UV-Vis spectroscopy by Dornbusch et al.[200] The authors showed there was a faster water uptake process and then a slow ion uptake which caused the initiation of corrosion at the interface. Several studies of diffusion behavior have used EIS. Hu et al. modeled ideal[201] and non-ideal[202] Fickian diffusion of water in polypropylene[203] and epoxy[204] coatings. Zhang et al.[205] looked at water uptake and Cl^- ion diffusion in epoxy primer. Maile et al.[206] showed the diffusion could be understood as a two-stage sorption process. Oxygen and water permeability were investigated by Popov[207] and Scully[208] and Walter[209] found that diffusion of the sodium ion is the rate-controlling step in the corrosion process. New models for extracting the diffusion rate from EIS data were proposed by Ding et al.[210] and Ghojavand et al.[211]

A three-electrode system is commonly used in EIS measurements, with the aluminum underneath the epoxy acting as the working electrode, a platinum disk as the counter electrode, and a saturated calomel electrode (SCE) as the reference electrode. The thickness of the epoxy film used in the EIS measurements in the dissertation research was on the order of tens of nanometers, much smaller than what is typically used in the coating industry, which is on the order of micrometers. An O-ring perspex cylinder was fixed to the surface of the coated epoxy to hold the electrolyte (Figure 3.9). The cylinder was filled with water or a 3.5 wt% NaCl solution as the working fluid. All measurements were done at room temperature (25°C); three samples were tested for each working fluid. The experimental data were analyzed using the ZIVE ZMAN 2.3 software developed by WonATech Co., Ltd.

4.3 Results and Discussion

4.3.1 X-ray and neutron reflectivity (XR/NR)

In both XR and NR measurements, the SLD plays an important part in determining the reflectivity data. The difference in SLD values between different pairs of layers in a model determines the contrast. D_2O (99.9% atom % of D, Sigma-Aldrich) and 3.5 wt % NaCl solutions in D_2O were used for the NR experiments, and 3.5 wt % or 7 wt % NaI solutions in H_2O were used for the XR experiments to provide contrast for distinguishing the differences in layer thicknesses and the values of interface roughnesses by nonlinear regression of the data. The simplest layered model that fits the data was accepted here. Epoxy films crosslinked with isophorone diamine (IPDA, Sigma-Aldrich Inc.) or EPIKURE 6870-W-53 (Hexion Inc.) were used in the XR and NR experiments, respectively. Following the work of Schaefer et al.[196] the curing agent EPIKURE 6870-W-53, which has a larger spacing between the two intramolecular amino groups than does IPDA, was used to make it easier for electrolyte or water to diffuse through the crosslinked epoxy coating, making the time required to see the diffusion fit into the typical beam time available for an NR experiment due to limited access to neutron sources. IPDA crosslinked epoxy films made the diffusion process slower than it was in films crosslinked with 6870-W-53.

As introduced in the experimental section, a lateral diffusion cell was used for the XR and NR measurements. Figure 4.3(a-c) compares the XR data for the dry condition measured at Areas 1, 2, and 3, and for 27, 33, 49 h after the 3.5 wt % NaI (aq) was injected into the lateral diffusion cell measured at Area 1, Area 2, and Area 3, respectively. The centers of Area 1, Area 2, and Area 3 were at 10 mm, 28 mm, and 46 mm from the scratch, respectively. Comparisons of the shapes of the curves are made in Figure 4.3(a-c). The spacing between fringes (Δq) is inversely proportional to the film thickness (d) by $d \cong 2\pi/\Delta q$.[93] Thus, the decrease in Δq is in Figure 4.3(a, b) implies an increase in the film thickness. After 27 hours of exposure, in Area 1, which is the region closest to the scratch, the data enlarged in the inset show there is a clear shift (0.0044 $Å^{-1}$) of the Kiessig fringes[99] to the left, which is an indication that the film is swelling. After another six hours in Area 2, which is another 18 mm farther from the scratch, a smaller shift (0.0031 $Å^{-1}$) to the left, relative to the curve for the dry state, is observed, indicating that the film in Area 2 has swelled less than did the film in Area 1 after 27 hours. Similarly, in Area 3, which is another 18 mm farther from the scratch than is Area 2, no change is observed.

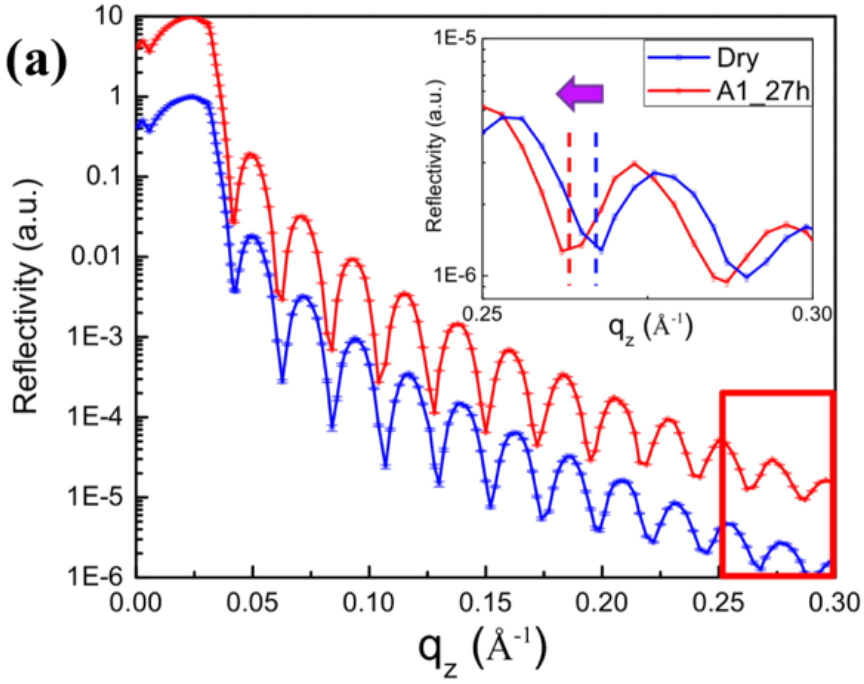
(a)
Reflectivity (a.u.)
10
1
0.1
0.01
1E-3
1E-4
1E-5
1E-6
0.00
0.05
0.10
0.15
0.20
0.25
0.30
q_z (Å^{-1})
Dry
A1_27h
1E-5
1E-6
Reflectivity (a.u.)
0.25
0.30
q_z (Å^{-1})

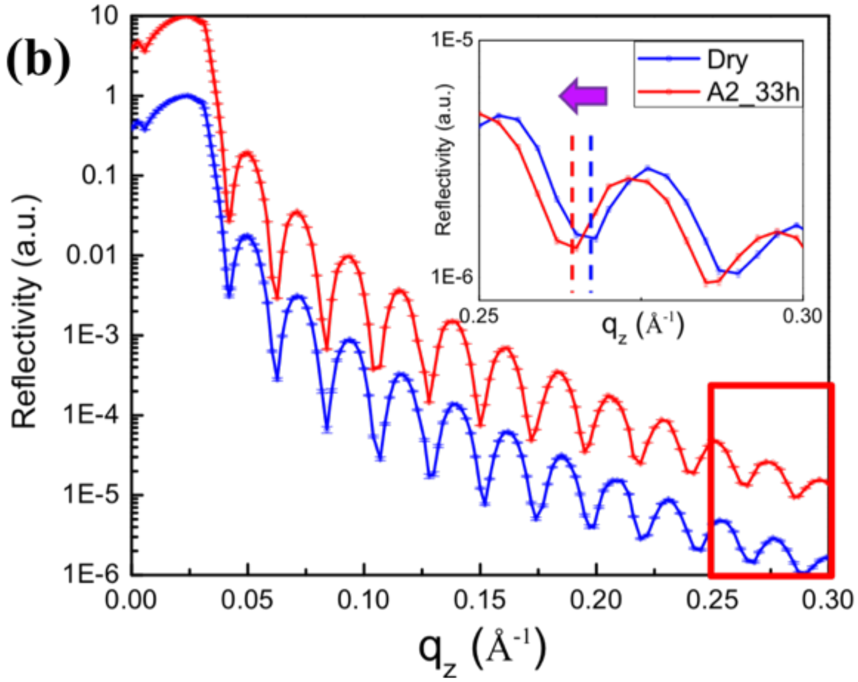
(b)
Reflectivity (a.u.)
10
1
0.1
0.01
1E-3
1E-4
1E-5
1E-6
0.00
0.05
0.10
0.15
0.20
0.25
0.30
q_z (Å^{-1})
Dry
A2_33h
1E-5
1E-6
Reflectivity (a.u.)
0.25
0.30
q_z (Å^{-1})

(c)

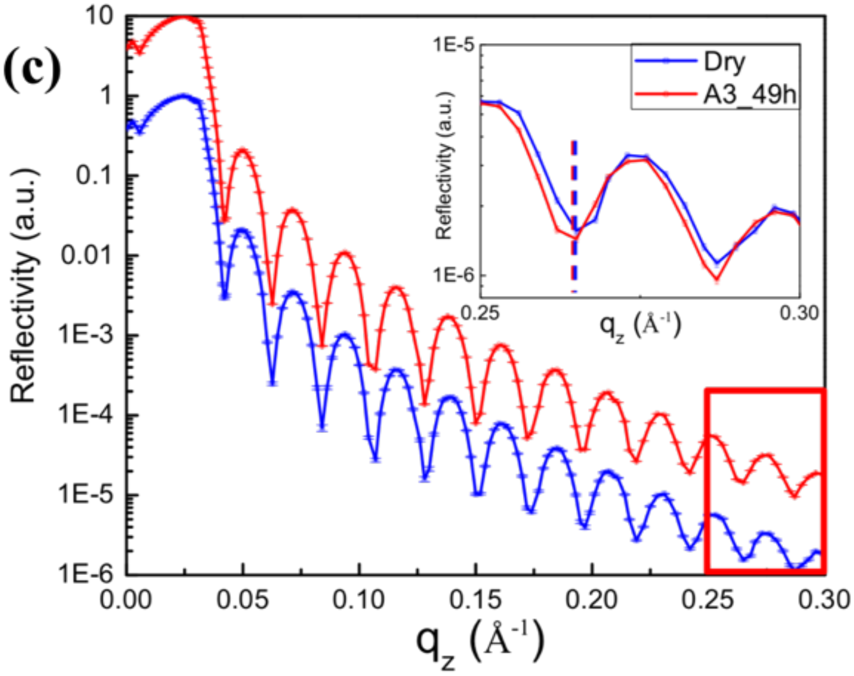

Figure 4.3 Comparisons of X-ray reflectivity (XR) data for the dry condition with that at 27, 33, and 49 h after 3.5 wt % NaI (aq) was injected into the lateral diffusion cell measured at (a) Area 1, (b) Area 2, and (c) Area 3, respectively. The reflectivity curves after exposure have been shifted vertically by a factor of ten for clarity.

Examples of quantitative analysis of the data collected from the Area 1 in the dry state and after 27 h of exposure to electrolyte are in Figure 4.4(a, b). A simple one layer model was used in the nonlinear regression fitting of the reflectivity data. From the SLD profile, it may be seen that the coating thickness increased by 4 Å and the SLD increased from 9.8 × 10^{-6} $Å^{-2}$ to 10.5 × 10^{-6} $Å^{-2}$. The SLD has increased because 3.5 wt % NaI (aq) has an SLD of 11.2 × 10^{-6} $Å^{-2}$. The electrolyte volume fraction in the film can be deduced from this change in SLD using the equation

$$\varphi_{electrolyte} = \frac{SLD_{wet} - SLD_{dry}}{SLD_{electrolyte}}, \tag{4.2}$$

where SLD_{wet}, SLD_{dry}, and $SLD_{\mathrm{electrolyte}}$ are the SLDs for the film after exposure in the lateral diffusion cell, the SLD for the as-prepared sample, and the SLD of the electrolyte used, respectively. From equation 4.2 we calculate, $\varphi_{\mathrm{electrolyte}} = 0.062$ after 27 h in the lateral diffusion cell.

We wish to infer a rate of mass transfer of electrolyte along the film due to the diffusion. First, we will neglect the complication that the movement of the water is not rigorously one-dimensional (i.e. water can diffuse laterally into the film and then be lost out of the top of the film). Then we will estimate the amount of electrolyte that crosses the polymer film cross-sectional area moving away from the scratch by calculating the change in total scattering length in the volume of the film that lies under the Area 1 on top of the film. The area of Area 1 is 4 cm^2. The coating is 27.1 nm thick, so the volume, V_{o}, initially under Area 1 is 1.08 × 10^{-5} cm^3. The total scattering length in that volume initially is $V_{\mathrm{o}} \cdot SLD_{dry} = 1.06 \times 10^{14}$ Å. After 27 h the total scattering length in that volume, b_{27h}, is $V_{27h} \cdot SLD_{27h} = 1.16 \times 10^{14}$ Å, where we have used the volume of the slightly swollen film.

The amount of scattering that has moved into Area 1 is given by $b_{27h} - b_o = 1.0\times 10^{13}$ Å. The amount of electrolyte that has moved, the net rate of mass transfer $J_{\text{electrolyte}}$ is then given by

$$N_{electrolyte} = \Delta b / b_{electrolyte} , \tag{4.3}$$

$$J_{electrolyte} = N_{electrolyte} \;/\; \Delta time , \tag{4.4}$$

in which $N_{\text{electrolyte}}$ is the number of molecules calculated from the SLD profile for a given exposure time and Δb is the increase in scattering length. The lateral diffusion coefficient may be related to the value of $J_{\text{electrolyte}}$ using the standard model for a film at steady state,

$$J_{electrolyte} = \frac{D_{electrolyte} \cdot K \cdot A}{d} \times \left(C_{scratch} - C_{centerline\ of\ Area\ 1}\right) \tag{4.5}$$

in which $J_{\text{electrolyte}}$ is the net rate of electrolyte diffusion across an area A, $D_{\text{electrolyte}}$ is the electrolyte diffusion coefficient (cm^2/s), A is the coating area (cm^2), K is the partition coefficient, d is the lateral dimension of the area along the direction of electrolyte diffusion (cm), and C is the concentration of electrolyte (mol/cm^3). $C_{scratch}$ comes from the density of liquid electrolyte, and $C_{centerline\ of\ Area\ 1}$ was calculated from SLD profile variation with time. This model assumes that the diffusion through the coating parallel to the substrate can be described using the known steady state solution for diffusion through a film[212] (i.e. ignores complications in the other dimensions). In this experiment, K is 0.2, $C_{scratch}$ is 0.0555 mol/cm^3, $C_{centerline\ of\ Area\ 1}$ is 6.2×10^{-3} mol/cm^3, and d is 1 cm. The electrolyte diffusion coefficient value derived from the set of equations including (4.1) (4.4) and (4.5) is 1.9×10^{-5} cm^2/s, This is a nominal value calculated from the behavior that occurs between the dry condition and after 27 hours after the injection of 3.5 wt % NaI (aq) electrolyte.

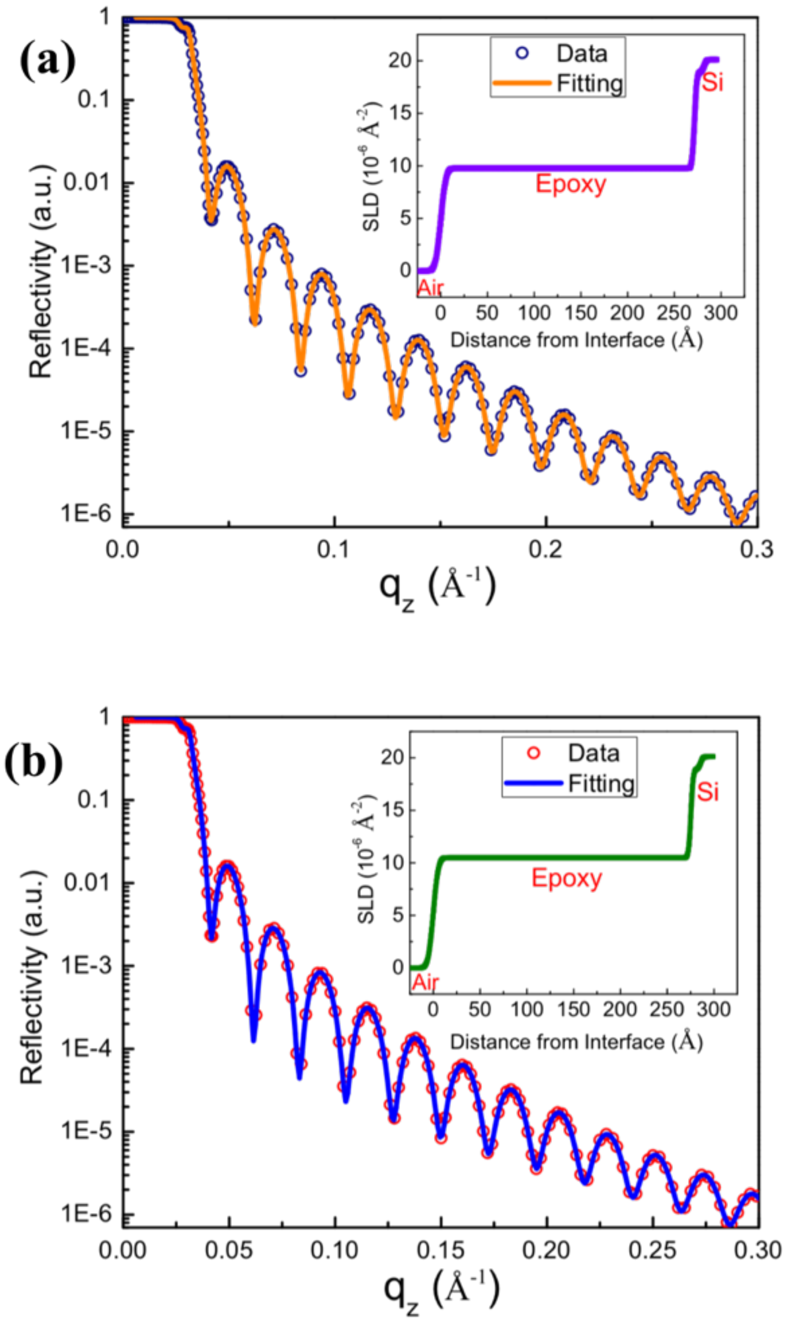

Figure 4.4 Fits (solid curves) of XR data (open circle) and SLD depth profiles corresponding to the fits for (a) dry condition and (b) 27 h after injection of 3.5 wt % NaI (aq) into the lateral diffusion cell measured at Area 1.

Data for another measurement, with a higher concentration of electrolyte, 7 wt % NaI (aq), at Area 1 after 49 hours are compared with the data for the dry state in Figure 4.5. No change was observed with such a high concentration of electrolyte, even with a longer exposure time as compared with the experiment in Figure 4.3(a). The presence of Na^+ and I^- ions impeded the diffusion of water or electrolyte. The limitation of the XR measurement is that it cannot distinguish the movement of Na^+ or I^- ions from that of the H_2O molecules because the contrast between their SLDs is small. However, using other characterization techniques, such as UV-Vis and EIS, as reported by Dornbusch et al.[200], it can be shown that the water/electrolyte uptake is a two-step process, with a faster water uptake and then a slow ion uptake. It was the ion uptake that initiated the corrosion at the interface. A separate study regarding water reorientation dynamics in concentrated ionic solutions by Zhang et al.[213] showed that water rotation was retarded in concentrated ionic solutions due to the ions effect on water structure dynamics. Zhang et al. attributed this to the cluster formation from cations and anions in concentrated solutions, and this slow cluster motion coupling with water frame rotations nearby retarded the water dynamics. In both cases, the ions in electrolyte were either slower in diffusion dynamics or inhibited the diffusion of H_2O, a finding which was consistent with the slower electrolyte diffusion with a higher concentration reflected by the XR measurements using the lateral diffusion cell. The nanoscale morphology change at the epoxy/metal interface after exposure to ions was investigated and is reported in Chapter V.

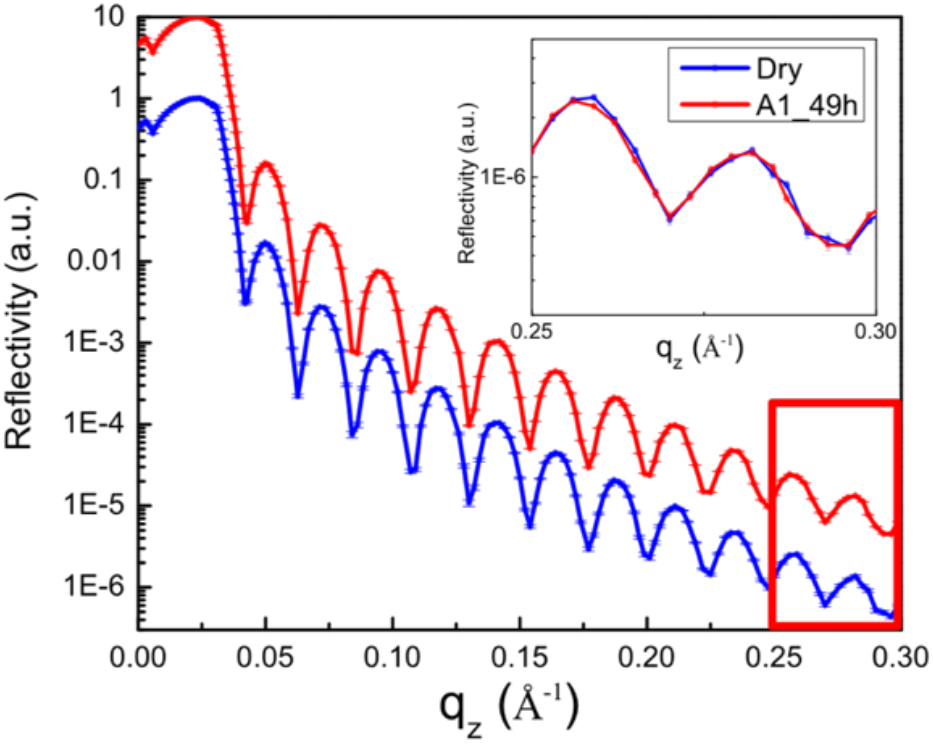

Figure 4.5 Comparisons of XR data for the dry condition and for a measurement in Area 1 49 hours after 7 wt % NaI (aq) was injected into the lateral diffusion cell.

NR measurements were performed using the lateral diffusion cell, but with an epoxy crosslinked with curing agent EPIKURE 6870-W-53 on an aluminum substrate. An example in Figure 4.6 was the measurements for Area 1 comparing the as-prepared sample and 2.5 hours after the injection of D_2O or 22 hours after the injection of 3.5 wt % NaCl solution in D_2O. Qualitatively, there is an obvious vertical shift of the Kiessig fringes[99] for the sample after 2.5-hour exposure to D_2O, which is attributed to the increase in the epoxy film SLD because of the diffusion of D_2O into the epoxy film. No obvious shift was observed for the sample even after 22-hour exposure to the 3.5 wt % NaCl solution in D_2O, which indicated that the electrolyte (NaCl in D_2O) showed a lower diffusion rate than pure D_2O in lateral diffusion along the epoxy film.

From the SLD profile corresponding to the fitting of NR data and equation (4.2), the D_2O volume fraction φ_{D_2O} is 1.90 % after 2.5 hours in the lateral diffusion cell. The D_2O diffusion coefficient was derived similarly from the calculation of the equation set including (4.1) (4.3) and (4.4). The D_2O diffusion coefficient D_{D_2O} is 3.19×10^{-5} cm^2/sec, calculated from the comparison of NR and SLD of the sample when it was dry and 2.5 hours after the injection of D_2O into the lateral diffusion cell measured at Area 1.

The diffusion coefficient of the electrolyte calculated from XR and that of D_2O from NR are both on the order of 10^{-5} cm^2/sec, which is four orders of magnitude larger than the conventional diffusion coefficient for water in bulk epoxy (on the order of 10^{-9} cm^2/sec)[214]. The D_2O diffusion coefficient, $D_{D_2O} = 3.19 \times 10^{-5}$ cm^2/sec, was larger than the electrolyte diffusion coefficient, $D_{\text{electrolyte}} = 1.92 \times 10^{-5}$ cm^2/sec, attributing to the less impedance on water diffusion resulting from the absence of ions and larger spacing between the two intramolecular amino groups in the curing agent EPIKURE 6870-W-53 used in the NR measurements.

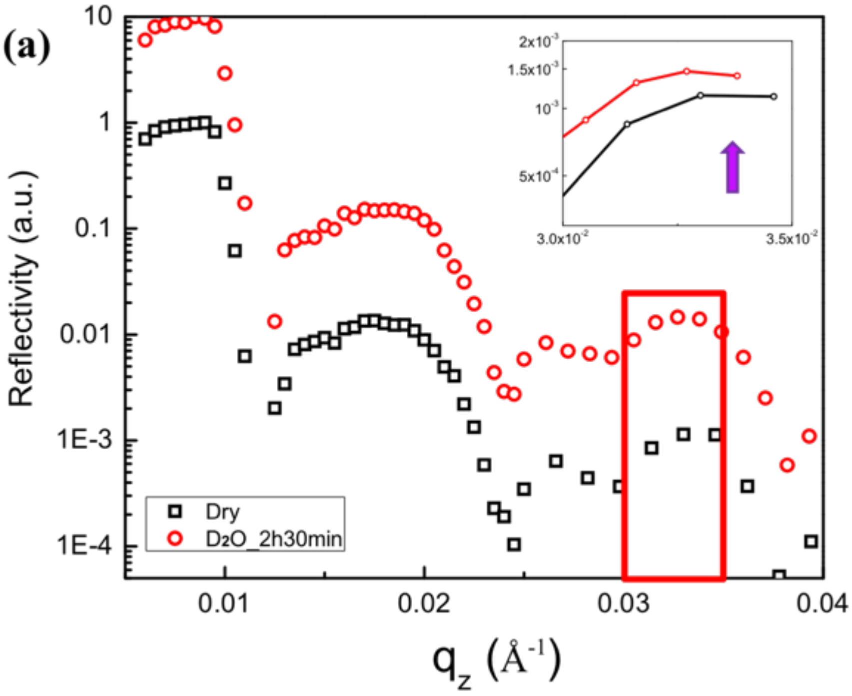
(a)
Reflectivity (a.u.)
10
1
0.1
0.01
1E-3
1E-4
0.01
0.02
0.03
0.04
q_z (Å^{-1})
Dry
D₂O_2h30min
2x10^{-3}
1.5x10^{-3}
10^{-3}
5x10^{-4}
3.0x10^{-2}
3.5x10^{-2}

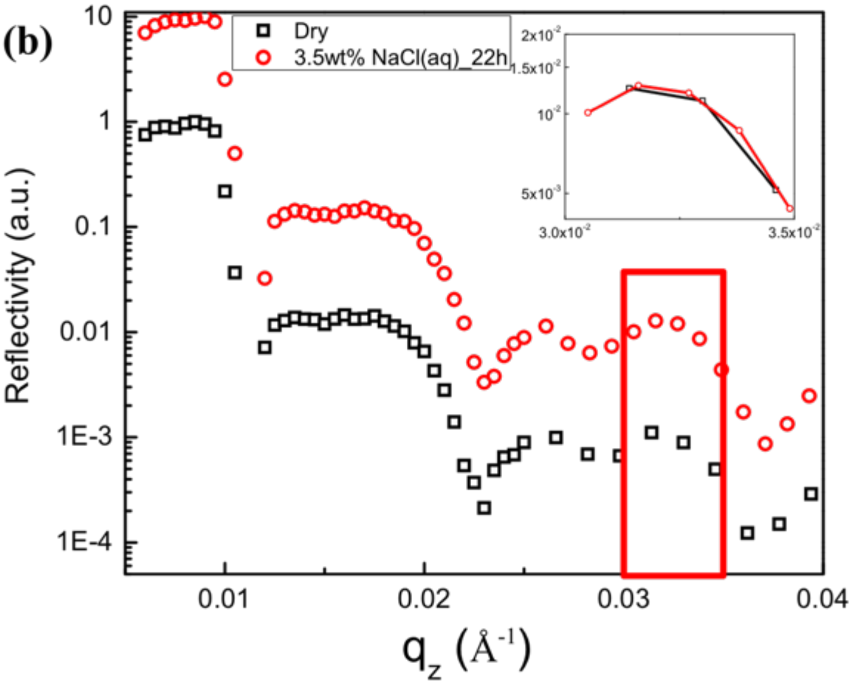
(b)
Reflectivity (a.u.)
10
1
0.1
0.01
1E-3
1E-4
0.01
0.02
0.03
0.04
q_z (Å^{-1})
Dry
3.5wt% NaCl(aq)_22h
2x10^{-2}
1.5x10^{-2}
10^{-2}
5x10^{-3}
3.0x10^{-2}
3.5x10^{-2}

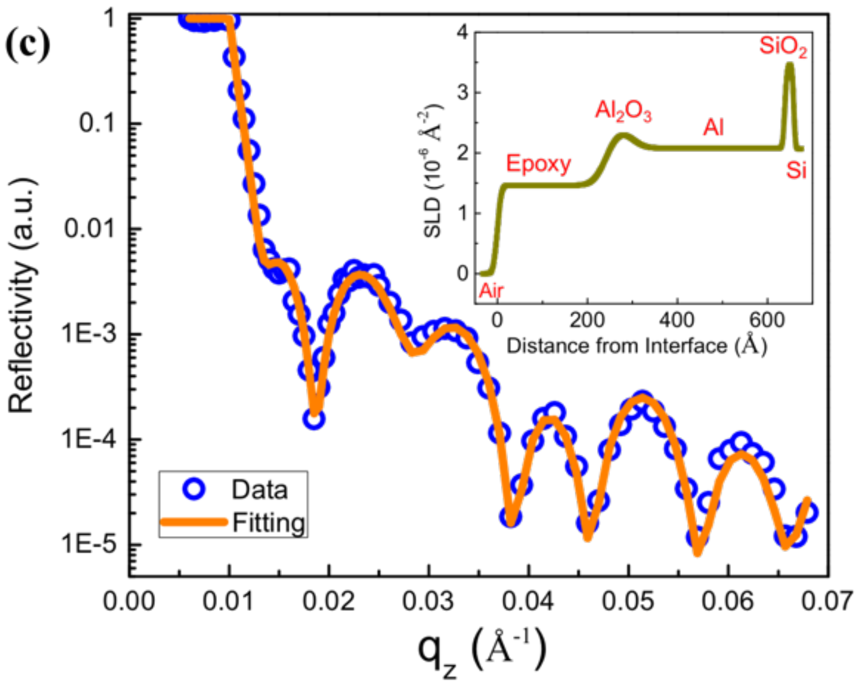

Figure 4.6 Comparisons of neutron reflectivity (NR) data measured for the dry condition and measured at Area 1 for (a) 2.5 hours after injection of D_2O, and (b) 22 hours after injection of 3.5 wt % NaCl solution in D_2O into the lateral diffusion cell. The Full NR curves are shifted vertically for clarity. In the insets they are not shifted. (c) Model fit (solid curve) of NR data (open circles) and (inset) SLD depth profiles corresponding to the as-prepared dry epoxy coating on aluminum substrate.

4.3.2 Electrochemical Impedance Spectroscopy (EIS)

The barrier properties of coatings on the corrosion protection and the diffusion of water or electrolytes to the interface between metal and coating by penetration have been extensively investigated by EIS[215]. EIS gives a previse and in situ characterization for the organic coating capacitance[205], which makes it a well-known tool for coating evaluations. In the analysis of EIS data, appropriate equivalent electrical circuit (EEC) is necessary. A simple model proposed by Mansfeld et al.[130] for organic coatings on metal substrates is shown in Figure 4.7(a). R_s denotes electrolyte resistance, R_c refers to the coating resistance, C_c is the coating capacitance, and Z_f is the interfacial electrochemical process. For an as-prepared dry coating, the R_c and Z_f are large enough that the total impedance is R_sC_s. As a result of the water/electrolyte diffusion into the coating, the EEC is converted into $R_s(C_cR_c)$, as indicated in Figure 4.7(b).

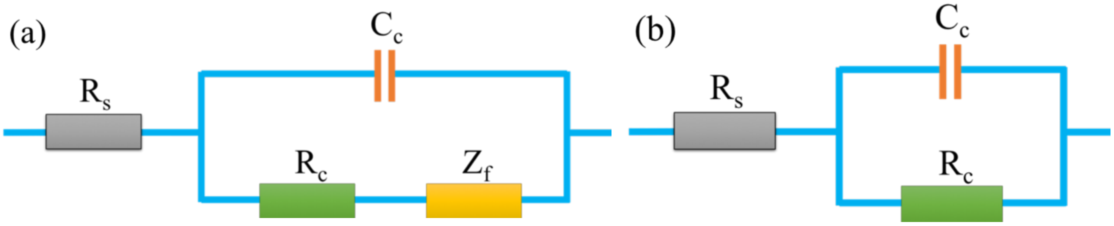

Figure 4.7 (a) A general equivalent electrical circuit (EEC) for organic coatings on metal substrates. (b) EEC used in the fitting of EIS data for the early water/electrolyte penetration diffusion process.

The effects of two different working fluids were compared, pure H_2O and 3.5 wt % NaCl aqueous solution. EIS was measured for each working fluid at time zero, and every hour until five hours after the working fluid was added to the three-electrode EIS setup. The results are compared in Figure 4.8.

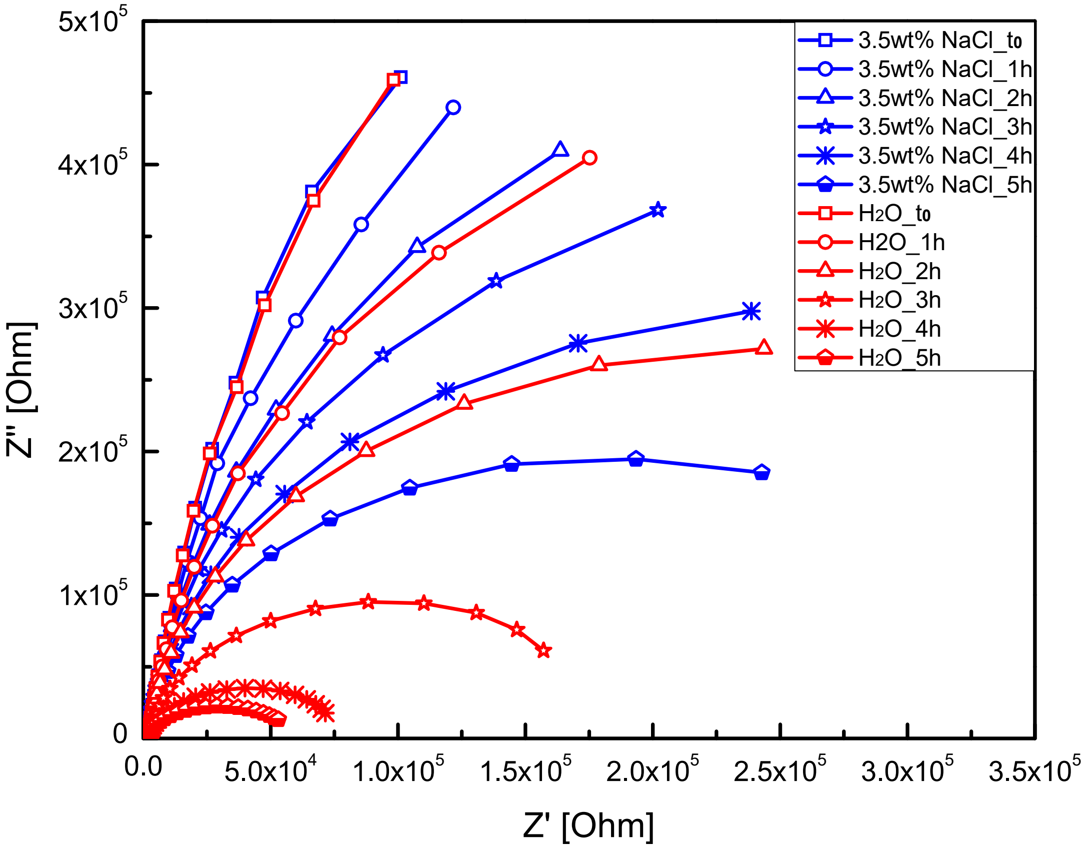

Figure 4.8 A Nyquist plot comparing EIS results from thin epoxy films exposed to H_2O or 3.5 wt% NaCl aqueous solution as the working fluid.

Qualitatively, the capacitive arcs for samples measured in H_2O and 3.5 wt % NaCl (aq) were reduced because of the diffusion of H_2O or electrolyte into the epoxy thin film. The rate of capacitive arc radius reduction was larger for measurements using H_2O as working fluid than for tests using 3.5 wt % NaCl (aq). This difference in arc reduction rate indicated a larger diffusion rate for H_2O than for 3.5 wt % NaCl(aq) in penetration through the epoxy coating. Quantitative analysis was performed with the EEC modelling using the software ZIVE ZMAN 2.3. Values of parameters in the model, coating capacitance (C_c), electrolyte resistance (R_s), and coating resistance (R_c) are derived from the fitting of the Nyquist plot. A summary of the coating capacitance values at each measurement is shown in Table 4.1. The capacitance values for such a thin epoxy film on the order of tens of nanometers is much larger than the values of the coating capacitance for films with thicknesses on the order of micrometers[216], which is usually on the order of 10^{-10} F. The different capacitance originates in the different epoxy films selected, and more importantly, in the significant difference in film thickness values.

Table 4.1 Epoxy film capacitance values from EEC fitting of Nyquist plot

Working fluids	Epoxy coating capacitance ($\times 10^{-5}$ F)					
	t = 0	t = 1 h	t = 2 h	t = 3h	t = 4h	t = 5h
H_2O	3.2	3.4	3.5	3.7	4.1	4.5
3.5 wt % NaCl(aq)	3.3	3.3	3.3	3.3	3.4	3.4

The increase in the capacitance of coating as a function of time has been correlated with water penetration in the coating[217]. The amount of water uptake can be derived from

$$\frac{\ln C(t)-\ln C_d}{\ln C_\infty-\ln C_d} = \frac{M(t)}{M_\infty} \tag{4.6}$$

in which $C(\text{t})$, C_d and C_∞ are the coating capacitance at time t, zero, and when the coating is fully saturated, respectively; $M(\text{t})$ and M_∞ are the amounts of adsorbed water at time t and equilibrium, respectively. Since the water diffusion in epoxy follows the Fickian diffusion law, and the fact that the measured data follow the equation[204],

$$\frac{M(t)}{M_\infty} = 1-\frac{8}{\pi^2}\cdot\sum_{n=0}^{\infty}\frac{1}{(2n+1)^2}\exp\left(\frac{-(2n+1)^2\cdot D\cdot\pi^2}{L^2}\cdot t\right)\ , \tag{4.7}$$

where L is the thickness of the film and D is the effective diffusion constant. By combining equations (4.6) and (4.7), and use of a series of expansion for (4.7) in the short time approximation, the following equation can be derived

$$\frac{\ln C(t)-\ln C_d}{\ln C_\infty-\ln C_d} = \frac{2\sqrt{D}}{L\sqrt{\pi}}\cdot\sqrt{t}\ . \tag{4.8}$$

The material water volume fraction is related to capacitance using the Brasher-Kingsbury (B-K) equation[217],

$$\varphi = \frac{\log(C_t/C_0)}{\log\varepsilon_w} \tag{4.9}$$

in which φ is the coating water volume fraction, C_t is the capacitance at time t, C_0 is the capacitance at time 0, ε_w is the working fluid relative permittivity, either H_2O or NaCl (aq). ε_w is 80.4 for pure water and 74.0 for the 3.5 wt % NaCl (aq) at room temperature.

The relative capacitance and water volume fraction variations of the coating as a function of time are shown in Figure 4.9(a, b). Both parameters increased with exposure to H_2O or NaCl(aq), but the increase in both parameters is more significant when using H_2O

as the working fluid. The Fickian diffusion constants for H_2O and 3.5 wt % NaCl (aq) in the penetration of epoxy coatings calculated from equations (4.6-4.8) are $D_{H_2O} = 4 \times 10^{-17}$ cm^2/s and $D_{NaCl(aq)} = 6 \times 10^{-18}$ cm^2/s. Results from the relative coating capacitance, water volume fraction, and Fickian diffusion constants showed consistently lower diffusion rates for NaCl (aq) compared to H_2O in this penetration process. Compared to the Fickian diffusion constants for H_2O in epoxy coatings on the order of 10^{-9} cm^2/s in some EIS literature[205,207], the Fickian diffusion constant here is orders of magnitude smaller, resulting from the large coating capacitance because of a smaller film thickness.

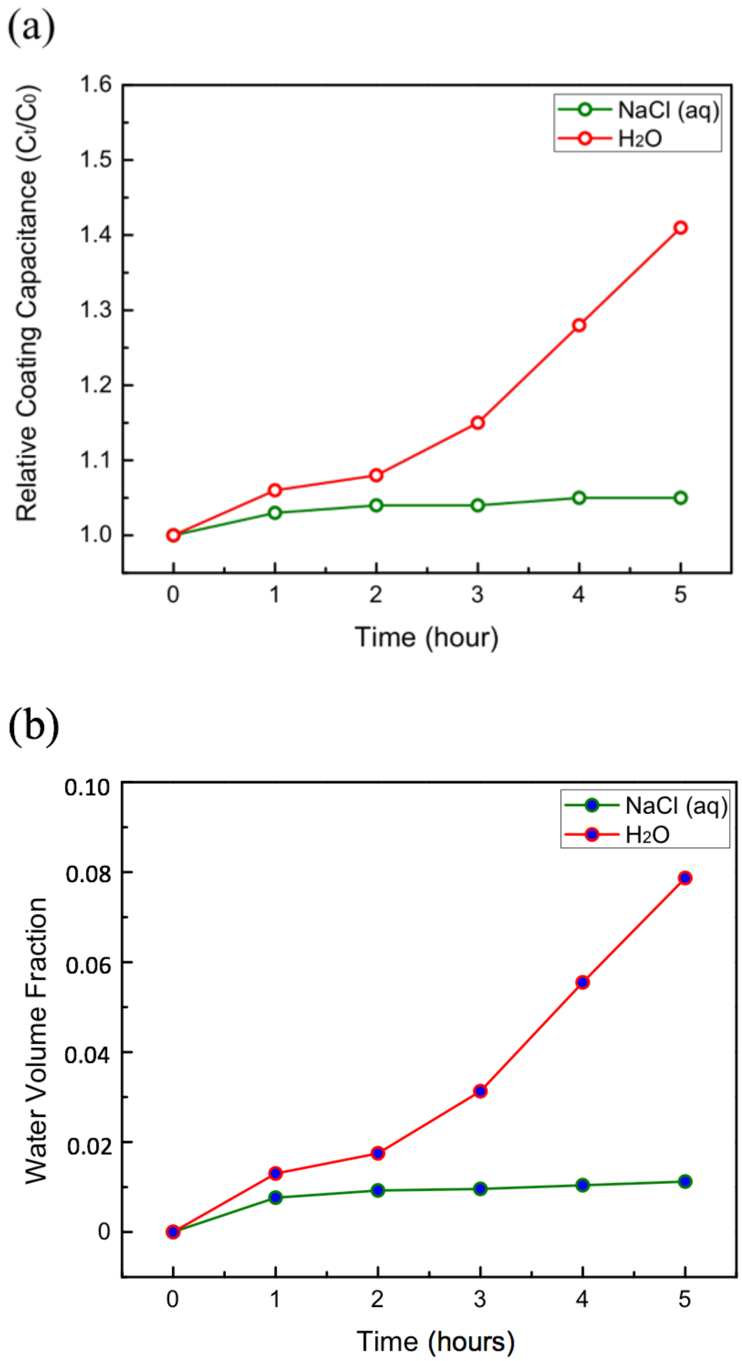

Figure 4.9 (a) Relative capacitance and (b) water volume fraction for epoxy films exposed to H_2O or 3.5 wt % NaCl aqueous solution as the working fluid in the EIS measurements.

4.4 Conclusions

The effect of ions on water diffusion in epoxy films was investigated with XR, NR and EIS. The diffusion of water/electrolyte in the nanometer scale thick organic films was distinguished by their moving directions: vertical movement (penetration) and lateral diffusion. XR/NR probed the lateral diffusion using a customized diffusion cell. EIS data analysis using EEC model fitting compared diffusions of H_2O or electrolyte perpendicular to the sample surface. The lateral diffusion of water or electrolyte was orders of magnitude faster than their diffusion in bulk epoxy; the penetration rate of water or electrolyte as a result from a small film thickness was orders of magnitude smaller than the diffusion rate in bulk epoxy. Such a large difference between the rates of lateral and vertical diffusion is consistent with the empirical observation that a scratched coating on metallic substrate makes the metal corrode much faster. Consistency in results from XR, NR and EIS showed that the diffusion rate of electrolyte is lower than that of water (H_2O/D_2O), and the higher the salt concentration, the lower the rate of diffusion. Both XR and NR used in this study are nondestructive, in situ techniques with depth resolution of 1-2 nm. The probing of changes over this short length scale (nm), and also short times (hours) is a key for advancing the understanding of water and electrolyte movement in organic coatings, which is considered as a first step in the study of metallic substrate corrosion. Reflectivity complements the wide use of EIS, and provides a means of quantitatively investigating phenomena that occur rapidly in the very early corrosion process.

CHAPTER V

ELECTROLYTE DISRUPTION OF METAL/COATING INTERFACE MORPHOLOGY CHARACTERIZED BY X-RAY OFF-SPECULAR SCATTERING

A challenge of broad interest in both materials science and biology is the study of interfaces that are buried within a structure, particularly multilayer structures. Despite the enormous costs of corrosion and many decades of corrosion research, details of the mechanisms of various sorts of corrosion are still not clear, in part due to the difficulty in interrogating the interface between the corroding metal and an organic coating which is typically used to mitigate corrosion. Generally the performance of such coatings is evaluated by visual inspection after exposure or by modeling impedance data, which is a process not straightforwardly connected to physical interface structures. “Rocking-curve” X-ray scattering measurements provide a means of probing such interfaces because of the capability of X-rays to penetrate materials. Here variations in the morphology of an interface between a protective coating and a metal substrate due to exposure to an electrolyte are derived from analysis of rocking-curve data in conjunction with Atomic Force Microscopy imaging of the outer coating surface. The interfaces of crosslinked epoxy coatings with aluminum are irreversibly changed after 12 h of contact between electrolyte solution and the face of the coating. The character of this change varies with molecule used to crosslink the coating. Since X-ray off-specular scattering is sensitive to changes on the nanometer scale it is also able to register interface degradation on time scales shorter than those probed by many other techniques, potentially expediting the evaluation of coatings for protection against degradation of the interface.

5.1 Introduction

The evolution of multilayer structures due to exposure to degradants or environmental stimuli is of interest in a variety of fields including supported lipid bilayers[218–223], semiconductor layers[224,225], perovskite superconductor[226] and corrosion[23]. Particularly challenging is quantitative description of change in interfaces lying inside a multilayer. Both XR and NR have been used to probe the laterally averaged structure of interfaces internal to layered structures[23,227–231]. However, to obtain information on the in-plane structure at a buried interface it is necessary to go to off-specular scattering, one example of which is shown in Figure 5.1. Such measurements can be useful for systems with very thin films, even those with layers of 2-D materials. Here we consider specifically the buried interface between a metal or metal oxide and a thin (ca. 60 nm) organic coating designed to bond strongly to the substrate and act as a physical barrier to corrosion accelerating species such as water or electrolyte[232].

Such interfaces are key to coating system performance in the aerospace, automobile and construction industries.[171] The structural evolution of this important interface is usually inferred using the study of samples exposed using one of two exposure protocols: outdoor exposure or accelerated weathering.[233] Even the "accelerated weathering" protocol typically involves weeks or months of exposure because the techniques used to detect changes associated with degradation are not highly spatially resolving and may be indirect as regards inferring interfacial structure. For example, Electrochemical Impedance Spectroscopy (EIS) measurements can complement visual inspection studies that use very long time corrosion investigations, but the modeling of the impedance data is not straightforwardly connected to physical interface structure. Usually the modeling involves postulating circuit elements of various sorts, the morphological significance of which is not intuitive.[1,178,232] A key for advancing the development of high performance, durable coatings that reduce corrosion rates is developing a nanoscale understanding of electrolyte movement to the interface and disruption of the interface by the electrolyte.

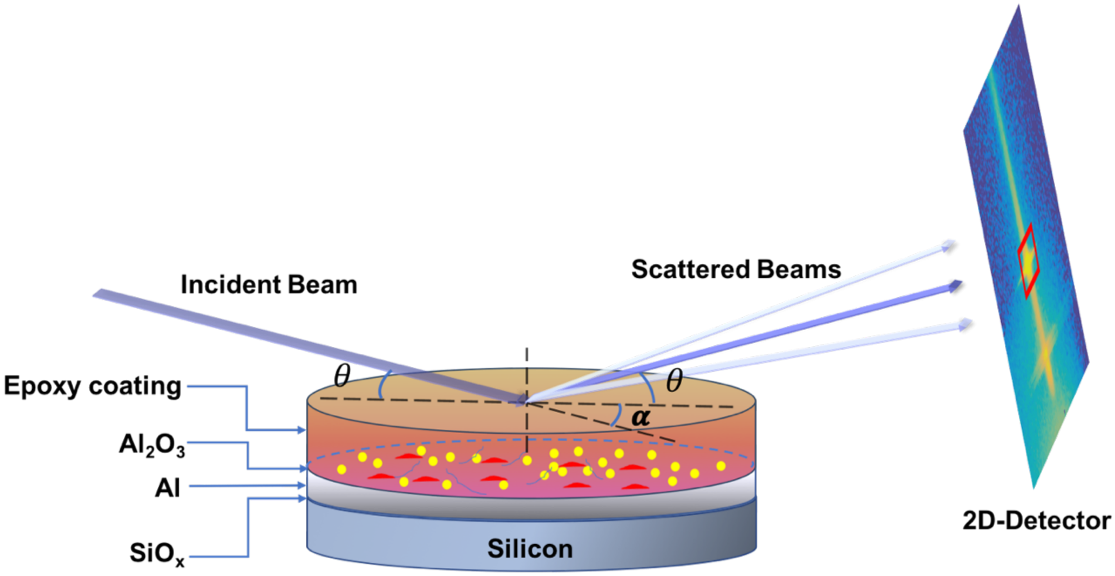

Figure 5.1 Schematic of the “rocking curve” off-specular scattering experiment to study the buried interface between an epoxy coating and aluminum substrate: spatial relationship between the sample and detector.

Our efforts to quantitatively describe the buried interface build on pioneering X-ray and neutron reflectivity (NR) studies by Vogt et al.[80] of water diffusion through polymeric coatings at the nanoscale and NR studies by Schaefer et al.[196] of NaCl aqueous solution penetration into an organic (silane) coating. Vogt et al.[80] revealed that the interfacial accumulation of water can be effectively controlled by modifying Al_2O_3 with alkylphosphonic acids and alkylchlorosilanes. The work of Schaefer et al.[196] addressed how epoxy-silane coating chemistry[196] impacts the salt exclusion and water uptake in the coating. The innovation in the work described below is to bring off-specular scattering to bear on a similar system to gain information on the interface in-plane structure. This is accomplished by using a geometry in which the angle of the incident beam relative to the surface is different than the angle of the scattered beam. In principle, off-specular measurements can be done with either X-rays or neutrons in a variety of "off-specular" geometries. Here the vastly stronger brilliance of a synchrotron X-ray beam is essential to obtaining data rapidly and with high resolution.

An analytical model for scattering by rough surfaces which regards the surface as composed of randomly disposed mirror-like facets was proposed and evaluated by Torrance et al.[16] in the 1960s. The theoretical description of the scattering of X-ray/neutron scattering from rough surfaces was treated at length in the late 1980s by Sinha et al.[17] and that opened the way for several experimental studies in the 1990s. Schwarz et al.[18] characterized the off-specular scattering of the water-vapor interface in 1990. In 1996 Sinha et al.[19,20] did time-resolved, in situ off-specular scattering measurements to study the electrochemical pitting of Cu surfaces immersed in electrolyte. Müller-Buschbaum et al.[21,22] in 1998 showed with "detector scan" off-specular measurements, first qualitatively[21], then quantitatively[22], that supported spun-cast polymer films had surface morphologies that were conformal with the polymer/substrate interface, thus implicitly probing both interfaces. With heating the conformality was lost, implying that thermal fluctuations changed the air/coating interface while the interface with the substrate likely remained unchanged within the resolution of the experiment, though this was not explicitly addressed. At the same time Tolan et al.[127] found evidence for capillary waves at the air/polymer interfaces of droplets from dewetted polymer films. In 2006, Singh et al.[23] used off-specular neutron scattering to describe the morphologies from two interfaces associated with a corroded Ni film, the top interface with air, and a buried interface between a less dense layer adjacent to air and the unperturbed Ni layer underneath. To the best of our knowledge, quantification of the evolution of the nanoscale 3-D interfacial morphology between a metal substrate and an organic coating on top of it has not been reported. No other techniques are available to interrogate this buried interface at these length scales. In this chapter, simultaneous analyses of X-ray off-specular scattering measurements and atomic force microscopy (AFM) images show that this buried interface is roughened on the scale of tens of nanometers with water exposure of the coating and that the details of this roughening differ with the type of crosslinker used in the coating.

The coatings we considered were epoxy coatings, which provide exceptional adhesion to metal substrates, and good resistance to water/electrolyte. They are representative of the most widely used primers in the coating industry.[1,171–178] X-ray "rocking curves" measurements were performed for epoxy coatings on aluminum as prepared, and after exposure to salt solution. The schematic of the experimental setup is in Figure 5.1. An incident beam with a small angle with regard to the surface is reflected or scattered in various directions. When the angle between the scattered beam and the surface is not the same as the incident angle, the scattering is "off-specular". With this approach, quantitative information about the morphology at the substrate/coating interface and its change with exposure of the coating to electrolyte is obtained by fitting the rocking curve data corrected for the beam footprint using a model of the substrate surface morphology. The manner in which change of the epoxy chemistry impacts water diffusion in the epoxy layer and disruption of the coating/aluminum interface was studied using two epoxy films made with crosslinkers differing in their spacings between the amino groups in the crosslinker. How the effect of electrolyte exposure changed with the type of anion was also explored. The nanoscale morphological change specifically at the buried interface was determined by combining the analyses of the off-specular scattering and the AFM data. This novel approach complements the wide use of EIS, and provides a means of investigating phenomena that occur rapidly very early in the corrosion process.

5.2 Experimental Section

Epoxy coatings provide exceptional adhesion to metal substrates, and good resistance to water and electrolyte. They are the most widely used primers in the coating industry.[1,171–178] In my study, a EPON SU-8 epoxy crosslinked with EPIKURE 6870-W-53 was used as a representative coating sample.

Silicon wafers (3 inch diameter, 1 mm thick, El-Cat Inc.) were cleaned using piranha solution (H_2O_2:H_2SO_4 = 3:7 by volume) at 100 °C for 30 minutes. (*Warning: Piranha solution presents an explosion danger and should be handled with extreme care; it is a strong oxidant and reacts violently with organic materials. All work should be performed in a fume hood. Wear proper protective equipment*.) Then a 40 nm thick layer of aluminum (Al) was deposited using thermal evaporation at the rate of 1 Å/s. Thermal evaporation provides controllability and uniformity over a relatively wide area on the substrate. A mixture for spin-coating was created from two solutions: a 4 wt % solution of tetraethoxysilane (TEOS, Sigma-Aldrich Inc.) in methanol and a methyl isobutyl ketone (MIBK, Sigma-Aldrich Inc.) solution of EPON SU-8 epoxy (Momentive Performance Materials Inc.) with epoxide equivalent weight (EEW) of 195-230 (g/eq) and curing agent EPIKURE 6870-W-53 (Hexion Inc.), or isophorone diamine (IPDA, Sigma-Aldrich Inc.) at stoichiometric ratios, r, of [NH]/[Epoxide] = 0.5. The TEOS solution was mixed with the epoxy resin solution at a weight ratio of TEOS:epoxy of 2:98. Films spun cast on Al layers from the hybrid coating precursor solution were dried and cured at 150 °C in vacuum (at 30 mm Hg, dry ice trap) for two hours.

Detailed information regarding the AFM characterization and scattering measurements including reflectivity and off-specular scattering are included in the results and discussion section.

5.3 Results and Discussion

5.3.1 Behavior with water vs. that with electrolyte

Changes in the coating/metal interface differed depending on whether the coating was exposed to water or to electrolyte. AFM tapping mode images from uncoated Al layers as-prepared, exposed to water for 20 min, to 1 wt % or 3.5 wt % NaCl aqueous solution for 20 min, and to 3.5 wt % NaCl aqueous solution for 40 min are shown in Figures. 5.2(a) and D.1. Surface roughness values inferred from the images are summarized in Table 5.1. The roughness of aluminum surface exposed to water is larger than that of dry aluminum. For aluminum exposed to electrolyte the surface roughness increases with an increase in electrolyte concentration or exposure time. The surface roughness of the epoxy coating on aluminum increases somewhat, but far less, in absolute terms than does the roughness of the aluminum upon exposure to water or salt solution, as shown in Table 5.2 and in the images in Figures 5.2(c) and D.2.

While the AFM images provide direct information on the changes in the surface, power spectral density (PSD) spectra[234–238] calculated from these images are also very helpful as they are analogous to the scattering curves obtained from X-ray measurements. As illustrated in Figure 5.2(a, b) and Table 5.1, the roughness of the aluminum surface deduced from AFM imaging changed from 1.52 ± 0.04 nm to 3.80 ± 0.12 nm with exposure to a NaCl aqueous solution, and the intensity in the PSD increased. The PSD intensity increased for all values of q, indicating that upon exposure the roughening of the aluminum surface features occurred at all length scales probed. For the epoxy surface shown in Figure 5.2(c) and described in Table 5.2, the roughness variation was small even after 24 h exposure. The shapes of the PSDs in Figure 5.2(d) are similar, consistent with the similarity of scattering features in the "rocking curve" off-specular data sets measured with the scattering geometry of Figure 5.3.

Table 5.1 Al surface roughness characterized by tapping mode AFM

Al samples	Rms roughness (nm)[a]
As-prepared, dry	1.52 ± 0.04
20 min exposure to H_2O	1.64 ± 0.04
20 min exposure to 1 wt % NaCl(aq)	1.76 ± 0.04
20 min exposure to 3.5 wt % NaCl(aq)	3.13 ± 0.06
40 min exposure to 3.5 wt % NaCl(aq)	3.80 ± 0.12

[a] Error at 96% confidence reflects variation among images from three locations.

Table 5.2 Roughness values of epoxy coatings from tapping mode AFM

Epoxy sample type	Rms roughness (nm)[a]
As-prepared, dry	0.39 ± 0.02
12 h exposure to 3.5 wt % NaCl(aq)	0.60 ± 0.04
24 h exposure to 3.5 wt % NaCl(aq)	0.59 ± 0.06

[a] Error at 96% confidence reflects variation among images from three locations.

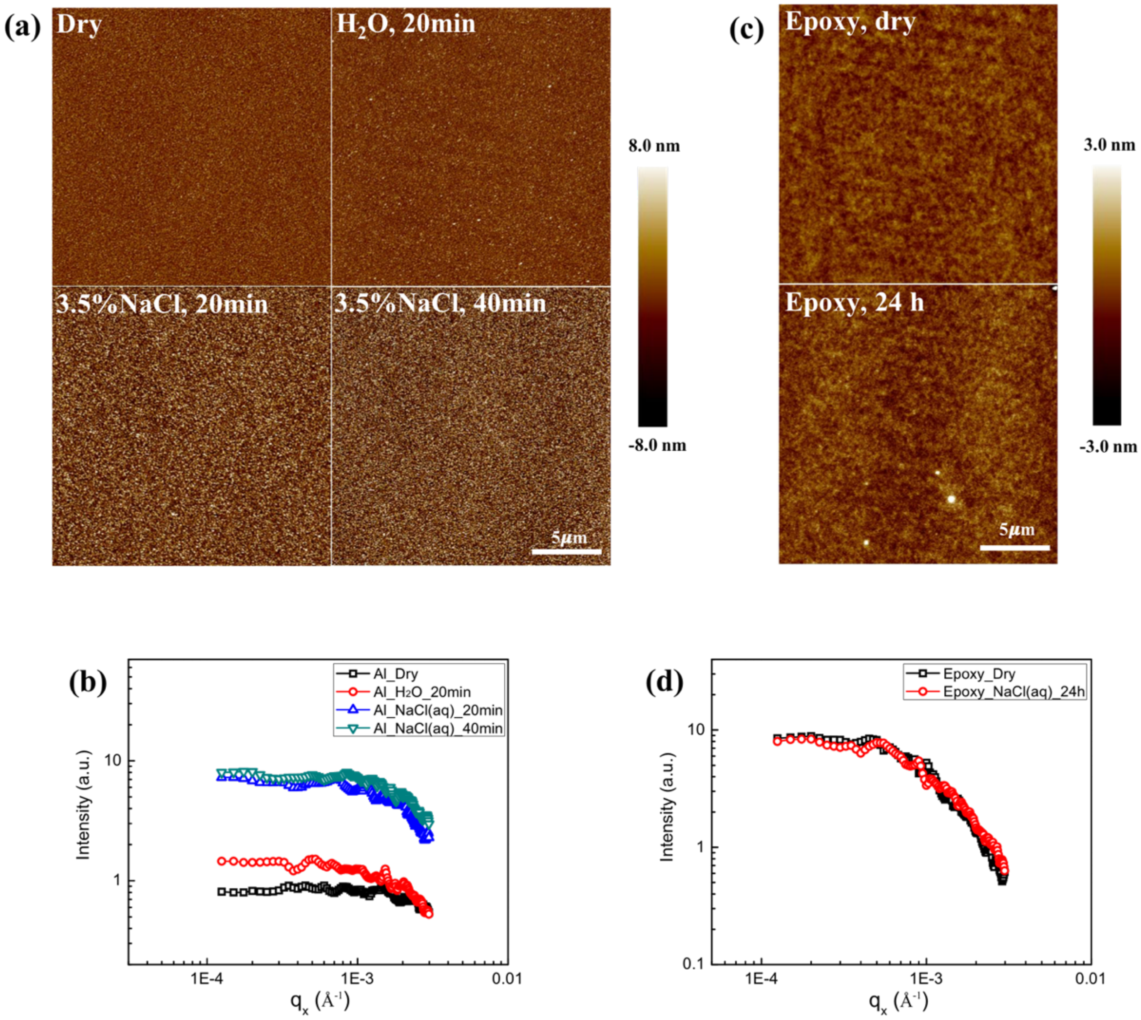

Figure 5.2 (a) Tapping mode AFM images (20 μm x 20 μm) of aluminum surface morphology as-prepared, and after exposure to H_2O or 3.5 wt % NaCl aqueous solution. (b) Power spectral density (PSD) derived from the AFM images of aluminum surfaces as-prepared and after exposure. (c) Tapping mode AFM images (20 μm x 20 μm) of epoxy coatings on aluminum as-prepared, and after 24-hour exposure to 3.5 wt % NaCl aqueous solution. (d) PSD derived from the AFM images of epoxy surfaces as-prepared and after exposure.

Rocking curves were measured at the Advanced Photon Source (APS) beamline 33-BM-C[239] using the experimental setup shown in Figure 5.3(a). An incident beam with a small angle with regard to the surface is reflected or scattered in various directions. When the angle between the scattered beam and the surface is the same as the incident angle, the reflected radiation is referred to as "specular" (Figure 5.3(b)); otherwise, it is called "off-specular" (Figure 5.3(c)). The incident angle is above the epoxy critical angle, so the incident X-rays can penetrate to the organic coating/metal oxide interface. Such an off-specular scattering measurement provides information from both the organic coating surface and the coating/metal oxide interface. For the rocking curve scattering experiments the detector position is fixed, while the sample is rocked about the specular reflection condition.

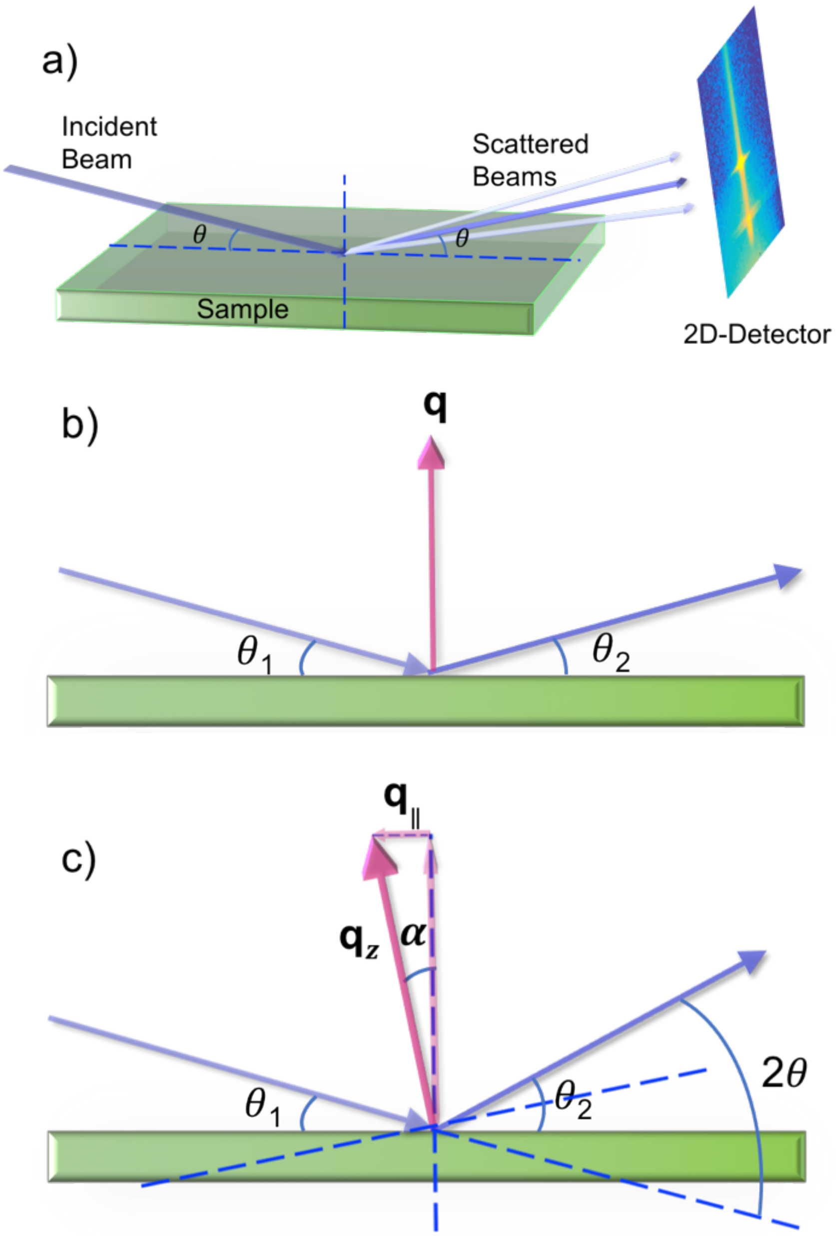

Figure 5.3 Schematics of the “rocking curve” off-specular scattering experiment to study the buried interface between an epoxy coating and aluminum substrate: (a) spatial relationship between the sample and detector, and the relationships among the incident and exit wave vectors and scattering vector for (b) the specular condition and (c) an off-specular condition.

As illustrated in Figure 5.3(c), the scattering angle 2θ is the sum of the angle of incidence, θ_1, and the angle of detection with respect to the sample surface, θ_2. For a reflectivity experiment, as in Figure 5.3(b), $\theta_1 = \theta_2$, and the scattering vector, $\boldsymbol{q}$, is perpendicular to the surface. Only information about the structure along the direction of the surface normal can be derived.[240,241] The reflectivity curve is interpreted by assuming a sample model structure consisting of various layers and varying the parameters of those layers in the model until a simulated reflectivity curve calculated from the model structure matches the measured curve. The model used reflects a lateral averaging of the thin film structure in the in-plane direction. In contrast, an off-specular scattering measurement (Figure 5.3(c)), involves also a scattering vector component parallel to the surface with magnitude $q_x = |\boldsymbol{q}|\sin(\alpha)$ and α being the rocking angle. Therefore the rocking curve scan, measured by varying α, probes details of the interface morphology in the in-plane direction[242].

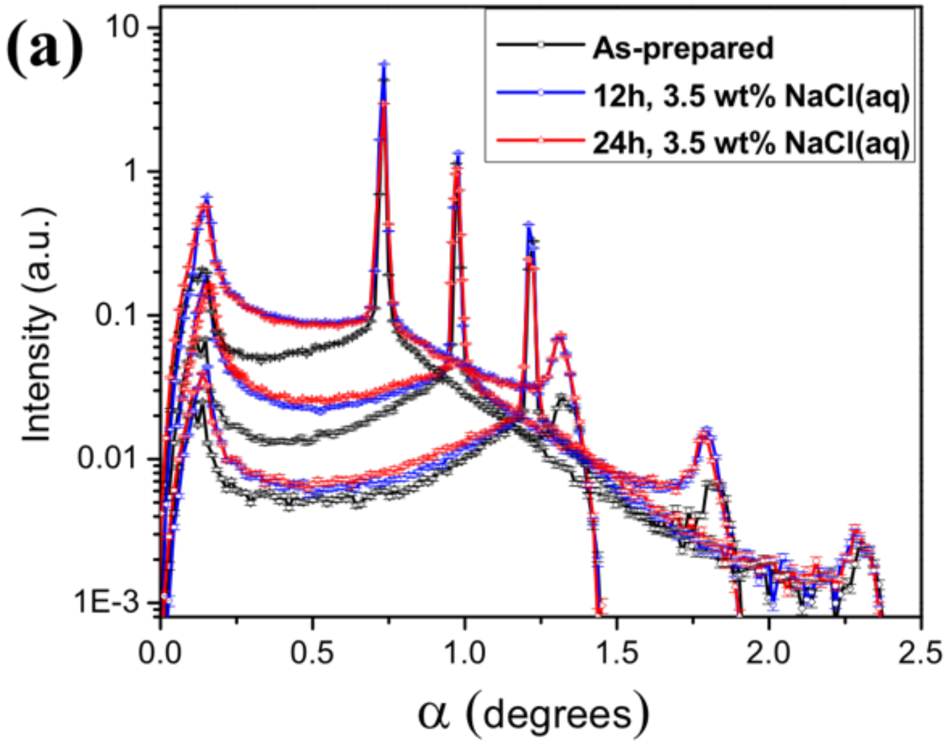

Figure 5.4 (a) X-ray scattering data for epoxy-coated (with crosslinker IPDA) aluminum: raw rocking curve data for as-prepared sample, and after 12-hour and 24-hour room temperature exposure to a 3.5 wt % NaCl solution measured at 2θ of 1.460°, 1.947°, and 2.434°.

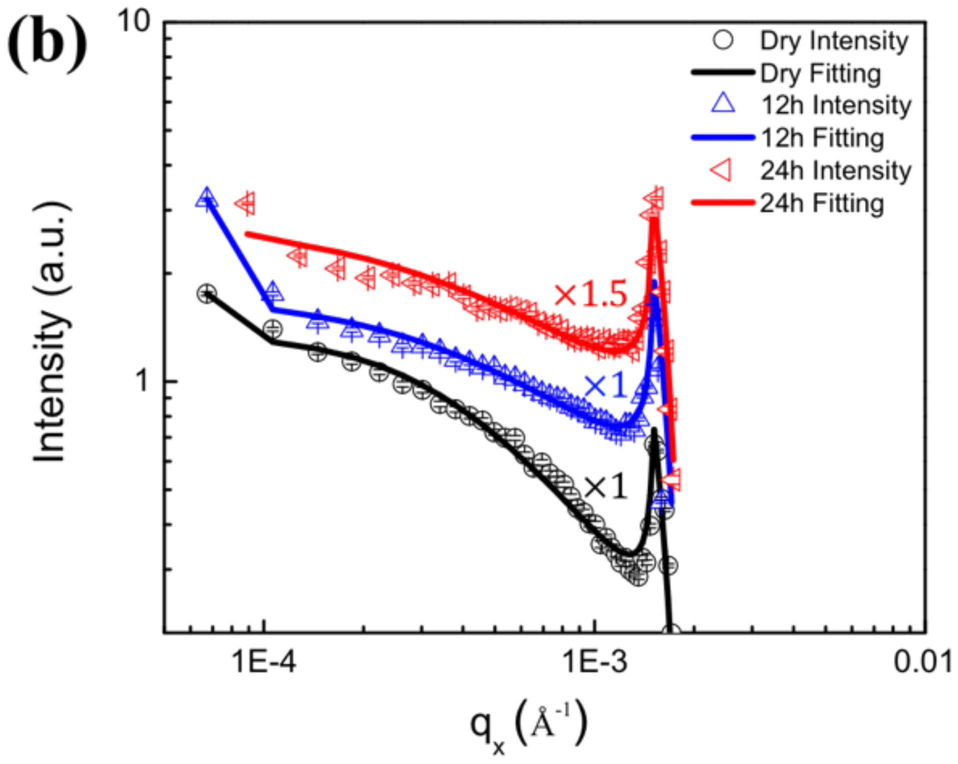

Figure 5.4 (b) X-ray scattering data for epoxy-coated (with crosslinker IPDA) aluminum: rocking curve intensities at 2θ = 1.460° for the sample dry (×1), after 12-hour (×1) and 24-hour (×1.5) exposure to a 3.5 wt % NaCl solution corrected for the beam footprint, as a function of in-plane scattering vector, compared with fits using the self-affine rough surface model.

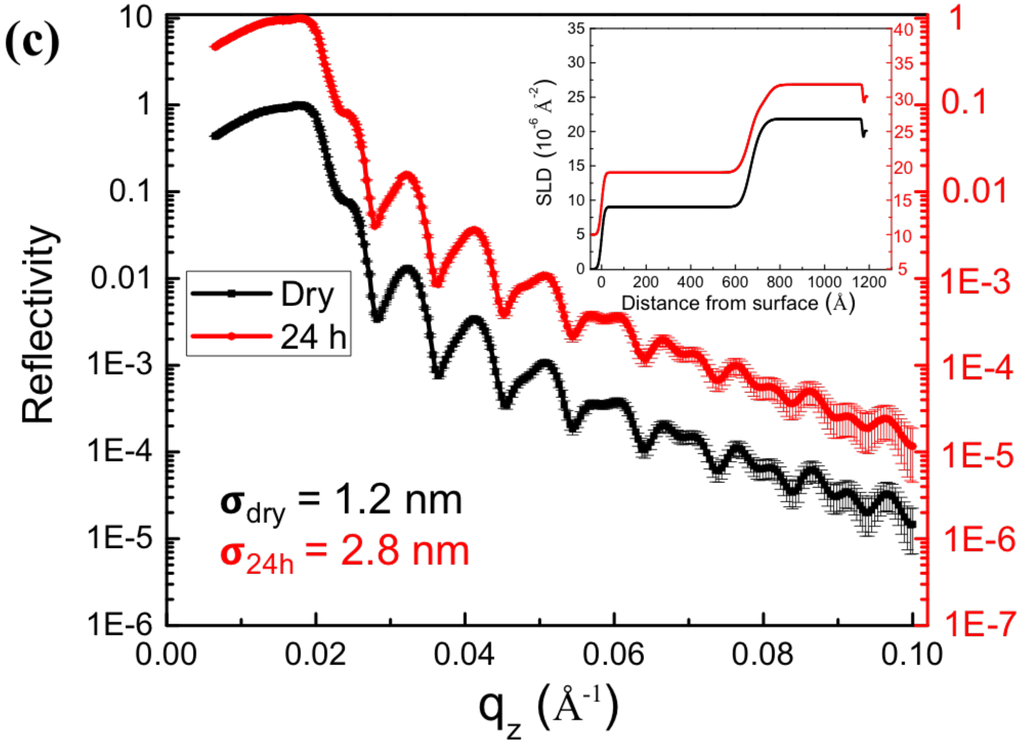

Figure 5.4 (c) X-ray scattering data for epoxy-coated (with crosslinker IPDA) aluminum: reflectivity curves and scattering length density (SLD) profiles for samples dry, and after 24-hour exposure to NaCl solution (offset by factor 10).

The off-specular scattering data measured at 2θ of 1.460°, 1.947°, and 2.424° can be interpreted to provide a picture of how the interface between aluminum (oxide) and coating change with exposure. Measurements at the smallest scattering angle (1.460°) were characterized by the largest intensities. Measurements at the largest scattering angle (2.434°) explore a wider range of in-plane scattering vector and therefore may be more sensitive to subtler features of the structure even though the intensities are lower and thus of statistically inferior quality. For each scattering angle, the sample was measured in three states: as-prepared, after 12-hour exposure to 3.5 wt % NaCl aqueous solution, and after 24-hour exposure. For the data for 2θ=1.460° in Figure 5.4(a), there is a clear difference between the data from the sample when dry and the data after exposure to NaCl aqueous solution. Since we know from AFM measurements that the epoxy-air interface morphology has not changed, this must be due to change occurring at the interface underneath the epoxy resulting from NaCl solution penetrating through the thin epoxy film. From the data for 2θ=1.947°, one sees not only the obvious difference between the data from the dry sample and data from the sample after exposure, but also can recognize subtle differences between the scattering curves for the two different exposure times. Data for all three scattering angles are compared in a single plot to make clearer the differences in shape and intensities as scattering angle is varied. Each of the rocking curves in Figure 5.4(a) has three peaks. The peak with highest intensity is due to specular reflection ($\alpha = 2\theta/2$). The other two are Yoneda peaks[17,241]. The Yoneda peak on the right side has lower intensity due to the higher incident angle. The Yoneda peak results from resonance enhancement of the scattering from the surface roughness that occurs when either the scattered beam or incident beam has an angle with regard to the surface is equivalent to a critical angle. Under this condition there is an evanescent wave at the interface which enhances the scattering intensity. In the region between the Yoneda peak and the specular peak of the curve, the intensity is higher after the longer exposure. Data for the highest scattering angle (2.434°) show trends consistent with those at scattering angles of 1.460° and 1.947°, as seen in Figure 5.4(a).

Quantitative information about the morphology at the substrate/coating interface and its change with exposure of the coating to electrolyte is obtained by fitting rocking curve data corrected for the beam footprint using a model of the substrate surface (Figure 5.4(b)). Sinha et al.[17] have described the scattering from a self-affine rough surface that can be characterized with a correlation function $C(X,Y) = \sigma^2\exp[-(R/\xi)^{2h}]$, where X and Y are the in-plane dimensions and $R = \sqrt{X^2 + Y^2}$. The roughness, σ, represents the root mean squared roughness. ξ is a correlation length in the plane of the surface, and h, the "Hurst parameter", illustrates the texture or jaggedness of the surface, with h approaching zero corresponding to jagged surfaces and h approaching 1 corresponding to surfaces with more gradually varying height. Examples of fits of this model to data for the dry coating, after 12-hour room temperature exposure to 3.5 wt % NaCl solution and after 24-hour exposure are in Figure 5.4(b). With exposure the log-log plot of the data shows a more pronounced change in slope with increasing q_x and the model parameters used to fit the data, summarized in Table 5.3, show consistent trends. With exposure the interface becomes more rough (σ increases), the correlation length drops, and the texture becomes somewhat more jagged.

Figure 5.4(c) shows the specular reflectivity for the coating with crosslinker IPDA dry and after 24-hour exposure to 3.5 wt % NaCl solution. Roughness values derived from fitting the specular reflectivity curves for the samples as-prepared, and after 12-hour and 24-hour temperature exposure to a 3.5 wt % NaCl solution were used in fitting of the off-specular data.[243] The rocking-curve measurements probe a correlated roughness laterally in the form of height-height correlation function within the coherence length of X-ray. The reflectivity measures a laterally averaged roughness in the footprint.[244,245] The two techniques provide complementary, but overlapping information. Using the roughnesses independently measured from the reflectivity measurements, which benefit from probing length scales perpendicular to the interface that are much smaller than probed in the rocking curves, improved the reliability of the determinations of the Hurst parameter and correlation length from fits to the rocking curve measurements.

Figure 5.5 shows how the interface roughness and correlation length change with duration of exposure to water or electrolyte for just the surface of the aluminum with its native oxide and for the aluminum/epoxy coating (with crosslinker IPDA) interface. The absolute values of these quantities are not readily compared because for the uncoated aluminum samples they have been measured using AFM, while for the buried interface e.g. the epoxy-coated aluminum the roughness has been measured with X-ray reflectivity and the correlation length with off-specular scattering. Since the ranges of q probed with the AFM and scattering measurements were not identical they cannot be expected, in general, to produce identical values of roughness and correlation length for a given interface. Nonetheless, rates of change in these quantities can be readily compared. For purposes of describing the characteristics of these curves, and in particular the initial rates of change, we have fit the data with the empirical functional form σ = a-b/exp(c·t). Several observations about the behavior may be made. First, the roughness starts higher and increases far more rapidly with exposure to electrolyte for the aluminum than it does for the epoxy-coated aluminum, as it should, since the coating provides protection. The initial rates of increase in rms roughness are 4 Å/h for Al in water, 48 Å/h for Al in electrolyte, and 0.6 Å/h for epoxy-coated Al in electrolyte. So, interface roughness increases 12x more rapidly with exposure to electrolyte than with exposure to water. Certainly it is known in the literature that corrosion progresses much more rapidly in electrolyte than in water[199,200,215], but the results here suggest that even the earlier stage of corrosion, which is disruption of the interface, also occurs more rapidly with the electrolyte. For the parameter of correlation length we also see large differences between the coated and uncoated Al in the rate of change. The correlation length decreases at an initial rate of about 82%/h for the unprotected Al in electrolyte vs. 4%/h for the epoxy-coated Al. The initial values of the correlation length agree well for the two aluminum samples dry, but the initial value for the epoxy coated aluminum is higher. The reason for the difference in correlation lengths between the epoxy coating and Al is not clear.

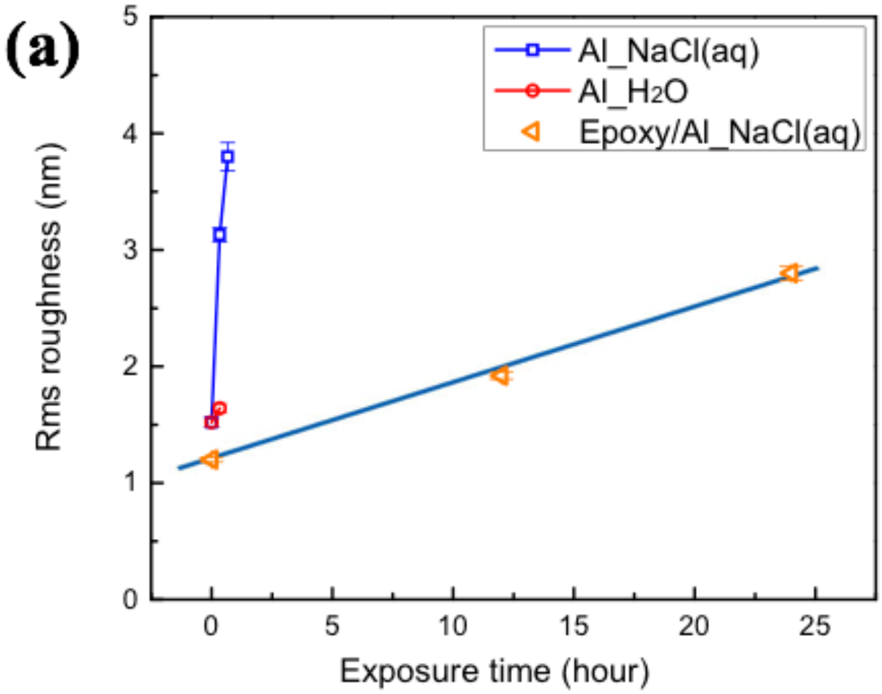

Figure 5.5 (a) Root mean square (rms) roughness (from tapping mode AFM images) of aluminum surface as-prepared, and after exposure to H_2O or 3.5 wt % NaCl aqueous solution with curves fit to the data using the phenomenological form in the text, and rms roughness (from X-ray reflectivity) of aluminum/epoxy coating interface as-prepared and after exposure to 3.5 wt % NaCl aqueous solution with empirical formula fitting.

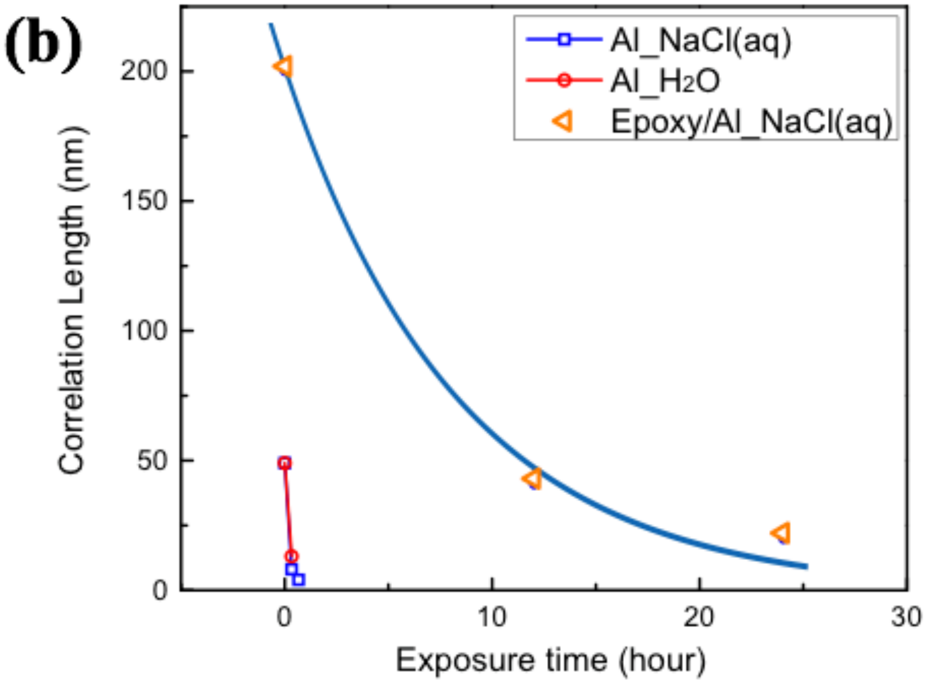

Figure 5.5 (b) Correlation length from PSD of tapping mode AFM images of aluminum surface as-prepared, and after exposure to 3.5 wt % NaCl aqueous solution with empirical formula fitting, and correlation length from "rocking curve" off-specular scattering fitting of aluminum/epoxy coating interface as-prepared, and after exposure to 3.5 wt % aqueous solution with empirical formula fitting.

Table 5.3 Parameters for the self-affine model providing best fits

Samples / Parameters	Electrolyte exposure (crosslinker IPDA)			Crosslinker used (12 h exposure)	
	Dry	12 h	24 h	IPDA	6870-W-53
Correlation length (nm)	202±8	43±4	26±3	43±4	94±5
Hurst parameter	0.44±0.02	0.26±0.01	0.22±0.01	0.26±0.01	0.38±0.02
Roughness (nm)	1.20±0.02	1.92±0.03	2.80±0.06	1.89±0.03	1.94±0.03

5.3.2 Change with crosslinker chemical structures

The manner in which change in epoxy chemistry impacts water diffusion in the epoxy layer and disruption of the coating/aluminum interface was studied using films of EPON SU-8 epoxy crosslinked with EPIKURE 6870-W-53 or isophorone diamine (IPDA). Both EPIKURE 6870-W-53 and IPDA are diamine crosslinkers, differing in their detailed chemical structures. Variation in hydrophobicity and the spacing between amino groups in the crosslinker should affect the capability of the crosslinked coating to resist water and electrolyte diffusion and subsequent corrosion. Different corrosion rates should result in the different interface morphologies for a given exposure time. Changes in interfacial morphology are reflected in the rocking curve data. Results from crosslinked samples exposed to 3.5 wt % NaCl solution for 12 hours are shown in Figure 5.6. The similarities and differences between the data sets for the two types of crosslinkers are consistent for the three values of scattering angle. First, we note that the intensities in Figure 5.6(a) at the specular condition and in the Yoneda peak region differ little with crosslinker. Secondly, the off-specular intensity near the Yoneda peak for the sample crosslinked with IPDA is higher than that for the sample crosslinked with EPIKURE 6870-W-53. Finally, the off-specular intensity near the specular peak is lower for the IPDA crosslinked epoxy than for the EPIKURE 6870-W-53 crosslinked material.

Figures 5.6(b) and D.3 show plots of intensities vs. in-plane scattering vector component q_x on log-log scales. Detailed analysis of these curves is complicated by the fact that the observed X-ray scattering comes from both the epoxy-substrate interface and the epoxy-air interface. However, here we may make some qualitative inferences, using the fact that the AFM images of the dry epoxy surfaces show no significant differences with crosslinker used and no change with exposure to water and drying again. This suggests that the differences in the rocking curves between samples and between before and after exposure depend significantly on the character of the interface between the epoxy and the substrate. The portions of the rocking curves for $q_x < 1\times10^{-4}$ Å^{-1} reflect simply the profile of the specular beam and are of no further interest here. For both samples, just above the specular peak there is a region of small negative slope, and at still larger values of q_x a power-law region with a larger negative slope. The transition in slope suggests the presence of some length characteristic of the surface morphology. Broadly speaking this shape of the rocking curve could be consistent with models used for describing surface fluctuations from a liquid surface that has been vitrified[116] or for a self-affine randomly rough surface[17,116]. As this characteristic length becomes larger, this transition or change of slope will move to lower value of q_x. Thus the structure of the epoxy-substrate interface appears to reflect a somewhat larger characteristic length for the sample crosslinked with EPIKURE 6870-W-53 than for the sample crosslinked with IPDA. From the self-affine model simulation at a scattering angle of 2θ=1.947°, as shown in Figure 5.6(b) and two rightmost columns of Table 5.3, the correlation length of the sample crosslinked with EPIKURE 6870-W-53 is about twice as that for the epoxy crosslinked with IPDA. We conjecture this maybe because the spacing between the two intramolecular amino groups in the EPIKURE 6870-W-53 crosslinked epoxy is larger than that in the IPDA crosslinked epoxy, which results in different rigidities and possibilities for water or electrolyte diffusion.

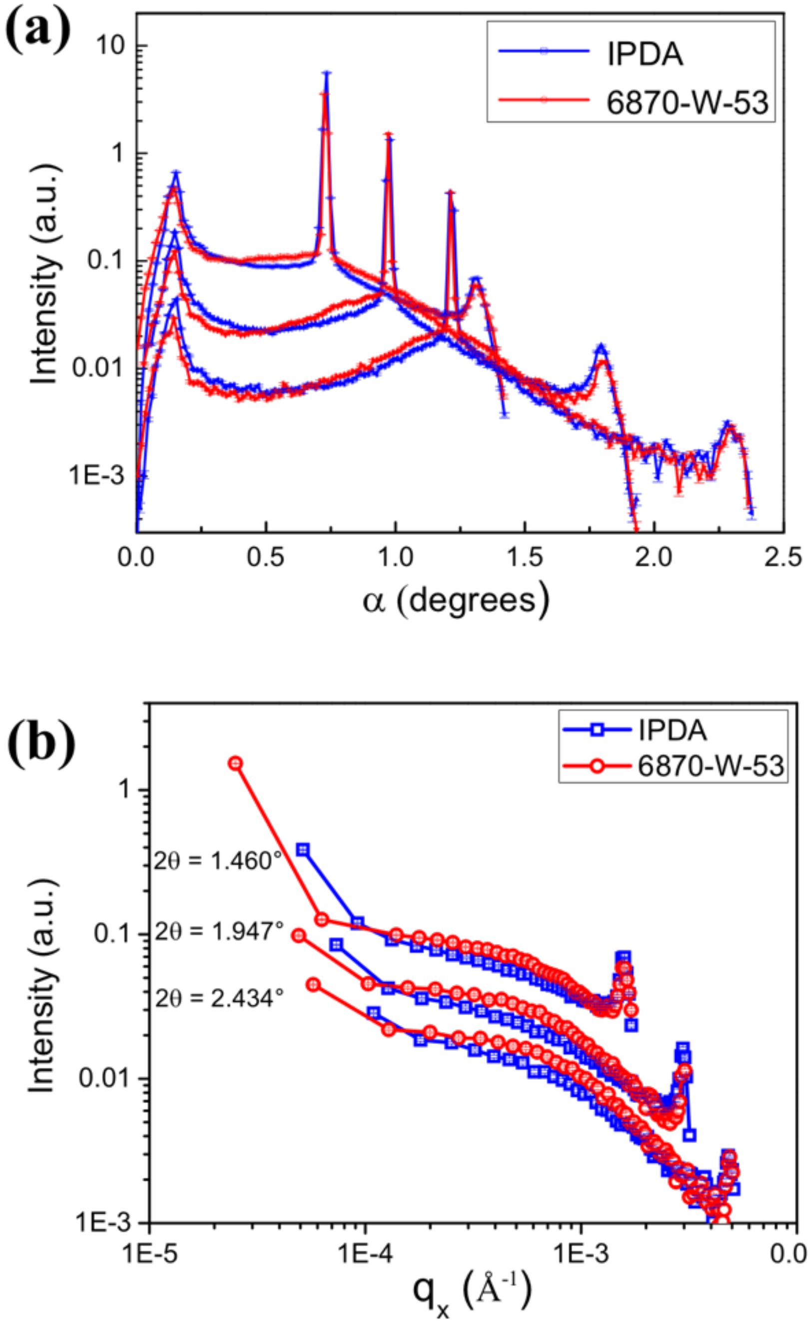

Figure 5.6 Rocking curve data after 12 h of exposure to 3.5 wt % NaCl solution for samples made from EPON SU-8 crosslinked with EPIKURE 6870-W-53 or isophorone diamine (IPDA) measured at scattering angles of 1.460°, 1.947°, and 2.434°.

5.3.3 Effect of salts in aqueous solution

It would be very helpful if X-ray scattering measurements were able to also provide information about how the effects of electrolyte exposure change with the identity of the anion. Therefore, measurements were made with NaI as well as with NaCl. The X-ray contrast between the epoxy and the electrolyte solution is slightly higher for NaI, but for the solution concentrations of interest here the difference may be neglected in making inferences about the morphology of the sample from the scattering data. Figure 5.7 compares the rocking curves from a sample exposed for 12 h to 3.5 wt % NaCl or NaI aqueous solution with that from a sample exposed to H_2O. The curves for the different salts overlap very substantially, indicating that NaCl and NaI solutions have similar effects on water diffusion to the interface and disruption of the interface morphology. Disruption of the interface morphology occurs about 12 times more rapidly with exposure to either electrolyte solutions than with exposure to water. Others have shown corrosion of Al proceeds more rapidly in the presence of electrolyte than that in the presence of water alone[199,200,215].

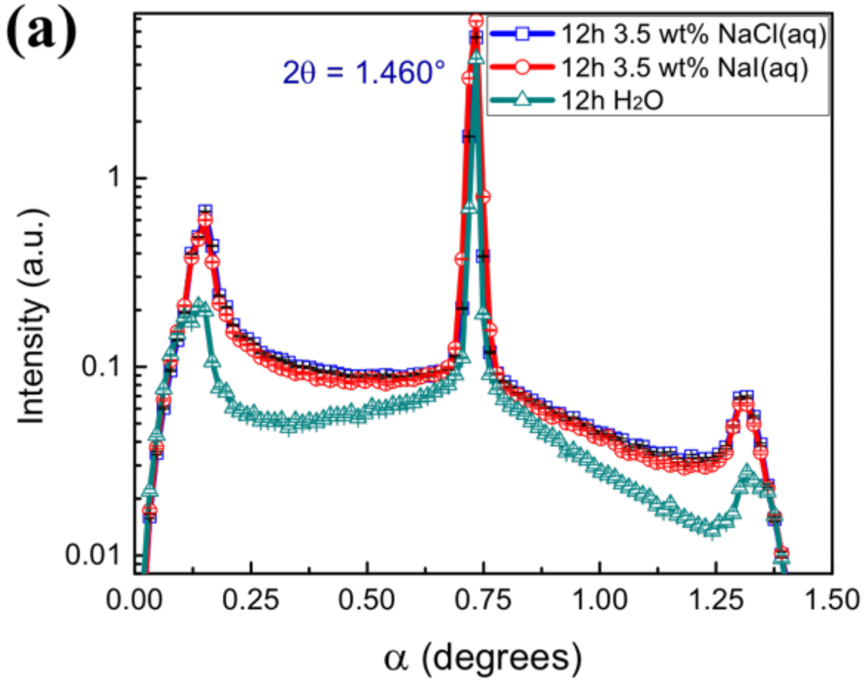
(a)
2θ = 1.460°
12h 3.5 wt% NaCl(aq)
12h 3.5 wt% NaI(aq)
12h H2O
Intensity (a.u.)
1
0.1
0.01
0.00
0.25
0.50
0.75
1.00
1.25
1.50
α (degrees)

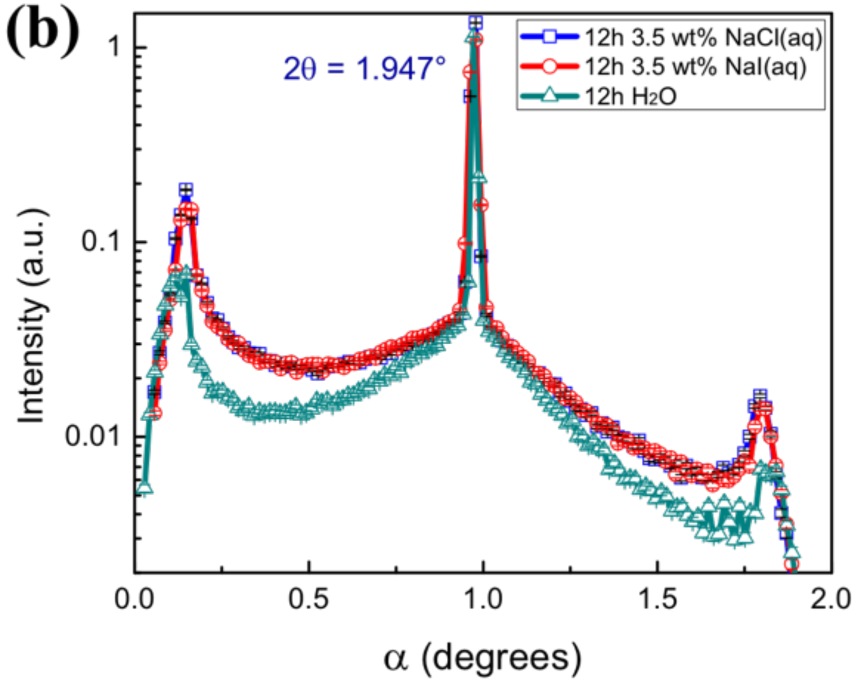
(b)
2θ = 1.947°
12h 3.5 wt% NaCl(aq)
12h 3.5 wt% NaI(aq)
12h H2O
Intensity (a.u.)
1
0.1
0.01
0.0
0.5
1.0
1.5
2.0
α (degrees)

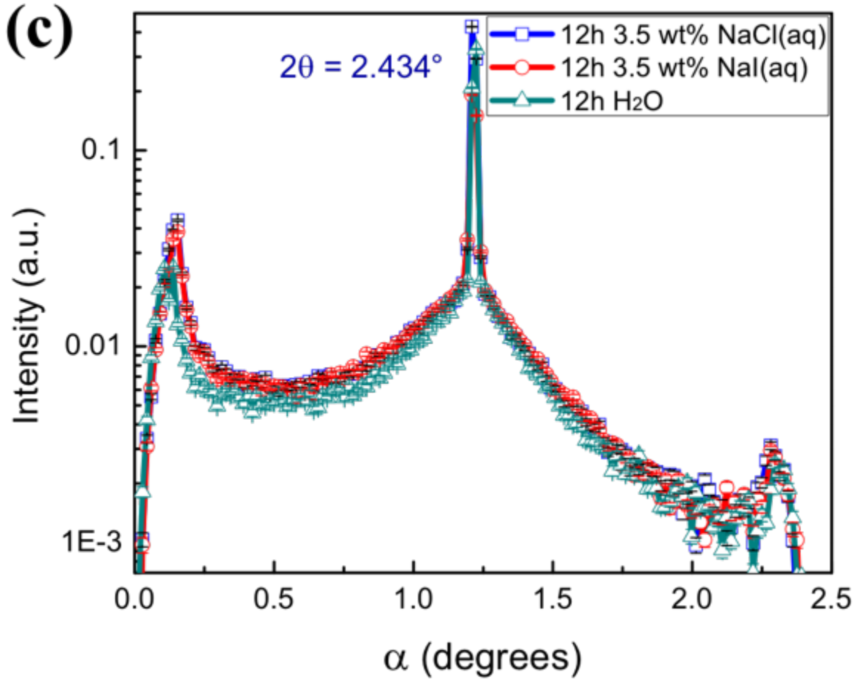

Figure 5.7 Rocking curve data for samples 12-hour exposure to 3.5 wt % NaCl aqueous solution, and NaI aqueous solution at scattering angles of (a) 1.460°; (b) 1.947°; and (c) 2.434°.

5.4 Conclusions

We have presented a way in which changes in the morphology of a buried interface caused by water or electrolyte disruption can be captured, even in the very early stages of a process typically studied over much longer times. By combining AFM imaging of the accessible surface with off-specular X-ray scattering measurements we can obtain parameters describing the buried interface morphology using a self-affine random roughness model. Analysis of the scattering curves reveals that when such a structure is exposed to water or electrolyte outside the coating the interface is disrupted. The in-plane correlation of the interface structure is reduced and the “jaggedness” of the interface increases along with the root mean squared roughness. The development of the interface morphology with exposure to NaCl is different for epoxies made using different crosslinkers. The crosslinker with larger spacing between amino groups within the molecule yields an epoxy/substrate interface for which the in-plane correlation is higher and the jaggedness less pronounced (larger h) for a given exposure. How this change in crosslinker yields the change in interface morphology development is still to be determined, since the hydrophobicity of the two crosslinkers differs as well and both hydrophobicity and crosslink spacing could be playing roles in the disruption of the interface by water or electrolyte. Over the early exposure times probed here the interface development is the same for NaCl and NaI electrolytes.

Combining AFM with off-specular scattering provides access to information specifically about the interface morphology that complements the information provided by the widely used EIS technique. EIS can see changes in performance with coating chemistry variation, but cannot readily link these changes to morphology. Because off-specular scattering measurements probe length scales much smaller than those characteristics of conventional analyses of outdoor exposure and accelerated weathering tests, the off-specular scattering measurement also provides a means of investigating phenomena that occur rapidly, very early in the corrosion process.

CHAPTER VI

SURFACE DYNAMICS MODIFICATION OF SUBSTRATE ADSORBED POLYMER MELT FILMS WITH GRAPHENE

The surface fluctuations of substrate adsorbed polystyrene (PS) thin films are substantially altered when the substrate is changed from silicon to graphene. For $8R_g$ thick entangled linear PS films, the surface dynamics can be illustrated using hydrodynamic continuum theory (HCT) which assumes the thin film viscosity is equivalent to the bulk viscosity throughout its entire depth. For 131000 g/mol linear PS, when the thickness of the film is less than $4R_g$, it shows confinement effects and surface dynamics are suppressed. The surface dynamics of $8R_g$ PS on graphene was slowed down more than two orders of magnitude compared with that on hydrogen-passivated silicon (H-Si). The thickness of the strongly adsorbed layer on graphene substrate (8.2 nm) is more than twice that on H-Si (3.4 nm), which is because of the difference in the substrate surface energy. The structure of graphene, which is a monolayer of sp^2 carbon atoms in an aromatic hexagonal lattice, has a great impact on the interaction with the thin film and the substrate, which dictates the thickness of the strongly adsorbed layer and further affects various properties of supported polymer melt films through long-range perturbations.

6.1 Introduction

The surface fluctuations of entangled melt films is a significant scientific and technological problem with application in the areas such as wetting, adhesion[46,47], and tribology. Thermally stimulated fluctuations depend on the mobility of the entangled chains not only at the surface but also at larger depth in the film[246]. The results of investigations of surface fluctuations using simulations[64,247] and experimental efforts with using X-ray reflectivity, off-specular scattering[24,248–251] and X-ray photon correlation spectroscopy[24–35] are often summarized or discussed by focusing on the behavior seen in a plot of normalized relaxation time, τ/h, as a function of the dimensionless in-plane scattering vector, $q_{||}h$, because a hydrodynamics continuum theory (HCT) by Jäckle[46] predicts a universal behavior in such a plot[25,36,37]. That is, when data for films with different thicknesses, h, for a given temperature much higher than the bulk glass transition temperature ($T_{\mathrm{g,bulk}}$) are plotted together the curves should overlap.

Nevertheless, when the thickness of a film of linear entangled PS melt is less than $4R_g$, a confinement effect manifests itself and the surface fluctuations are slower than predicted by the HCT theory. For example static off-specular X-ray scattering data[250] show the surface fluctuations for films of 90000 g/mol linear PS are suppressed (or slowed). The authors of that study suggested this was because of strong van der Waals interactions with the Si substrate. Dynamics measurements with XPCS later showed that when the thickness of an entangled melt film of somewhat larger M, 123000 g/mol, decreased to about $4R_g$, the universal behavior was lost; for such a film with thickness comparable to $1R_g$, no fluctuations were observed[25]. This confinement was attributed to the physisorption of PS segments to the substrate, and inclusion of an elasticity modulus in the HCT was vital in order to represent the variation in relaxation time with scattering vector[25]. The group of Foster and coworkers has studied melt films of custom synthesized polystyrenes of different topologies[26] such as linear, star-branched, end-branched star, cyclic, and tadpole and illustrated the influence of molecular architectures on the thickness, h^*, at which confinement effects appear[252]. The differences in value of h^* for different architectures have been attributed to the variations in thickness with chain architecture of the strongly adsorbed layer which forms at the substrate upon annealing of the melt film[253]. That group also demonstrated that the substrate surface chemistry can have a remarkable effect on the strongly adsorbed layer thickness and thus alter the surface fluctuations[92]. They did that by modifying substrate surface chemistry of a silicon wafer by coating it with a very thin (4 nm) plasma polymerized maleic anhydride (ppMA) coating, quantifying the surface fluctuations, and evidencing a change in the strongly adsorbed layer thickness using an approach proposed by Guiselin[51]. In 1992 he proposed one could investigate the formation and structure of a layer of irreversibly, strongly adsorbed molecules at the melt/substrate interface by rinsing away chains not so strongly adsorbed. Koga et al.[51], Fujii et al.[254] and Napolitano et al.[255,256] have all used this approach to study various attributes of such strongly adsorbed layers. It has been shown that the strongly adsorbed layer at the substrate interface is influenced by the surface energy of the substrate, and changes in this layer cause changes at larger depth in the film or at its surface through long-range perturbations. We would anticipate that changing or tailoring the behavior of the strongly adsorbed layer is not only a matter of adjusting the surface energy of the substrate, but could involve more specific characteristics of that substrate surface, such as opportunities for epitaxy arrangement of polymer segments on the substrate or opportunities for particular interactions between functionality on the polymer and functionality in the substrate surface. Here we show that modification of the substrate surface with a 2-D material, graphene, offers extraordinary opportunities to tune the surface fluctuations of thin films or the interactions of the chains in that film with the substrate. Such tailoring of melt dynamics near a solid substrate could have application, for example, in designing highly effective corrosion protection systems for high value applications.

Graphene, a monolayer of sp^2 carbon atoms in an aromatic hexagonal lattice, is a perfect two-dimensional crystalline material. Because of its exceptional properties such as impermeability, thermodynamic stability, transparency and flexibility, there has been massive interest in it since its discovery[84,85]. Intensive efforts have been made in the fabrication of large pieces of graphene of high quality[86], both for academic and industrial purposes. The potential application of graphene in the areas of composites, membranes, energy, coatings, biomedical drug delivery, sensors and electronics is the driving rationale in a wide variety of graphene-based research topics[87]. The perfect two-dimensional of graphene has a great impact on a thin film adsorbed to it; thus, a key issue in graphene-based scientific and technological research is the understanding of their interactions at this interface between graphene and the adsorbed thin film. Simulations by Rissanou et al.[48] showed the effect of the graphene layer numbers on the dynamical properties of a graphene sheet supported PS film. Tsige et al.[49] demonstrated the most significant difference in relaxation time between PS on graphite (a close cousin of graphene) and α-quartz occurs within 3 nm from the substrate. No experimental investigations have been reported for the graphene-polymer interfacial interaction, most probably because this is a “buried” interface, and not easily probed. This problem can be met, however, using XPCS[50] to probe the surface fluctuations at a thin melt film surface a short distance from this interface and using the Guiselin[51] approach to provide an artifact, the structure of which is intimately linked with that of strongly adsorbed layer present at the melt/solid interface at the temperature of interest. Both methods provide information pertinent to the dynamics of polymer chain segments at the interface between graphene and the polymer thin film adsorbed to it.

6.2 Experimental Materials and Methods

6.2.1 Graphene growth on copper (Cu) foil

A copper (Cu) foil (Sigma-Aldrich 349178, thickness 0.25 mm, 99.98% trace metals basis) was immersed in a solution of 1 mol/L $(NH_4)_2S_2O_8$ (1.14 g $(NH_4)_2S_2O_8$, 50 mL H_2O) for 10 minutes, and washed with dilute HCl solution ($HCl:H_2O$ = 1:10 by volume), ultrasonically washed with spectroscopic grade acetone, reagent grade ethanol, and dried with high-purity (99.999%) nitrogen (N_2). After this cleaning process, it was placed into the quartz tube of a homemade chemical vapor deposition (CVD) system including a tube furnace (Lindberg/Blue Model TF55030A), gas flow control system, and a roughing vacuum pump. Keeping the Cu foil in the cold zone, the furnace was heated to 1040°C under a flow of argon (Ar) and hydrogen (H_2) at a pressure of 524 mTorr, and at flow rates of 100 and 60 sccm (standard cubic centimeters per minute), respectively. The Cu foil was moved into the hot zone and was annealed for 20 minutes. Then a flow of methane (CH_4)

was started at a rate of 6 sccm for 7 minutes, under a pressure of 537 mTorr. The methane gas flow was stopped after the reaction. The Cu foil was moved to the cold zone using the magnetic rod, and was cooled down to room temperature under the original flow rates of Ar/H_2 mixture.

6.2.2 Graphene transfer to silicon wafer

The graphene that formed on the Cu surface was transferred to a silicon wafer (El-Cat Inc. 0.7 mm × 16 mm × 20 mm) that had been cleaned using piranha solution ($H_2O_2:H_2SO_4$ = 3:7 by volume) at 100 °C for 30 min and treated with dilute hydrofluoric acid (HF) to etch away the native oxide. (*Warning: Piranha solution presents an explosion danger and should be handled with extreme care; it is a strong oxidant and reacts violently with organic materials. All work should be performed in a fume hood. Wear proper protective equipment.*) A thermal release (TR) tape (Nitto Americas Inc., CA) was applied to the graphene-coated Cu foil with caution, and 6.25 N/cm^2 compression force was applied for 10 minutes. The graphene on the opposite side of the Cu foil was removed by contact with oxygen plasma for 5 minutes. The Cu foil was removed from the graphene layer by etching in $(NH_4)_2S_2O_8$ aqueous solution (1 mol/L) for 12 hours, rinsing with deionized (DI) water ten times, and blowing dry with high-purity N_2. The graphene side of the graphene-TR tape assembly was adhered to the HF-treated silicon wafer at room temperature using a compression force of 12.5 N/cm^2 for 10 minutes. Finally, the TR tape was released from the graphene by heating the wafer for a few seconds on a hot plate at 110°C, leaving the graphene layer on the silicon wafer. The contaminants on the transferred graphene surface were removed by annealing the Graphene/Si with a gas flow of Ar and H_2 (200 and 60 sccm, respectively) at 400°C for 4 hours.

6.2.3 Graphene characterization

Raman spectroscopy was done with a 532 nm laser Horiba LabRam HR Micro Raman Spectrometer using a 50× objective, 400 µm pinhole, and 100 µm slit size. The spectra were collected from 10 spots and averaged minimize the impact of local variations. An optical image corresponding to the Raman spectrum was obtained with the Olympus BX41 camera on the Raman spectrometer. The optical image and the Raman spectrum are shown in Figure 6.1, and discussed in the next section.

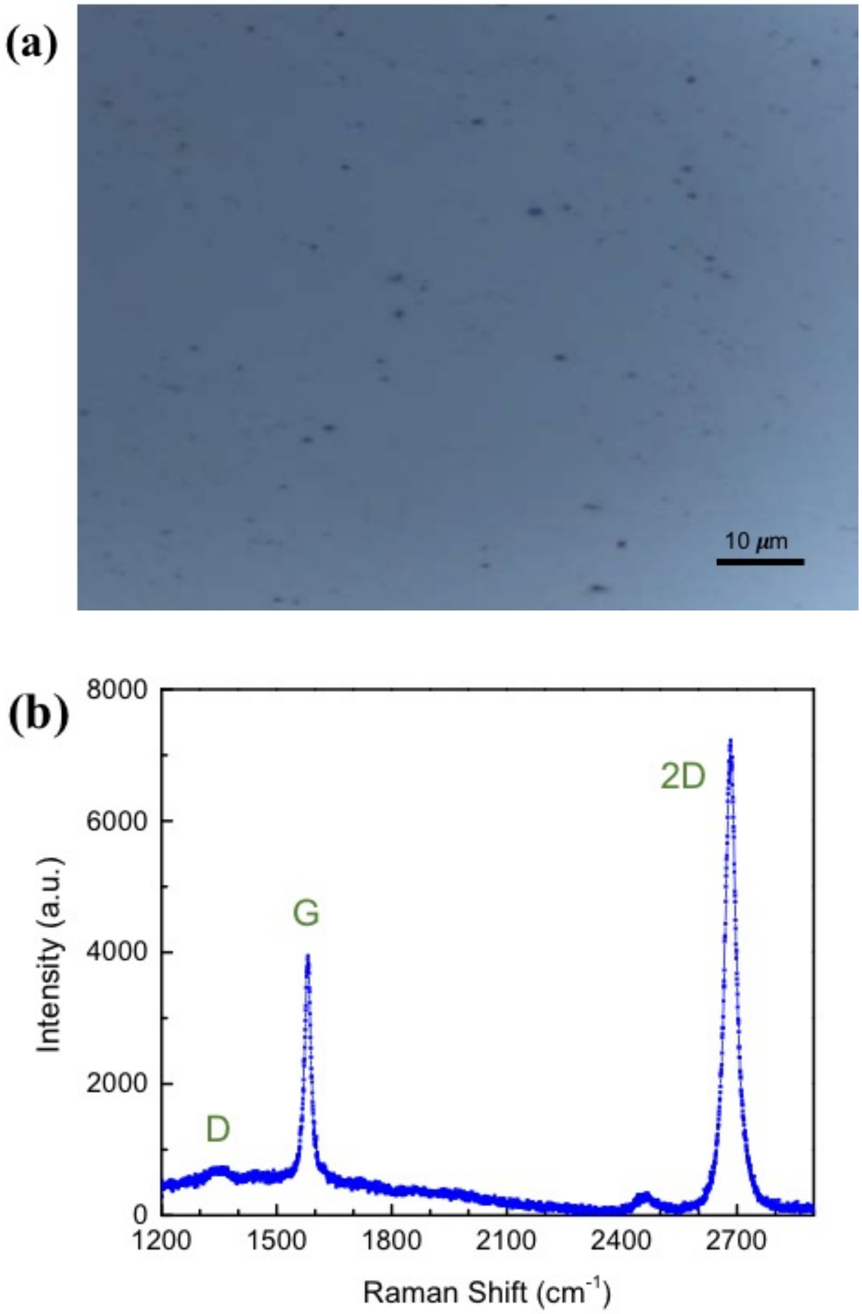

Figure 6.1 (a) Reflection mode optical microscopy image of transferred graphene surface on silicon wafer. Spots are dust particles on the sample surface. (b) Raman spectrum of the transferred graphene surface on silicon. The large intensity ratios for the I_G/I_D and I_{2D}/I_G indicate a graphene sheet with low density of defects.

6.2.4 Polystyrene thin film preparation

Linear PS (M_w = 131000 g/mol, PDI = 1.05, synthesized from living anionic polymerization) was obtained from Polymer Source Inc., and was used as received. Toluene (99.5%, for spectroscopy ACS) was purchased from Acros Organics Inc. Two concentrations of PS solutions were made: 0.75 wt % (PS 0.0401g, toluene 5.3110g), and 1.5 wt % (PS 0.0800g, toluene 5.2541g). Films of linear PS were spun-cast from their toluene solutions at a rate of 2000 rpm onto two types of substrates: piranha-cleaned, HF-treated silicon wafers and silicon substrates covered with a single layer of graphene. All spun cast films were annealed at 150°C in high vacuum (ca. 1×10^{-7} Pa) for 12 h before XPCS measurements.

6.2.5 X-ray photon correlation spectroscopy (XPCS) and X-ray reflectivity (XR)

XPCS were measured at beamline 8-ID-I at the APS, Argonne National Laboratory, using a reflection geometry and analyzed using a procedure described elsewhere[107,108]. A partially coherent monochromatic X-ray beam (E = 7.35 keV, 20×20 μm^2) was used, with the incident angle (θ=0.14°) below the PS critical angle (0.16°). The X-ray beam penetration in the film was limited to 9 nm in depth so scattering from the interface between the film and the substrate can be neglected, and scattering from density fluctuations within the film neglected due to the dominating contrast at the vacuum/melt interface. The intensity was recorded using a two-dimensional CCD camera located 4027 nm downstream of the sample[107]. Full frame mode was used to capture the off-specular scattering meaning the entire detector surface was used for every frame. The $q_{||}$ range was 10^{-4} Å^{-1} to 10^{-3} Å^{-1}.

The range of relaxation times accessible with the setup was from 10^{-1} to 10^{3} seconds. The X-ray beam intensity was about 5×10^{9} photons/second, with coherence lengths of 140 μm and 7 μm in the vertical and horizontal directions, respectively. Each XPCS measurement was started after 20 minutes of thermal equilibration.

The fluctuations in the coherent speckle pattern from the thermally stimulated surface fluctuations of the polymer film. The dynamics of these surface fluctuation are captured by the normalized intensity-intensity autocorrelation function (g_2),

$$g_2\,(q_{\|}, t') = \frac{\langle I(q_{\|}, t')I(q_{\|}, t'+t)\rangle}{\langle I(q_{\|}, t')\rangle^2} \tag{6.1}$$

where $I(q_{\|}, t')$ is the scattering intensity at $q_{||}$ at time t', and the angular brackets denote ensemble averages for the delay time, t. A single-exponential decay function, $g_2 = 1 + \beta \exp\,(-2t/\tau)$, was used in fitting the g_2 data consistent with those data resulting from overdamped capillary waves[108], with β being the coherent contrast and τ being the relaxation time for equilibrium surface height fluctuations. None of the correlation discussed here displayed a "stretched" exponential shape. XR was performed before and after every XPCS measurement to acquire the thickness of the film and also to provide secondary evidence for X-ray beam radiation damage. Primarily, comparisons between correlation functions derived from the first and second halves of the frames in a run were made in order to exclude frames showing evidence of beam damage.

6.2.6 Strongly adsorbed layer measurement with X-ray reflectivity (XR)

After XPCS measurements, the linear PS films were rinsed with toluene (Acros Organics Inc., 99.5%, for spectroscopy ACS) by immersing them in toluene for 10 minutes and blow drying with high-purity N_2 and then repeating this procedure four times before drying the film in a high vacuum (ca. 1×10^{-7} Pa) at room temperature overnight. XR was measured using a Rigaku SmartLab X-ray Diffractometer with a sealed tube source (40 kV, 44 mA, $\lambda = 1.54$ Å) and parallel beam optic. A layered model was used in the fitting of the XR data, to obtain values of film thickness, density and interface roughness. The scattering length density profiles for the cases discussed here are shown in section 6.3.

6.2.7 Nanoindentation measurement

The hardness and elastic modulus of the silicon wafer and various samples of PS on silicon or PS on supported graphene were estimated by analyzing of the load-displacement curves garnered with a standardized loading and unloading process with a Hysitron premier nanoindentation system[151–153]. A Berkovich diamond tip was used and the unloading curve analysis provided using the approach coded in the TriboScan software provided with the instrument.

6.3 Results and Discussion

6.3.1 Raman Spectroscopy

As introduced in section 3.2.4, Raman spectroscopy is used to evaluate the quality and the number of layers of graphene[135,136] in a sample. In Figure 6.1, the intensity ratio of the *G* peak to the *D* peak is very large, indicating a large grain size, low defect density[257]. The *2D* peak intensity is slightly more than twice that of the *G* peak and the FWHM of the *2D* peak is ca. 26 cm^{-1}, indicating the transferred sample is a monolayer of graphene[146,258].

6.3.2 X-ray Photon Correlation Spectroscopy (XPCS)

The behavior of PS surface fluctuations are different for the film supported on graphene than for the film on silicon is immediately evident from the raw XPCS data. Three kinds of samples were measured. The samples are designated using a name that contains first the thickness specified as a multiple of R_g, then the abbreviation for the polymer and then the material contacting the melt (Graphene or Si). Sample thicknesses of $8R_g$ (ca. 80 nm) and $3R_g$ (ca. 30 nm) were studied so that the designations for the three samples are "$8R_g$ PS/Graphene", "$3R_g$ PS/Graphene", and "$3R_g$ PS/Si". With an incident angle θ=0.14°, the penetration depth into polystyrene is limited to 9 nm and the scattering from the fluctuations of the film surface is much stronger than the scattering due to density fluctuations internal to the film. Thus the XPCS data capture only the surface fluctuation dynamics. A typical 2-D false color plot of the scattering intensity in the detector plane is shown in the upper left corner of Figure 6.2(a) where the two axes correspond to the two real space directions perpendicular to the sample surface (right to left) and perpendicular to the scattering plane (top to bottom); the axes are notated with pixel numbers. This scattering pattern is also referred to as a speckle pattern. Each time the speckle pattern is captured, the resulting data set, corresponding to a specific delay time since the beginning of the measurement is referred to as a "frame". One XPCS data is composed of frames from 1 to N. A comparison of a plot resulting from an average of the intensities in each pixel over the first N/2 frames with a plot resulting from an average in each pixel over the second N/2 frames provides a quick qualitative indication of the degree to which the surface has fluctuated over the time scale of the experiment. Consider such a pixel by pixel average along the line shown in two false color intensity plots on the right side of Figure 6.2. Since the scattering measured here is coherent scattering, when the intensity measured in a given pixel over the first half of the run differs outside the statistical uncertainty from the intensity measured in that pixel over the second half of the run one may infer that some real space feature of the surface relaxed over the time the elapsed from the middle of the first half to the middle of the second half of the run. For a given set of experimental condition, if few pixels show statistically significant changes in intensity the surface is not moving on that time scale. In Figure 6.3(a) the plots of averaged intensity in each pixel from the first 160 frames, i.e. first 336 seconds and the second 160 frames, i.e. second 336 seconds of an experiments. This is for the sample on graphene that is $8R_g$ thick at 170°C. For some pixels the intensities from the average of the first half and average of the second half are quite similar. For other pixels the two averages differ significantly. Thus, the surface is relaxing on the time scale of 336 seconds. In Figure 6.3(b) is shown such a comparison for the $3R_g$ thick sample on graphene at a much higher temperature of 220°C.

Despite the sample being at a temperature 50°C higher, the average intensities for the two different sets of frames are the same within the counting uncertainty for nearly all the pixels. Thus the surface of this thinner film is not fluctuating on this time scale.

According to the HCT theory introduced in section 3.1.3, a given temperature and a given polymer but with different thickness values, τ/h and $q_{||}h$ should collapse onto a single universal curve. A deviation from this universal curve will be an evidence of the existence of confinement effects. The surface tensions and bulk viscosities of 131000 g/mol linear PS at different temperatures shown in Table 6.1 are derived from literature data[92,259].

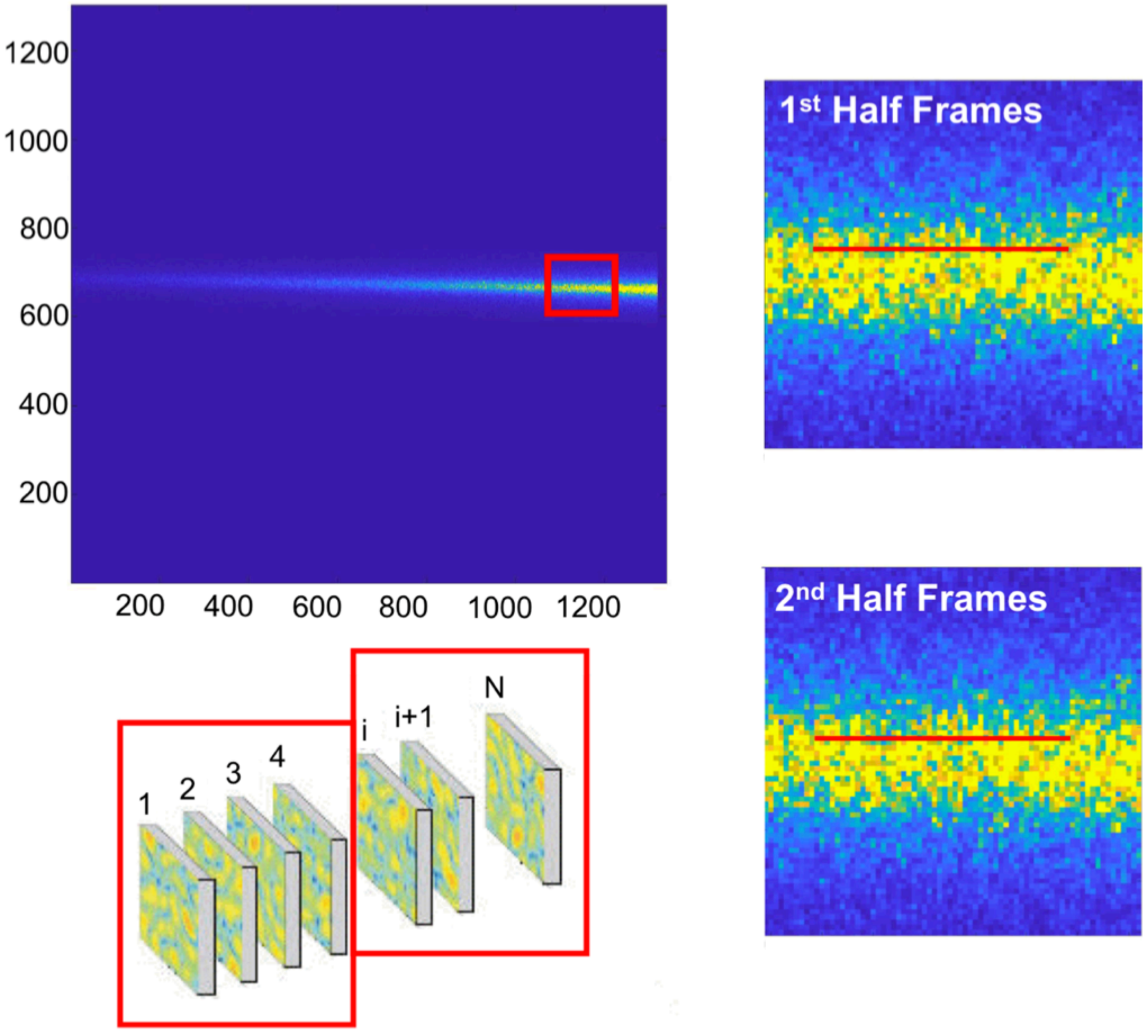

Figure 6.2 Upper left: An example speckle pattern from the CCD detector. Low left: schematic of the process of averaging intensity patterns from the first half of a run and the second half of a run. Right side: Examples of the averaged intensity patterns for a region of interest on the detector (shown in red box) from the first and second half of a run. Both averages still have the character of “speckle patterns”. That is, jumps in intensity between neighboring pixels make the pixels very evident, meaning the sample is not moving on the time scale over which the averaging was done. Lines mark the pixels for which intensities are plotted in Figure 6.3 (a) and (b).

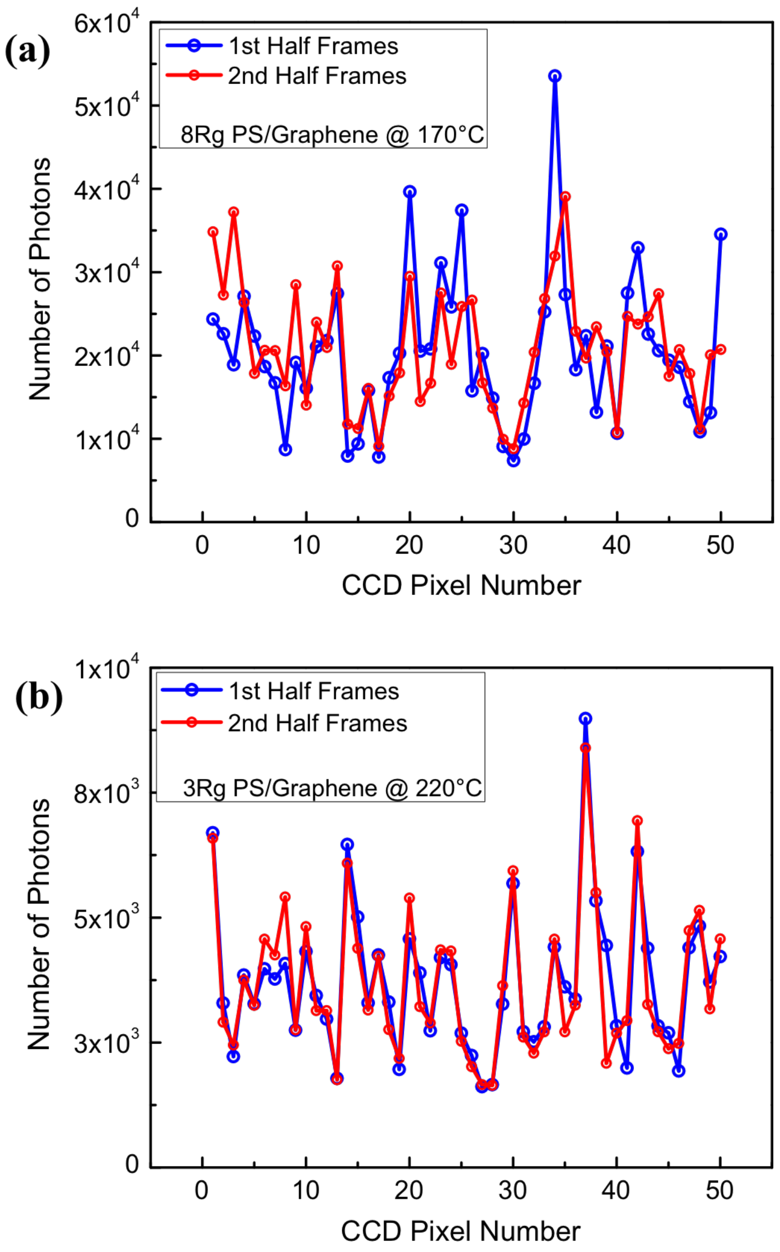

Figure 6.3 Plot of intensity in each pixel along the line shown in Figure 6.2 for the first 336 seconds (open symbols, blue) and second 336 seconds (closed symbols, red) of a run for (a) 8R_g PS/Graphene at 170°C and (b) 3R_g PS/Graphene at 220°C. On the time scale of 672 seconds the 8R_g sample changes some, but the 3R_g sample surface has not relaxed appreciably.

Table 6.1 Surface tensions and bulk viscosities of 131k linear PS at various temperatures.

Temp (°C)	γ_{linear}[a] (mN/m)	η_{bulk} (Pa s)
150	31.30	3.4×10^6
160	30.62	9.7×10^5
170	29.94	3.1×10^5
180	29.26	1.2×10^5

[a] Reprinted with permission from *ACS Macro Letters* **2017**, 6, 915-919. Copyright (2017) American Chemical Society.

[b] The uncertainty of the surface tension is about ±5%.

The fitting of the autocorrelation functions was done with the XPCS Analysis Program 3.0 (Copyright 2008) by Zhang Jiang and Michael Sprung. Using one fixed mask for all the analysis allowed for the incorporation of data reflecting always the same length scales of motion, resulting in more consistent comparisons among different measurements. Fitting of the g_2 data in equation (6.1) with the single-exponential decay function, $g_2 = 1 + \beta \exp(-2t/\tau)$, yielded the normalized relaxation time, τ/h, as a function of the dimensionless in-plane scattering vector, $q_{||}h$. Plots of these results for the $8R_g$ PS/Graphene and $3R_g$ PS/Si samples are shown in Figure 6.4. Consider first the $3R_g$ PS/Si sample data for 170°C. The normalized relaxation time decreases as dimensionless scattering vector increases with a power-law dependence of about -3.8, which is what one expects for overdamped surface fluctuations. When the thickness of the PS is the same,

$3R_g$, but the substrate is changed from Si to graphene, the speckle patterns do not change at all over the measurement times used, even for temperatures as high as 220°C. That is, on the length scales and time scales probed the surface for the $3R_g$ PS/Graphene appears solid like. The corresponding g_2 functions are horizontal lines with values above the baseline and it is not possible to define a value for the relaxation time beyond defining a lower bound. If the relaxation time had been less than 336 seconds for at least some values of q, we should have been able to see at least the first part of the relaxation in the g_2 function. Since we cannot, we can say that the value of τ for the $3R_g$ PS/Graphene even at 220°C lies above 336 seconds for all values of $q_{||}$ studied here. This result is captured in Figure 6.4 by showing a dotted line at a high value of τ for $3R_g$ PS/Graphene at 220°C. In order to be able to quantify measurable relaxations a thicker sample of $8R_g$ PS on graphene was measured. At 170°C, the surface fluctuations are measurable for this $8R_g$ film. However, even though the sample on graphene is much thicker than the $3R_g$ PS film on Si, it fluctuates much more slowly than does the $3R_g$ PS on Si. The fluctuations of the film on graphene appear to be about three orders of magnitude slower than the fluctuations of the film on Si. This is a dramatic difference, which is because of the attractive PS/Graphene interactions that are much stronger than those between PS and Si. This leads to a more profound slowing down of the PS chains next to graphene and the formation of a thicker strongly adsorbed layer on graphene.

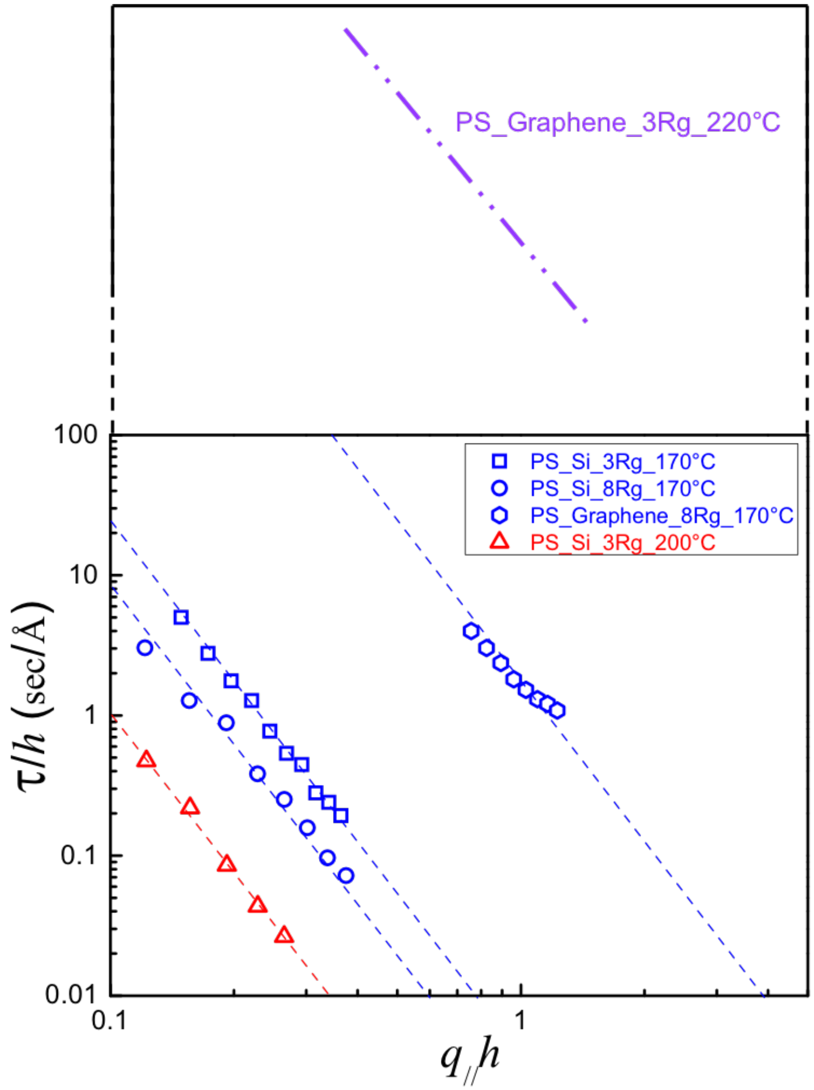

Figure 6.4 τ/h vs. $q_{//}h$ at 170°C, 180°C, 190°C for $3R_g$ PS thin films on silicon and $8R_g$ PS thin film on graphene. The dashed curve for $3R_g$ PS/Graphene 220°C indicates that the relaxation for that sample is outside the measurable range, even at 220°C. The dashed curves shown with the data correspond to fits with the HCT and a two layer model in which the bottom layer is considered immobile on the probed time scales and the top layer has an effective thickness much less than the total layer thickness and a viscosity equal to the experimentally measured bulk viscosity.

Evidence of the structure of the strongly adsorbed film that was in place in the melt at the temperature of the XPCS measurement was obtained using XR and ellipsometry. The XR curves for the strongly adsorbed layers are shown in Figure 6.5. This was done first by rinsing with good solvent a room temperature sample that had been measured with XPCS following the protocol of Koga et al.[253] The layer that is left on the substrate after the rinsing and drying is a collapsed version of the strongly adsorbed layer that was present in the melt[260]. That is, in the melt state at temperature there would have been "loops" and "tails" and portions of chains from the adsorbed layer that extended up into the melt adjacent to the adsorbed layer. These parts of chains could still be extending away from the densest part of the layer when the rinsed sample is still in solvent, but upon the last removal from solvent, these sections of chains that had been extended out collapse onto the rest of the adsorbed layer, since air is a poor solvent for the chains. The SLD profiles according to the best fits of the XR curves for the strongly adsorbed layers are shown in Figure 6.5. Nominal thicknesses of these collapsed versions of the strongly adsorbed layers on silicon and graphene were calculated as the distance between the middle of the interface with air to the middle of the interface with the substrate. Those thicknesses were 3.4 ± 0.1 nm and 8.2 ± 0.2 nm, respectively, as measured by XR. This value of thickness on the silicon substrate is consistent with our earlier work[92] and with results from Koga et al.[253] Further details of the differences between the structures of the adsorbed layers on the two substrates can be gleaned from the SLD profiles. The SLD profile for the strongly adsorbed layer on Si after rinsing appears to describe a PS layer that has an SLD value in its densest part (the plateau) that is 9.7×10^{-6} Å^{-2}, which is about 9% larger than the bulk SLD value of 8.9×10^{-6} Å^{-2}.

Then there is an interface with the air that appears either rough (with rms roughness of about 8 Å) or to correspond to a gradual transition from this heightened density next to the substrate to low density next to air. The SLD profile for the layer adsorbed to graphene showing a densest part with SLD of 11.0×10^{-6} Å^{-2}, which is 24% larger than the bulk SLD, and a transition in SLD from PS layer to air that is about 4.5 times broader than that on for the Si substrate. Again, from XR data alone it is not possible to say is this breadth is due to diffuseness, or roughness, or both. Schematics of the strongly adsorbed layers are in Figure 6.6. The strongly adsorbed layer thickness on silicon is comparable to what has been reported in the literature[247,254,261–263], given similar molecular weight, temperature, and annealing time. For the purposes of modeling the dynamic behavior (τ/h vs. $q_{||}h$ behavior) it proves to be sufficient to neglect the gradient in structure that most likely exists in the melt film and just estimate the dynamic character of the melt film as reflecting model of two layers, one highly viscous layer at the substrate and a second with bulk viscosity on the surface. The 170°C data from the $3R_g$ PS/Si, $8R_g$ PS/Si and the $8R_g$ PS/Graphene sample collapse on a universal curve using a two-layer model with a 75 nm (ca. $7R_g$) highly viscous layer on graphene and a 14 nm (ca. $1.5R_g$) on silicon, as shown in Figure 6.7. This is additional evidence that indicates a strong interaction between the graphene layer and that of the film adsorbed to it.

These experimental results may be compared with the results of molecular dynamics (MD) simulations of concentrated chains obtained by Prof. Mesfin Tsige in a separate study[264]. These were performed with the optimized potential for liquid simulations-all-atom (OPLS-AA) force field and equilibrating for an integration time step of 1 fs. The position of each atom was recorded every 2 ps during heating and every 10 ps during cooling. Snapshots of selected chains of PS 60-mer near a hydroxylated α-quartz and graphite (5 layers of graphene) surface are shown in Appendix E. For the PS chains next to the hydroxylated α-quartz, “loops” are formed, and the phenyl rings on the chain are dominantly pointing toward the substrate. For the PS chains next to graphite, most chains have one end, and many repeat units adjacent to that chain end, lying on the substrate to maximize contact, and the rest of the chain is in the melt away from the surface. In the case shown in the appendix about 20 sequential repeat units are on the substrate surface. The phenyl rings are pointing away from the substrate and the $-CH_2$ groups are pointing toward the substrate due to quadrupole interactions.

It has been shown in earlier work from our group[92] that a silicon substrate surface can also be modified so that the strongly adsorbed layer thickness on that substrate is much less than that in silicon. Zhou et al. considered a coating of $3R_g$ PS on a silicon wafer covered with a 5 nm thick plasma polymerized maleic anhydride (ppMA) film. They could explain the XPCS data for that sample using a two layer model in which the highly viscous layer was only 15 nm ($1.5R_g$) thick, and no layer at all was found by XR on the substrate after rinsing. Although the two-layer model with a highly viscous layer is an approximation, it is sufficient to illustrate clearly that the influence on the film hydrodynamics for PS on a substrate extends over a distance much bigger than the strongly adsorbed layer thickness left after rinsing for graphene, silicon, and the plasma polymerized MA coating.

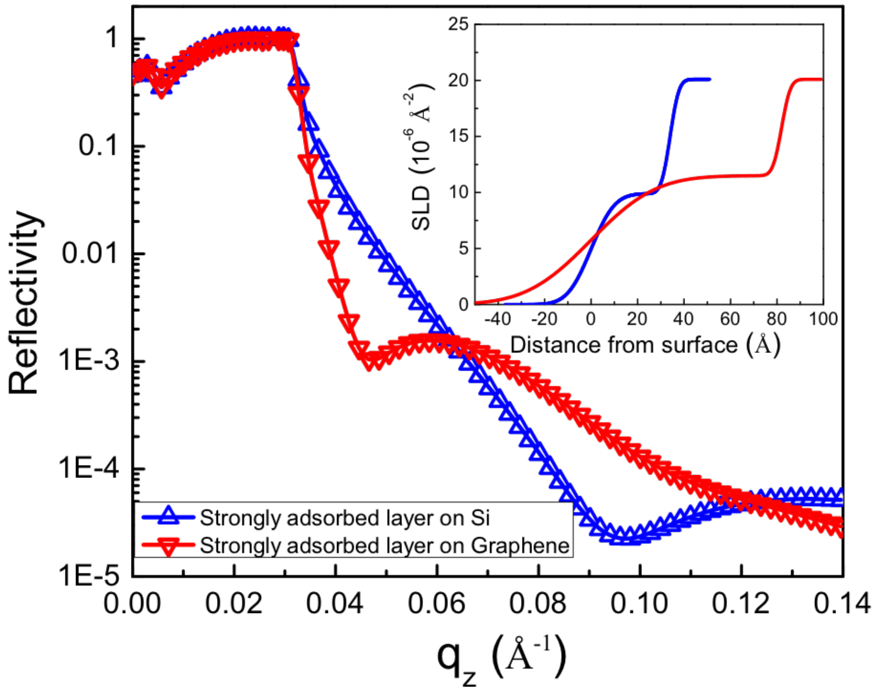

Figure 6.5 X-ray reflectivity (XR) curves with the nonlinear least square regression using a multilayer structural model and (inset) the scattering length density (SLD) profiles according to the best fits for the strongly adsorbed layers on Si and on graphene after rinsing.

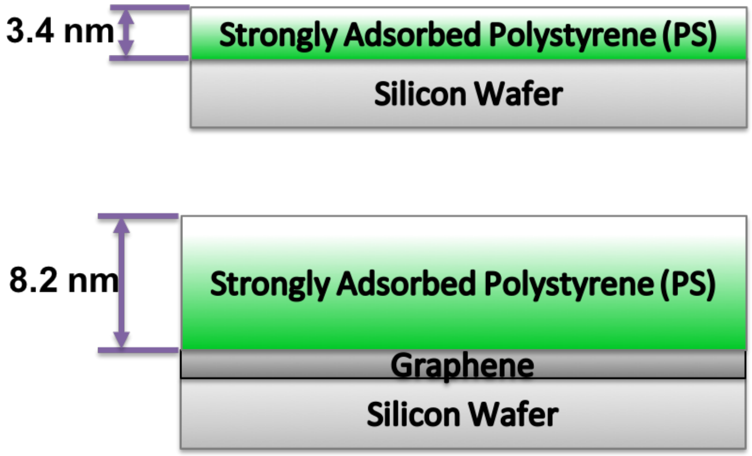

Figure 6.6 Cartoon for strongly adsorbed PS on silicon and graphene substrate.

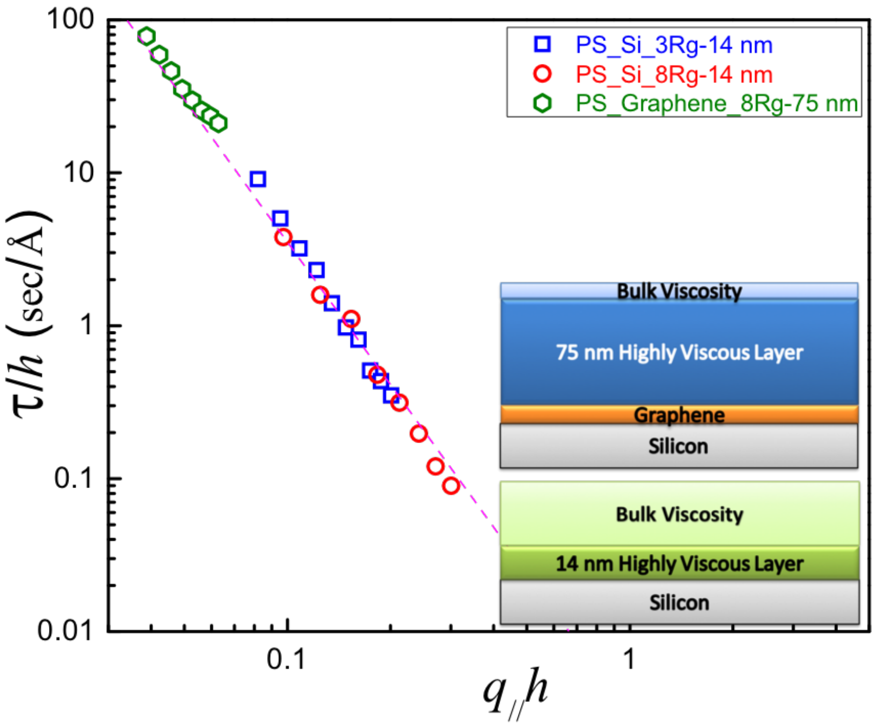

Figure 6.7 *τ/h vs.* $q_{//}h$ at 170°C for PS thin films on silicon and graphene assuming effective thicknesses reflecting reductions from the actual thicknesses by the amounts shown in the legend.

6.3.3 Nanoindentation

In the previous section a large change in the surface fluctuation behavior of PS melt films was seen as a result of interposing a single monolayer of graphene between the silicon substrate and the PS melt. Is it possible that the PS-graphene interactions could likewise have a large effect on the behavior of the PS film once it has cooled through its glass transition temperature and become a glass? Although precise inferences about the effect of the underlying graphene on the PS glassy film are challenging to draw from nanoindentation measurements, a small study is highly suggestive that the effects are substantial.

The force-displacement curves for the silicon wafer, $3R_g$ PS/Si, $3R_g$ PS/Graphene, $8R_g$ PS/Si, and $8R_g$ PS/Graphene are compared in Figure 6.8. Values of apparent elastic modulus and hardness of each sample derived from fitting of the unloading curves ignoring the complication of the sample being a thin film on a much harder substrate are summarized in Table 6.2. The values found experimentally for modulus and hardness for the Si alone is in reasonable agreement with values in the literature[265]. The hardness and elastic modulus values of bulk PS are from the literature[266] are quote for comparison, while the rest of the apparent elastic modulus and hardness values in Table 6.2 are experimentally determined averages over three locations spaced 200 μm apart. The maximum vertical displacement in each nanoindentation measurement was 10 nm; nonetheless the apparent hardness and elastic modulus values were influenced by the substrate at a much larger depth because deformation of the film at a given depth invokes processes deeper in the sample. For both $3R_g$ and $8R_g$ PS films, the apparent elastic modulus and hardness values for PS on graphene were substantially larger than those on silicon. We conjecture this is because of the stronger interactions between the PS and the graphene. For PS films on the same type of substrate, when the thickness decreased from $8R_g$ to $3R_g$, the values of apparent hardness and elastic modulus increased, since the substrate effect became important. For hardness the apparent value on graphene was about 10 times larger than that on Si for both thicknesses. For modulus the similarity of the apparent modulus values for $3R_g$ and $8R_g$ films on graphene was puzzling, since the modulus values on Si dropped by about a factor of 2 in going from a thickness of $3R_g$ to a thickness of $8R_g$. This difference should be studied further. However, the first results of nanoindentation measurements suggest a picture consistent with those from XPCS and characterization of the morphology of the strongly adsorbed layer, providing additional evidence of stronger interaction between the PS and graphene than between PS and Si.

Table 6.2 Elastic modulus and hardness values of different samples

Sample Name	Elastic Modulus (GPa)	Hardness (GPa)
PS bulk	2.6 ± 0.1	0.09 ± 0.02
Silicon	202.2 ± 5.8	20.5 ± 1.2
3Rg_PS/Si	51.7 ± 5.0	1.1 ± 0.2
3Rg_PS/Graphene	188.2 ± 6.9	11.8 ± 0.6
8Rg_PS/Si	27.6 ± 0.4	0.44 ± 0.05
8Rg_PS/Graphene	188.8 ± 2.4	4.7 ± 0.2

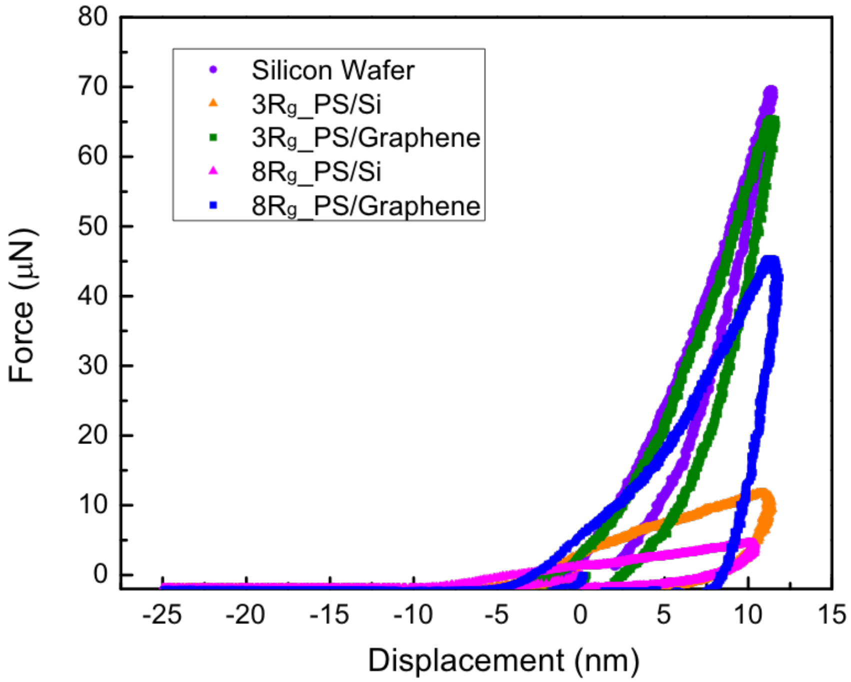

Figure 6.8 Force-displacement curves for the silicon wafer, 3R_g PS/Si, 3R_g PS/Graphene, 8R_g PS/Si, and 8R_g PS/Graphene. The maximum displacement is 10 nm.

6.4 Conclusion

It has been proposed that in the area of corrosion, higher atom density in the protective coating near the metal surface could provide better corrosion protection[44,45]. As a monolayer of sp^2 carbon atoms sitting in a hexagonal lattice, graphene shows a range of special properties[84,267,268], including apparent benefits in the development of corrosion protection[38,40] in coatings. Therefore, XPCS, investigation of surface fluctuations on films next to graphene should help us better understand the role of graphene in corrosion protection as well as graphene's role in other applications in areas involving wetting and adhesion[46,47] of thin films on this extraordinary material, In addition, such studies may contribute in the decades-long debate on the T_g in polymer films and its change[52,53], with film thickness[54–63], and with polymer type[53,64,65], since it seems that the T_g behavior could also very well, in the case of supported films, depend upon modification of the interactions with the substrate, which seem to be quite substantial with graphene.

The XPCS measurements show that the $8R_g$ PS/Graphene surface fluctuations are three orders of magnitude slower than those of $8R_g$ PS/Si. The 170°C data from the $3R_g$ PS/Si, $8R_g$ PS/Si and the $8R_g$ PS/Graphene sample collapse on a universal curve using a two-layer model with a highly viscous layer of 75 nm (ca. $7R_g$) thick on graphene and a 14 nm (ca. $1.5R_g$) thick layer on silicon. The strongly adsorbed layer on graphene left after the rinsing and drying procedure was 2.4 times thicker than that on silicon. All the results here suggest a strong interaction between a monolayer graphene as the substrate and the adsorbed film. Such interaction could perturb the behavior of the melt over a distance from substrate significantly greater than the strongly adsorbed layer thickness. Graphene is one of the most widely used materials in various fields especially electronics, sensors, supercapacitors, superconductors and coatings[84,85]. The investigation of the effect of this fascinating monolayer, graphene, on the sufficiently thin films will help in developing a systematic understanding of the effects of substrate chemistry on confinement and surface fluctuations.

CHAPTER VII

CONCLUSION

The objective of the work involved in this dissertation was to understand the water or electrolyte diffusion, organic coating/metal substrate interface disruption, and surface fluctuations of polymer melt films on graphene. It shows an effort to understand corrosion, which is important both scientifically and technologically. The investigation on the nanometer length scale helps to establish an understanding of the corrosion mechanism, which makes it probable to reduce the time-consuming macroscopic empirical organic coating performance evaluations such as outdoor exposure and accelerated weathering. The surface fluctuation study of adsorbed PS films on graphene or silicon substrate addresses important interfacial properties such as wetting, adhesion[46,47], and tribology. The information garnered from XPCS measurements, which probe behavior dictated by viscosity will also provide a complementary perspective to help with the ongoing debate on the correlation between glass transition temperature (T_g) (which is related to segmental dynamics) and its change[52,53], with film thickness[54–63], and with polymer type[53,64,65], since it seems that the T_g behavior could also very well, in the case of supported films, depend upon modification of the interactions with the substrate. This modification seems to be quite substantial with graphene. The study of surfaces and interfaces on such small length scale is challenging since the behavior observed can be altered by surface or interface layers of only a few Ångströms thickness.

Water/electrolyte diffusion in organic films of tens of nanometers thickness were distinguished in terms of the direction of diffusion: vertical penetration or lateral diffusion. The lateral rate of diffusion of water or electrolyte probed by XR/NR was orders of magnitude larger than the diffusion rate in bulk epoxy, and the rate of penetration of water or electrolyte films of small thickness characterized by EIS was orders of magnitude smaller than the diffusion rate in bulk epoxy. Such a large difference between the rates in the directions parallel or perpendicular to the plane of the coating is consistent with the empirical observation that a scratched coating on metallic substrate makes the metal corrode much faster. Consistency in results from XR, NR and EIS showed that the diffusion rate of electrolyte is lower than that of water (H_2O/D_2O), and the higher the salt concentration, the lower the rate of diffusion. The probing of diffusion over this short length scale (nm) and short times (hours) is a key for advancing the understanding of water and electrolyte diffusion in organic coatings, which is considered as a first step in the study of metallic substrate corrosion. Reflectivity complements the wide use of EIS, and provides a means of quantitatively investigating phenomena that occur rapidly in the very early corrosion process.

Next, the scattering from a self-affine surface was compared to the experimental data in the analysis of the "rocking curve" off-specular scattering data. The morphology at the substrate/coating interface and its change with exposure of the coating to electrolyte was described statistically. The fitting of the off-specular data gave the jaggedness and correlation length of the interface. With exposure the interface becomes more rough, less correlated, and more jagged. The characteristic length scale at which the morphology of an interface between an epoxy corrosion prevention coating and a metal surface is roughened by exposure of the coating to water differs for the two crosslinkers. The properties of the crosslinker affect the capability of the crosslinked coating to resist water or electrolyte diffusion and subsequent corrosion. The larger spacing between the two intramolecular amino groups in the crosslinked epoxy results in different rigidities and possibilities for water or electrolyte diffusion. The involvement of off-specular scattering and AFM in the investigation of the differences in nanoscale morphological variation at a buried interface due to the corrosion process caused by variations in coating chemistry is a novel approach that complements the widely used technique of EIS, which can see changes in performance with coating chemistry variation, but cannot readily link these changes to morphology.

In the last part of this dissertation, XPCS measurements show that the $8R_g$ PS/Graphene surface fluctuations are three orders of magnitude slower than those of $8R_g$ PS/Si. The 170°C data from the $3R_g$ PS/Si, $8R_g$ PS/Si and the $8R_g$ PS/Graphene sample collapse on a universal curve using a two-layer model with a highly viscous layer of 75 nm (ca. $7R_g$) thick on graphene and a 14 nm (ca. $1.5R_g$) thick layer on silicon. The strongly adsorbed layer on graphene left after the rinsing and drying procedure is 2.4 times thicker than that on silicon. All the results here suggest a strong interaction between a monolayer graphene as the substrate and the adsorbed film. Such interaction could perturb the behavior of the melt over a distance from the substrate significantly greater than the thickness of the strongly adsorbed layer. Graphene is one of the most widely used materials in various fields especially electronics, sensors, supercapacitors, superconductors and coatings[84,85]. The investigation of the effect of this fascinating monolayer, graphene, on thin films will help in developing a systematic understanding of the effects of substrate chemistry on confinement and surface fluctuations.

In summary, scattering methods using X-rays and neutrons provide nanoscale resolution in the investigation of water or electrolyte diffusion, organic coating/metal substrate interface disruption, and surface dynamics of polymer melt films on graphene. Such efforts to understand corrosion at short length and time scales help to establish an understanding of the mechanism of corrosion, facilitate the coating performance evaluation, and benefit a number of interfacial applications, including wetting and adhesion.

REFERENCES

(1) Sørensen, P. A.; Kiil, S.; Dam-Johansen, K.; Weinell, C. E. Anticorrosive Coatings: A Review. *J. Coatings Technol. Res.* **2009**, *6* (2), 135–176.

(2) Fehlner, F. P.; Mott, N. F. Low-Temperature Oxidation. *Oxid. Met.* **1970**, *2* (1), 59–99.

(3) Chiles, R. M. *If They Come, We Will Build It: In Vitro Meat and the Discursive Struggle over Future Agrofood Expectations*; FHWA-RD-01-156, NACE International, 2013; Vol. 30.

(4) De'Nève, B.; Shanahan, M. E. R. Water Absorption by an Epoxy Resin and Its Effect on the Mechanical Properties and Infra-Red Spectra. *Polymer.* **1993**, *34* (24), 5099–5105.

(5) Kaszowska, Z.; Malek, K.; Pańczyk, M.; Mikołajska, A. A Joint Application of ATR-FTIR and SEM Imaging with High Spatial Resolution: Identification and Distribution of Painting Materials and Their Degradation Products in Paint Cross Sections. *Vib. Spectrosc.* **2013**, *65*, 1–11.

(6) Philippe, L.; Sammon, C.; Lyon, S. B.; Yarwood, J. An FTIR/ATR in Situ Study of Sorption and Transport in Corrosion Protective Organic Coatings 1. Water Sorption and the Role of Inhibitor Anions. *Prog. Org. Coatings* **2004**, *49* (4), 302–314.

(7) Wapner, K.; Grundmeier, G. Spatially Resolved Measurements of the Diffusion of Water in a Model Adhesive/Silicon Lap Joint Using FTIR-Transmission-Microscopy. *Int. J. Adhes. Adhes.* **2004**, *24* (3), 193–200.

(8) Nguyen, T.; Byrd, E.; Bentz, D.; Lin, C. In Situ Measurement of Water at the Organic Coating/Substrate Interface. *Prog. Org. Coatings* **1996**, *27* (1–4), 181–193.

(9) Wapner, K.; Stratmann, M.; Grundmeier, G. In Situ Infrared Spectroscopic and Scanning Kelvin Probe Measurements of Water and Ion Transport at Polymer/Metal Interfaces. *Electrochim. Acta* **2006**, *51* (16), 3303–3315.

(10) Posner, R.; Titz, T.; Wapner, K.; Stratmann, M.; Grundmeier, G. Transport Processes of Hydrated Ions at Polymer/Oxide/Metal Interfaces. Part 2. Transport on Oxide Covered Iron and Zinc Surfaces. *Electrochim. Acta* **2009**, *54* (3), 900–908.

(11) Posner, R.; Giza, G.; Marazita, M.; Grundmeier, G. Ion Transport Processes at Polymer/Oxide/Metal Interfaces under Varying Corrosive Conditions. *Corros. Sci.* **2010**, *52* (5), 1838–1846.

(12) Posner, R.; Wapner, K.; Amthor, S.; Roschmann, K. J.; Grundmeier, G. Electrochemical Investigation of the Coating/Substrate Interface Stability for Styrene/Acrylate Copolymer Films Applied on Iron. *Corros. Sci.* **2010**, *52* (1), 37–44.

(13) Posner, R.; Wapner, K.; Stratmann, M.; Grundmeier, G. Transport Processes of Hydrated Ions at Polymer/Oxide/Metal Interfaces. Part 1. Transport at Interfaces of Polymer Coated Oxide Covered Iron and Zinc Substrates. *Electrochim. Acta* **2009**, *54* (3), 891–899.

(14) Hughes, A. E.; Trinchi, A.; Chen, F. F.; Yang, Y.; Sellaiyan, S.; Carr, J.; Lee, P. D.; Thompson, G. E.; Xiao, T. Q. Structure and Transport in Coatings from Multiscale Computed Tomography of Coatings - New Perspectives for Eelectrochemical Impedance Spectroscopy Modeling? *Electrochim. Acta* **2016**, *202*, 243–252.

(15) Taylor, S. R.; Moongkhamklang, P. The Delineation of Local Water Interaction with Epoxy Coatings Using Fluorescence Microscopy. *Prog. Org. Coatings* **2005**, *54* (3), 205–210.

(16) Torrance, K. E.; Sparrow, E. M. Theory for Off-Specular Reflection From Roughened Surfaces. *J. Opt. Soc. Am.* **1967**, *57* (9), 1105-1114.

(17) Sinha, S. K.; Sirota, E. B.; Garoff, S.; Stanley, H. B. X-Ray and Neutron Scattering from Rough Surfaces. *Phys. Rev. B* **1988**, *38* (4), 2297–2311.

(18) Schwartz, D. K.; Schlossman, M. L.; Kawamoto, E. H.; Kellogg, G. J.; Pershan, P. S.; Ocko, B. M. Thermal Diffuse X-Ray-Scattering Studies of the Water-Vapor Interface. *Phys. Rev. A* **1990**, *41* (10), 5687–5690.

(19) Melendres, C. A.; Feng, Y. P.; Lee, D. D.; Sinha, S. K. X-Ray Diffuse Scattering for the In Situ Study of Electrochemically Induced Pitting on Metal Surfaces. *J. Electrochem. Soc.* **1995**, *142* (1), L19–L21.

(20) Feng, Y. P.; Sinha, S. K.; Melendres, C. A.; Lee, D. D. X-Ray off-Specular Reflectivity Studies of Electrochemical Pitting of Cu Surfaces in Sodium Bicarbonate Solution. *Phys. B Condens. Matter* **1996**, *221* (1–4), 251–256.

(21) Müller-Buschbaum, P.; Stamm, M. Correlated Roughness, Long-Range Correlations, and Dewetting of Thin Polymer Films. *Macromolecules* **1998**, *31* (11), 3686–3692.

(22) Müller-Buschbaum, P.; Gutmann, J. S.; Lorenz, C.; Schmitt, T.; Stamm, M. Decay of Interface Correlation in Thin Polymer Films. *Macromolecules* **1998**, *31* (26), 9265–9272.

(23) Singh, S.; Basu, S. Microscopic Characterization of Corrosion Morphology: A Study in Specular and Diffuse Neutron Reflectivity. *Surf. Sci.* **2006**, *600* (2), 493–496.

(24) Seo, Y. S.; Koga, T.; Sokolov, J.; Rafailovich, M. H.; Tolan, M.; Sinha, S. Deviations from Liquidlike Behavior in Molten Polymer Films at Interfaces. *Phys. Rev. Lett.* **2005**, *94* (15), 157802.

(25) Jiang, Z.; Kim, H.; Jiao, X.; Lee, H.; Lee, Y. J.; Byun, Y.; Song, S.; Eom, D.; Li, C.; Rafailovich, M. H.; et al. Evidence for Viscoelastic Effects in Surface Capillary Waves of Molten Polymer Films. *Phys. Rev. Lett.* **2007**, *98* (22), 227801.

(26) Wang, S. F.; Yang, S.; Lee, J.; Akgun, B.; Wu, D. T.; Foster, M. D. Anomalous Surface Relaxations of Branched-Polymer Melts. *Phys. Rev. Lett.* **2013**, *111* (6), 068303.

(27) Zhao, J.; Sakellariou, G.; Green, P. F. Phase Behavior of Diblock Copolymer/Star-Shaped Polymer Thin Film Mixtures. *Soft Matter* **2016**, *12* (17), 3849–3853.

(28) Jiang, Z.; Mukhopadhyay, M. K.; Song, S.; Narayanan, S.; Lurio, L. B.; Kim, H.; Sinha, S. K. Entanglement Effects in Capillary Waves on Liquid Polymer Films. *Phys. Rev. Lett.* **2008**, *101* (24), 246104.

(29) Mukhopadhyay, M. K.; Jiao, X.; Lurio, L. B.; Jiang, Z.; Stark, J.; Sprung, M.; Narayanan, S.; Sandy, A. R.; Sinha, S. K. Thickness Induced Structural Changes in Polystyrene Films. *Phys. Rev. Lett.* **2008**, *101* (11), 115501.

(30) Akgun, B.; Uğur, G.; Jiang, Z.; Narayanan, S.; Song, S.; Lee, H.; Brittain, W. J.; Kim, H.; Sinha, S. K.; Foster, M. D. Surface Dynamics of "Dry" Homopolymer Brushes. *Macromolecules* **2009**, *42* (3), 737–741.

(31) Koga, T.; Li, C.; Endoh, M. K.; Koo, J.; Rafailovich, M.; Narayanan, S.; Lee, D. R.; Lurio, L. B.; Sinha, S. K. Reduced Viscosity of the Free Surface in Entangled Polymer Melt Films. *Phys. Rev. Lett.* **2010**, *104* (6), 066101.

(32) Wang, S. F.; Jiang, Z.; Narayanan, S.; Foster, M. D. Dynamics of Surface Fluctuations on Macrocyclic Melts. *Macromolecules* **2012**, *45* (15), 6210–6219.

(33) Evans, C. M.; Narayanan, S.; Jiang, Z.; Torkelson, J. M. Modulus, Confinement, and Temperature Effects on Surface Capillary Wave Dynamics in Bilayer Polymer Films near the Glass Transition. *Phys. Rev. Lett.* **2012**, *109* (3), 038302.

(34) Kim, D.; Srivastava, S.; Narayanan, S.; Archer, L. A. Polymer Nanocomposites: Polymer and Particle Dynamics. *Soft Matter* **2012**, *8* (42), 10813–10818.

(35) Liu, B.; Narayanan, S.; Wu, D. T.; Foster, M. D. Polymer Film Surface Fluctuation Dynamics in the Limit of Very Dense Branching. *Macromolecules* **2013**, *46* (8), 3190–3197.

(36) Jäckle, J. The Spectrum of Surface Waves on Viscoelastic Liquids of Arbitrary Depth. *J. Phys. Condens. Matter* **1998**, *10* (32), 7121–7131.

(37) Sutton, M. X-Ray Intensity Fluctuation Spectroscopy. *Neutron X-ray Spectrosc.* **2006**, *9*, 297–318.

(38) Prasai, D.; Tuberquia, J. C.; Harl, R. R.; Jennings, G. K.; Bolotin, K. I. Graphene: Corrosion-Inhibiting Coating. *ACS Nano* **2012**, *6* (2), 1102–1108.

(39) Kirkland, N. T.; Schiller, T.; Medhekar, N.; Birbilis, N. Exploring Graphene as a Corrosion Protection Barrier. *Corros. Sci.* **2012**, *56*, 1–4.

(40) Schriver, M.; Regan, W.; Gannett, W. J.; Zaniewski, A. M.; Crommie, M. F.; Zettl, A. Graphene as a Long-Term Metal Oxidation Barrier: Worse than Nothing. *ACS Nano* **2013**, *7* (7), 5763–5768.

(41) Kyhl, L.; Nielsen, S. F.; Čabo, A. G.; Cassidy, A.; Miwa, J. A.; Hornekær, L. Graphene as an Anti-Corrosion Coating Layer. *Faraday Discuss.* **2015**, *180*, 495–509.

(42) Cui, C.; Lim, A. T. O.; Huang, J. A Cautionary Note on Graphene Anti-Corrosion Coatings. *Nat. Nanotechnol.* **2017**, *12* (9), 834–835.

(43) Bonn, S. Graphene against Corrosión. *Nat. Nanotech.* **2014**, *9*, 741–742.

(44) Kraljić, M.; Mandić, Z.; Duić, L. Inhibition of Steel Corrosion by Polyaniline Coatings. *Corros. Sci.* **2003**, *45* (1), 181–198.

(45) Zheludkevich, M. L.; Salvado, I. M.; Ferreira, M. G. S. Sol–Gel Coatings for Corrosion Protection of Metals. *J. Mater. Chem.* **2005**, *15* (48), 5099-5111.

(46) Tang, T.; Jagota, A.; Chaudhury, M. K.; Hui, C. Y. Thermal Fluctuations Limit the Adhesive Strength of Compliant Solids. *J. Adhes.* **2006**, *82* (7), 671–696.

(47) Ghatak, A.; Chaudhury, M. K. Adhesion-Induced Instability Patterns in Thin Confined Elastic Film. *Langmuir* **2003**, *19* (7), 2621–2631.

(48) Rissanou, A. N.; Harmandaris, V. Structural and Dynamical Properties of Polystyrene Thin Films Supported by Multiple Graphene Layers. *Macromolecules* **2015**, *48* (8), 2761–2772.

(49) Jiang, N.; Sen, M.; Endoh, M. K.; Koga, T.; Langhammer, E.; Bjöörn, P.; Tsige, M. Thermal Properties and Segmental Dynamics of Polymer Melt Chains Adsorbed on Solid Surfaces. *Langmuir* **2018**, *34* (14), 4199–4209.

(50) Seydel, T.; Madsen, A.; Tolan, M.; Grübel, G.; Press, W. Capillary Waves in Slow Motion. *Phys. Rev. B* **2001**, *63* (7), 073409.

(51) Guiselin, O. Irreversible Adsorption of a Concentrated Polymer Solution. *Epl* **1992**, *17* (3), 225–230.

(52) Yang, Z.; Fujii, Y.; Lee, F. K.; Lam, C.-H.; Tsui, O. K. C. Glass Transition Dynamics and Surface Layer Mobility in Unentangled Polystyrene Films. *Science.* **2010**, *328* (5986), 1676–1679.

(53) Ediger, M. D.; Forrest, J. A. Dynamics near Free Surfaces and the Glass Transition in Thin Polymer Films: A View to the Future. *Macromolecules* **2014**, *47* (2), 471–478.

(54) Kim, S.; Torkelson, J. M. Distribution of Glass Transition Temperatures in Free-Standing, Nanoconfined Polystyrene Films: A Test of de Gennes' Sliding Motion Mechanism. *Macromolecules* **2011**, *44* (11), 4546–4553.

(55) Pye, J. E.; Roth, C. B. Two Simultaneous Mechanisms Causing Glass Transition Temperature Reductions in High Molecular Weight Freestanding Polymer Films as Measured by Transmission Ellipsometry. *Phys. Rev. Lett.* **2011**, *107* (23), 235701.

(56) Bäumchen, O.; McGraw, J. D.; Forrest, J. A.; Dalnoki-Veress, K. Reduced Glass Transition Temperatures in Thin Polymer Films: Surface Effect or Artifact? *Phys. Rev. Lett.* **2012**, *109* (5), 055701.

(57) Boucher, V. M.; Cangialosi, D.; Yin, H.; Schönhals, A.; Alegría, A.; Colmenero, J. Tg Depression and Invariant Segmental Dynamics in Polystyrene Thin Films. *Soft Matter* **2012**, *8* (19), 5119–5122.

(58) Tress, M.; Erber, M.; Mapesa, E. U.; Huth, H.; Müller, J.; Serghei, A.; Schick, C.; Eichhorn, K. J.; Voit, B.; Kremer, F. Glassy Dynamics and Glass Transition in Nanometric Thin Layers of Polystyrene. *Macromolecules* **2010**, *43* (23), 9937–9944.

(59) Erber, M.; Tress, M.; Mapesa, E. U.; Serghei, A.; Eichhorn, K. J.; Voit, B.; Kremer, F. Glassy Dynamics and Glass Transition in Thin Polymer Layers of PMMA Deposited on Different Substrates. *Macromolecules* **2010**, *43* (18), 7729–7733.

(60) Alcoutlabi, M.; McKenna, G. B. Effects of Confinement on Material Behaviour at the Nanometre Size Scale. *J. Phys. Condens. Matter* **2005**, *17* (15), R461–R524.

(61) Roth, C. B.; Dutcher, J. R. Glass Transition and Chain Mobility in Thin Polymer Films. *J. Electroanal. Chem.* **2005**, *584* (1), 13–22.

(62) van Zanten, J. H.; Wallace, W. E.; Wu, W. li. Effect of Strongly Favorable Substrate Interactions on the Thermal Properties of Ultrathin Polymer Films. *Phys. Rev. E - Stat. Physics, Plasmas, Fluids, Relat. Interdiscip. Top.* **1996**, *53* (3), R2053–R2056.

(63) Forrest, J. a; Dalnoki-Veress, K. The Glass Transition In Thin Polymer Films. *Adv. Coll. Interf. Sci.* **2001**, *94* (1–3), 167–196.

(64) Hudzinskyy, D.; Lyulin, A. V.; Baljon, A. R. C.; Balabaev, N. K.; Michels, M. A. J. Effects of Strong Confinement on the Glass-Transition Temperature in Simulated Atactic Polystyrene Films. *Macromolecules* **2011**, *44* (7), 2299–2310.

(65) Inoue, R.; Nakamura, M.; Matsui, K.; Kanaya, T.; Nishida, K.; Hino, M. Distribution of Glass Transition Temperature in Multilayered Poly(Methyl Methacrylate) Thin Film Supported on a Si Substrate as Studied by Neutron Reflectivity. *Phys. Rev. E - Stat. Nonlinear, Soft Matter Phys.* **2013**, *88* (3), 032601.

(66) Shreir, L. L.; Burstein, G. T.; Jarman, R. A. *Corrosion*; Butterworth-Heinemann Ltd, 1994.

(67) Bradford, S. A. *Corrosion Control*; CASTI Publishing Inc., 2001.

(68) Argandoña, A. Ethical Aspects of an Urban Catastrophe. *J. Bus. Ethics* **1995**, *14* (7), 511–530.

(69) Hasan, F.; Iqbal, J.; Ahmed, F. Stress Corrosion Failure of High-Pressure Gas Pipeline. *Eng. Fail. Anal.* **2007**, *14* (5), 801–809.

(70) Vargel, C. *Corrosion of Aluminium*; Elsevier Science Ltd, 2015.

(71) Jeurgens, L. P. H.; Sloof, W. G.; Tichelaar, F. D.; Mittemeijer, E. J. Growth Kinetics and Mechanisms of Aluminum-Oxide Films Formed by Thermal Oxidation of Aluminum. *J. Appl. Phys.* **2002**, *92* (3), 1649–1656.

(72) Jeurgens, L. P. H.; Sloof, W. G.; Tichelaar, F. D.; Mittemeijer, E. J. Thermodynamic Stability of Amorphous Oxide Films on Metals: Application to Aluminum Oxide Films on Aluminum Substrates. *Phys. Rev. B* **2000**, *62* (7), 4707–4719.

(73) Barthés-Labrousse, M. G. Mechanisms of Formation of the Interphase in Epoxy-Amine/Aluminium Joints. *J. Adhes.* **2012**, *88* (8), 699–719.

(74) Roberge, P. *Corrosion Engineering: Principles and Practice*; McGraw-Hill, 2008.

(75) Wen, J.; Wilkes, G. L. Organic/Inorganic Hybrid Network Materials by the Sol-Gel Approach. *Chem. Mater.* **1996**, *8* (8), 1667–1681.

(76) Chou, T. P.; Chandrasekaran, C.; Limmer, S. J.; Seraji, S.; Wu, Y.; Forbess, M. J.; Nguyen, C.; Cao, G. Z. Organic-Inorganic Hybrid Coatings for Corrosion Protection. *J. Non. Cryst. Solids* **2001**, *290* (2–3), 153–162.

(77) Raps, D.; Hack, T.; Wehr, J.; Zheludkevich, M. L.; Bastos, A. C.; Ferreira, M. G. S.; Nuyken, O. Electrochemical Study of Inhibitor-Containing Organic-Inorganic Hybrid Coatings on AA2024. *Corros. Sci.* **2009**, *51* (5), 1012–1021.

(78) Ni, H.; Skaja, A. D.; Sailer, R. A.; Soucek, M. D. Moisture-Curing Alkoxysilane-Functionalized Isocyanurate Coatings. *Macromol. Chem. Phys.* **2000**, *201* (6), 722–732.

(79) Shimizu, K.; Tokuta, Y.; Oishi, A.; Kuriyama, T.; Kunioka, M. Weatherability of Polypropylene by Accelerated Weathering Tests and Outdoor Exposure Tests in Japan. *J. Polym.* **2016**, *2016*, 1–14.

(80) Vogt, B. D.; Prabhu, V. M.; Soles, C. L.; Satija, S. K.; Lin, E. K.; Wu, W. L. Control of Moisture at Buried Polymer/Alumina Interfaces through Substrate Surface Modification. *Langmuir* **2005**, *21* (6), 2460–2464.

(81) Wang, P.; Schaefer, D. W. Why Does Silane Enhance the Protective Properties of Epoxy Films? *Langmuir* **2008**, *24* (23), 13496–13501.

(82) Karul, A.; Tan, K. T.; White, C. C.; Hunston, D. L.; Marshall, S. T.; Akgun, B.; Satija, S. K.; Soles, C. L.; Vogt, B. D. Impact of Polymer Modulus/Chain Mobility on Water Accumulation at Polymer/Metal Oxide Interfaces. *Polymer.* **2009**, *50* (14), 3234–3239.

(83) Wood, M. H.; Wood, T. J.; Welbourn, R. J. L.; Poon, J.; Madden, D. C.; Clarke, S. M. An X-Ray and Neutron Reflectometry Study of Iron Corrosion in Seawater. *Langmuir* **2018**, *34* (21), 5990–6002.

(84) Novoselov, K. S.; Jiang, D.; Schedin, F.; Booth, T. J.; Khotkevich, V. V.; Morozov, S. V.; Geim, A. K. Two-Dimensional Atomic Crystals. *Proc. Natl. Acad. Sci.* **2005**, *102* (30), 10451–10453.

(85) Geim, A. K.; Novoselov, K. S. The Rise of Graphene. *Nat. Mater.* **2007**, *6* (3), 183–191.

(86) Wang, X.; Li, J.; Zhong, Q.; Zhong, Y.; Zhao, M. Wafer-Scale Synthesis and Transfer of Monolayer Graphene. *Proc. IEEE Conf. Nanotechnol.* **2013**, 652–655.

(87) Li, X.; Rui, M.; Song, J.; Shen, Z.; Zeng, H. Carbon and Graphene Quantum Dots for Optoelectronic and Energy Devices: A Review. *Adv. Funct. Mater.* **2015**, *25* (31), 4929–4947.

(88) Schriver, M.; Regan, W.; Gannett, W. J.; Zaniewski, A. M.; Crommie, M. F.; Zettl, A. Graphene as a Long-Term Metal Oxidation Barrier: Worse than Nothing. *ACS Nano* **2013**, *7* (7), 5763–5768.

(89) Ramezanzadeh, B.; Niroumandrad, S.; Ahmadi, A.; Mahdavian, M.; Mohamadzadeh Moghadam, M. H. Enhancement of Barrier and Corrosion Protection Performance of an Epoxy Coating through Wet Transfer of Amino Functionalized Graphene Oxide. *Corros. Sci.* **2016**, *103*, 283–304.

(90) Singh Raman, R. K.; Tiwari, A. Graphene: The Thinnest Known Coating for Corrosion Protection. *Jom* **2014**, *66* (4), 637–642.

(91) Aneja, K. S.; Böhm, H. L. M.; Khanna, A. S.; Böhm, S. Functionalised Graphene as a Barrier against Corrosion. *FlatChem* **2017**, *1*, 11–19.

(92) Zhou, Y.; He, Q.; Zhang, F.; Yang, F.; Narayanan, S.; Yuan, G.; Dhinojwala, A.; Foster, M. D. Modifying Surface Fluctuations of Polymer Melt Films with Substrate Modification. *ACS Macro Lett.* **2017**, *6* (9), 915–919.

(93) Roe, R.-J. *Methods of X-Ray and Neutron Scattering in Polymer Science*; Oxford University Press, 2000.

(94) Holy, V.; Kubena, J.; Ohlidal, I.; Lischka, K.; Plotz, W. X-Ray Reflection from Rough Layered Systems. *Phys. Rev. B* **1993**, *47* (23), 15896–15903.

(95) Yoneda, Y. Anomalous Surface Reflection of X Rays. *Phys. Rev.* **1963**, *131* (5), 2010–2013.

(96) Croce, P.; Devant, G.; Sere, M. G.; Verhaeghe, M. F. Thin Film Surface Studies by X-Ray Reflection. *Surf. Sci.* **1970**, *22* (1), 173–186.

(97) Wong, P. Z.; Bray, A. J. Scattering by Rough Surfaces. *Phys. Rev. B* **1988**, *37* (13), 7751–7758.

(98) Pynn, R. Neutron Scattering by Rough Surfaces at Grazing Incidence. *Phys. Rev. B* **1992**, *45* (2), 602–612.

(99) Foster, M. D. X-Ray Scattering Methods for the Study of Polymer Interfaces. *Crit. Rev. Anal. Chem.* **1993**, *24* (3), 179–241.

(100) Press, W.; Tolan, M.; Stettner, J.; Seeck, O. H.; Schlomka, J. P.; Nitz, V.; Schwalowsky, L.; Müller-Buschbaum, P.; Bahr, D. Roughness of Surfaces and Interfaces. *Phys. B Condens. Matter* **1996**, *221* (1–4), 1–9.

(101) Seydel, T.; Madsen, A.; Sprung, M.; Tolan, M.; Grübel, G.; Press, W. Setup for in Situ Surface Investigations of the Liquid/Glass Transition with (Coherent) X Rays. *Rev. Sci. Instrum.* **2003**, *74* (9), 4033–4040.

(102) Leheny, R. L. XPCS: Nanoscale Motion and Rheology. *Curr. Opin. Colloid Interface Sci.* **2012**, *17* (1), 3–12.

(103) Riese, D. O.; Vos, W. L.; Wegdam, G. H.; Poelwijk, F. J.; Abernathy, D. L.; Grübel, G. *Photon Correlation Spectroscopy: X Rays versus Visible Light*; 2000; Vol. 61.

(104) Sutton, M.; Mochrie, S. G. J.; Greytak, T.; Nagler, S. E.; Berman, L. E.; Held, G. A.; Stephenson, G. B. Observation of Speckle by Diffraction with Coherent X-Rays. *Nature* **1991**, *352* (6336), 608–610.

(105) Nogales, A.; Fluerasu, A. X Ray Photon Correlation Spectroscopy for the Study of Polymer Dynamics. *Eur. Polym. J.* **2016**, *81*, 494–504.

(106) Cristofolini, L. Synchrotron X-Ray Techniques for the Investigation of Structures and Dynamics in Interfacial Systems. *Curr. Opin. Colloid Interface Sci.* **2014**, *19* (3), 228–241.

(107) Wang, S. F.; Jiang, Z.; Narayanan, S.; Foster, M. D. Dynamics of Surface Fluctuations on Macrocyclic Melts. *Macromolecules* **2012**, *45* (15), 6210–6219.

(108) Kim, H.; Rühm, A.; Lurio, L. B.; Basu, J. K.; Lal, J.; Lumma, D.; Mochrie, S. G. J.; Sinha, S. K. Surface Dynamics of Polymer Films. *Phys. Rev. Lett.* **2003**, *90* (6), 068302.

(109) Lin, N.; Huang, J.; Dufresne, A. Preparation, Properties and Applications of Polysaccharide Nanocrystals in Advanced Functional Nanomaterials: A Review. *Nanoscale* **2012**, *4* (11), 3274–3294.

(110) Katz, E.; Willner, I. Biomolecule-Functionalized Carbon Nanotubes: Applications in Nanobioelectronics. *ChemPhysChem* **2004**, *5* (8), 1084–1104.

(111) Méndez-Vilas, A.; Bruque, J. M.; González-Martín, M. L. Sensitivity of Surface Roughness Parameters to Changes in the Density of Scanning Points in Multi-Scale AFM Studies. Application to a Biomaterial Surface. *Ultramicroscopy* **2007**, *107* (8), 617–625.

(112) Novoselov, K. S.; Jiang, D.; Schedin, F.; Booth, T. J.; Khotkevich, V. V.; Morozov, S. V.; Geim, A. K. Two-Dimensional Atomic Crystals. *Proc. Natl. Acad. Sci.* **2005**, *102* (30), 10451–10453.

(113) Yoon, H.; Jang, J. Conducting-Polymer Nanomaterials for High-Performance Sensor Applications: Issues and Challenges. *Adv. Funct. Mater.* **2009**, *19* (10), 1567–1576.

(114) He, Q.; Zeng, Z.; Yin, Z.; Li, H.; Wu, S.; Huang, X.; Zhang, H. Fabrication of Flexible MoS2thin-Film Transistor Arrays for Practical Gas-Sensing Applications. *Small* **2012**, *8* (19), 2994–2999.

(115) Binnig, G.; Quate, C. F.; Gerber, C. Atomic Force Microscope. *Phys. Rev. Lett.* **1986**, *56* (9), 930–933.

(116) Akgun, B.; Lee, D. R.; Kim, H.; Zhang, H.; Prucker, O.; Wang, J.; Rühe, J.; Foster, M. D. Self-Affine Surfaces of Polymer Brushes. *Macromolecules* **2007**, *40* (17), 6361–6369.

(117) McLean, R. S.; Sauer, B. B. Tapping-Mode AFM Studies Using Phase Detection for Resolution of Nanophases in Segmented Polyurethanes and Other Block Copolymers. *Macromolecules* **1997**, *30* (26), 8314–8317.

(118) Stankovich, S.; Piner, R. D.; Chen, X.; Wu, N.; Nguyen, S. T.; Ruoff, R. S. Stable Aqueous Dispersions of Graphitic Nanoplatelets via the Reduction of Exfoliated Graphite Oxide in the Presence of Poly(Sodium 4-Styrenesulfonate). *J. Mater. Chem.* **2006**, *16* (2), 155–158.

(119) Harron, H. R.; Pritchard, R. G.; Cope, B. C.; Goddard, D. T. An Atomic Force Microscope (AFM) and Tapping Mode AFM Study of the Solvent-Induced Crystallization of Polycarbonate Thin Films. *J. Polym. Sci. Part B Polym. Phys.* **1996**, *34* (1), 173–180.

(120) Domke, J.; Radmacher, M. Measuring the Elastic Properties of Thin Polymer Films with the Atomic Force Microscope. *Langmuir* **1998**, *14* (12), 3320–3325.

(121) Velegol, S. B.; Logan, B. E. Contributions of Bacterial Surface Polymers, Electrostatics, and Cell Elasticity to the Shape of AFM Force Curves. *Langmuir* **2002**, *18* (13), 5256–5262.

(122) Boltau, M.; Walheim, S.; Mlynek, J.; Krausch, G.; Steiner, U. Surface-Induced Structure Formation of Polymer Blends on Patterned Substrates. *Nature* **1998**, *391* (6670), 877–879.

(123) Alsteens, D.; Gaub, H. E.; Newton, R.; Pfreundschuh, M.; Gerber, C.; Müller, D. J. Atomic Force Microscopy-Based Characterization and Design of Biointerfaces. *Nat. Rev. Mater.* **2017**, *2* (5), 17008.

(124) Black, J. M.; Zhu, M.; Zhang, P.; Unocic, R. R.; Guo, D.; Okatan, M. B.; Dai, S.; Cummings, P. T.; Kalinin, S. V.; Feng, G.; et al. Fundamental Aspects of Electric Double Layer Force-Distance Measurements at Liquid-Solid Interfaces Using Atomic Force Microscopy. *Sci. Rep.* **2016**, *6* (1), 32389.

(125) Dufrêne, Y. F.; Ando, T.; Garcia, R.; Alsteens, D.; Martinez-Martin, D.; Engel, A.; Gerber, C.; Müller, D. J. Imaging Modes of Atomic Force Microscopy for Application in Molecular and Cell Biology. *Nat. Nanotechnol.* **2017**, *12* (4), 295–307.

(126) Kang, H.; Qian, X.; Guan, L.; Zhang, M.; Li, Q.; Wu, A.; Dong, M. Studying the Adhesion Force and Glass Transition of Thin Polystyrene Films by Atomic Force Microscopy. *Nanoscale Res. Lett.* **2018**, *13* (1), 5.

(127) Tolan, M.; Seeck, O. H.; Schlomka, J. P.; Press, W.; Wang, J.; Sinha, S. K.; Li, Z.; Rafailovich, M. H.; Sokolov, J. Evidence for Capillary Waves on Dewetted Polymer Film Surfaces: A Combined X-Ray and Atomic Force Microscopy Study. *Phys. Rev. Lett.* **1998**, *81* (13), 2731–2734.

(128) Urquidi-Macdonald, M.; Real, S.; Macdonald, D. D. Applications of Kramers-Kronig Transforms in the Analysis of Electrochemical Impedance Data-III. Stability and Linearity. *Electrochim. Acta* **1990**, *35* (10), 1559–1566.

(129) Retter, U.; Lohse, H. Electrochemical Impedance Spectroscopy. In *Electroanalytical Methods: Guide to Experiments and Applications*; Springer Berlin Heidelberg: Berlin, Heidelberg, 2010; pp 159–177.

(130) Mansfeld, F.; Kendig, M. W.; Tsai, S. EVALUATION OF CORROSION BEHAVIOR OF COATED METALS WITH Ac IMPEDANCE MEASUREMENTS. *Corrosion* **1982**, *38* (9), 478–485.

(131) Aspnes, D. E. Spectroscopic Ellipsometry - Past, Present, and Future. *Thin Solid Films* **2014**, *571* (P3), 334–344.

(132) Jellison, G. E. Data Analysis for Spectroscopic Ellipsometry. *Thin Solid Films* **1993**, *234* (1–2), 416–422.

(133) Vedam, K. Spectroscopic Ellipsometry: A Historical Overview. *Thin Solid Films* **1998**, *313–314*, 1–9.

(134) Langereis, E.; Heil, S. B. S.; Knoops, H. C. M.; Keuning, W.; van de Sanden, M. C. M.; Kessels, W. M. M. In Situ Spectroscopic Ellipsometry as a Versatile Tool for Studying Atomic Layer Deposition. *J. Phys. D. Appl. Phys.* **2009**, *42* (7), 073001.

(135) Heller, E. J.; Yang, Y.; Kocia, L.; Chen, W.; Fang, S.; Borunda, M.; Kaxiras, E. Theory of Graphene Raman Scattering. *ACS Nano* **2016**, *10* (2), 2803–2818.

(136) Graf, D.; Molitor, F.; Ensslin, K.; Stampfer, C.; Jungen, A.; Hierold, C.; Wirtz, L. Raman Imaging of Graphene. *Solid State Commun.* **2007**, *143* (1–2), 44–46.

(137) Rümmeli, M. H.; Gorantla, S.; Bachmatiuk, A.; Phieler, J.; Geißler, N.; Ibrahim, I.; Pang, J.; Eckert, J. On the Role of Vapor Trapping for Chemical Vapor Deposition (CVD) Grown Graphene over Copper. *Chem. Mater.* **2013**, *25* (24), 4861–4866.

(138) Zhao, P.; Kumamoto, A.; Kim, S.; Chen, X.; Hou, B.; Chiashi, S.; Einarsson, E.; Ikuhara, Y.; Maruyama, S. Self-Limiting Chemical Vapor Deposition Growth of Monolayer Graphene from Ethanol. *J. Phys. Chem. C* **2013**, *117* (20), 10755–10763.

(139) Warner, J. H.; Schaffel, F.; Rummeli, M.; Bachmatiuk, A.; Schäffel, F.; Bachmatiuk, A.; Rümmeli, M. H. *Graphene Fundamentals and Emergent Applications*; Elsevier, 2013; Vol. 17.

(140) Pang, J.; Bachmatiuk, A.; Fu, L.; Yan, C.; Zeng, M.; Wang, J.; Trzebicka, B.; Gemming, T.; Eckert, J.; Rummeli, M. H. Oxidation as A Means to Remove Surface Contaminants on Cu Foil Prior to Graphene Growth by Chemical Vapor Deposition. *J. Phys. Chem. C* **2015**, *119* (23), 13363–13368.

(141) Pimenta, M. A.; Dresselhaus, G.; Dresselhaus, M. S.; Cançado, L. G.; Jorio, A.; Saito, R. Studying Disorder in Graphite-Based Systems by Raman Spectroscopy. *Phys. Chem. Chem. Phys.* **2007**, *9* (11), 1276–1290.

(142) Kalbac, M.; Kong, J.; Dresselhaus, M. S. Raman Spectroscopy as a Tool to Address Individual Graphene Layers in Few-Layer Graphene. *J. Phys. Chem. C* **2012**, *116* (35), 19046–19050.

(143) Cançado, L. G.; Reina, A.; Kong, J.; Dresselhaus, M. S. Geometrical Approach for the Study of G′ Band in the Raman Spectrum of Monolayer Graphene, Bilayer Graphene, and Bulk Graphite. *Phys. Rev. B* **2008**, *77* (24), 245408.

(144) Lee, J.-U.; Yoon, D.; Kim, H.; Lee, S. W.; Cheong, H. Thermal Conductivity of Suspended Pristine Graphene Measured by Raman Spectroscopy. *Phys. Rev. B* **2011**, *83* (8), 081419.

(145) Ni, Z. H.; Yu, T.; Luo, Z. Q.; Wang, Y. Y.; Liu, L.; Wong, C. P.; Miao, J.; Huang, W.; Shen, Z. X. Probing Charged Impurities in Suspended Graphene Using Raman Spectroscopy. *ACS Nano* **2009**, *3* (3), 569–574.

(146) Ferrari, A. C.; Meyer, J. C.; Scardaci, V.; Casiraghi, C.; Lazzeri, M.; Mauri, F.; Piscanec, S.; Jiang, D.; Novoselov, K. S.; Roth, S.; et al. Raman Spectrum of Graphene and Graphene Layers. *Phys. Rev. Lett.* **2006**, *97* (18), 187401.

(147) Ferrari, A. C. Raman Spectroscopy of Graphene and Graphite: Disorder, Electron–Phonon Coupling, Doping and Nonadiabatic Effects. *Solid State Commun.* **2007**, *143* (1–2), 47–57.

(148) Cançado, L. G.; Takai, K.; Enoki, T.; Endo, M.; Kim, Y. A.; Mizusaki, H.; Jorio, A.; Coelho, L. N.; Magalhães-Paniago, R.; Pimenta, M. A. General Equation for the Determination of the Crystallite Size La of Nanographite by Raman Spectroscopy. *Appl. Phys. Lett.* **2006**, *88* (16), 163106.

(149) Reina, A.; Jia, X.; Ho, J.; Nezich, D.; Son, H.; Bulovic, V.; Dresselhaus, M. S.; Kong, J. Large Area, Few-Layer Graphene Films on Arbitrary Substrates by Chemical Vapor Deposition. *Nano Lett.* **2009**, *9* (1), 30–35.

(150) Malard, L. M.; Pimenta, M. A.; Dresselhaus, G.; Dresselhaus, M. S. Raman Spectroscopy in Graphene. *Phys. Rep.* **2009**, *473* (5–6), 51–87.

(151) VanLandingham, M. R. Review of Instrumented Indentation. *J. Res. Natl. Inst. Stand. Technol.* **2003**, *108* (4), 249-265.

(152) Briscoe, B. J.; Fiori, L.; Pelillo, E. Nano-Indentation of Polymeric Surfaces. *J. Phys. D. Appl. Phys.* **1998**, *31*, 2395–2405.

(153) VanLandingham, M. R.; Villarrubia, J. S.; Guthrie, W. F.; Meyers, G. F. Nanoindentation of Polymers: An Overview. *Macromol. Symp.* **2001**, *167*, 15–43.

(154) Ion, R. H.; Pollock, H. M.; Roques-Carmes, C. Micron-Scale Indentation of Amorphous and Drawn PET Surfaces. *J. Mater. Sci.* **1990**, *25* (2), 1444–1454.

(155) Briscoe, B. J.; Savio Sebastian, K. The Elastoplastic Response of Poly(Methyl Methacrylate) to Indentation. *Proc. R. Soc. A Math. Phys. Eng. Sci.* **1996**, *452* (1946), 439–457.

(156) Burger, G. B.; Gupta, A. K.; Jeffrey, P. W.; Lloyd, D. J. Microstructural Control of Aluminum Sheet Used in Automotive Applications. *Mater. Charact.* **1995**, *35* (1), 23–39.

(157) Starke, E. A.; Staley, J. T. Application of Modern Aluminum Alloys to Aircraft. *Prog. Aerosp. Sci.* **1996**, *32* (2–3), 131–172.

(158) Nakai, M.; Eto, T. New Aspect of Development of High Strength Aluminum Alloys for Aerospace Applications. *Mater. Sci. Eng. A* **2000**, *285* (1–2), 62–68.

(159) Siva Kumar, C.; Mayanna, S. M.; Mahendra, K. N.; Sharma, A. K.; Uma Rani, R. Studies on White Anodizing on Aluminum Alloy for Space Applications. *Appl. Surf. Sci.* **1999**, *151* (3), 280–286.

(160) Rode, D. L.; Gaddam, V. R.; Yi, J. H. Subnanometer Surface Roughness of Dc Magnetron Sputtered Al Films. *J. Appl. Phys.* **2007**, *102* (2), 024303.

(161) Van Gils, S.; Dimogerontakis, T.; Buytaert, G.; Stijns, E.; Terryn, H.; Skeldon, P.; Thompson, G. E.; Alexander, M. R. Optical Properties of Magnetron-Sputtered and Rolled Aluminum. *J. Appl. Phys.* **2005**, *98* (8), 083505.

(162) Wendt, R.; Ellmer, K.; Wiesemann, K. Thermal Power at a Substrate during ZnO:Al Thin Film Deposition in a Planar Magnetron Sputtering System. *J. Appl. Phys.* **1997**, *82* (5), 2115–2122.

(163) Cremer, R.; Witthaut, M.; Neuschütz, D.; Erkens, G.; Leyendecker, T.; Feldhege, M. Comparative Characterization of Alumina Coatings Deposited by RF, DC and Pulsed Reactive Magnetron Sputtering. *Surf. Coatings Technol.* **1999**, *120–121*, 213–218.

(164) Nohava, J.; Dessarzin, P.; Karvankova, P.; Morstein, M. Characterization of Tribological Behavior and Wear Mechanisms of Novel Oxynitride PVD Coatings Designed for Applications at High Temperatures. *Tribol. Int.* **2015**, *81*, 231–239.

(165) Sanchette, F.; Ducros, C.; Billard, A.; Rébéré, C.; Berziou, C.; Reffass, M.; Creus, J. Nanostructured Aluminium Based Coatings Deposited by Electron-Beam Evaporative PVD. *Thin Solid Films* **2009**, *518* (5), 1575–1580.

(166) De Araujo, P.; Steyer, P.; Millet, J.-P.; Damond, E.; Stauder, B.; Jacquot, P. PVD Aluminium Alloy Coatings: Environmentally Friendly Alternative to Protect Steel Parts Against Corrosion. *Surf. Eng.* **2003**, *19* (4), 304–309.

(167) Thornton, J. A. Influence of Apparatus Geometry and Deposition Conditions on the Structure and Topography of Thick Sputtered Coatings. *J. Vac. Sci. Technol.* **1974**, *11* (4), 666–670.

(168) Thornton, J. A. Influence of Substrate Temperature and Deposition Rate on Structure of Thick Sputtered Cu Coatings. *J. Vac. Sci. Technol.* **1975**, *12* (4), 830–835.

(169) Patten, J. W. The Influence of Surface Topography and Angle of Adatom Incidence on Growth Structure in Sputtered Chromium. *Thin Solid Films* **1979**, *63* (1), 121–129.

(170) Clapeyron, B. E. Memoire Sur La Puissance Motrice de La Chaleur. *J. l'Ecole R. Polytech.* **1834**, *23* (14), 153–190.

(171) Hodgkin, J. H.; Simon, G. P.; Varley, R. J. Thermoplastic Toughening of Epoxy Resins: A Critical Review. *Polym. Adv. Technol.* **1998**, *9* (1), 3–10.

(172) Ramezanzadeh, B.; Niroumandrad, S.; Ahmadi, A.; Mahdavian, M.; Mohamadzadeh Moghadam, M. H. Enhancement of Barrier and Corrosion Protection Performance of an Epoxy Coating through Wet Transfer of Amino Functionalized Graphene Oxide. *Corros. Sci.* **2016**, *103*, 283–304.

(173) Ramezanzadeh, B.; Raeisi, E.; Mahdavian, M. Studying Various Mixtures of 3-Aminopropyltriethoxysilane (APS) and Tetraethylorthosilicate (TEOS) Silanes on the Corrosion Resistance of Mild Steel and Adhesion Properties of Epoxy Coating. *Int. J. Adhes. Adhes.* **2015**, *63*, 166–176.

(174) Mišković-Stanković, V. B. The Mechanism of Cathodic Electrodeposition of Epoxy Coatings and the Corrosion Behaviour of the Electrodeposited Coatings. *J. Serbian Chem. Soc.* **2002**, *67* (5), 305–324.

(175) Sangermano, M.; Calvara, L.; Chiavazzo, E.; Ventola, L.; Asinari, P.; Mittal, V.; Rizzoli, R.; Ortolani, L.; Morandi, V. Enhancement of Electrical and Thermal Conductivity of Su-8 Photocrosslinked Coatings Containing Graphene. *Prog. Org. Coatings* **2015**, *86*, 143–146.

(176) Wang, D.; Bierwagen, G. P. Sol-Gel Coatings on Metals for Corrosion Protection. *Prog. Org. Coatings* **2009**, *64* (4), 327–338.

(177) Twite, R. L.; Bierwagen, G. P. Review of Alternatives to Chromate for Corrosion Protection of Aluminum Aerospace Alloys. *Prog. Org. Coatings* **1998**, *33* (2), 91–100.

(178) Vosgien Lacombre, C.; Bouvet, G.; Trinh, D.; Mallarino, S.; Touzain, S. Water Uptake in Free Films and Coatings Using the Brasher and Kingsbury Equation: A Possible Explanation of the Different Values Obtained by Electrochemical Impedance Spectroscopy and Gravimetry. *Electrochim. Acta* **2017**, *231*, 162–170.

(179) Li, X.; Zhu, Y.; Cai, W.; Borysiak, M.; Han, B.; Chen, D.; Piner, R. D.; Colomba, L.; Ruoff, R. S. Transfer of Large-Area Graphene Films for High-Performance Transparent Conductive Electrodes. *Nano Lett.* **2009**, *9* (12), 4359–4363.

(180) Zhang, Z.; Du, J.; Zhang, D.; Sun, H.; Yin, L.; Ma, L.; Chen, J.; Ma, D.; Cheng, H. M.; Ren, W. Rosin-Enabled Ultraclean and Damage-Free Transfer of Graphene for Large-Area Flexible Organic Light-Emitting Diodes. *Nat. Commun.* **2017**, *8*, 14560.

(181) Lu, W.; Zeng, M.; Li, X.; Wang, J.; Tan, L.; Shao, M.; Han, J.; Wang, S.; Yue, S.; Zhang, T.; et al. Controllable Sliding Transfer of Wafer-Size Graphene. *Adv. Sci.* **2016**, *3* (9), 1600006.

(182) Gao, L.; Ni, G. X.; Liu, Y.; Liu, B.; Castro Neto, A. H.; Loh, K. P. Face-to-Face Transfer of Wafer-Scale Graphene Films. *Nature* **2014**, *505* (7482), 190–194.

(183) Dreyer, D. R.; Park, S.; Bielawski, C. W.; Ruoff, R. S. The Chemistry of Graphene Oxide. *Chem. Soc. Rev.* **2010**, *39* (1), 228–240.

(184) Stankovich, S.; Dikin, D. A.; Piner, R. D.; Kohlhaas, K. A.; Kleinhammes, A.; Jia, Y.; Wu, Y.; Nguyen, S. B. T.; Ruoff, R. S. Synthesis of Graphene-Based Nanosheets via Chemical Reduction of Exfoliated Graphite Oxide. *Carbon N. Y.* **2007**, *45* (7), 1558–1565.

(185) Emtsev, K. V.; Bostwick, A.; Horn, K.; Jobst, J.; Kellogg, G. L.; Ley, L.; McChesney, J. L.; Ohta, T.; Reshanov, S. A.; Röhrl, J.; et al. Towards Wafer-Size Graphene Layers by Atmospheric Pressure Graphitization of Silicon Carbide. *Nat. Mater.* **2009**, *8* (3), 203–207.

(186) Berger, C.; Song, Z.; Li, X.; Wu, X.; Brown, N.; Naud, C.; Mayou, D.; Li, T.; Hass, J.; Marchenkov, A. N.; et al. Electronic Confinement and Coherence in Patterned Epitaxial Graphene. *Science.* **2006**, *312* (5777), 1191–1196.

(187) Ismach, A.; Druzgalski, C.; Penwell, S.; Schwartzberg, A.; Zheng, M.; Javey, A.; Bokor, J.; Zhang, Y. Direct Chemical Vapor Deposition of Graphene on Dielectric Surfaces. *Nano Lett.* **2010**, *10* (5), 1542–1548.

(188) Kim, H.; Song, I.; Park, C.; Son, M.; Hong, M.; Kim, Y.; Kim, J. S.; Shin, H. J.; Baik, J.; Choi, H. C. Copper-Vapor-Assisted Chemical Vapor Deposition for High-Quality and Metal-Free Single-Layer Graphene on Amorphous SiO_2 substrate. *ACS Nano* **2013**, *7* (8), 6575–6582.

(189) Zeng, M.; Tan, L.; Wang, J.; Chen, L.; Rümmeli, M. H.; Fu, L. Liquid Metal: An Innovative Solution to Uniform Graphene Films. *Chem. Mater.* **2014**, *26* (12), 3637–3643.

(190) Wang, H.; Wang, G.; Bao, P.; Yang, S.; Zhu, W.; Xie, X.; Zhang, W. J. Controllable Synthesis of Submillimeter Single-Crystal Monolayer Graphene Domains on Copper Foils by Suppressing Nucleation. *J. Am. Chem. Soc.* **2012**, *134* (8), 3627–3630.

(191) Geng, D.; Wang, H.; Yu, G. Graphene Single Crystals: Size and Morphology Engineering. *Adv. Mater.* **2015**, *27* (18), 2821–2837.

(192) Wu, W.; Jauregui, L. A.; Su, Z.; Liu, Z.; Bao, J.; Chen, Y. P.; Yu, Q. Growth of Single Crystal Graphene Arrays by Locally Controlling Nucleation on Polycrystalline Cu Using Chemical Vapor Deposition. *Adv. Mater.* **2011**, *23* (42), 4898–4903.

(193) Singla, S.; Anim-Danso, E.; Islam, A. E.; Ngo, Y.; Kim, S. S.; Naik, R. R.; Dhinojwala, A. Insight on Structure of Water and Ice next to Graphene Using Surface-Sensitive Spectroscopy. *ACS Nano* **2017**, *11* (5), 4899–4906.

(194) Shimizu, K.; Tokuta, Y.; Oishi, A.; Kuriyama, T.; Kunioka, M. Weatherability of Polypropylene by Accelerated Weathering Tests and Outdoor Exposure Tests in Japan. *J. Polym.* **2016**, *2016*, 1–14.

(195) Nguyen, A. S.; Causse, N.; Musiani, M.; Orazem, M. E.; Pébère, N.; Tribollet, B.; Vivier, V. Determination of Water Uptake in Organic Coatings Deposited on 2024 Aluminium Alloy: Comparison between Impedance Measurements and Gravimetry. *Prog. Org. Coatings* **2017**, *112*, 93–100.

(196) Wang, P.; Schaefer, D. W. Salt Exclusion in Silane-Laced Epoxy Coatings. *Langmuir* **2010**, *26* (1), 234–240.

(197) Pan, G.; Yim, H.; Kent, M. S.; Majewski, J.; Schaefer, D. W. Neutron Reflectivity Investigation of Bis-Amino Silane Films. *J. Adhes. Sci. Technol.* **2003**, *17* (16), 2175–2189.

(198) Wang, Y.; Wang, P.; Kohls, D.; Hamilton, W. A.; Schaefer, D. W. Water Absorption and Transport in Bis-Silane Films. *Phys. Chem. Chem. Phys.* **2009**, *11* (1), 161–166.

(199) Zhou, Q.; Wang, Y. Comparisons of Clear Coating Degradation in NaCl Solution and Pure Water. *Prog. Org. Coatings* **2013**, *76* (11), 1674–1682.

(200) Dornbusch, M.; Kirsch, S.; Henzel, C.; Deschamps, C.; Overmeyer, S.; Cox, K.; Wiedow, M.; Tromsdorf, U.; Dargatz, M.; Meisenburg, U. Characterization of the Water Uptake and Electrolyte Uptake of Organic Coatings and the Consequences by Means of Electrochemical Impedance Spectroscopy and UV-Vis Spectroscopy. *Prog. Org. Coatings* **2015**, *89*, 332–343.

(201) Perez, C.; Collazo, A.; Izquierdo, M.; Merino, P.; Novoa, X. R. Characterisation of the Barrier Properties of Different Paint Systems. Part I. Experimental Set-up and Ideal Fickian Diffusion. *Prog. Org. Coatings* **1999**, *36* (1), 102–108.

(202) Pérez, C.; Collazo, A.; Izquierdo, M.; Merino, P.; Nóvoa, X. R. Characterisation of the Barrier Properties of Different Paint Systems. Part II. Non-Ideal Diffusion and Water Uptake Kinetics. *Prog. Org. Coatings* **1999**, *37* (3), 169–177.

(203) Zhang, J. T.; Hu, J. M.; Zhang, J. Q.; Cao, C. N. Studies of Impedance Models and Water Transport Behaviors of Polypropylene Coated Metals in NaCl Solution. *Prog. Org. Coatings* **2004**, *49* (4), 293–301.

(204) Zhang, J. T.; Hu, J. M.; Zhang, J. Q.; Cao, C. N. Studies of Water Transport Behavior and Impedance Models of Epoxy-Coated Metals in NaCl Solution by EIS. *Prog. Org. Coatings* **2004**, *51* (2), 145–151.

(205) Hu, J. M.; Zhang, J. Q.; Cao, C. N. Determination of Water Uptake and Diffusion of Cl-Ion in Epoxy Primer on Aluminum Alloys in NaCl Solution by Electrochemical Impedance Spectroscopy. *Prog. Org. Coatings* **2003**, *46* (4), 273–279.

(206) Maile, F. J.; Schauer, T.; Eisenbach, C. D. Evaluation of the Delamination of Coatings with Scanning Reference Electrode Technique. *Prog. Org. Coatings* **2000**, *38* (2), 117–120.

(207) Popov, B. N. Using Electrochemical Impedance Spectroscopy as a Tool for Organic Coating Solute Saturation Monitoring. *J. Electrochem. Soc.* **1993**, *140* (4), 947.

(208) Scully, J. R. Electrochemical Impedance of Organic-Coated Steel: Correlation of Impedance Parameters with Long-Term Coating Deterioration. *J. Electrochem. Soc.* **1989**, *136* (4), 979-990.

(209) Walter, G. W. A Critical Review of the Protection of Metals by Paints. *Corros. Sci.* **1986**, *26* (1), 27–38.

(210) Ding, R.; Cong, W. wei; Jiang, J. ming; Gui, T. jiang. Study of Impedance Model and Water Transport Behavior of Modified Solvent-Free Epoxy Anti-Corrosion Coating by EIS II. *J. Coatings Technol. Res.* **2016**, *13* (6), 501–515.

(211) Ghojavand, S.; Arefinia, R.; Sahrayi, H. On the Diffusion Phenomenon of Solvent within Polymeric Coatings: Development of a New Model. *Prog. Org. Coatings* **2016**, *97*, 301–306.

(212) Stein, W. D. *Transport and Diffusion across Cell Membranes*, 1st ed.; Elsevier Science, 1986.

(213) Zhang, Q.; Wu, T.; Chen, C.; Mukamel, S.; Zhuang, W. Molecular Mechanism of Water Reorientational Slowing down in Concentrated Ionic Solutions. *Proc. Natl. Acad. Sci.* **2017**, *114* (38), 10023–10028.

(214) Coniglio, N.; Nguyen, K.; Kurji, R.; Gamboa, E. Characterizing Water Sorption in 100% Solids Epoxy Coatings. *Prog. Org. Coatings* **2013**, *76* (9), 1168–1177.

(215) Hu, J. M.; Zhang, J. Q.; Cao, C. N. Determination of Water Uptake and Diffusion of Cl-Ion in Epoxy Primer on Aluminum Alloys in NaCl Solution by Electrochemical Impedance Spectroscopy. *Prog. Org. Coatings* **2003**, *46* (4), 273–279.

(216) Wang, H.; Zhou, Q. Evaluation and Failure Analysis of Linseed Oil Encapsulated Self-Healing Anticorrosive Coating. *Prog. Org. Coatings* **2018**, *118*, 108–115.

(217) Brasher, D. M.; Kingsbury, A. H. Electrical Measurements in the Study of Immersed Paint Coatings on Metal. I. Comparison between Capacitance and Gravimetric Methods of Estimating Water-Uptake. *J. Appl. Chem.* **2007**, *4* (2), 62–72.

(218) Malaquin, L.; Charitat, T.; Daillant, J. Supported Bilayers: Combined Specular and Diffuse X-Ray Scattering. *Eur. Phys. J. E* **2010**, *31* (3), 285–301.

(219) Wacklin, H. P. Neutron Reflection from Supported Lipid Membranes. *Curr. Opin. Colloid Interface Sci.* **2010**, *15* (6), 445–454.

(220) Schneck, E.; Demé, B.; Gege, C.; Tanaka, M. Membrane Adhesion via Homophilic Saccharide-Saccharide Interactions Investigated by Neutron Scattering. *Biophys. J.* **2011**, *100* (9), 2151–2159.

(221) Jablin, M. S.; Zhernenkov, M.; Toperverg, B. P.; Dubey, M.; Smith, H. L.; Vidyasagar, A.; Toomey, R.; Hurd, A. J.; Majewski, J. In-Plane Correlations in a Polymer-Supported Lipid Membrane Measured by off-Specular Neutron Scattering. *Phys. Rev. Lett.* **2011**, *106* (13), 138101.

(222) Hemmerle, A.; Malaquin, L.; Charitat, T.; Lecuyer, S.; Fragneto, G.; Daillant, J. Controlling Interactions in Supported Bilayers from Weak Electrostatic Repulsion to High Osmotic Pressure. *Proc. Natl. Acad. Sci.* **2012**, *109* (49), 19938–19942.

(223) Alsop, R. J.; Armstrong, C. L.; Maqbool, A.; Toppozini, L.; Dies, H.; Rheinstädter, M. C. Cholesterol Expels Ibuprofen from the Hydrophobic Membrane Core and Stabilizes Lamellar Phases in Lipid Membranes Containing Ibuprofen. *Soft Matter* **2015**, *11* (24), 4756–4767.

(224) Penfold, J.; Thomas, R. K. The Application of the Specular Reflection of Neutrons to the Study of Surfaces and Interfaces. *J. Phys. Condens. Matter* **1990**, *2* (6), 1369–1412.

(225) Chakhalian, J.; Freeland, J. W.; Srajer, G.; Strempfer, J.; Khaliullin, G.; Cezar, J. C.; Charlton, T.; Dalgliesh, R.; Bernhard, C.; Cristiani, G.; et al. Magnetism at the Interface between Ferromagnetic and Superconducting Oxides. *Nat. Phys.* **2006**, *2* (4), 244–248.

(226) Stahn, J.; Chakhalian, J.; Niedermayer, C.; Hoppler, J.; Gutberlet, T.; Voigt, J.; Treubel, F.; Habermeier, H. U.; Cristiani, G.; Keimer, B.; et al. Magnetic Proximity Effect in Perovskite Superconductor/Ferromagnet Multilayers. *Phys. Rev. B - Condens. Matter Mater. Phys.* **2005**, *71* (14), 140509.

(227) Nieh, M.-P.; Glinka, C. J.; Krueger, S.; Prosser, R. S.; Katsaras, J. SANS Study of the Structural Phases of Magnetically Alignable Lanthanide-Doped Phospholipid Mixtures. *Langmuir* **2001**, *17* (9), 2629–2638.

(228) Nieh, M. P.; Glinka, C. J.; Krueger, S.; Scott Prosser, R.; Katsaras, J. SANS Study on the Effect of Lanthanide Ions and Charged Lipids on the Morphology of Phospholipid Mixtures. *Biophys. J.* **2002**, *82* (5), 2487–2498.

(229) Datta, S. A. K.; Curtis, J. E.; Ratcliff, W.; Clark, P. K.; Crist, R. M.; Lebowitz, J.; Krueger, S.; Rein, A. Conformation of the HIV-1 Gag Protein in Solution. *J. Mol. Biol.* **2007**, *365* (3), 812–824.

(230) Castellanos, M. M.; Clark, N. J.; Watson, M. C.; Krueger, S.; McAuley, A.; Curtis, J. E. Role of Molecular Flexibility and Colloidal Descriptions of Proteins in Crowded Environments from Small-Angle Scattering. *J. Phys. Chem. B* **2016**, *120* (49), 12511–12518.

(231) Zhang, W.; Shen, H.; Guralnick, B. W.; Kirby, B. J.; Nguyen, N. A.; Remy, R.; Majkrzak, C. F.; Mackay, M. E. Correlation between Morphology and Device Performance of PBTTT:PC71BM Solar Cells. *Sol. Energy Mater. Sol. Cells* **2016**, *155*, 387–396.

(232) Prasai, D.; Tuberquia, J. C.; Harl, R. R.; Jennings, G. K.; Bolotin, K. I. Graphene: Corrosion-Inhibiting Coating. *ACS Nano* **2012**, *6* (2), 1102–1108.

(233) Shimizu, K.; Tokuta, Y.; Oishi, A.; Kuriyama, T.; Kunioka, M. Weatherability of Polypropylene by Accelerated Weathering Tests and Outdoor Exposure Tests in Japan. *J. Polym.* **2016**, *2016*, 1–14.

(234) Esfahani, Z.; Rahimi, E.; Sarvghad, M.; Rafsanjani-Abbasi, A.; Davoodi, A. Correlation between the Histogram and Power Spectral Density Analysis of AFM and SKPFM Images in an AA7023/AA5083 FSW Joint. *J. Alloys Compd.* **2018**, *744*, 174–181.

(235) Senthilkumar, M.; Sahoo, N. K.; Thakur, S.; Tokas, R. B. Characterization of Microroughness Parameters in Gadolinium Oxide Thin Films: A Study Based on Extended Power Spectral Density Analyses. *Appl. Surf. Sci.* **2005**, *252* (5), 1608–1619.

(236) Gavrila, R.; Dinescu, A.; Mardare, D. AFM Applications to the Study of Thin Films Morphology: A Power Spectral Density Approach. In *Proceedings of the International Semiconductor Conference, CAS*; IEEE, 2007; Vol. 1, pp 167–170.

(237) Marx, E.; Malik, I. J.; Strausser, Y. E.; Bristow, T.; Poduje, N.; Stover, J. C. Power Spectral Densities: A Multiple Technique Study of Different Si Wafer Surfaces. *J. Vac. Sci. Technol. B Microelectron. Nanom. Struct.* **2002**, *20* (1), 31-41.

(238) Gong, Y.; Misture, S. T.; Gao, P.; Mellott, N. P. Surface Roughness Measurements Using Power Spectrum Density Analysis with Enhanced Spatial Correlation Length. *J. Phys. Chem. C* **2016**, *120* (39), 22358–22364.

(239) Karapetrova, E.; Ice, G.; Tischler, J.; Hong, H.; Zschack, P. Design and Performance of the 33-BM Beamline at the Advanced Photon Source. *Nucl. Instruments Methods Phys. Res. Sect. A Accel. Spectrometers, Detect. Assoc. Equip.* **2011**, *649* (1), 52–54.

(240) Parratt, L. G. Surface Studies of Solids by Total Reflection of X-Rays. *Phys. Rev.* **1954**, *95* (2), 359–369.

(241) Yoneda, Y. Anomalous Surface Reflection of X Rays. *Phys. Rev.* **1963**, *131* (5), 2010–2013.

(242) Reiter, G. Dewetting as a Probe of Polymer Mobility in Thin Films. *Macromolecules* **1994**, *27* (11), 3046–3052.

(243) Kim, H.; Zhang, H.; Narayanan, S.; Wang, J.; Prucker, O.; Rühe, J.; Foster, M. D. Surface Fluctuations of Polymer Brushes Probed by Diffuse X-Ray Scattering. *Polymer.* **2005**, *46* (7), 2331–2337.

(244) Lee, D.; Park, Y. Nonspecular X-Ray-Reflectivity Study of Partially Correlated Interface Roughness of a Mo/Si Multilayer. *Phys. Rev. B - Condens. Matter Mater. Phys.* **1998**, *57* (15), 8786–8789.

(245) Jiang, J. S.; Pearson, J. E.; Liu, Z. Y.; Kabius, B.; Trasobares, S.; Miller, D. J.; Bader, S. D.; Lee, D. R.; Haskel, D.; Srajer, G.; et al. Improving Exchange-Spring Nanocomposite Permanent Magnets. *Appl. Phys. Lett.* **2004**, *85* (22), 5293–5295.

(246) He, Q.; Narayanan, S.; Wu, D. T.; Foster, M. D. Confinement Effects with Molten Thin Cyclic Polystyrene Films. *ACS Macro Lett.* **2016**, *5* (9), 999–1003.

(247) Jiang, N.; Sen, M.; Endoh, M. K.; Koga, T.; Langhammer, E.; Bjöörn, P.; Tsige, M. Thermal Properties and Segmental Dynamics of Polymer Melt Chains Adsorbed on Solid Surfaces. *Langmuir* **2018**, *34* (14), 4199–4209.

(248) Tidswell, I. M.; Rabedeau, T. A.; Pershan, P. S.; Kosowsky, S. D. Complete Wetting of a Rough Surface: An x-Ray Study. *Phys. Rev. Lett.* **1991**, *66* (16), 2108–2111.

(249) Tolan, M.; Vacca, G.; Wang, J.; Sinha, S. K.; Li, Z.; Rafailovich, M. H.; Sokolov, J.; Gibaud, A.; Lorenz, H.; Kotthaus, J. P. Thin Polymer Films on Rough Surfaces. *Phys. B Condens. Matter* **1996**, *221* (1–4), 53–59.

(250) Wang, J.; Tolan, M.; Seeck, O. H.; Sinha, S. K.; Bahr, O.; Rafailovich, M. H.; Sokolov, J. Surfaces of Strongly Confined Polymer Thin Films Studied by X-Ray Scattering. *Phys. Rev. Lett.* **1999**, *83* (3), 564–567.

(251) Seeck, O. H.; Müller-Buschbaum, P.; Tolan, M.; Press, W. Diffuse X-Ray Scattering in Specular Direction: Analysis of a Wetting Film. *Epl* **1995**, *29* (9), 699–704.

(252) Zhang, F.; He, Q.; Zhou, Y.; Narayanan, S.; Wang, C.; Vogt, B. D.; Foster, M. D. Anomalous Confinement Slows Surface Fluctuations of Star Polymer Melt Films. *ACS Macro Lett.* **2018**, *7* (7), 834–839.

(253) Koga, T.; Jiang, N.; Gin, P.; Endoh, M. K.; Narayanan, S.; Lurio, L. B.; Sinha, S. K. Impact of an Irreversibly Adsorbed Layer on Local Viscosity of Nanoconfined Polymer Melts. *Phys. Rev. Lett.* **2011**, *107* (22), 225901.

(254) Fujii, Y.; Yang, Z.; Leach, J.; Atarashi, H.; Tanaka, K.; Tsui, O. K. C. Affinity of Polystyrene Films to Hydrogen-Passivated Silicon and Its Relevance to the T_g of the Films. *Macromolecules* **2009**, *42* (19), 7418–7422.

(255) Napolitano, S.; Wübbenhorst, M. The Lifetime of the Deviations from Bulk Behaviour in Polymers Confined at the Nanoscale. *Nat. Commun.* **2011**, *2* (1), 260.

(256) Napolitano, S.; Sferrazza, M. How Irreversible Adsorption Affects Interfacial Properties of Polymers. *Adv. Colloid Interface Sci.* **2017**, *247*, 172–177.

(257) Yan, Z.; Lin, J.; Peng, Z.; Sun, Z.; Zhu, Y.; Li, L.; Xiang, C.; Samuel, E. L.; Kittrell, C.; Tour, J. M. Toward the Synthesis of Wafer-Scale Single-Crystal Graphene on Copper Foils. *ACS Nano* **2012**, *6* (10), 9110–9117.

(258) Li, X.; Cai, W.; An, J.; Kim, S.; Nah, J.; Yang, D.; Piner, R.; Velamakanni, A.; Jung, I.; Tutuc, E.; et al. Large-Area Synthesis of High-Quality and Uniform Graphene Films on Copper Foils. *Science* **2009**, *324* (5932), 1312–1314.

(259) Plazek, D. J.; O'Rourke, V. M. Viscoelastic Behavior of Low Molecular Weight Polystyrene. *J. Polym. Sci. Part A-2 Polym. Phys.* **1971**, *9* (2), 209–243.

(260) Carrillo, J.-M. Y.; Cheng, S.; Kumar, R.; Goswami, M.; Sokolov, A. P.; Sumpter, B. G. Untangling the Effects of Chain Rigidity on the Structure and Dynamics of Strongly Adsorbed Polymer Melts. *Macromolecules* **2015**, *48* (12), 4207–4219.

(261) Gin, P.; Jiang, N.; Liang, C.; Taniguchi, T.; Akgun, B.; Satija, S. K.; Endoh, M. K.; Koga, T. Revealed Architectures of Adsorbed Polymer Chains at Solid-Polymer Melt Interfaces. *Phys. Rev. Lett.* **2012**, *109* (26), 265501.

(262) Housmans, C.; Sferrazza, M.; Napolitano, S. Kinetics of Irreversible Chain Adsorption. *Macromolecules* **2014**, *47* (10), 3390–3393.

(263) Jiang, N.; Shang, J.; Di, X.; Endoh, M. K.; Koga, T. Formation Mechanism of High-Density, Flattened Polymer Nanolayers Adsorbed on Planar Solids. *Macromolecules* **2014**, *47* (8), 2682–2689.

(264) Negash, S.; Tatek, Y. B.; Tsige, M. Effect of Tacticity on the Structure and Glass Transition Temperature of Polystyrene Adsorbed onto Solid Surfaces. *J. Chem. Phys.* **2018**, *148* (13), 134705.

(265) Bhushan, B.; Li, X. Micromechanical and Tribological Characterization of Doped Single-Crystal Silicon and Polysilicon Films for Microelectromechanical Systems Devices. *J. Mater. Res.* **1997**, *12* (1), 54–63.

(266) Du, B.; Tsui, O. K. C.; Zhang, Q.; He, T. Study of Elastic Modulus and Yield Strength of Polymer Thin Films Using Atomic Force Microscopy. *Langmuir* **2001**, *17* (11), 3286–3291.

(267) Stankovich, S.; Dikin, D. A.; Dommett, G. H. B.; Kohlhaas, K. M.; Zimney, E. J.; Stach, E. A.; Piner, R. D.; Nguyen, S. B. T.; Ruoff, R. S. Graphene-Based Composite Materials. *Nature* **2006**, *442* (7100), 282–286.

(268) Novoselov, K. S.; Geim, A. K.; Morozov, S. V.; Jiang, D.; Zhang, Y.; Dubonos, S. V.; Grigorieva, I. V.; Firsov, A. A. Electric Field in Atomically Thin Carbon Films. *Science.* **2004**, *306* (5696), 666–669.

APPENDICES

APPENDIX A

MATLAB CODE FOR ROCKING CURVE FITTING FROM JIANG ZHANG

```
% --- simulate rocking curves
% capillary wave + bending rigidity
clear all;

global logFlag

%% some constants
% some constant
kb       = 1.3806503e-23;          % Boltzmann constant (SI unit)
planck  = 6.626068E-34 ;           % Planck constant
sol       = 299792458;              % Speed of light
ec        = 1.60217646E-19;        % Elementary charge
re        = 2.8179e-15;             % Thomson constant (m)
euler    = 0.5772;                  % Euler constant

%% setup
xenergy = 12;                                                   % x-ray energy (keV)
lambda  = double(planck*sol/(xenergy*1000.0*ec)*1e10);    % wavelength (A)
k       = 2*pi/lambda;                                          % wave vector

%% load data
s=xlsread('File_Name.xlsx');      %data file
roi1 = s(:,66);
roi2 = s(:,42);
I0 = s(:,65);

qx = s(:,1);
```

```
theta = s(:,5);
qz = mean(s(:,3),'omit');
twotheta = mean(s(:,4),'omit');

roi12 = roi1-roi2;
I = (roi1-roi2)./I0;

sigma_roi12 = sqrt(roi1+roi2);
sigma_I = sqrt( (sigma_roi12./roi12).^2 + (sqrt(I0)./I0 ).^2 ) .* I;

qxthetaI = [qx,theta,I,sigma_I];
qxthetaI(I<=0,:) = [];

figure
errorbar(theta,I,sigma_I,'o-');
set(gca,'yscale','log');

%% geometric correction for rocking scan
Ls = 4*32;                                          % sample length mm
Lb = 0.1;                                           % beam size  mm;
footprint_angle = asind(Lb/Ls);
f = sind(footprint_angle)./sind(qxthetaI(:,2));
f(theta<footprint_angle) = 1;

qxthetaI_corr = qxthetaI;
qxthetaI_corr(:,3:4) = qxthetaI(:,3:4)./repmat(f,1,2);

figure
hold on;
plot(qxthetaI_corr(:,1),qxthetaI_corr(:,3),'o-');
plot(-qxthetaI_corr(:,1),qxthetaI_corr(:,3),'s-');
set(gca,'yscale','log')
set(gca,'xscale','log')

%% choose side for fitting
sL = qxthetaI_corr;
sL(:,1) = -sL(:,1);
```

```
sL(sL(:,1)<=0,:) = [];
sL = flipud(sL);


sR = qxthetaI_corr;
sR(sR(:,1)<=0,:) = [];


figure
hold on; box on;
plot(sL(:,1),sL(:,3));
plot(sR(:,1),sR(:,3));

set(gca,'yscale','log')
set(gca,'xscale','log')

sFit = sL;                  % sR right side; sL left side

%% sample properties
rho_al          = 2.7;                    % mass density of al substrate
rho_al2o3       = 3.95;                 % mass density of al2o3 film
al2o3           = refrac('Al2O3',xenergy,rho_al2o3);
al              = refrac('Al',xenergy,rho_al);
n               = 1 - al.dispersion + 1i*al.absorption;


res_qx            = 2.5e-5;                % qx resolution : A^-1
zeta              = 2e3;                   % effective self affine correlation length (A)
h                 = 0.7;                   % self affine Hurst parameter
r0                = 1.4;                   % molecular distance
sigma_film        = 7.8237170549775;       % film roughness
I0                = .02;

%% initialize fitting
% define fit range
fRange = 1:size(sFit,1);
```

```
qx          = sFit(:,1);
Intens      = sFit(:,3);

% --- calculate incident and exit angle
alpha   = sFit(:,2);
beta    = twotheta-alpha;

% --- calculate transimittion coefficents
Ti2    = abs(2*sind(alpha)./( sind(alpha) + sqrt( n^2-cosd(alpha).^2) )).^2;
Tf2    = abs(2*sind(beta) ./( sind(beta)  + sqrt( n^2-cosd(beta).^2)  )).^2;
Ti2Tf2  = Ti2.*Tf2;

% --- Fresnel reflection critical angle
qc      = 2*k*sqrt(2*real(1-n));

% -- simulation
qx_sim          = logspace(-6,-2.5,200)';
alpha_sim       = asind(qx_sim/qz) + twotheta/2;
beta_sim        = twotheta - alpha_sim;
Ti2_sim         = abs(2*sind(alpha_sim)./( sind(alpha_sim) + sqrt( n^2-
cosd(alpha_sim).^2) )).^2;
Tf2_sim         = abs(2*sind(beta_sim) ./( sind(beta_sim)  + sqrt( n^2-
cosd(beta_sim).^2)  )).^2;
Ti2Tf2_sim      = Ti2_sim.*Tf2_sim;
I_sim  = diff_selfaffine(qx_sim,qz,k,res_qx,zeta,h,r0,sigma_film,Ti2Tf2_sim,qc,I0);  %
evaluate function

figure
errorbar(qx,Intens,sFit(:,4),'o');        %,'markersize',markersize);
hold on;
plot(qx_sim,I_sim);
set(gca,'yscale','log')
set(gca,'xscale','log')


%return
```

```
%% --- fitting routine
logFlag = 0;
if logFlag == 1
   Ifit = log10(Intens(fRange));
else
   Ifit = Intens;
end

% initialize fitting parameters
x         = [res_qx    zeta    h    r0     sigma_film      I0        ];
lb        = [1e-7      1       0    1      1               eps       ];      % eps is a small
number
ub        = [1e-4      Inf     1    20     Inf             100000    ];      % Inf is infinite
fitFlag  = [1          1       1    0      1               1         ];
x1 = x(find(fitFlag==1));
x2 = x(find(fitFlag==0));
lb1 = lb(find(fitFlag==1));
ub1 = ub(find(fitFlag==1));
options = optimset (...
   'Display','Iter',...
    'TolX',1e-6,...
    'TolFun',1e-6,...
    'MaxFunEvals',5000,...
    'MaxIter',3000);
[fittedX1,resnorm,residual,exitflag,output,~,jacobian] =
lsqcurvefit(@rocking_selfaffine_fit,x1,qx(fRange),Ifit,lb1,ub1,options,x2,fitFlag,qz,k,Ti2
Tf2(fRange),qc);

% --- error estimation
s2=resnorm/(length(residual) - 3);
[Q,R]=qr(jacobian,0);
Rinv=inv(R);
sigmaest=(Rinv*Rinv')*s2;
stderrors=sqrt(diag(sigmaest));
[fittedX1',full(stderrors)]
exitflag
```

```
%% --- smooth and plot curves
% plot raw data
% plot raw data
markersize = 6;
linewidth = 2;

hFig = figure(...
    'position',[100,20,500,600],...
    'PaperPosition',[0.25,0.25,8.25,10.75]);
subplot(7,1,1:5);
hold on;
errorbar(qx,Intens,sFit(:,4),'o','markersize',markersize);

% plot fitting curve
x=zeros(1,length(fitFlag));
x(find(fitFlag==1)) = fittedX1;
x(find(fitFlag==0)) = x2;
res_qx    = x(1);
zeta   = x(2);
h     = x(3);
r0    = x(4);
sigma_film  = x(5);
I0    = x(6);
Im   = diff_selfaffine(qx,qz,k,res_qx,zeta,h,r0,sigma_film,Ti2Tf2,qc,I0);     % evaluate function
residual = (Intens-Im);
plot(qx,Im,'linewidth',linewidth);
set(gca,'yscale','log','xscale','log');
set(gca,'yminortick','on','xminortick','on');
ylabel('Diffuse Intensity (a.u.)');
xlabel('q_x (A^{-1})');
box on; grid on;

% plot residual
subplot(7,1,6:7);
plot(qx,residual,'o-','markersize',markersize);
ylabel('Residual');
```

```
xlabel('q_x (A^{-1})');
box on; grid on;
set(gca,'xscale','log');

return


%% assemble result
fresult = [sFit, Im];
save File Name.dat fresult -ASCII -Tabs
```

APPENDIX B

DIFFERENTIAL SCANNING CALORIMETRY (DSC) FOR POLYSTYRENE

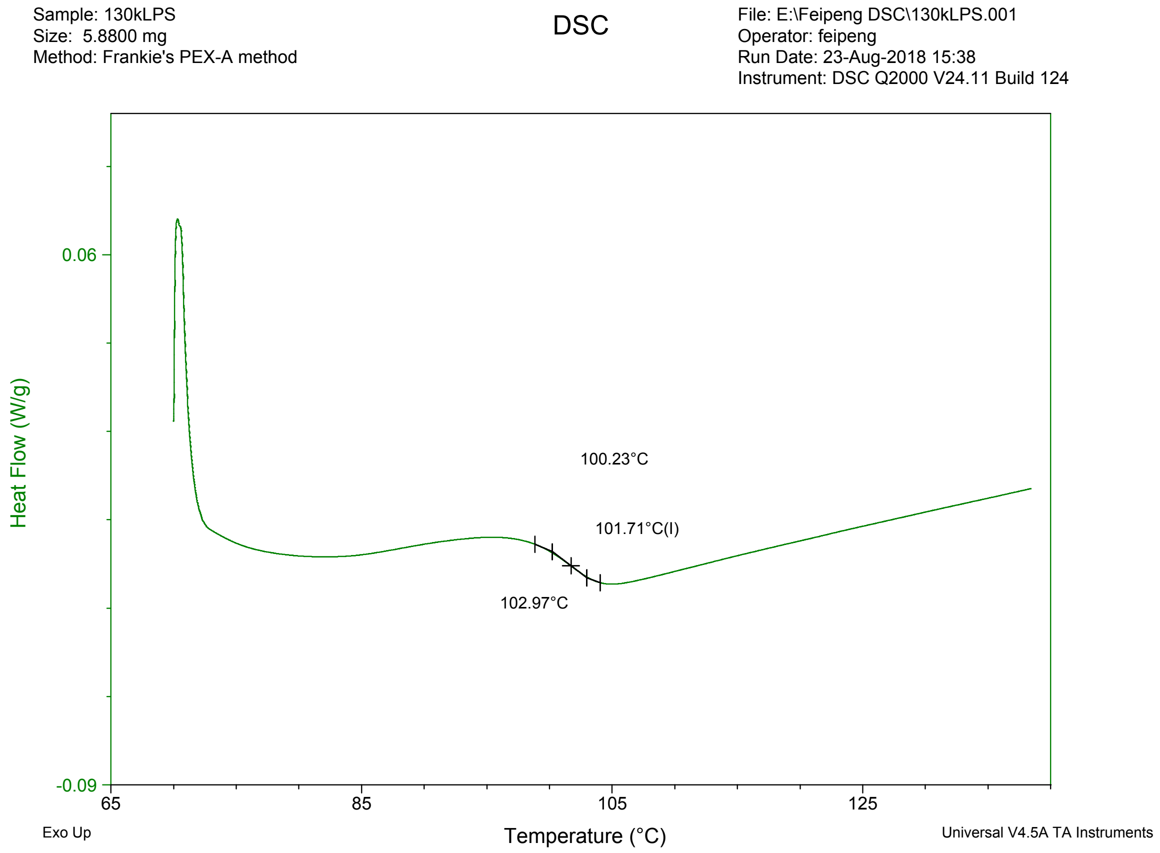

APPENDIX C

EQUIVALENT ELECTRICAL CIRCUIT FITTING OF THE NYQUIST PLOT

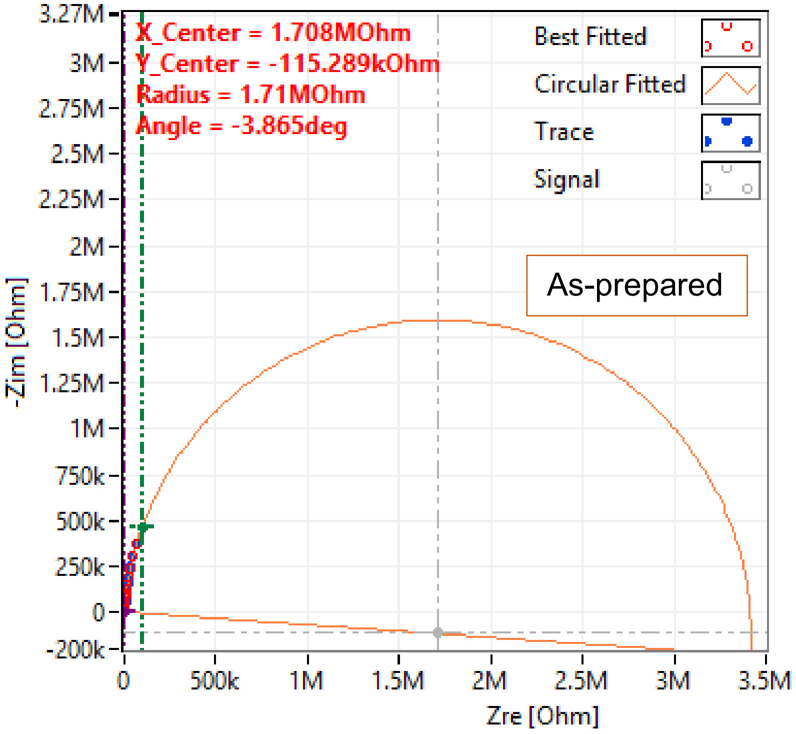

Figure C.1 Equivalent electrical circuit (EEC) fitting of the Nyquist plot of as-prepared SU-8 epoxy crosslinked with IPDA.

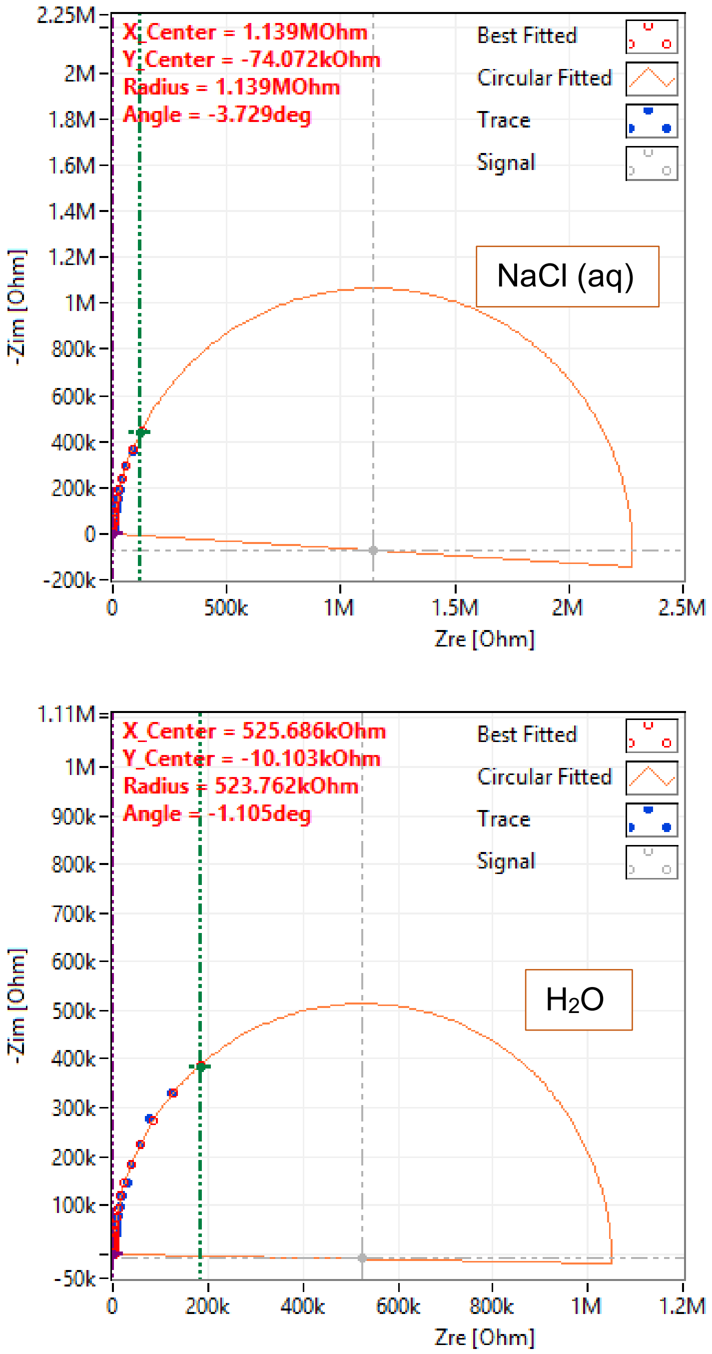

Figure C.2 Equivalent electrical circuit (EEC) fitting of the Nyquist plot of SU-8 epoxy crosslinked with IPDA after 1 hour exposure to H_2O or 3.5 wt % NaCl aqueous solution.

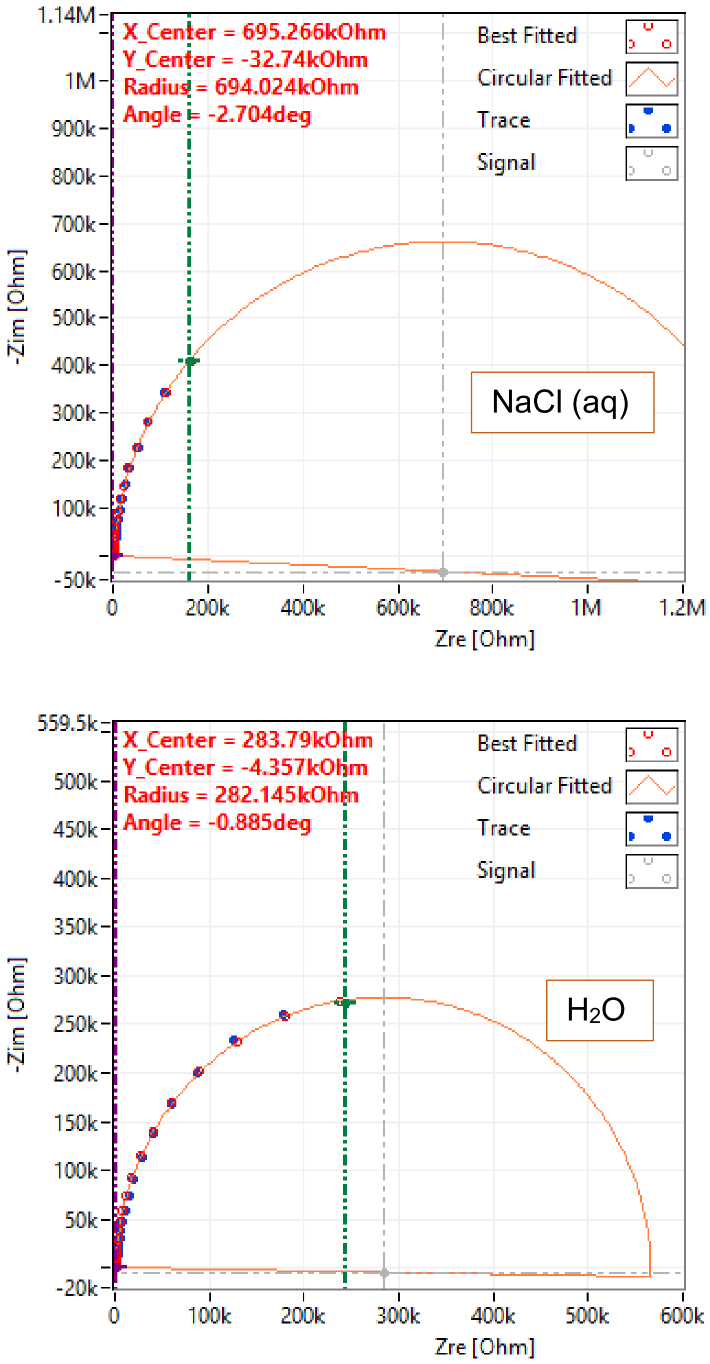

Figure C.3 Equivalent electrical circuit (EEC) fitting of the Nyquist plot of SU-8 epoxy crosslinked with IPDA after 2 hour exposure to H_2O or 3.5 wt % NaCl aqueous solution.

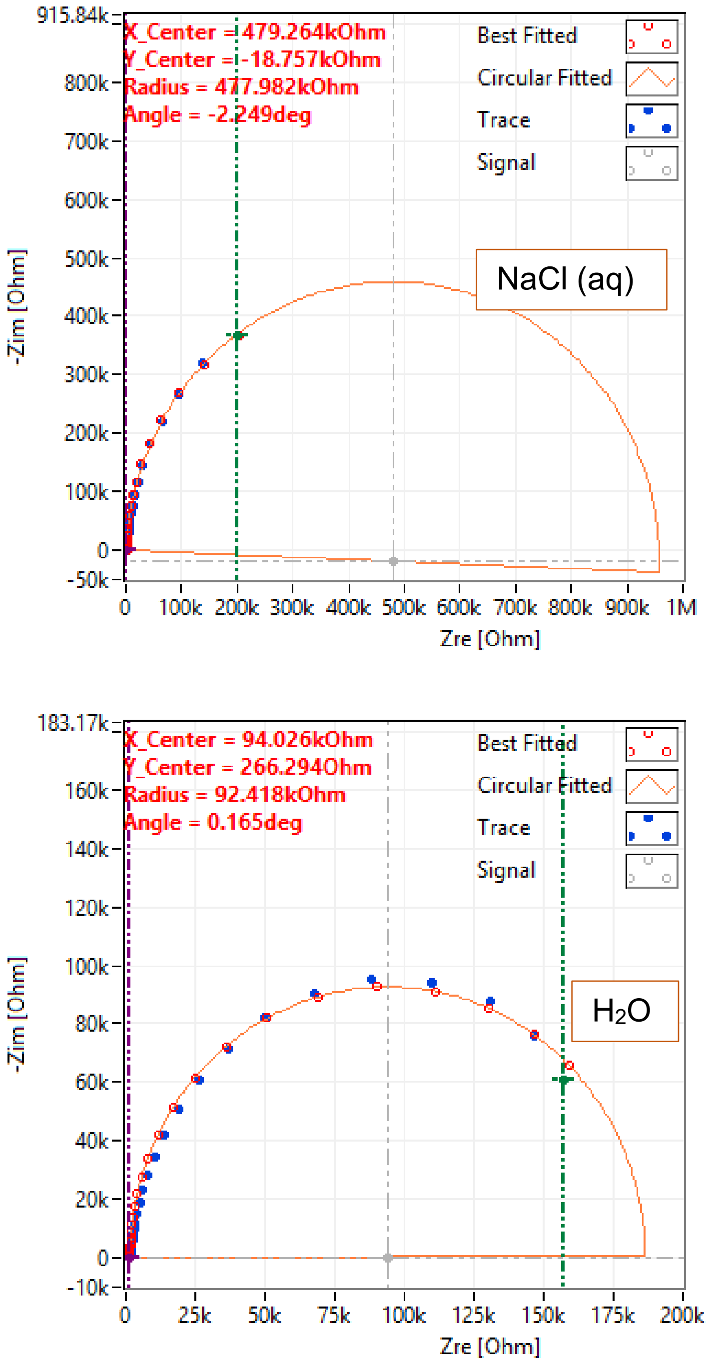

Figure C.4 Equivalent electrical circuit (EEC) fitting of the Nyquist plot of SU-8 epoxy crosslinked with IPDA after 3 hour exposure to H_2O or 3.5 wt % NaCl aqueous solution.

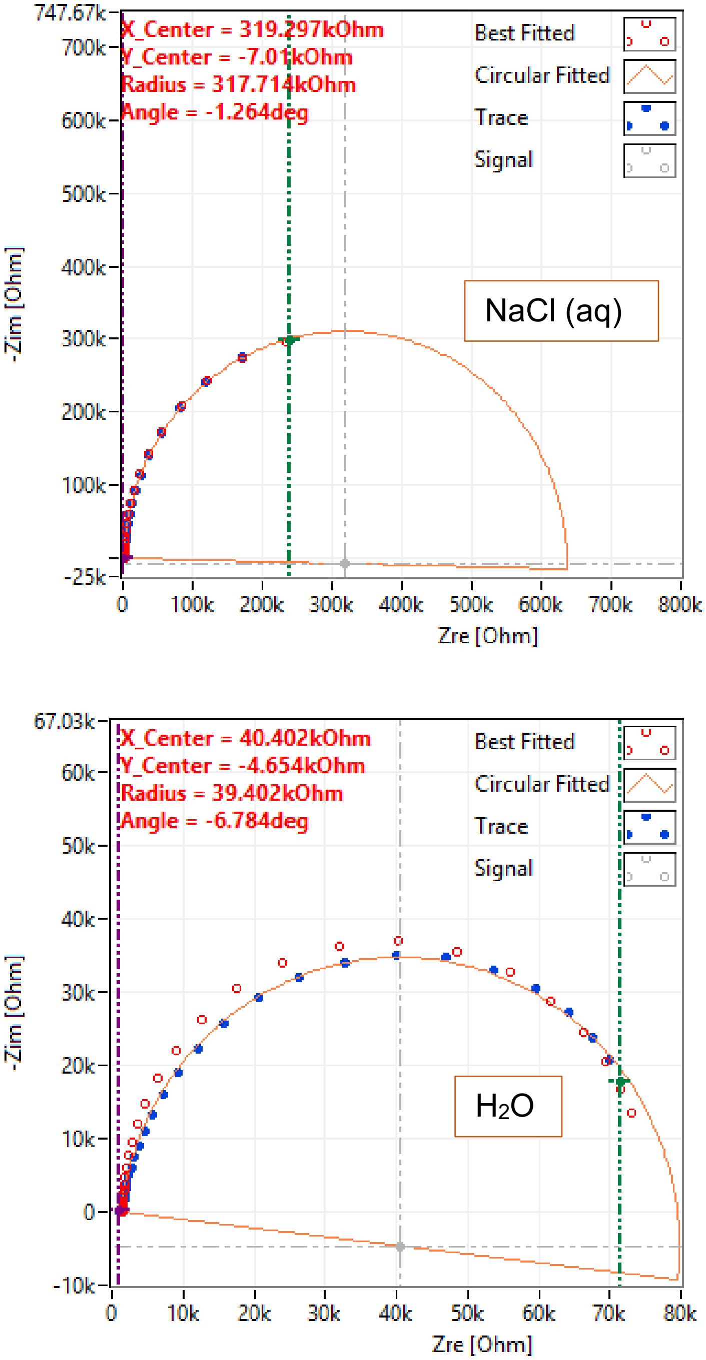

Figure C.5 Equivalent electrical circuit (EEC) fitting of the Nyquist plot of SU-8 epoxy crosslinked with IPDA after 4 hour exposure to H_2O or 3.5 wt % NaCl aqueous solution.

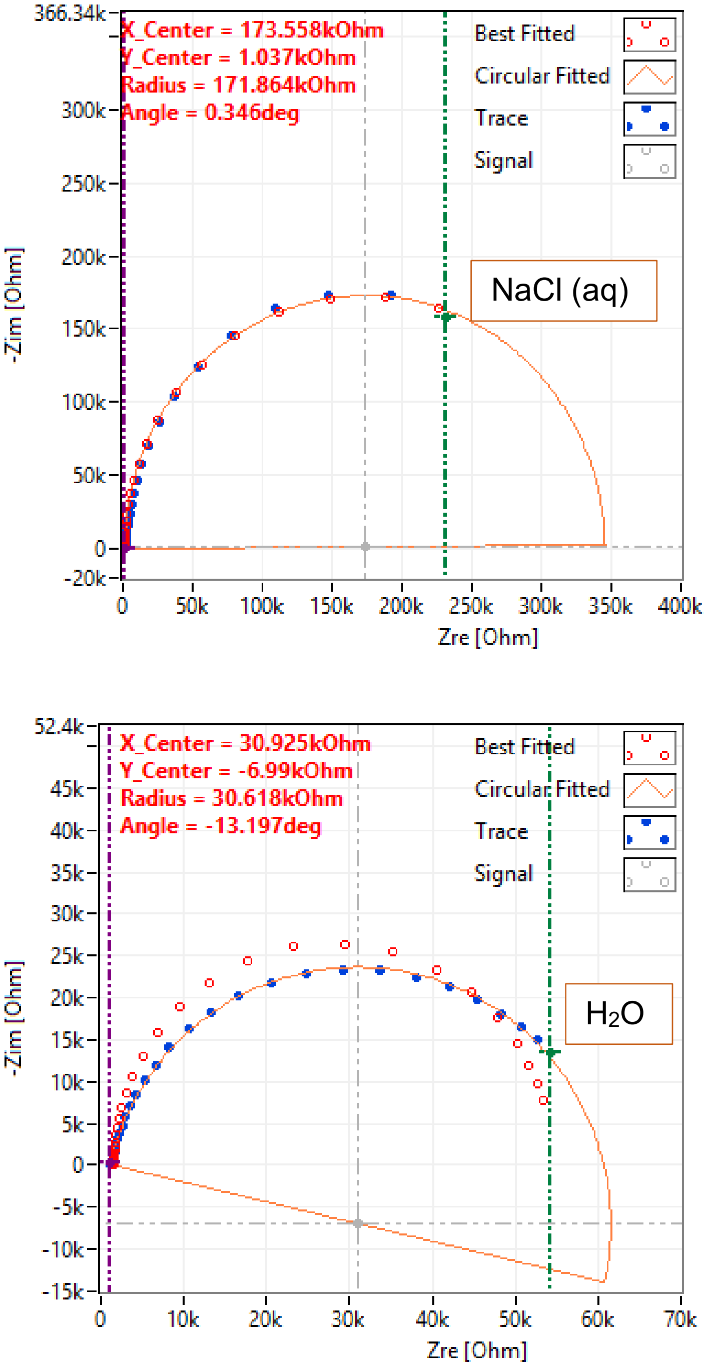

Figure C.6 Equivalent electrical circuit (EEC) fitting of the Nyquist plot of SU-8 epoxy crosslinked with IPDA after 5 hour exposure to H_2O or 3.5 wt % NaCl aqueous solution.

APPENDIX D

TAPPING MODE AFM IMAGES AND ROCKING CURVE FITTING

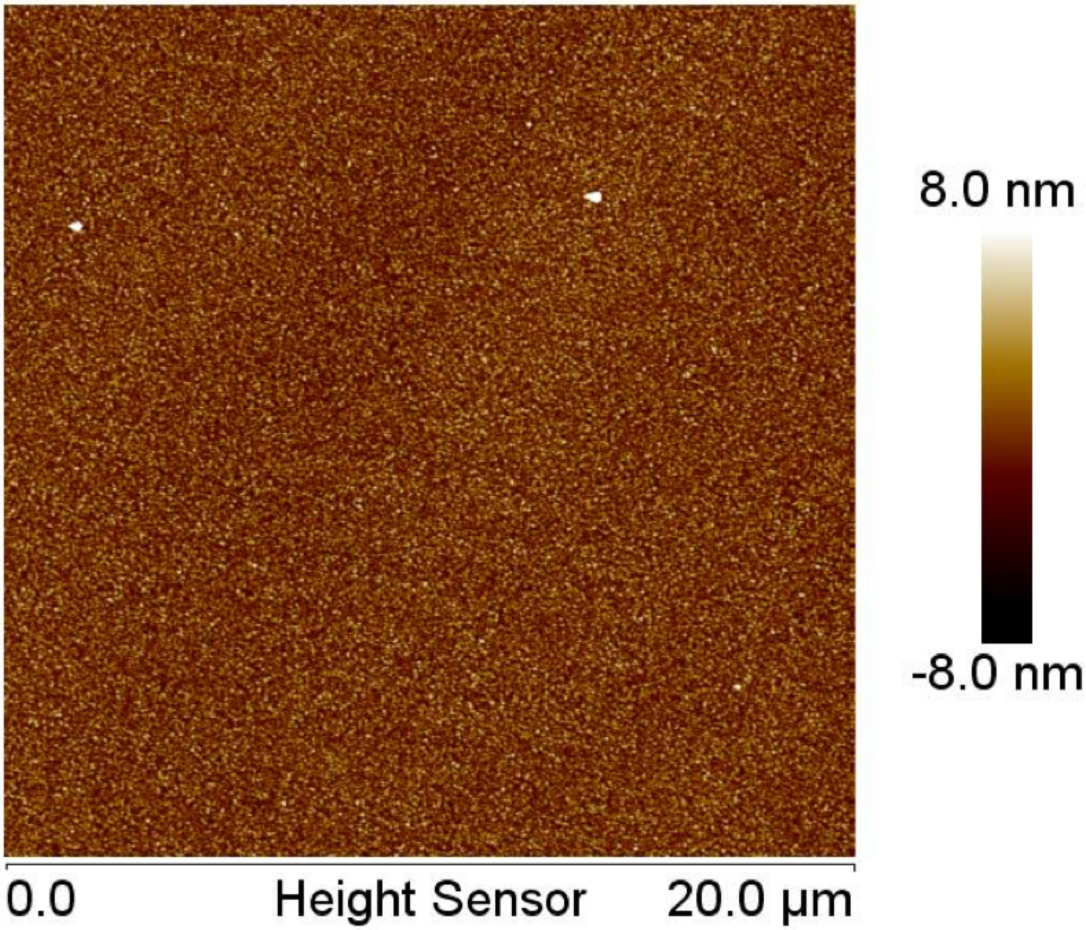

Figure D.1 Tapping mode AFM images (20 µm × 20 µm) of Al surface morphology after 20 min exposure to 1 wt % NaCl aqueous solution.

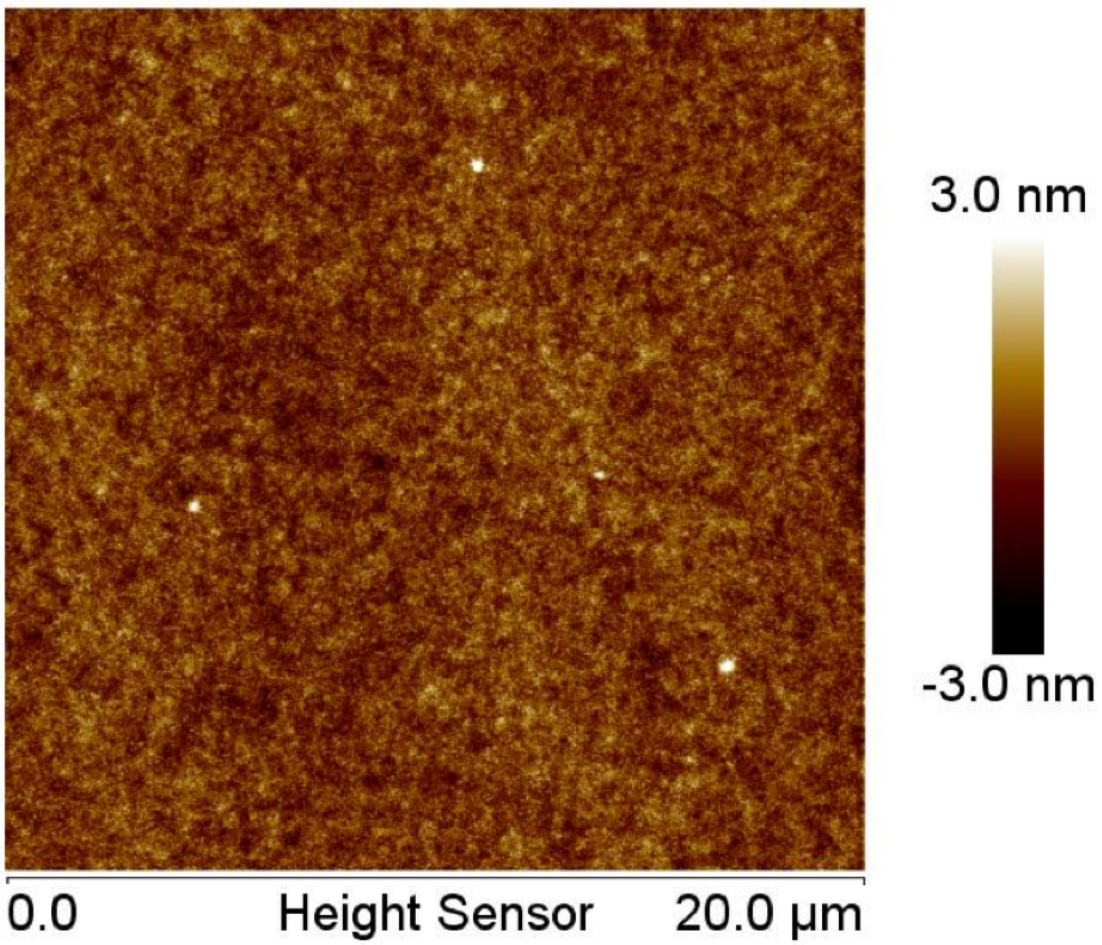

Figure D.2 Tapping mode AFM images (20 µm × 20 µm) of epoxy coating on aluminum after 12-hour exposure to 3.5 wt % NaCl aqueous solution.

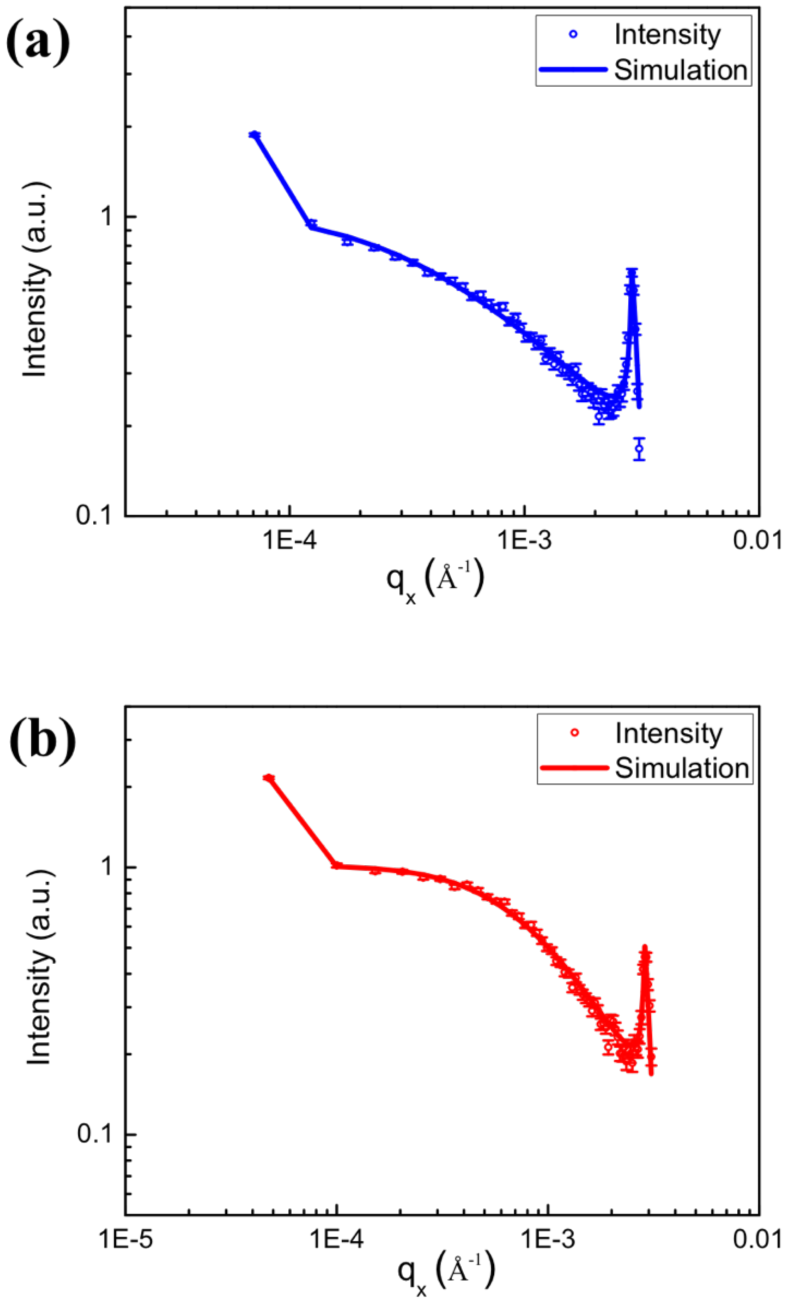

Figure D.3 Self-affine model fitting of rocking curve data for samples from EPON SU-8 crosslinked with (a) isophorone diamine (IPDA) and (b) EPIKURE 6870-W-53 measured at scattering angle of 1.460°.

APPENDIX E

PS CHAIN CONFORMATION ON QUARTZ/GRAPHITE SUBSTRATE

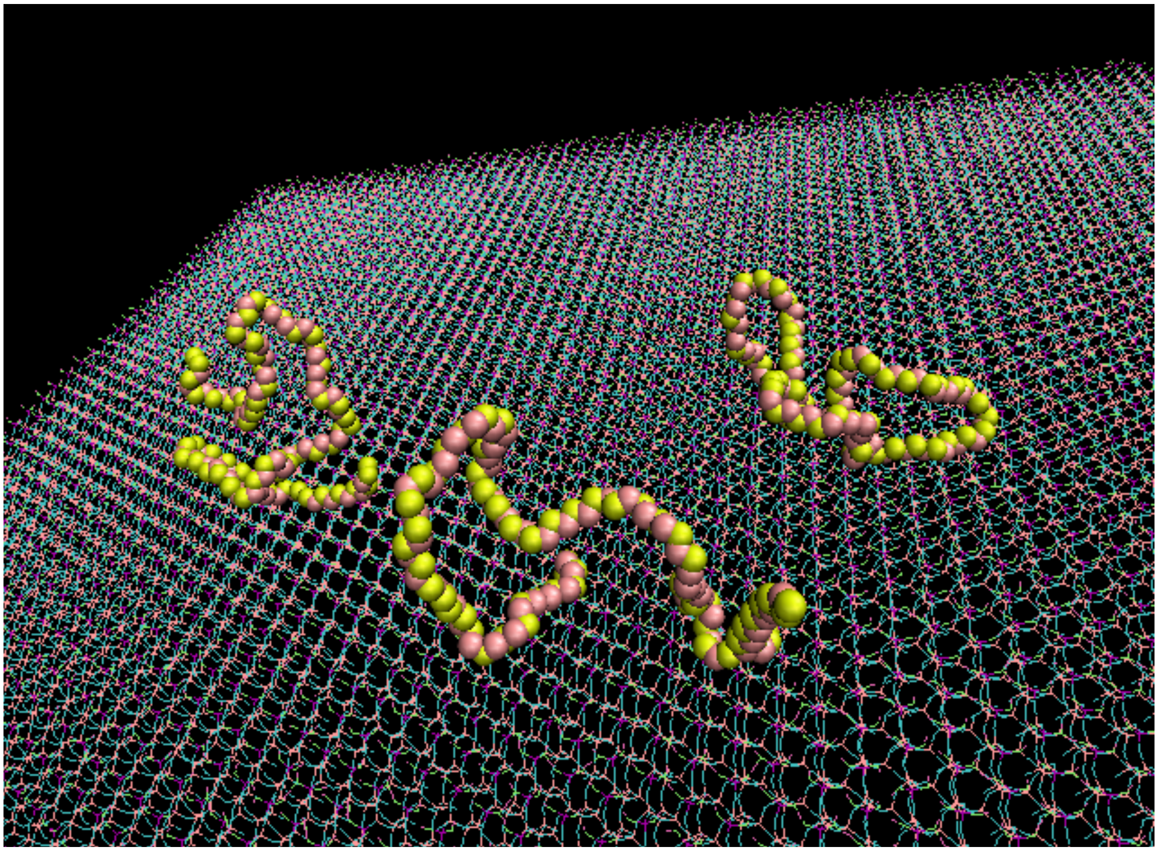

Figure E.1 Space filling model for polystyrene (PS) chains forming loops on hydroxylated α-quartz. Selected few chains in a 13 nm polymer film adsorbed on the substrate are shown for clarity. Simulation provided by Mesfin Tsige.

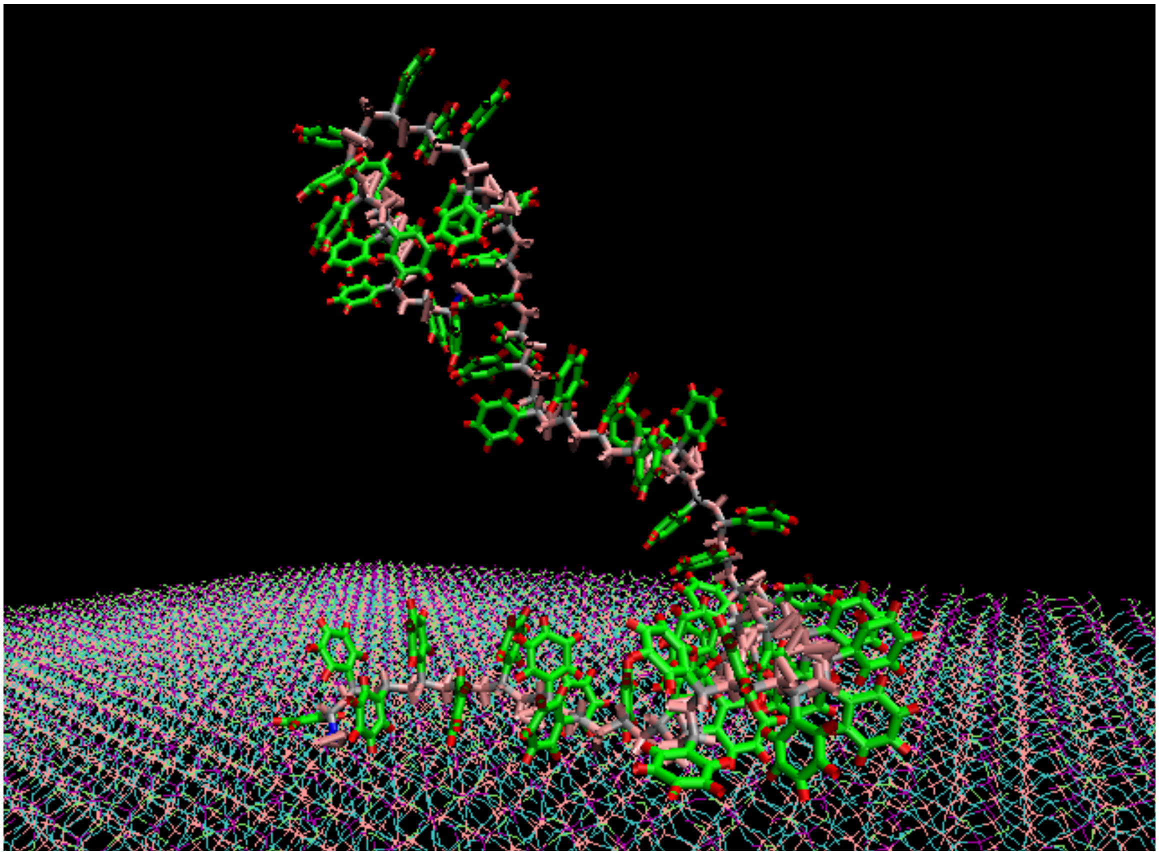

Figure E.2 Stick model for PS chains on hydroxylated α-quartz in which phenyl rings are dominantly pointing towards the substrate. A single selected chain in a 13 nm polymer film adsorbed on the substrate is shown for clarity; different coloring is used for clarity. Simulation provided by Mesfin Tsige.

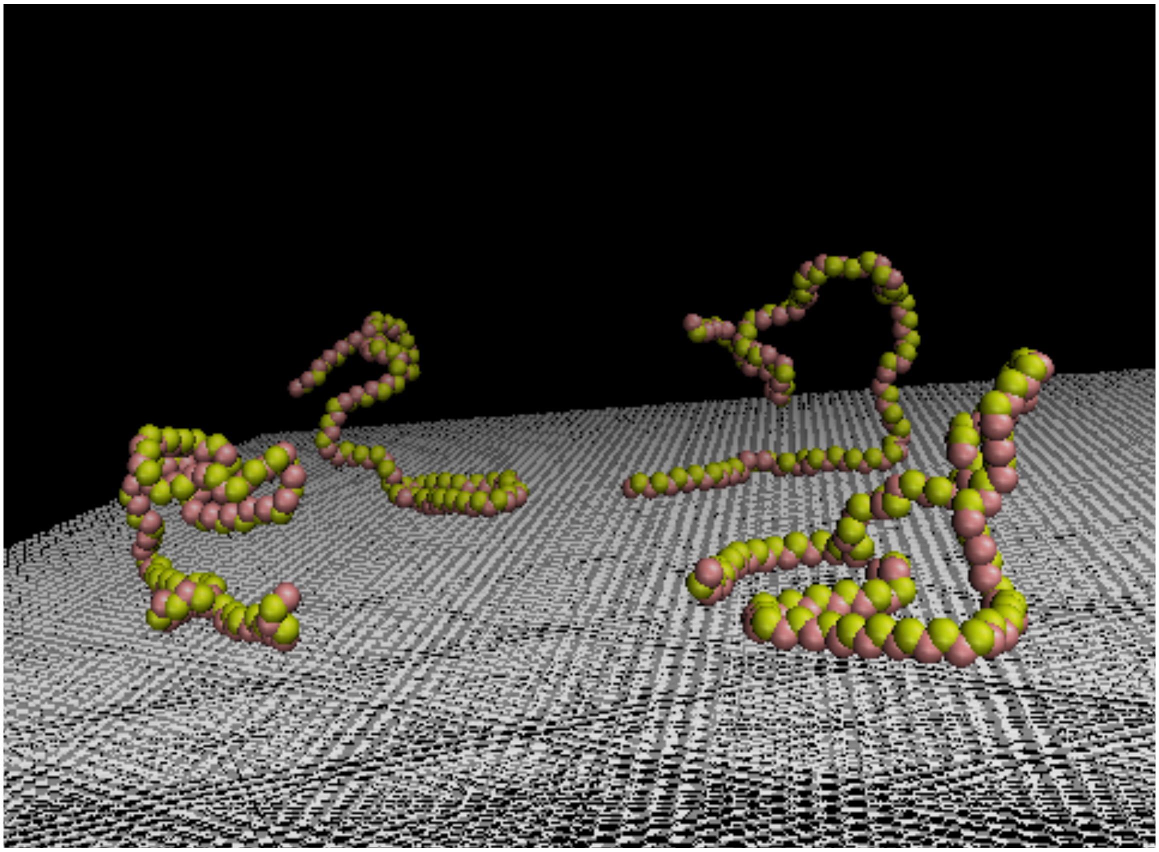

Figure E.3 Space filling model for polystyrene (PS) chains forming loops on graphite. Selected few chains in a 13 nm polymer film adsorbed on the substrate are shown for clarity. Simulation provided by Mesfin Tsige.

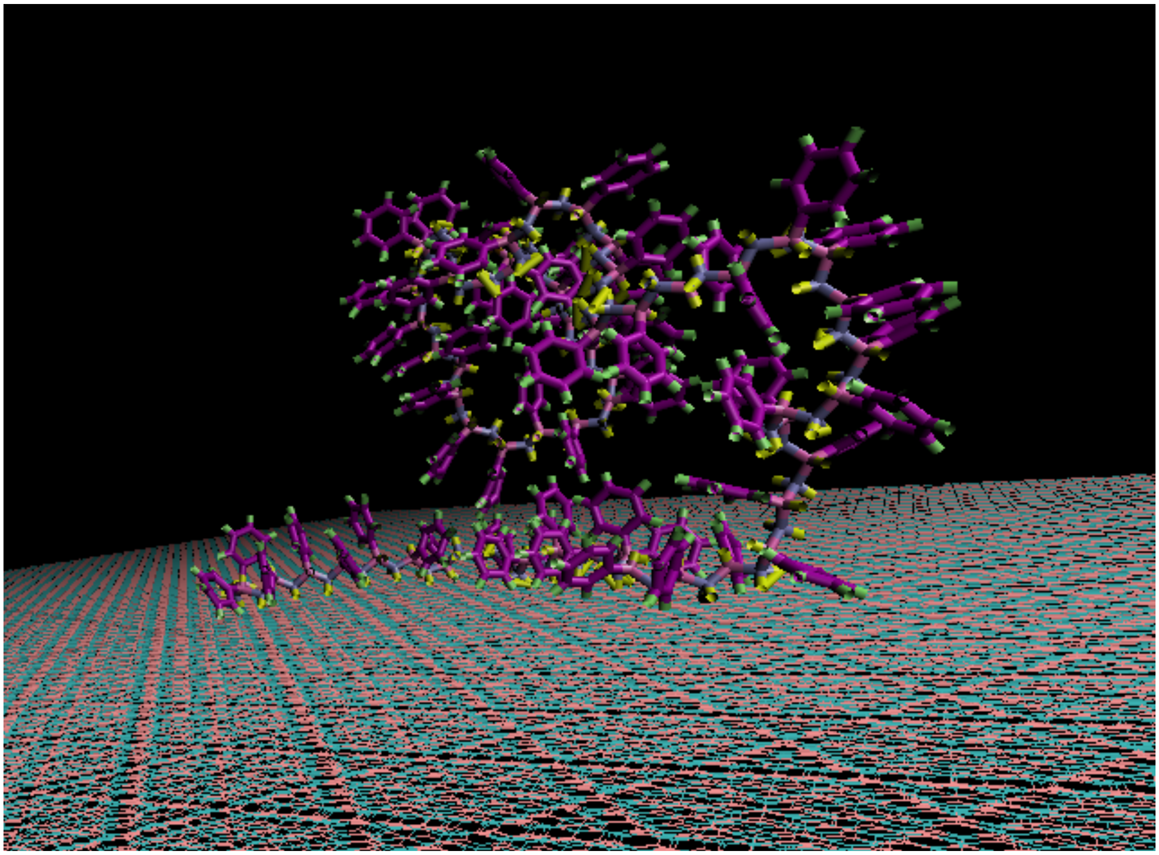

Figure E.4 Stick model for PS chains on graphite in which -CH_2 groups are pointing toward the substrate. A single selected chain in a 13 nm polymer film adsorbed on the substrate is shown for clarity; different coloring is used for clarity. Simulation provided by Mesfin Tsige.